

Understanding Intermolecular Attraction:  
Fundamental Science and Environmental Applications

A DISSERTATION  
SUBMITTED TO THE FACULTY OF THE  
UNIVERSITY OF MINNESOTA  
BY

Rebecca B. Mackenzie

IN PARTIAL FULFILLMET OF THE REQUIREMENTS  
FOR THE DEGREE OF  
DOCTOR OF PHILOSOPHY

Dr. Kenneth R. Leopold, Advisor

October, 2016

Copyright © 2016 by Rebecca B. Mackenzie

## Acknowledgments

Much of my success in graduate school is due to the support and kindness of my advisor, Ken Leopold. He is an exceptional scientist and mentor. From conventional advisor-student conversations about tunneling and the gender gap in science to less standard topics like musical productions and spice combinations, Ken was always available. His integrity as a scientist is unparalleled and I respect him deeply for it. He has always acted with my best interests in mind. A better advisor could not be imagined.

Many thanks to my lab mates, Brooke, Chris, CJ and Anna, for being wonderful peers and colleagues. Chris Dewberry requires special acknowledgment for his tireless work developing and building the chirped-pulse FTMW. Will Isley is an accomplished scientist, perhaps an even better gamer, and an outstanding friend. Many thanks to him for his guidance with theoretical calculations as well as discussions on fantasy fiction novels, and excellent board game recommendations. Ben Geisbauer not only improved our lab with his inventive woodworking but also has become a great friend over the last few years. To the rest of the physical chemistry professors and graduate students, thank you for the community you have created and for your constructive criticism of my work.

To any student I worked with who even slightly insinuated that I helped them understand a concept- thank you. Those moments of encouragement, no matter how small, were invaluable in keeping my spirits up.

I could not ask for more supportive friends. Julie, Sara, Jessie, Kelsey, Betsy, and Zindzi have been a veritable force of good cheer over the last five years. Thanks to my family- regardless of the situation, I know that we will always be there for each other.

To my two favorite bears, Ani Mackenzie and Lulu Fahrner, thanks for being constant reminders of what is most important in life. Coming home to your unconditional love brought sunshine to every day. Being responsible for you is my favorite job. And finally, much gratitude is due to my partner, Sam. Much like our girls, you put life in perspective. Whether I needed a shoulder to cry on, a friend to get a beer with, a person to rant to, or an email editor, you were there.

Dedication

For Jane Bell Mackenzie

## Table of Contents

List of Tables.....	iv
List of Figures .....	vii
Introduction .....	1
Chapter 1 : Gas Phase Observation and Microwave Spectroscopic Characterization of Formic Sulfuric Anhydride .....	6
Chapter 2 : The Trimethylamine - Formic Acid Complex .....	17
Chapter 3 : The Formic Acid – Nitric Acid Complex: Microwave Spectrum, Structure, and Proton Transfer .....	32
Chapter 4 : Intramolecular Competition Between n-Pair and $\pi$ -Pair Hydrogen Bonding: Microwave Spectrum and Internal Dynamics of the Pyridine – Acetylene Hydrogen-Bonded Complex .....	60
Chapter 5 : Multidimensional Large Amplitude Dynamics in the Pyridine – Water Complex .....	86
Chapter 6 : Effects of a Remote Binding Partner on the Electric Field and Electric Field Gradient at an Atom in a Weakly Bound Trimer .....	98
References .....	119
Appendices .....	142
Appendix A : Supplemental Material for Chapter 1 .....	143
Appendix B : Supplemental Material for Chapter 2.....	160
Appendix C : Supplemental Material for Chapter 3.....	164
Appendix D : Supplemental Material for Chapter 4 .....	175
Appendix E : Supplemental Material for Chapter 5.....	191
Appendix F : Supplemental Material for Chapter 6.....	205

## List of Tables

Table 1.1 Comparison of Experimental and Theoretical Intermolecular Distances .....	12
Table 1.2 Experimental and Calculated Rotational Constants for FSA .....	13
Table 2.1 Fitted Spectroscopic Constants for Three Isotopologues of TMA-HCOOH ....	23
Table 3.1 Observed Spectroscopic Constants for Isotopologues of HNO <sub>3</sub> -HCOOH Without Substitution in the H-Bonds .....	40
Table 3.2 Observed Spectroscopic Constants for Isotopologues of HNO <sub>3</sub> -HCOOH with Substitution in the H-Bonds .....	41
Table 3.3 Selected <i>Ab Initio</i> Structural Parameters for HCOOH-HNO <sub>3</sub> .....	45
Table 3.4 Comparison Between HCOOH-HNO <sub>3</sub> and Several Carboxylic Acid Dimers .	46
Table 3.5 Experimental Structural Parameters for Isotopologues of HNO <sub>3</sub> -HCOOH .....	54
Table 4.1 Spectroscopic Constants for H <sub>5</sub> C <sub>5</sub> N-HCCH and -DCCD .....	73
Table 4.2 Spectroscopic Constants for H <sub>5</sub> C <sub>5</sub> N-DCCH, and -HCCD.....	74
Table 4.3 Spectroscopic Constants for H <sub>5</sub> C <sub>5</sub> N-HCCH with <sup>13</sup> C-pyridine substitutions ..	75
Table 4.4 Experimental Structural Parameters for Py-HCCH .....	82
Table 5.1 Spectroscopic Constants for Py-H <sub>2</sub> O and Py-D <sub>2</sub> O.....	94
Table 6.1 Spectroscopic Constants of Kr-SO <sub>3</sub> and Kr-SO <sub>3</sub> -CO .....	103
Table 6.2 Experimental Structural Parameters for Kr-SO <sub>3</sub> and Kr-SO <sub>3</sub> -CO.....	107
Table 6.3 Properties of Kr-SO <sub>3</sub> and Kr-SO <sub>3</sub> -CO.....	108
Table 6.4 BLW Decomposition Results for Kr-SO <sub>3</sub> and Kr-SO <sub>3</sub> -CO.....	111
Table A.1 Comparison of Theoretical Rotational Constants with Experimental Results and Predicted Dipole Moment Components.....	149
Table A.2 Theoretical Predictions for SO <sub>3</sub> , H <sub>2</sub> O, and HCOOH complexes.....	150
Table A.3 Selected FSA Structural Parameters from M06-2X and MP2 Calculations...	151
Table A.4 Cartesian Coordinates for Previously Unstudied Species from Theory.....	152
Table A.5 Observed Transitions for the Parent Isotopologue of FSA (HOSO <sub>3</sub> CHO) ....	153
Table A.6 Observed Transitions for the <sup>34</sup> S Isotopologue of FSA (HO <sup>34</sup> SO <sub>3</sub> CHO).....	154
Table A.7 Observed Transitions for the <sup>13</sup> C Isotopologue of FSA (HOSO <sub>3</sub> <sup>13</sup> CHO) .....	155
Table A.8 Observed Transitions of DOSO <sub>3</sub> CHO.....	156
Table A.9 Observed Transitions of HOSO <sub>3</sub> CDO.....	158
Table A.10 Spectroscopic Constants for Observed Isotopologues of FSA .....	159

Table B.1 Observed Transitions for TMA-HCOOH.....	160
Table B.2 Observed Transitions for TMA-DCOOH.....	161
Table B.3 Observed Transitions for TMA( <sup>13</sup> C11)-HCOOH .....	162
Table B.4 Theoretical Atomic Cartesian Coordinates for the Complex.....	163
Table C.1 Observed Transitions for HCOOH-HNO <sub>3</sub> 0 <sup>+</sup> State .....	164
Table C.2 Observed Transitions for HCOOH-HNO <sub>3</sub> 0 <sup>-</sup> State.....	166
Table C.3 Observed Transitions for HCOOH-H <sup>15</sup> NO <sub>3</sub> 0 <sup>+</sup> State.....	167
Table C.4 Observed Transitions for HCOOH-H <sup>15</sup> NO <sub>3</sub> 0 <sup>-</sup> State.....	168
Table C.5 Observed Transitions for HCOOD-HNO <sub>3</sub> .....	169
Table C.6 Observed Transitions for HCOOD-H <sup>15</sup> NO <sub>3</sub> .....	171
Table C.7 Observed Transitions for H <sup>13</sup> COOH-HNO <sub>3</sub> .....	172
Table C.8 Observed Transitions for HCOOH-DNO <sub>3</sub> .....	173
Table C.9 Observed Transitions for DCOOH-HNO <sub>3</sub> .....	174
Table D.1 Observed Transitions for H <sub>5</sub> C <sub>5</sub> N-HCCH 0 <sup>+</sup> State.....	175
Table D.2 Observed Transitions for H <sub>5</sub> C <sub>5</sub> N-HCCH 0 <sup>-</sup> State .....	178
Table D.3 Observed Transitions for H <sub>5</sub> C <sub>5</sub> N-DCCD 0 <sup>+</sup> State.....	181
Table D.4 Observed Transitions for H <sub>5</sub> C <sub>5</sub> N-DCCD 0 <sup>-</sup> State .....	182
Table D.5 Observed Transitions for H <sub>5</sub> C <sub>5</sub> N-DCCH 0 <sup>+</sup> State.....	183
Table D.6 Observed Transitions for H <sub>5</sub> C <sub>5</sub> N-DCCH 0 <sup>-</sup> State .....	184
Table D.7 Observed Transitions for H <sub>5</sub> C <sub>5</sub> N-HCCD 0 <sup>+</sup> State.....	185
Table D.8 Observed Transitions for H <sub>5</sub> C <sub>5</sub> N-HCCD 0 <sup>-</sup> State .....	186
Table D.9 Observed Transitions for Inner-meta <sup>13</sup> C- H <sub>5</sub> C <sub>5</sub> N-HCCH .....	187
Table D.10 Observed Transitions for Outer-meta <sup>13</sup> C- H <sub>5</sub> C <sub>5</sub> N-HCCH.....	188
Table D.11 Observed Transitions for Inner-ortho <sup>13</sup> C- H <sub>5</sub> C <sub>5</sub> N-HCCH.....	189
Table D.12 Observed Transitions for Outer-ortho <sup>13</sup> C- H <sub>5</sub> C <sub>5</sub> N-HCCH .....	190
Table E.1 H <sub>2</sub> O - Pyridine Transitions.....	191
Table E.2 D <sub>2</sub> O - Pyridine Transitions.....	197
Table E.3 H <sub>2</sub> O - Pyridine Minimum Energy Structure Coordinates .....	201
Table E.4 In-Plane Rocking Motion Transition State Coordinates.....	202
Table E.5 Free Proton Wag Transition State Coordinates .....	203

Table E.6 Water Rotation Transition State Coordinates .....	203
Table E.7 C <sub>2</sub> Rotation of Water Transition State Coordinates .....	204
Table F.1 Observed transitions for Kr-SO <sub>3</sub> and Kr-SO <sub>3</sub> -CO isotopologues.....	205



## List of Figures

Figure 1.1 Experimental Setup and Results for FSA .....	11
Figure 1.2 FSA Energetics .....	14
Figure 2.1 Predicted Structure of TMA-HCOOH.....	21
Figure 2.2 Chirp Spectrum of TMA-HCOOH.....	23
Figure 2.3 Definition of Variables Used to Describe the Structure of TMA-HCOOH....	26
Figure 2.4 Comparison of $Q_{PT}^B$ for TMA-acid Complexes .....	29
Figure 2.5 Correlation Between the Proton Transfer Parameter and Proton Affinity .....	29
Figure 3.1 Cavity Spectrum of HCOOH-H <sup>15</sup> NO <sub>3</sub> .....	38
Figure 3.2 Equilibrium and Transition State Structures of HCOOH-HNO <sub>3</sub> .....	47
Figure 3.3 Definitions of Structural Parameters for HCOOH-HNO <sub>3</sub> .....	52
Figure 4.1 HCl-H <sub>2</sub> CO Complex .....	63
Figure 4.2 Cavity and Chirped-Pulse Spectrum of py-HCCH.....	66
Figure 4.3 1-Dimensional Potential Proposed for py-HCCH .....	69
Figure 4.4 Structure Parameters of the py-HCCH Complex.....	78
Figure 4.5 Recommended Experimental Structure for py-HCCH .....	81
Figure 5.1 Theoretical Results for the py-H <sub>2</sub> O Complex .....	89
Figure 5.2 Depiction of Possible py-H <sub>2</sub> O Internal Motions .....	90
Figure 5.3 Comparison of the $3_{13} - 2_{12}$ Transitions for H <sub>2</sub> O – and D <sub>2</sub> O – pyridine .....	91
Figure 5.4 Chirped-Pulse Spectra of py-H <sub>2</sub> O $K=0$ Transitions.....	93
Figure 5.5 Cavity Spectra of py - H <sub>2</sub> O .....	93
Figure 5.6 Qualitative Energy Diagram Resulting from Multiple Internal Motions.....	96
Figure 6.1 Cavity Spectrum of <sup>83</sup> Kr-SO <sub>3</sub> -CO .....	102
Figure 6.2 Definition of Structural Coordinates for Kr-SO <sub>3</sub> and Kr-SO <sub>3</sub> -CO.....	105
Figure 6.3 Structural Results for Kr-SO <sub>3</sub> and Kr-SO <sub>3</sub> -CO .....	106
Figure 6.4 Electron Density Difference (EDD) maps .....	112
Figure 6.5 Summary of the BLW Decomposition of $E_z$ at the Kr Nucleus .....	116
Figure 6.6 Summary of the BLW Decomposition of $eQq$ of <sup>83</sup> Kr .....	117
Figure A.1 Cavity Spectrum of FSA Rotational Transition .....	144
Figure A.2 DFT Potential Energy Landscape of H <sub>2</sub> O, SO <sub>3</sub> , and HCOOH.....	145
Figure A.3 Energy Comparison of SO <sub>3</sub> -HCOOH Isomers .....	146

Figure A.4 Energy Comparison of FSA Isomers .....	147
Figure A.5 Potential Energy Surface for the Formation of FSA Analogues .....	148

## Introduction

Intermolecular forces are ubiquitous throughout nature, and though individually weak, in aggregate they conspire to define the condensed phase. Thus, these forces underlie many chemical phenomena. While much can be gained by studying intermolecular forces in the bulk phase, research on molecular clusters provides a unique perspective. Probing just a few molecules simplifies the system, allowing for detailed analysis of the individual forces that bind molecules together. Furthermore, clusters are the intermediate step between isolated molecules and the condensed phase, providing insight into how macroscopic properties evolve. Studying successively larger clusters allows chemists to identify when exactly chemical change occurs. This approach can be applied to a number of fundamental questions. For example, what level of solvation is necessary to ionize an acid, i.e. how many water molecules are required? Of course, at the macroscopic level, we describe the strength of an acid by its  $pK_a$ . While the  $pK_a$  likely correlates with the number of water molecules required to achieve ionization, it does not directly address the question. An analysis of clusters could answer this question satisfactorily.<sup>1</sup> Take for another example the minimum size of an ice crystal. The crystal structure of bulk ice is well-known, but that does not translate into answering how small an ice crystal can be. Again, research of progressively smaller clusters is central in addressing this question.<sup>2</sup> These questions are representative of the goals of cluster science, capturing the common themes of solvation, chemical change, and phase change.

Many varieties of spectroscopy have been used to probe the structure, energetics, and dynamics of small to mid-size molecular clusters. The Leopold group uses Fourier transform microwave spectroscopy (FTMW) to gather information on the molecular and electronic structure of complexes. FTMW has proven a powerful tool for studying clusters, with a rich history dating back to the 1980s when the Balle-Flygare spectrometer<sup>3</sup> was first introduced, eventually replacing the microwave studies that used molecular beam electric resonance spectroscopy.

However, much of the work presented here was made possible by more recent advances in microwave technology. Similar to the renaissance experienced in the 80s, the

introduction of the broadband chirped-pulse spectrometer has opened new doors for microwave spectroscopists. Developed in the Pate lab in 2008, the chirped-pulse FTMW can collect large swaths of rotational spectra concurrently.<sup>4</sup> In contrast, the Balle-Flygare spectrometer, a Fabry-Perot cavity instrument, provides exceptional resolution and sensitivity but is greatly limited by the speed with which data can be collected.

The cavity spectrometer in the Leopold lab was renovated in 2013 to incorporate the chirped-pulse technology.<sup>5</sup> Building on our existing spectrometer, microwave horns and circuitry were added along the axis perpendicular to the cavity mirrors. Briefly, our chirped-pulse spectrometer collects in 3 GHz segments with bounds of 6 and 18 GHz. A 3 GHz sweep is mixed with a microwave signal and coupled into the vacuum chamber via a microwave horn. The subsequent molecular emission is collected by a partner horn and recorded by an oscilloscope, which executes a Fourier transform and provides a frequency spectrum. Apart from economizing equipment and space, the tandem design of the instrument is beneficial in that both experiments can be performed without tampering with the molecular source.

The advantages of the chirped-pulse FTMW are demonstrated throughout my research. The speed of the chirped-pulse spectrometer was established with formic sulfuric anhydride (FSA) and the trimethylamine – formic acid complex, as both were observed and assigned in a matter of days (if not hours). Furthermore, we may never have observed even a single FSA transition on the cavity spectrometer, as it was an unexpected species far removed from our predictions. Similarly, we likely would not have deciphered the spectrum of pyridine-water as some transitions were hundreds of MHz away from their predictions due to severe perturbations. Lastly, direct comparison of signal intensities is occasionally useful in assigning a transition. Comparisons of cavity intensities are generally unreliable, whereas chirped-pulse intensities can be reasonably compared. This provided useful information in assigning the rotational spectrum of pyridine-acetylene. In sum, the chirped-pulse FTMW makes more challenging projects accessible, making this an exciting time in microwave spectroscopy.

Along with data gathered from FTMW experiments, every project was supplemented by theoretical work. Both *ab initio* and density functional theory methods have proven reliable for predicting the structure of small molecular complexes. The subsequently predicted rotational spectrum can often be an excellent starting point, especially for complexes that are relatively rigid. However, for clusters with complex internal dynamics, the predicted rotational spectrum is less instructive. The spectroscopic consequences of internal dynamics are extremely difficult to predict, requiring accurate knowledge of the barrier height and the effective reduced mass of the motion. Furthermore, the motions are often multidimensional, adding another level of complexity.

*For my dissertation, I have studied a variety of small clusters. These projects roughly fall into two categories: complexes that may be relevant to atmospheric aerosol formation and complexes that exhibit internal dynamics.*

With regard to the first subject, aerosols can be directly emitted or formed in the atmosphere. They are formed either through heterogeneous or homogeneous nucleation. The latter is the process through which particles are formed from isolated gas molecules and is an area where cluster science departs from the fundamental and is directly applicable.

Although much has been learned in the last few decades, predicting the rate of nucleation remains a challenge for atmospheric scientists. It has long been known that sulfuric acid is a central component for particle formation. Formed in the atmosphere from sulfur dioxide, sulfuric acid is a low-volatility compound that is highly hygroscopic. However, binary models using only water and sulfuric acid do not consistently predict particle formation rates. Thus, researchers have increased the complexity of their models, incorporating other common atmospheric molecules such as amines and the oxidation products of hydrocarbons.<sup>6</sup> These have led to more successful ternary models but the impact of aerosols remains one of the leading sources of uncertainty in current climate models.<sup>7</sup>

While the clusters I have studied are much smaller than the particles that directly impact the climate and air quality, homogeneous nucleation necessarily starts with small molecular clusters. The strength of these initial interactions, the subsequent change in the dipole moment, and the progress towards ionization (in the case of acid and base complexes) are relevant properties to the subsequent growth and development towards larger particles.

In particular, we became interested in recent research on the involvement of carboxylic acids in nucleation processes. Formic acid has been investigated in an alternative sulfuric acid formation mechanism<sup>8</sup> and its complexes with sulfuric acid<sup>9</sup> and amines<sup>10,11</sup> have been considered as potential accelerators in particle formation. Chapter 1 presents work on FSA, which was a delightfully unexpected project that emerged from our efforts to characterize the sulfuric acid – formic acid complex.<sup>12</sup> Chapter 2 details our work on the trimethylamine – formic acid complex, in which we aimed to measure the degree of proton transfer.<sup>13</sup> In the future, we hope to build off of these successes, using the chirped-pulse FTMW to track structural change in higher order clusters.

Chapters 3-5 deal with complexes that exhibit interesting internal dynamics. These projects were challenging, as internal motions can severely perturb the rotational spectrum in ways we cannot fully predict. In the examples presented here, the perturbations arise from the existence of two degenerate configurations. The configurations are separated by a finite barrier, resulting in a symmetric double-well potential. As the barrier increases, the vibrational levels collapse (i.e. the ground and first excited states approach each other). This results in a few spectroscopic consequences: (i) the rotational levels of the excited vibrational state may become populated, (ii) near-degeneracies may arise between Coriolis coupled states, resulting in strong perturbations in the spectrum and (iii) transitions between the ground and excited vibrational states may now be in the microwave region. How these exactly manifest in the spectrum also depends on the motion and dipole moment components. Furthermore, not only is it a challenge to assign the rotational spectrum, it can also be challenging to identify which motion (or motions) is causing the perturbation.

The work presented here on formic acid – nitric acid complex,<sup>14</sup> the pyridine – acetylene complex,<sup>15</sup> and the pyridine – water complex demonstrate how differently internal motions can affect the rotational spectra. They also showcase the entwined nature of structure and dynamics. These studies give depth to the static structure calculated at the minimum of a potential energy surface. We hope that this work can provide experimental touchstones for theoretical treatments of multidimensional large amplitude dynamics.

**Chapter 1 : Gas Phase Observation and Microwave Spectroscopic  
Characterization of Formic Sulfuric Anhydride**

From R. B. Mackenzie, C. T. Dewberry, K. R. Leopold, *Science* **349**, 58-61 (2015).  
Reprinted with permission from AAAS.



## Abstract

We report the observation of a covalently bound species, formic sulfuric anhydride (FSA), that is produced from formic acid and sulfur trioxide under supersonic jet conditions. FSA has been structurally characterized by means of microwave spectroscopy and further investigated by using density functional theory and ab initio calculations. Theory indicates that a  $\pi_2 + \pi_2 + \sigma_2$  cycloaddition reaction between  $\text{SO}_3$  and  $\text{HCOOH}$  is a plausible pathway to FSA formation and that such a mechanism would be effectively barrierless. We speculate on the possible role that FSA may play in the Earth's atmosphere.

There is an extensive literature on the chemistry of sulfur oxides and their derivatives. The area is rich in fundamental science and finds applications ranging from industrial chemistry to laboratory synthesis. Sulfur compounds are also active species in the atmosphere.<sup>16</sup> and, in particular, the oxides and oxyacids are important players in the formation of atmospheric aerosol.<sup>6</sup> Here, we present a microwave spectroscopic study of the anhydride derived from formic and sulfuric acids, produced in a supersonic jet containing HCOOH and SO<sub>3</sub>.

The present work was stimulated by a series of studies concerned with the formation of sulfuric acid in the atmosphere. The acid, which can form via both gas phase and aqueous phase processes, is generated in the gas phase by the oxidation of SO<sub>2</sub> to SO<sub>3</sub>, which is subsequently hydrated to give H<sub>2</sub>SO<sub>4</sub>,



Both theoretical and experimental studies of this reaction indicate that viable gas phase mechanisms involve a facilitator molecule. Using *ab initio* theory, Morokuma and Muguruma<sup>8</sup> showed that the addition of a second water molecule to H<sub>2</sub>O...SO<sub>3</sub> significantly lowers the activation barrier for eq. 1, and indeed kinetic data show a second order dependence on water concentration.<sup>17</sup> More recently, computational work by Hazra and Sinha has indicated that the conversion is essentially barrierless within the complex HCOOH...H<sub>2</sub>O...SO<sub>3</sub>.<sup>18</sup> Upon considering the concentration of formic acid, one of the most common atmospheric volatile organic compounds (VOCs), these authors argued that this pathway may be significant for the formation of sulfuric acid. Furthermore, this mechanism terminates in the formation of the hydrogen bonded complex H<sub>2</sub>SO<sub>4</sub>...HCOOH, which may be a preliminary step in a nucleation process. Indeed, the involvement of organic compounds in new particle formation has become a central topic in atmospheric particle research and it now has been shown that organics participate not only in particle growth<sup>11,19,20</sup> but in nucleation as well.<sup>9,21-26</sup> Carboxylic acids are abundant in the atmosphere<sup>27</sup> and thus, their primary interactions with sulfur-containing atmospheric species are of significant interest.

Previous work in our laboratory has characterized a variety of atmospheric molecular complexes including  $\text{SO}_3 \cdots \text{H}_2\text{O}$ ,<sup>28</sup>  $\text{H}_2\text{SO}_4 \cdots \text{H}_2\text{O}$ ,<sup>29</sup> and  $\text{HNO}_3 \cdots (\text{H}_2\text{O})_{n=1-3}$ ,<sup>30</sup> in a supersonic jet using microwave spectroscopy. Such systems, in general, are important to study because of the roles they play as intermediates in chemical reactions and precursors to atmospheric aerosol. Although conditions in the jet do not mimic those in the atmosphere, they can produce the same species, albeit under conditions amenable to microwave spectroscopy (i.e., in a collisionless environment that is cold enough to ensure population of only the lowest rotational energy levels). Spectral analysis yields accurate information about gas-phase molecular and electronic structure, which in turn provides an important touchstone for computational studies. Therefore, inspired by Hazra and Sinha, and by the recent research suggesting the involvement of organic acids in aerosol formation, we set out to investigate the complexes such as  $\text{H}_2\text{SO}_4 \cdots \text{HCOOH}$  and  $\text{SO}_3 \cdots \text{HCOOH}$  by microwave spectroscopy in a supersonically expanded mixture of  $\text{SO}_3$ ,  $\text{H}_2\text{O}$ , and  $\text{HCOOH}$  seeded in argon. What we found was entirely unexpected.

Rotational spectra were observed by Fourier transform microwave (FTMW) spectroscopy. Two methods were employed: conventional cavity-type FTMW spectroscopy and the newer broadband, chirped-pulse FTMW technique. The cavity spectrometer in our laboratory has been described elsewhere.<sup>31</sup> Briefly, molecules enter a tuned microwave cavity and are coherently excited by a 1 to 2  $\mu\text{s}$  pulse of radiation. The resulting free induction decay is heterodyne-detected, digitized, and Fourier transformed to produce a signal in the frequency domain. Uncertainties in spectral transition frequencies are typically on the order of 2 to 3 kHz. In our broadband spectrometer,<sup>32</sup> which applies the methods developed by Pate and coworkers,<sup>4</sup> the cavity is eliminated and the radiation for sample excitation is generated by upconversion of a 0.2 to 3.2 GHz chirped pulse to the microwave spectral region of interest. A 20 W amplifier boosts the power before irradiation of the molecular sample, which is accomplished via a microwave horn. The resulting free induction decay is received by an identical companion horn, down-converted for digitization, and Fourier transformed to produce a 3 GHz wide segment of the microwave spectrum. Linewidths are typically  $\sim 90$  kHz and the apparatus is less sensitive than that of the cavity spectrometer, but it allows for rapid

location and identification of spectra. In this work, spectra were initially recorded with the broadband spectrometer and subsequently re-measured at high resolution using the cavity system.

A key feature of this experiment was the molecular source,<sup>31</sup> which consisted of a supersonic expansion of  $\text{SO}_3$  in Ar, to which a flowing stream of formic acid and water vapor was added. The argon carrier gas was seeded with  $\text{SO}_3$  by entrainment upon passage over solid, polymerized  $\text{SO}_3$ . A gaseous mixture of  $\text{HCOOH}$  and  $\text{H}_2\text{O}$  was added by bubbling Ar through 88% aqueous formic acid and injecting it into the expansion (Figure 1.1a). This configuration provides “on-the-fly” mixing of reactive reagents during the first few tens of microseconds of the supersonic expansion.

Transitions from a variety of known species, including  $\text{Ar}\cdots\text{SO}_3$ ,  $\text{H}_2\text{O}\cdots\text{SO}_3$ ,  $\text{H}_2\text{SO}_4$  (formed from  $\text{SO}_3 + \text{H}_2\text{O}$ ),  $\text{H}_2\text{SO}_4\cdots\text{H}_2\text{O}$ ,  $\text{Ar}\cdots\text{HCOOH}$ , and  $\text{H}_2\text{O}\cdots\text{HCOOH}$  were observable, as were numerous lines of unknown origin (Figure 1.1b). Among these was a set of strong transitions whose pattern made them readily identifiable as the *a*-type spectrum of an asymmetric rotor, and a preliminary least squares fit to a Watson A-reduced Hamiltonian gave residuals of under 5 kHz. The appearance of these transitions required the presence of  $\text{HCOOH}$ , and our initial hypothesis was that they were due either to the  $\text{H}_2\text{SO}_4\cdots\text{HCOOH}$  or  $\text{SO}_3\cdots\text{HCOOH}$  weakly bound complex. However, theoretical predictions of the rotational constants for both species using the density functional M06-2X (Table A.1) clearly indicated that neither is the carrier of the observed spectrum. Indeed, the computed rotational constants of  $\text{H}_2\text{SO}_4\cdots\text{HCOOH}$  as well as those of several weakly bound isomers of  $\text{SO}_3\cdots\text{HCOOH}$  (Table A.1 and Figure A.3) differ by up to ~1 GHz and ~200 MHz, respectively, from those fitted from experimental data.

Additional calculations near the global minimum energy configuration of  $\text{SO}_3\cdots\text{HCOOH}$  were performed with starting configurations at progressively shorter intermolecular separations. These eventually revealed a new chemically bonded species in which the acidic proton of the formic acid transfers to the  $\text{SO}_3$  and a new sulfur-oxygen bond is formed (Tables A.2 and A.3). Frequency calculations were performed to verify the

authenticity of the potential energy minimum and the DFT results were confirmed with MP2 calculations. The structure of this molecule, formic sulfuric anhydride (FSA), is shown in Table 1.1.

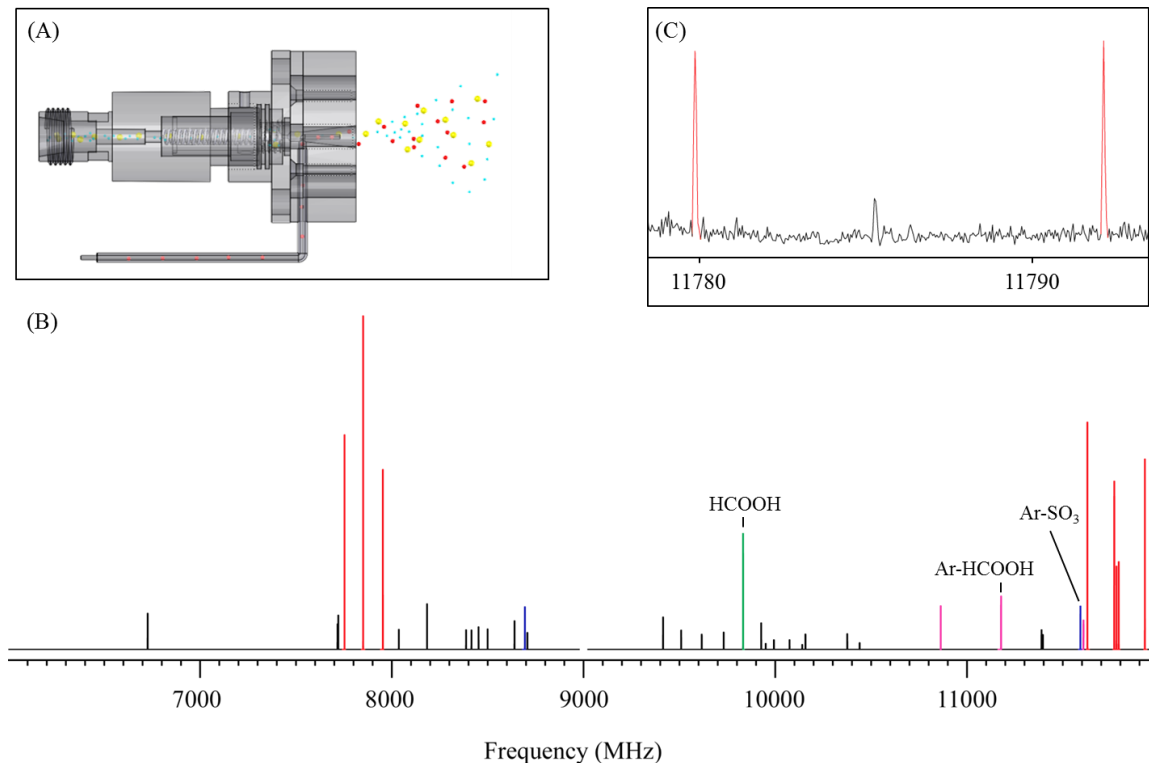


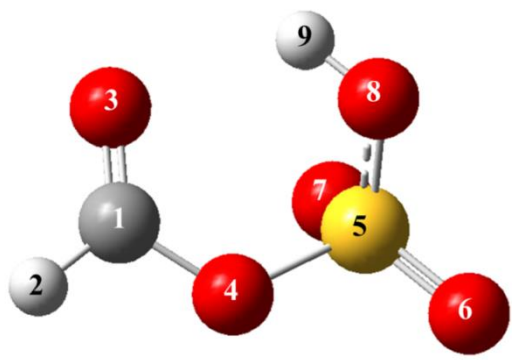
### Figure 1.1 Experimental Setup and Results for FSA

(A) A diagram of the nozzle source. HCOOH/H<sub>2</sub>O/Ar was introduced a few millimeters downstream of the start of the expansion through a 0.016-inch inner-diameter hypodermic needle. (B) Stick spectrum of transitions observed using the chirped-pulse spectrometer and confirmed on the cavity system from an Ar, SO<sub>3</sub>, H<sub>2</sub>O, and HCOOH mixture for the 6-12 GHz region. Unassigned transitions that were independent of HCOOH are not shown. The relative intensities were maintained from the original chirped-pulse data (average of 50,000 FIDs) and are comparable for broadband spectra within the same spectral region (e.g., 6-9 and 9-12 GHz, demarcated by the break in the spectrum). Red lines represent FSA transitions. Transitions assigned to Ar-SO<sub>3</sub>, Ar-HCOOH, and HCOOH were left in the spectrum for comparison to FSA transitions and are marked in blue, pink, and green, respectively. The strongest transition observed for each is labeled on the figure. Black lines are unassigned. (C) Portion of the 9-12 GHz spectrum showing two FSA transitions highlighted in red.

This structure has substantial dipole moment components along each of its three inertial axes ( $\mu_a$ ,  $\mu_b$ , and  $\mu_c = 3.19$ , 0.48, and 0.97 D, respectively;  $\mu_{\text{Total}} = 3.37$  D) and indeed with this information, *b*-type and *c*-type transitions were easily predicted and located. With *a*, *b*, and *c*-type transitions recorded, a final fit was performed to yield the rotational

constants listed in Table 1.2. As indicated in the table, the predicted rotational constants of FSA match the experimental values to within 0.7% (32 MHz for *A* and 14 MHz for *B* and *C*).

**Table 1.1 Comparison of Experimental and Theoretical Intermolecular Distances**



	Distance*	M06-2X <sup>†</sup>	MP2 <sup>†</sup>	Experiment <sup>‡</sup>
	<i>C1-S5</i>	2.589	2.593	2.594(5)
	<i>C1-H2</i>	1.092	1.091	1.11(1)
	<i>C1-H9</i>	2.634	2.572	2.62(1)
	<i>S5-H9</i>	2.085	2.069	2.025(3)
	<i>S5-H2</i>	3.514	3.520	3.513(2)

\* All distances in Å.

<sup>†</sup> M06-2X and MP2 calculations done with 6-311++G(3df,3pd) basis set.

<sup>‡</sup> Determined from Kraitchman's equations.

As a final test, spectra of the <sup>34</sup>S-, <sup>13</sup>C-, and both monodeuterated isotopologues were predicted and observed. <sup>34</sup>S- and <sup>13</sup>C- isotopologue spectra were recorded in natural abundance and experiments on the deuterated species employed isotopically enriched HCOOD or DCOOH. Transition frequencies and fitted spectroscopic constants for the observed isotopologues are provided in Tables A.4-A.9. All observed isotope shifts were in excellent agreement with those predicted from the theoretical structure. When HCOOD was used, the deuterium was found in the H9 position, confirming the occurrence (direct or indirect) of proton transfer;<sup>33</sup> isotopic substitutions allowed determination of several interatomic distances using Kraitchman's equations.<sup>34</sup> These results are given and compared with the theoretical values in Table 1.1, where agreement is again seen to be excellent. The agreement between experimental and theoretical rotational constants, their isotope shifts, and the computed interatomic distances unambiguously establishes that the observed species is FSA.

**Table 1.2 Experimental and Calculated Rotational Constants for FSA**

Constant	Observed*	Theoretical**†	(obs.-calc.)*	% Difference
<i>A</i>	4510.1155(12)	4542	-32	-0.7%
<i>B</i>	2013.28751(13)	2027	-14	-0.7%
<i>C</i>	1913.33629(13)	1927	-14	-0.7%

\* All values in MHz.

† Calculations were done with the M06-2X functional and 6-311++G(3df,3pd) basis set.

The literature on compounds related to FSA appears sparse, though a few prior condensed phase studies are noteworthy. The sodium salt of acetic sulfuric anhydride has been described,<sup>35</sup> but the parent acid ( $\text{CH}_3\text{COOSO}_3\text{H}$ ) is reportedly unstable with respect to rearrangement or decomposition.<sup>36,37</sup> Dissolved salts of form  $[\text{M}^{n+}][\text{SO}_3\text{OCHO}^-]_n$  have also been described in a patent concerning the preparation of isoflavones in a variety of non-aqueous solvents.<sup>38</sup> We are unaware, however, of any previous gas phase observations of FSA or its analogs. To better understand the pathway for the formation of FSA in the gas phase, calculations were performed<sup>32</sup> to locate the transition state connecting it with the  $\text{SO}_3\cdots\text{HCOOH}$  van der Waals complex (Table A.10). For these calculations, using the optimized MP2 geometries, single point CCSD(T) calculations were done using the complete basis set extrapolation scheme of Neese and Valeev with the ANO-pVDZ to ANO-pVTZ basis sets.<sup>39</sup> The transition state (TS in Figure 1.2a) was found and corresponds to a concerted  $\pi_2 + \pi_2 + \sigma_2$  cycloaddition (Figure 1.2b), in which the acidic proton is transferred as the new S–O bond is formed. A similar reaction has been proposed for  $\text{SO}_2\cdots\text{HCOOH}$  but the formation of the resulting monomer, formic sulfurous anhydride, from  $\text{SO}_2$  and  $\text{HCOOH}$  is endothermic.<sup>40</sup> In the current case, however, FSA is 4.4 (4.2) kcal/mol lower in energy than the  $\text{SO}_3\cdots\text{HCOOH}$  van der Waals complex, where the value in parentheses is zero-point corrected. The energy of the transition state is 2.2 (0.2) kcal/mol higher than that of  $\text{SO}_3\cdots\text{HCOOH}$  indicating that its conversion to FSA, with zero-point corrections, is essentially barrierless. In this light, it is not surprising that transitions of FSA were among the most prominent features in the observed spectrum. Note that a second conformer of FSA, with the OH bond rotated  $180^\circ$ , was also identified from the M06-2X calculations (Figure A.5). However, this local

minimum lies 4.0 kcal/mol above the global minimum of Table 1.1, and no spectra corresponding to this structure were identified, presumably due to insufficient population in the supersonic jet.

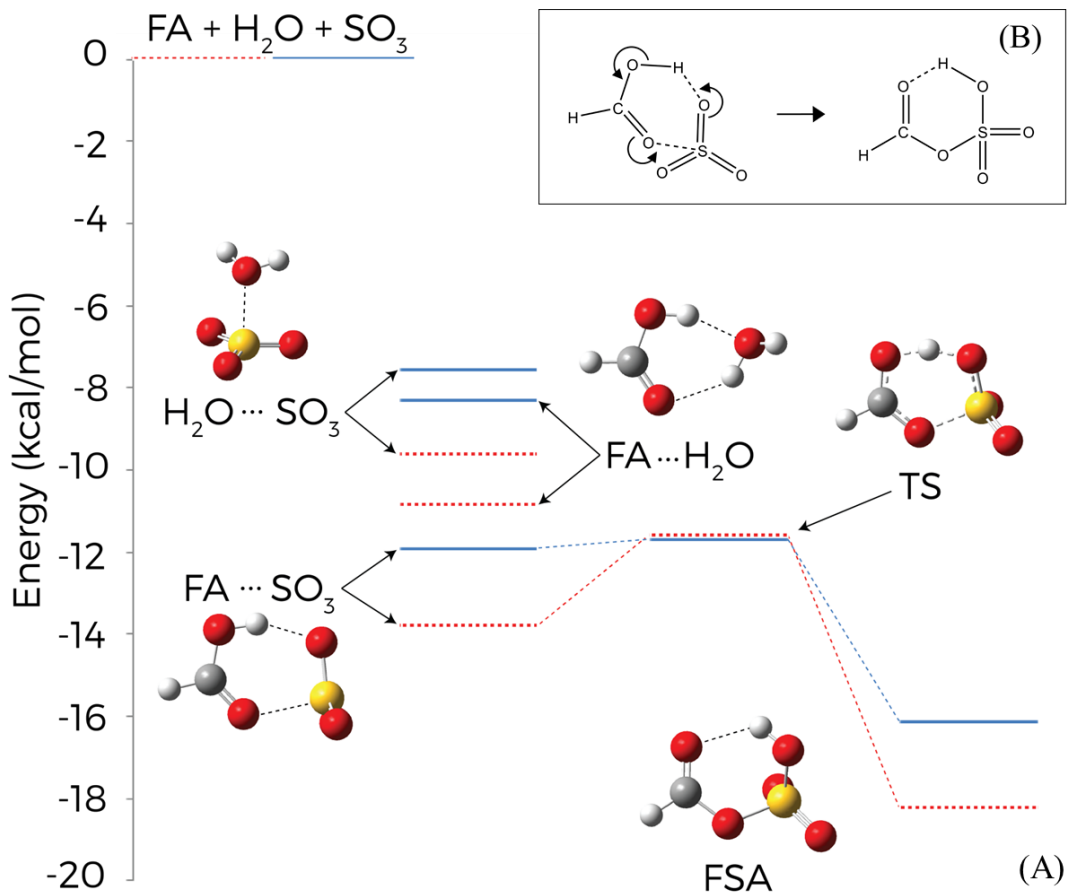


**Figure 1.2 FSA Energetics**

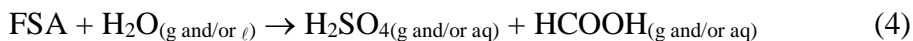
(A) Potential energy landscape of the bimolecular complexes formed between  $\text{H}_2\text{O}$ ,  $\text{SO}_3$ , and  $\text{HCOOH}$ . Geometries were optimized using MP2/6-311++G(3df,3pd) and single point electronic energies were computed using CCSD(T)/CBS(D-T). The red (dashed) trace is uncorrected for ZPE. The blue (solid) trace is ZPE corrected with frequencies from the MP2/6-311++G(3df,3pd) calculations. Zero is defined as the sum of the monomer energies with and without ZPE corrections for the blue (solid) and red (dashed) traces, respectively. The barrier to conversion from the complex to FSA is 2.2 kcal/mol without ZPE corrections and 0.2 kcal/mol with ZPE corrections. (B) Possible formation mechanism of FSA from  $\text{SO}_3$  and  $\text{HCOOH}$ .

We also sought to establish the stability of the putative FSA precursor,  $\text{SO}_3\cdots\text{HCOOH}$ , relative to that of other bimolecular complexes with potential roles as sulfuric acid and/or aerosol precursors. Computed energies of the complexes formed from  $\text{SO}_3$ ,  $\text{H}_2\text{O}$ , and  $\text{HCOOH}$ , are included in Figures 1.2a and A.4, and in Table A.10. With zero point



corrections, the  $\text{SO}_3\cdots\text{HCOOH}$  complex is 3.6 and 4.4 kcal/mol more stable than  $\text{H}_2\text{O}\cdots\text{HCOOH}$  and  $\text{H}_2\text{O}\cdots\text{SO}_3$ , respectively. Similar calculations for  $\text{H}_2\text{O}\cdots\text{HCOOH}$  and  $\text{H}_2\text{O}\cdots\text{SO}_3$  have been given elsewhere<sup>6,18</sup> but are reproduced here to ensure comparisons at a uniform level of theory.

Both carboxylic and sulfonic acid anhydrides hydrolyze in water, and the hydrolysis of acetic sulfuric anhydride has been studied.<sup>37,41</sup> Thus, it is reasonable to hypothesize that the formation of  $\text{SO}_3\cdots\text{HCOOH}$  with a barrierless conversion to FSA, followed by reaction with water and/or uptake into liquid droplets may constitute an alternate pathway for  $\text{H}_2\text{SO}_4$  production in the atmosphere



Although such a mechanism is not expected to dominate over established pathways involving direct reaction with water, we note that it requires only the formation of a bimolecular, not a trimolecular complex, and may contribute, especially in areas with elevated concentrations of carboxylic acids. Additionally, eq. 4 occurring in small water-containing clusters and/or liquid droplets may provide a pathway for the incorporation of volatile organic compounds into atmospheric aerosol. The mechanism may also be significant if extended to compounds of low volatility, which are more likely to contribute to pre-nucleation clusters.<sup>42</sup> Indeed, we have performed additional calculations with larger carboxylic acids, which confirm the viability of their reaction to form FSA analogues (Figure A.6). Moreover, laboratory studies that generated  $\text{H}_2\text{SO}_4$  *in situ* have suggested that sulfur-containing species other than  $\text{H}_2\text{SO}_4$  could be the initial nucleating agent.<sup>43</sup> Under such a conclusion, FSA or its analogues could be nucleating agents themselves. Thus, while the atmospheric importance of eqs. 2-4 is by no means certain, we suggest that scenarios involving FSA and larger sulfuric – carboxylic anhydrides should be explored in conjunction with models that involve trimolecular complexes such

as  $(\text{H}_2\text{O})_2 \cdots \text{SO}_3$  and  $\text{H}_2\text{O} \cdots \text{HCOOH} \cdots \text{SO}_3$ , and in mechanisms for the early incorporation of organics in nucleation schemes. This could include, but is not limited to, mechanistic studies of the hydrolysis of sulfuric-carboxylic anhydrides in both water-containing clusters and bulk phase.

### **Acknowledgements**

This work was supported by the National Science Foundation (grant CHE-1266320) and the Minnesota Supercomputing Institute. We are grateful to P. McMurry, T. Hoyer, and M. Canagaratna for helpful conversations. We also thank W. Isley for assistance with the CCSD(T) calculations and J. Mendez and the Tektronix Corporation for invaluable aid in construction of the broadband spectrometer.

**Chapter 2 : The Trimethylamine - Formic Acid Complex**  
**Microwave Characterization of a Prototype for Potential Precursors to**  
**Atmospheric Aerosol**

Adapted with permission from R. B. Mackenzie, C. T. Dewberry, and K. R. Leopold,  
*J. Phys. Chem. A*, **120**, 2268-2273 (2016).  
© 2016 American Chemical Society.

## Abstract

The reactions of amines and carboxylic acids have recently received attention for their possible role in the formation of atmospheric aerosol. Here, we report a microwave study of the trimethylamine – formic acid hydrogen bonded complex, a simple prototype in which to study amine – carboxylic acid interactions. Spectra of three isotopologues of the system have been observed using a tandem cavity and chirped-pulse Fourier transform microwave spectrometer. The complex has a plane of symmetry, with the acidic proton of the formic acid directed toward the lone pair of the nitrogen. The zero point averaged hydrogen bond length is 1.702 Å and the O–H...N angle is 177°. <sup>14</sup>N nuclear quadrupole hyperfine structure has been used to assess the degree of proton transfer from the formic acid to the trimethylamine. Experimental results are supplemented with density functional theory calculations. M06-2X/6-311++G(3df,3pd) calculations indicate a binding energy of 16.8 kcal/mol with counterpoise correction (17.4 kcal/mol without counterpoise correction).

## Introduction

Recent research on atmospheric aerosols indicates that organic compounds contribute to early stages of new particle growth.<sup>9-10,21-26,44-45</sup> While exact mechanisms have not been elucidated, one possible route involves the reaction of organic acids with other atmospheric species.<sup>9,10,21,22,25,44</sup> The idea is that if such reactions form products of low volatility, the critical cluster size can be reduced and, moreover, the resulting new particles will necessarily contain their organic precursors. Carboxylic acids are known to be abundant in the atmosphere,<sup>27,46</sup> and in this light, their interaction with other atmospheric species is a particularly intriguing topic of investigation.

Here, we focus on work involving the formation of organic salts from carboxylic acids and amines. Using theoretical modeling, Barsanti et al. explored the contribution of various alkylammonium carboxylates to new particle growth in the atmosphere and provided preliminary evidence that such compounds may, indeed, play a role in atmospheric nucleation.<sup>10</sup> A subsequent study by Smith et al.<sup>11</sup> indicated that, while the formation of organic salts likely does not account for all growth due to organic compounds, such salts do have a significant impact on nanoparticle formation. Indeed in their study, thermal desorption chemical ionization mass spectrometric experiments in an urban environment showed that protonated amines corresponded to 47% of the detected positive ions. Similar experiments at a remote forested site recorded 23% of the detected ions arising from alkylammonium salts. More recently, general formulations of the contribution of acid-base chemistry to atmospheric particle growth have been considered.<sup>47,48</sup>

In the above context, Barsanti et al. have emphasized the need for experimental information on organic salts.<sup>10</sup> Therefore, in this work, we use the complex formed from trimethylamine (TMA) and formic acid (HCOOH) as a prototype for the gas-phase interactions of amines and carboxylic acids. Microwave spectroscopy in a supersonic jet, together with density function theory calculations are used to provide information about the structure, binding energy, and degree of ion pair formation in an isolated

TMA–HCOOH complex. Although the supersonic jet does not mimic atmospheric conditions, this work provides a detailed physical characterization of the gas-phase interaction between these moieties and in doing so, provides a basis for understanding the steps that may lead to salt formation and ultimately new particle formation in the atmosphere.

### **Experimental and Computational Methods**

Rotational spectra of the TMA – formic acid complex were collected from 5.4 -18 GHz using a tandem cavity and chirped-pulse Fourier transform microwave spectrometer. The cavity instrument has been described elsewhere<sup>31,49</sup> and its conversion to incorporate a chirped-pulse spectrometer was detailed recently.<sup>5</sup> A 1% gas mixture of TMA in Ar at a stagnation pressure of 1.4 atm was pulsed into the spectrometer through a 0.8 mm diameter nozzle and an argon - formic acid mixture was introduced a few millimeters downstream of the nozzle via a 0.012" ID stainless steel needle, as described previously.<sup>50</sup> The mixture was created in a small reservoir of HCOOH (85%) through which Ar was flowed at a pressure of 0.7 atm. <sup>13</sup>C isotopic substitution experiments were performed in natural abundance and deuterium substitution experiments utilized DCOOH purchased from Sigma Aldrich. For the parent and DCOOH isotopologues, spectra were first recorded with the chirped pulse spectrometer and most transitions were subsequently re-measured on the cavity system. For the <sup>13</sup>C substituted species, all transitions were located and measured on the cavity spectrometer. Uncertainties were typically between 40 and 90 kHz in the chirped-pulse spectra (depending on the transition) and ~4 kHz in the cavity spectra.

Liljefors and Norrby have reported single point energy calculations at a series of levels of theory at the HF/6-31+G\* structure.<sup>51</sup> Here, the structure of TMA–HCOOH was optimized using M06-2X/6-311++G(3df,3pd) with an ultrafine integral grid, and frequency calculations were done to confirm that the structure indeed corresponded to a minimum on the potential energy surface. Figure 2.1 shows the calculated structure. The binding energy is 16.8 kcal/mol with counterpoise correction<sup>52</sup> (17.4 kcal/mol without

correction). The predicted hydrogen bond length is 1.623 Å, with a N⋯H-O angle of 177.2°. <sup>53</sup> Note that the pseudo-C<sub>3</sub> axis of the TMA lies in the plane of the formic acid, rendering two of the methyl groups equivalent. Atomic Cartesian coordinates are included in Appendix B.

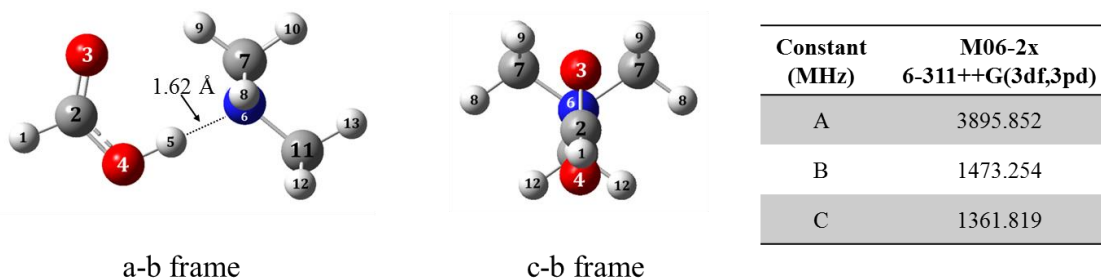


### Figure 2.1 Predicted Structure of TMA-HCOOH

The structure of TMA-HCOOH determined from M06-2X/6-311++G(3df,3pd) calculations. Equivalent atoms are given the same label.

The dipole moment of the complex was also computed at the M06-2X/6-311++G(3df,3pd) level of theory and found to be 2.883 D, with components of 2.808, 0.649, and 0.000 D along the *a*-, *b*-, and *c*-inertial axes, respectively. At the same level of theory, the dipole moments of monomeric TMA and HCOOH were computed to be 0.641 D and 1.530 D, these values being 5% and 7% greater than the experimental values of 0.612(3) D<sup>54</sup> and 1.4253(18) D,<sup>55</sup> respectively.

For comparison, similar calculations were done for NH<sub>3</sub>-HCOOH at the same level of theory. In this case, the binding energies with and without counterpoise corrections are 14.0 kcal/mol and 14.4 kcal/mol, respectively, and the hydrogen bond length is 1.731 Å with an N⋯H-O angle of 166.0°. <sup>53</sup>

## Results

A chirped-pulse spectrum of a mixture of the parent isotopologues from 6-18 GHz, collected in 3 GHz segments, is shown in Figure 2.2. The broad coverage of the spectrum facilitated spectral assignments which were then confirmed on the basis of a preliminary

fit to a Watson A-reduced Hamiltonian. Many of these transitions were subsequently re-measured at high resolution using the cavity spectrometer and were then incorporated into a revised fit to produce the final set of spectroscopic constants given in Table 2.1. For the parent species, 20 *a*-type rotational transitions up to  $J = 6 \leftarrow 5$  and  $K_{-J} = 3$  were included, and  $\Delta_J$  and  $\Delta_{JK}$  were the only centrifugal distortion constants necessary to achieve a satisfactory fit. Nuclear electric quadrupole hyperfine structure resulting from the  $^{14}\text{N}$  nucleus was observed for all spectra recorded with the cavity spectrometer. Hyperfine structure was analyzed in the usual manner, using the  $F=J+I$  coupling scheme, where  $I = 1$  is the nuclear spin of the  $^{14}\text{N}$ . Tables of transition frequencies, assignments, and residuals are provided in Appendix B.

Transitions of the isotopically substituted species were readily located by applying the isotope shifts in the rotational constants calculated on the basis of the theoretical structure to the observed rotational constants of the parent species. For the DCOOH isotopologue, no hyperfine structure arising from the deuterium was resolved and thus no deuterium quadrupole coupling constants were determined. Searches for complexes containing the  $^{13}\text{C}$  isotopologues of TMA were first conducted for the  $^{13}\text{C}11$  species (i.e., the in-plane carbon of the TMA, see Figure 2.1 for atom labeling). While a number of weak lines were observed, their intensities were low enough to preclude observation of the entire spectrum. However, the other carbon of TMA (C7) belongs to a pair of equivalent carbons and hence was expected to be twice as abundant. Thus, we abandoned  $^{13}\text{C}11$  in favor of measuring the spectrum of the  $^{13}\text{C}7$ -substituted species. In the course of these experiments, no additional rotational transitions were observed in the immediate vicinity of the  $^{13}\text{C}7$  transitions, providing further evidence of the exact equivalence of the C7 carbons. Spectroscopic constants for the isotopically substituted species are also reported in Table 2.1. Note that the rms residuals in the fit for the  $^{13}\text{C}$  substituted form is slightly smaller than those for the parent and DCOOH species because the latter resulted from fits that included both high resolution cavity data and lower resolution chirped-pulse data.<sup>56</sup> For DCOOH, unresolved deuterium hyperfine structure may also contribute to the rms residuals.



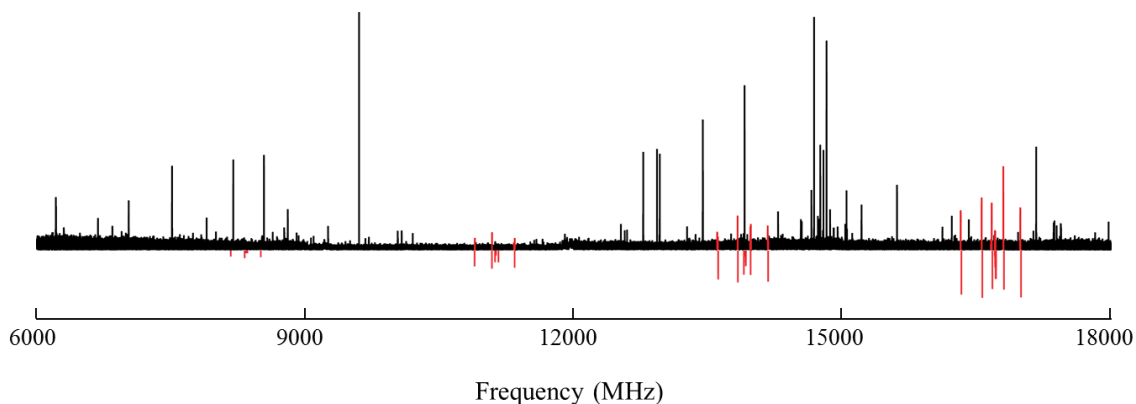


**Figure 2.2 Chirp Spectrum of TMA-HCOOH**

Upper Trace: Chirped-pulse microwave spectrum of HCOOH, TMA, and trace water in an Ar expansion from 6–18 GHz. The spectrum was collected in segments of 3 GHz, which are marked on the horizontal axis. TMA monomer lines and known instrumental artifacts have been removed. Transitions highlighted in red were assigned to the TMA–HCOOH complex. Lower (inverted) Trace: Predicted transitions frequencies using spectroscopic constants from the final least square fit for the parent isotopologue.

**Table 2.1 Fitted Spectroscopic Constants for Three Isotopologues of TMA-HCOOH**

Constant	TMA-HCOOH	TMA( <sup>13</sup> C7)-HCOOH	TMA-DCOOH <sup>a</sup>
$A$ (MHz)	3826.54(12)	3767.41(16)	3812.69(10)
$B$ (MHz)	1446.37300(27)	1435.39458(42)	1404.23803(64)
$C$ (MHz)	1334.66883(23)	1327.80905(37)	1297.05980(37)
$\chi_{aa}$ (MHz) <sup>b</sup>	−2.8190(22)	−2.867(17)	−2.913(67)
$(\chi_{bb}-\chi_{cc})$ (MHz) <sup>b</sup>	−1.7240(52)	−1.508(60)	−1.53(10)
$\Delta_J$ (kHz)	0.5676(85)	0.588(14)	0.6019(77)
$\Delta_{JK}$ (kHz)	1.846(65)	1.667(81)	1.846 <sup>d</sup>
RMS (kHz)	18 <sup>c</sup>	3	11 <sup>c</sup>
$N^e$	53	22	19

- (a) Deuterium hyperfine structure was not resolved for the TMA–DCOOH isotopologue.  
 (b) Nuclear quadrupole coupling constants are for the <sup>14</sup>N nucleus.  
 (c) The least squares fit for the parent and DCOOH species contains a combination of transitions observed using the cavity instrument (uncertainty of ~4 kHz) and the chirped-pulse instrument (uncertainty of 40 – 90 kHz). Transition frequencies were weighted in the fit according to their estimated uncertainty. Details are provided in Appendix B along with the transition frequencies and assignments.  
 (d)  $\Delta_{JK}$  was not well determined using the transitions observed for TMA–DCOOH and was therefore fixed to the parent value.  
 (e) Number of distinct lines in the fit (includes nuclear hyperfine components).

### Analysis of Rotational Constants

With only three isotopologues observed, a complete structure analysis was not achievable. However, with the usual assumption that the monomer geometries are unchanged upon complexation, a structure could be derived that reproduced the experimental rotational constants quite satisfactorily. First, the planar moment about the *a-b* plane,

$$P_c = (1/2)(I_{aa} + I_{bb} - I_{cc}) \quad (1)$$

is equal to  $\sum m_i c_i^2$  and is therefore dominated by the out-of-plane mass. Using the rotational constants of Table 2.1 to determine  $I_{aa}$ ,  $I_{bb}$ , and  $I_{cc}$  for the parent complex, we obtain a value of  $P_c = 51.414 \text{ amu } \text{Å}^2$ . This is very close to the value of  $50.696 \text{ amu } \text{Å}^2$  calculated from the published structure<sup>57,58</sup> of free TMA about a plane which contains one of the methyl groups. In other words, the planar moment of the complex is very nearly equal to that of free TMA about an equivalent plane. This suggests that one methyl carbon lies in the plane of the formic acid, with the other two symmetrically positioned about it (in agreement with the theoretical structure). Therefore, the complex was assumed to have a plane of symmetry that contains the formic acid and one of the methyl carbons of the TMA.

The geometrical parameters needed to further specify the geometry of the complex are shown in Figure 2.3.  $R_1$  and  $R_2$  are the distances between the centers of mass of the monomers and the center of mass of the complex, and their sum,  $R_{cm}$ , is the center of mass separation.  $\theta_{TMA}$  and  $\theta_{HCOOH}$  are the angles that  $R_{cm}$  forms with the *c*-axis of TMA and the *a*-axis of HCOOH, respectively. Noting that the *c*-inertial axis of the complex is perpendicular to the *X-Z* plane, and recalling that the TMA monomer is an oblate top, the parallel axis theorem gives

$$I_{cc}^{complex} = \mu R_{cm}^2 + I_{cc}^{HCOOH} + I_{aa}^{TMA} \quad (2)$$

where  $\mu$  is the pseudodiatom reduced mass of the complex and each  $I_{gg}$  is the moment of inertia of the indicated monomer about its  $g$ -inertial axis. Using values of  $I_{CC}^{HCOOH}$  and  $I_{aa}^{TMA}$  obtained from published rotational constants,<sup>57-61</sup> a value of  $R_{cm} = 3.244064 \text{ \AA}$  was obtained for the parent isotopologue.<sup>62</sup>

Further specification of the geometry of the complex requires that  $\theta_{HCOOH}$  and  $\theta_{TMA}$  be determined. To do so, the distance between H1 and the center of mass of the parent complex was first determined from the rotational constants of the parent and DCOOH isotopologues to be  $3.31778 \text{ \AA}$  using Kraitchman's equations.<sup>63</sup> The value  $\theta_{HCOOH}$  was then adjusted so as to reproduce this distance (with  $R_{cm}$  held at the above value), with the result that  $\theta_{HCOOH} = 104.70^\circ$ . A similar calculation using the C7 substitution data on the TMA gave a distance of  $1.83615 \text{ \AA}$  between C7 and the center of mass of the parent complex, with a corresponding value of  $\theta_{TMA} = 23.65^\circ$ . Using these results for  $R_{cm}$ ,  $\theta_{HCOOH}$ , and  $\theta_{TMA}$ , and the known structures of the monomer units,<sup>57-61</sup> the zero point vibrationally averaged hydrogen bond length for the complex is determined to be  $1.702 \text{ \AA}$ , with a vibrationally averaged O-H...N angle of  $177.3^\circ$ . These results are both chemically reasonable and in good agreement with the theoretical results, which give equilibrium values of the hydrogen bond length and bond angle of  $1.623 \text{ \AA}$  and  $177.2^\circ$ , respectively. The experimentally determined N6-O4-C2 angle is  $108.1^\circ$ .

Uncertainties in the experimental values are difficult to ascertain in view of the limited isotopic substitution that could be used to test the isotopic invariance of the reported structure. However, experience with similar types of analyses indicates that values on the order of  $\pm 0.02 \text{ \AA}$  for the hydrogen bond distance and  $\pm 2^\circ$  for the hydrogen bond angle would be reasonable.<sup>14,15</sup> Note that the use of unperturbed monomer geometries could also introduce error into the reported results. However, the calculations described above were repeated using monomer geometries that were corrected for the small, computationally derived changes upon complexation, but no appreciable changes in the intermolecular structural parameters were obtained.

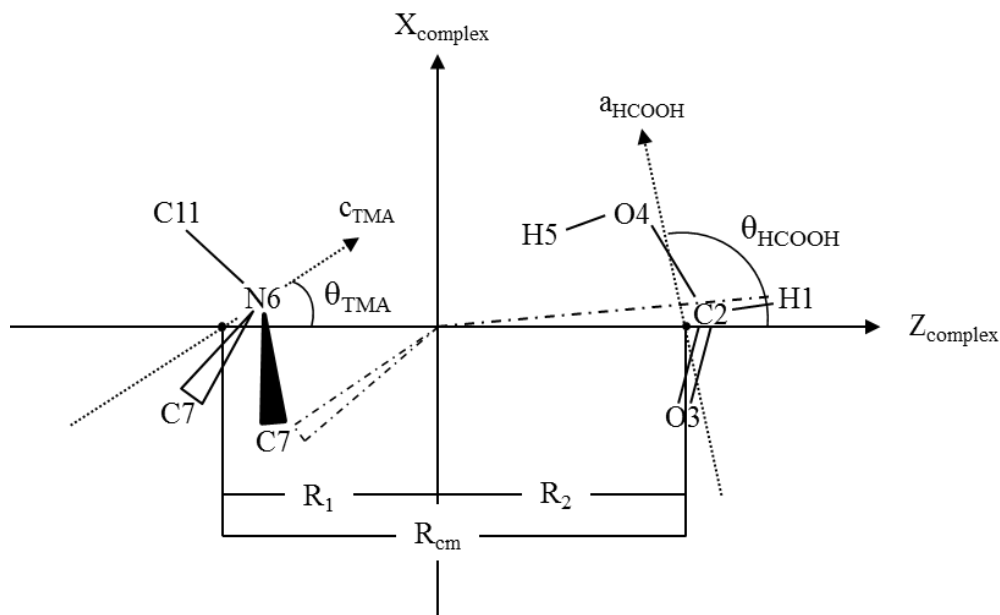


**Figure 2.3 Definition of Variables Used to Describe the Structure of TMA–HCOOH**  
 $R_{cm}$  was calculated using the parallel axis theorem and was 3.244064 Å for the parent isotopologue.  $\theta_{HCOOH}$  and  $\theta_{TMA}$  were obtained from distances derived from Kraitchman's equations using data for the C7 and H1 substituted species (dashed lines).  $\theta_{HCOOH}$  and  $\theta_{TMA}$  were determined to be 104.7° and 23.7°, respectively. See text for discussion.

### Discussion

As indicated by both experimental and theoretical results, TMA–HCOOH is a hydrogen bonded complex in which the acidic proton of the HCOOH is directed toward the nitrogen lone pair of the TMA. The experimental, zero point averaged hydrogen bond length of 1.702 Å is 0.079 Å longer than the theoretical, equilibrium value of 1.623 Å. This difference is likely due to a combination of errors in the computational result, model errors in the experimental result, and the zero point extension of the hydrogen bond distance. The small difference aside, however, the hydrogen bond is rather short, consistent with the large calculated binding energy of 16.8 kcal/mol for the complex. The experimental and theoretical O–H⋯N hydrogen bond, 177.3° and 177.2°, respectively, are in exceptionally good agreement. The near linearity of the hydrogen bond is further consistent with a strong interaction between the moieties.

The theoretical hydrogen bond length in TMA–HCOOH is 0.108 Å shorter than that in H<sub>3</sub>N–HCOOH, consistent with the result that its binding energy is 2.8 kcal/mol larger than that of the ammonia complex. The increased binding energy and shorter hydrogen bond length in TMA–HCOOH are sensible in light of the greater basicity of TMA relative to that of ammonia.

The experimentally determined nuclear quadrupole coupling constants are the components of the <sup>14</sup>N quadrupole coupling tensor expressed in the inertial axis system of the complex. Since the symmetry axis of free TMA is not aligned with any of the inertial axes of TMA–HCOOH, the observed values of  $\chi_{aa}$  and  $\chi_{bb}$  of the complex are determined not only by the electric field gradient at the nitrogen nucleus, but by the orientation of the TMA as well. However, due to the plane of symmetry of the complex, the *c*-component of its quadrupole coupling tensor,  $\chi_{cc}$ , is aligned with an axis perpendicular to the pseudo-*C*<sub>3</sub> axis of the TMA. Thus, to the extent that the electric field gradient at the nitrogen nucleus remains unchanged upon complexation,  $\chi_{cc}$  of the complex should equal  $\chi_{\perp}$  for free TMA, where the latter is the component of the quadrupole coupling tensor of free TMA perpendicular to its symmetry axis. A change in  $\chi_{cc}$  upon complexation, therefore, may be interpreted as reflecting a perturbation in the electronic environment at the nitrogen nucleus. Thus, a comparison of  $\chi_{cc}$  for the complex with the values of  $\chi_{\perp}$  for free TMA and TMAH<sup>+</sup> provides some measure of the degree to which the systems lies between the limits of “no proton transfer” and “full proton transfer”. This idea has been previously exploited for complexes of HNO<sub>3</sub>, including TMA–HNO<sub>3</sub>,<sup>64</sup> and is embodied in the definition of a proton transfer parameter  $Q_{PT}^B$ , defined in equation 3.

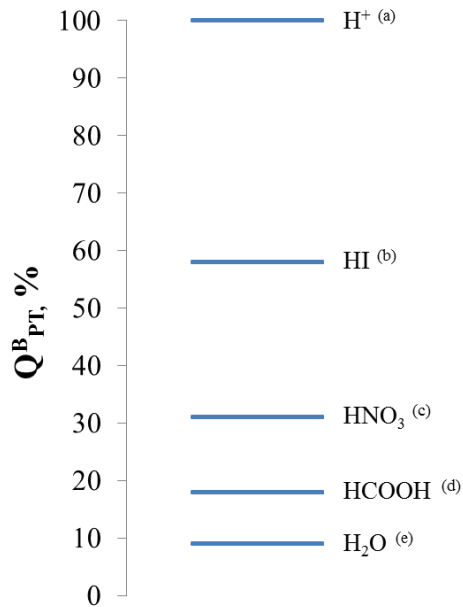
$$Q_{PT}^B = \frac{\chi_{cc}^{complex} - \chi_{\perp}^{TMA}}{\chi_{\perp}^{TMAH^+} - \chi_{\perp}^{TMA}} \times 100\% \quad (3)$$

The superscript “B” in this equation is a reminder that this particular measure of proton transfer is derived from the base (TMA in this case), and  $\chi_{\perp}^{TMA}$  represents the component of the quadrupole coupling tensor of the TMA monomer perpendicular to its symmetry

axis (2.7512 MHz).<sup>65</sup>  $\chi_{\perp}^{TMAH^+}$  is the corresponding quantity for TMAH<sup>+</sup>. Domene et al. have calculated the axial component of the quadrupole coupling tensor of TMAH<sup>+</sup> to be  $-0.2644$  MHz,<sup>66</sup> and thus  $\chi_{\perp}^{TMAH^+}$  has an estimated value of 0.1322 MHz. Using the value of  $\chi_{cc}^{complex} = 2.2715$  MHz determined from  $\chi_{aa}$  and  $(\chi_{bb} - \chi_{cc})$ <sup>67</sup> (Table 2.1) gives  $Q_{PT}^B = 18\%$ .

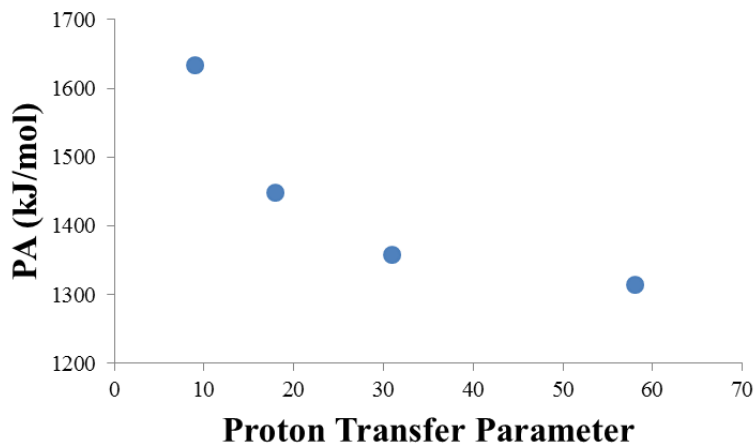
The value of  $Q_{PT}^B$  for TMA–HCOOH is compared in Figure 2.4 with values obtained from published data for other complexes of TMA. It is apparent that proton transfer in TMA–HCOOH exceeds that in TMA–H<sub>2</sub>O but is not as large as that in TMA–HNO<sub>3</sub>. The degree of proton transfer in TMA–HI is the largest among the complexes represented, consistent with the previous assessment that it is best regarded as a gas phase ion pair.<sup>68</sup> Overall, the values of  $Q_{PT}^B$  correlate with the degree of acidity of the binding partners, as measured by the proton affinities of their conjugate bases. Indeed, a plot of  $Q_{PT}^B$  vs. the proton affinities (Figure 2.5) shows a smooth, albeit nonlinear trend, with the strongest acids (lowest conjugate base proton affinity) displaying the largest proton transfer parameter.

Figure 2.5 suggests that proton affinity may be a useful parameter in estimating the degree of proton transfer in complexes that fall in a known series, but for which microwave spectra have not been observed. We emphasize, however, that “the degree of proton transfer” is defined only by the method used to measure it and, indeed, we have noted previously that proton transfer estimates in HNO<sub>3</sub> complexes can differ by as much as a factor of two between those determined from hyperfine structure on the acid the base moieties. Specifically, in TMA–HNO<sub>3</sub>,<sup>64</sup> the values of the proton transfer parameter based on the HNO<sub>3</sub> and TMA hyperfine structure are 62% and 31%, respectively. This difference is understood to arise from the differing sensitivity of the electric field gradient at the reporting nucleus to proton position at different points along the proton transfer coordinate. Thus, it is important that proton transfer parameters in a series of complexes only be compared between those determined from hyperfine structure arising from the same nucleus.



**Figure 2.4 Comparison of  $Q_{PT}^B$  for TMA–acid Complexes**

Values for TMA and  $TMAH^+$  define 0% and 100% proton transfer, respectively.  $Q_{PT}^B$  values are taken or derived from data in reference 66 (HI), reference 64 ( $HNO_3$ ), this work (HCOOH), and reference 69 ( $H_2O$ ).



**Figure 2.5 Correlation Between the Proton Transfer Parameter and Proton Affinity**

Correlation between  $Q_{PT}^B$  of the TMA–acid complex and the proton affinity (PA) of the acid's conjugate base. From left to right,  $OH^-$ ,  $HCOO^-$ ,  $NO_3^-$ , and  $I^-$ . Proton affinities are taken from reference 70.

Finally, from the point of view of reducing the critical cluster size during nucleation, the degree of proton transfer may find its greatest importance in its contribution to the enhancement of the dipole moment of the complex. The contribution is not directly comparable from system to system, however, as the dipole moment of the complex depends strongly on the relative orientation of the monomers. Nonetheless, we can say that in the case of TMA–HCOOH, the calculated dipole moment of the complex exceeds the sum of the monomer dipole moments by 0.71 D, representing a 33% increase in polarity upon complexation which may, indeed, be a contributing factor to a reduced “evaporation rate” and a smaller critical cluster size. We note, however, that previous calculations have indicated that a single water molecule is insufficient to stabilize the ion pair,<sup>51</sup> and thus full realization of the role of charge separation may not occur before further growth of the cluster.

## Conclusion

Microwave spectroscopy has been used to characterize the 1:1 complex formed from formic acid and trimethylamine. The acidic proton of the formic acid is directed toward the nitrogen lone pair in the complex, with a zero point averaged hydrogen bond length of 1.702 Å. The counterpoise-corrected binding energy, determined at the M06-2X/6-311++G(3df,3pd) level of theory, is 16.8 kcal/mol (17.4 kcal/mol without counterpoise correction) and the computed total dipole moment of the complex (2.883 D) is 33% larger than the sum of the computed dipole moments of HCOOH and TMA. Based on an analysis of the <sup>14</sup>N hyperfine structure, the degree of proton transfer in the complex is ~20%, and comparison with other acid – TMA complexes reveals a correlation with the proton affinity of the acid’s conjugate base. Such a correlation could, in principle, allow for an estimation of the degree of proton transfer in systems for which nuclear hyperfine structure has not been measured. The HCOOH–TMA system is a simple prototype for larger amine – carboxylic complexes, which are under investigation elsewhere for their possible role in the nucleation of atmospheric aerosol. The significant degree of proton transfer and the concomitant increase in polarity should contribute to loss of volatility and hence an increase in co-nucleation rates.



**Acknowledgement**

This work was supported by the National Science Foundation (Grant # CHE-1266320), the Minnesota Supercomputer Institute, and a University of Minnesota Doctoral Dissertation Fellowship awarded to RBM.

## Chapter 3 : The Formic Acid – Nitric Acid Complex: Microwave Spectrum, Structure, and Proton Transfer

Adapted with permission from R. B. Mackenzie, C. T. Dewberry, and K. R. Leopold,  
*J. Phys. Chem. A*, **118**, 7975-7985 (2014).  
© 2014 American Chemical Society.

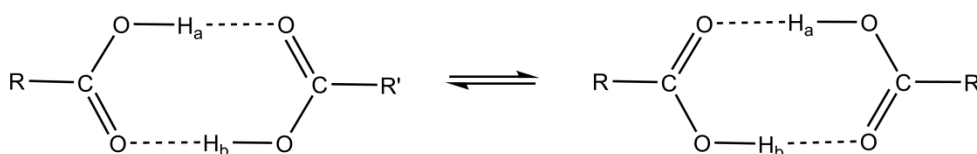
## Abstract

Rotational spectra are reported for seven isotopologues of the complex HCOOH–HNO<sub>3</sub> in a supersonic jet. The system is planar and bound by a pair of hydrogen bonds, much like the more widely studied carboxylic acid dimers. Double proton exchange interconverts the system between a pair of equivalent structures, as revealed by a splitting of the a-type spectrum that disappears when one of the hydrogen bonding protons is replaced by deuterium. The observation of relative intensities that are consistent with nuclear spin statistics in a symmetric and antisymmetric pair of tunneling states provides additional evidence for such a motion. The observed splittings in the pure rotational spectrum are one to two orders of magnitude smaller than those recently reported in the pure rotational spectra of several related carboxylic acid dimers. This is a curious difference, though we note that because the observed spectra do not cross the tunneling doublet, the splittings are a measure of the difference in effective rotational constants for the two states, not the tunneling frequency itself. The observed rotational constants have been used to determine an accurate vibrationally averaged structure for the complex. The two hydrogen bond lengths, 1.686(17) Å and 1.813(10) Å for the hydrogen bonds involving the HNO<sub>3</sub> and HCOOH protons, respectively, differ by 0.127(27) Å. Likewise, the associated oxygen-oxygen distances determined for the parent species, 2.631 and 2.794 Å, differ by 0.163 Å. These results suggest that the double proton transfer is necessarily accompanied by substantial motion of the heavy atom frame and thus this system, in principle, provides an excellent prototype for multidimensional tunneling processes. *Ab initio* calculations of the binding energy and the barrier height are presented. Excellent agreement between the calculated equilibrium structure and the experimental, vibrationally averaged structure suggests that the vibrational wavefunction is not highly delocalized in the region between the equivalent potential wells. <sup>14</sup>N nuclear quadrupole hyperfine structure is interpreted in terms of the degree to which the HNO<sub>3</sub> releases its proton in either of the equivalent potential energy minima.

## Introduction

Proton transfer is among the most elementary chemical processes.<sup>71,72</sup> It occurs in a wide range of systems, from simple aqueous acids to living cells,<sup>73,74</sup> and serves as the basis for the well-known Brønsted – Lowry definition of acids and bases.<sup>75,76</sup> While variations on the basic theme encompass topics such as proton-coupled electron transfer,<sup>77,78</sup> excited state proton transfer,<sup>79</sup> and “very strong” hydrogen bonds,<sup>80</sup> the simplicity of the process has also made it an attractive subject for numerous theoretical investigations.<sup>71-74</sup>

An important facet of the proton transfer problem involves systems in which the exchange of a pair of protons is a viable process. Such reactions are not only theoretically interesting,<sup>71,72</sup> but may be biologically important in processes such as the spontaneous development of point mutations in DNA<sup>81-84</sup> and the tautomerization of porphyrins and related compounds.<sup>85-87</sup> Carboxylic acid dimers have long provided convenient prototypes for double proton transfer because they universally adopt a doubly hydrogen bonded geometry that is well configured to support a degenerate double proton transfer process. Specifically, as illustrated below, the exchange of protons *a* and *b* creates an identical configuration and gives rise to the possibility of tunneling through an energy barrier that separates the potential energy minima.

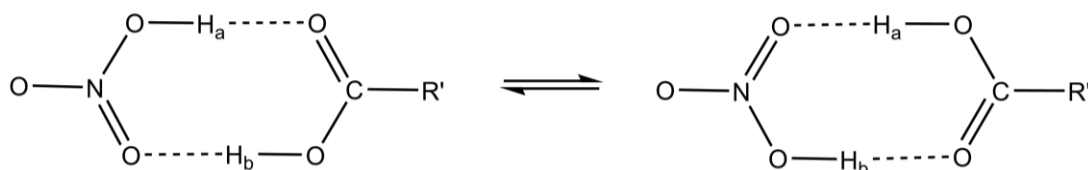


Quantitative understanding of the tunneling frequency requires knowledge of the height of the barrier, the separation between potential minima, and the effective mass for the tunneling motion. Moreover, as such processes are often multidimensional, the identification of a suitable reaction coordinate is necessary (though not always obvious), and indeed there has been much work developing methods for treating the dynamics of multidimensional tunneling problems.<sup>88-95</sup> The same is true, of course, in systems involving single intramolecular proton transfer such as malonaldehyde and tropolone,<sup>96</sup>

but for double proton transfer, there is the additional question as to whether the exchange is simultaneous or sequential.<sup>85-87,97-100</sup>

Experimental work on carboxylic acid dimers dates back many decades<sup>101,102</sup> and includes numerous spectroscopic studies which are at somewhat low resolution by today's standards. More recently, however, there has been a resurgence of interest in applying modern experimental and theoretical techniques to the study of these systems. Most closely related to the present work is a series of microwave spectroscopic studies that have determined structures and/or tunneling frequencies for complexes such as HCCCOOH-HCOOH,<sup>103-105</sup> C<sub>6</sub>H<sub>5</sub>COOH-HCOOH,<sup>106</sup> CH<sub>3</sub>COOH-HCOOH,<sup>107</sup> CF<sub>3</sub>COOH-HCOOH,<sup>108</sup> CF<sub>3</sub>COOH-CH<sub>3</sub>COOH,<sup>108</sup> CF<sub>3</sub>COOH-C<sub>3</sub>H<sub>5</sub>COOH,<sup>109</sup> CH<sub>2</sub>=CHCOOH-CHF<sub>2</sub>COOH,<sup>110</sup> CH<sub>2</sub>=CHCOOH-HCOOH,<sup>111</sup> and the polar conformer of (CH<sub>2</sub>=CHCOOH)<sub>2</sub>.<sup>112</sup> Infrared spectroscopy<sup>113-122</sup> has also provided valuable information and is particularly important for symmetric dimers that have no dipole moment and are therefore inaccessible to microwave investigations. Formic acid dimer, the simplest of carboxylic acid dimers, is especially noteworthy in this regard. Other experimental methods, including degenerate four-wave mixing<sup>123,124</sup> and electron diffraction,<sup>125,127</sup> have also been applied. In parallel with these studies, theoretical work aimed at predicting and interpreting observed tunneling frequencies in both ground and vibrationally excited states has been reported.<sup>128-137</sup>

In the carboxylic acid dimers, the two sites involved in hydrogen bonding are both COOH groups and thus the two hydrogen bonds across which tunneling takes place are typically very similar (if not identical). In this work, we replace one of the carboxylic acids with HNO<sub>3</sub>. As indicated below, this substitution retains the symmetry necessary for double proton transfer



but due to the involvement of the highly acidic  $\text{HNO}_3$  proton, the hydrogen bond lengths and associated  $\text{O}\cdots\text{O}$  distances differ significantly. Double proton exchange is necessarily accompanied by reorientation of the monomer units themselves and this system, therefore, may ultimately provide some broadened insight into the role of heavy atom motion in the double proton transfer process. We present microwave spectra of seven isotopologues of  $\text{HCOOH-HNO}_3$  from which we determine an accurate experimental structure for the system and, moreover, provide definitive evidence for the existence of double proton exchange. *Ab initio* calculations of the binding energy and barrier to proton exchange are presented and the results are compared with those of similar studies for carboxylic acid dimers. Finally, a somewhat different aspect of the proton transfer problem is explored through interpretation of the observed  $^{14}\text{N}$  nuclear quadrupole coupling constants, which are used to assess the degree of “partial proton transfer” associated with the complex at either of its minimum energy configurations.

### **Experimental Methods**

Rotational spectra of  $\text{HCOOH-HNO}_3$  were recorded between 4.7 and 15.0 GHz using a pulsed-nozzle Fourier transform microwave spectrometer, details of which have been given elsewhere.<sup>31,49</sup> Nitric acid was introduced into the system by passing argon over a reservoir of 90% nitric acid, which was then expanded through a 0.8 mm diameter nozzle into the microwave cavity with a stagnation pressure of 1.3 atm. Formic acid entrained in argon at a pressure of 0.7 atm was added through a continuous flow line, as previously described.<sup>50,138-141</sup> The flow line terminated in an “injection needle” of inner diameter 0.005", which was placed a few millimeters downstream of the nozzle orifice and bent so as to introduce the gas along the axis of the expansion. Optimal signals were obtained when the amount of water was limited; signals were significantly weakened when the concentrations of  $\text{HNO}_3$  and  $\text{HCOOH}$  were less than 80%. The nozzle was pulsed at a rate of 4 Hz and four free induction decay signals were collected per pulse with a data collection time of 140.8  $\mu\text{s}$ . Transition frequencies were typically accurate to 3 kHz, except in cases of severely congested and/or very weak spectra, for which the uncertainties may be as high as 13 kHz.

The rotational spectra of the isotopologues  $\text{HCOOH-H}^{15}\text{NO}_3$ ,  $\text{HCOOD-H}^{15}\text{NO}_3$ ,  $\text{HCOOH-DNO}_3$ ,  $\text{DCOOH-HNO}_3$ ,  $\text{HCOOD-HNO}_3$ ,  $\text{H}^{13}\text{COOH-HNO}_3$  were collected using the same instrumental setup, with the exception that the sample reservoirs were smaller.  $\text{DCOOH}$ ,  $\text{HCOOD}$  and  $\text{H}^{13}\text{COOH}$  were obtained from Sigma Aldrich.  $\text{H}^{15}\text{NO}_3$  was prepared by reacting 5 g of  $\text{Na}^{15}\text{NO}_3$  from Sigma Aldrich with 9 mL 96%  $\text{H}_2\text{SO}_4$  from Mallinckrodt.<sup>142</sup> Approximately 2.8 g of pure  $\text{H}^{15}\text{NO}_3$  were obtained at  $\sim 153$  °C and 680 mm Hg pressure over 3.5 hours.  $\text{DNO}_3$  was prepared similarly from the reaction of  $\text{NaNO}_3$  with  $\text{D}_2\text{SO}_4$ .

### Microwave Spectrum

Formic acid – nitric acid is a planar, near-prolate, asymmetric top bound by two hydrogen bonds. According to both chemical intuition and *ab initio* calculation (presented below), the complex has a large dipole moment component along the *a*-inertial axis, and a much smaller component along the *b*-inertial axis. Thus, only *a*-type rotational transitions were recorded for the seven isotopologues studied. For species with protons in both hydrogen bonds, a doubling of the spectrum was observed, indicating the existence of a pair of states which are labeled  $0^+$  and  $0^-$  in anticipation of their identification as a pair of tunneling states, as discussed below. These splittings were on the order of tens of kHz, rendering the components highly intertwined with the  $^{14}\text{N}$  nuclear hyperfine structure and therefore initially difficult to identify. However, analysis of the  $^{15}\text{N}$  isotopologue, in which the hyperfine structure is absent, provided a clear picture and led to eventual assignments. The appearance of the two, clearly resolved states in the  $2_{02} \leftarrow 1_{01}$  and  $2_{12} \leftarrow 1_{11}$  transitions of  $\text{HCOOH-H}^{15}\text{NO}_3$  is shown in Figure 3.1.

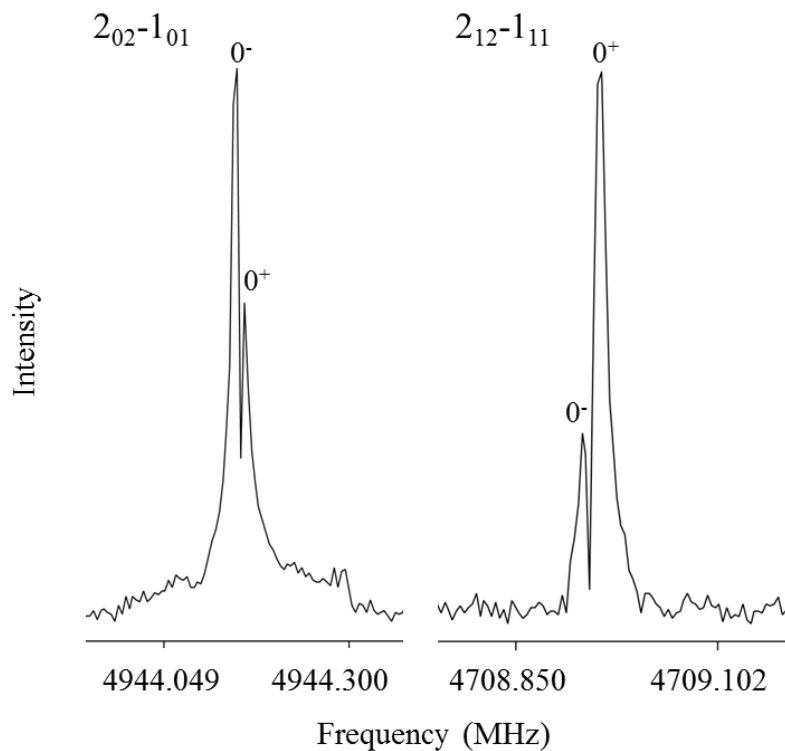


**Figure 3.1 Cavity Spectrum of  $\text{HCOOH-H}^{15}\text{NO}_3$**

The  $2_{02} \leftarrow 1_{01}$  and  $2_{12} \leftarrow 1_{11}$  transitions of  $\text{HCOOH-H}^{15}\text{NO}_3$  in the  $0^+$  and  $0^-$  states. The spectra illustrate the dependence of the relative intensities (1:3 or 3:1) for the two states on the parity of  $K_{-j}$ . Doppler doubling does not appear in these spectra. See text for discussion.

Because the observed splittings were only tens of kHz, careful attention was paid to distinguishing them from the Doppler doubling that is often observed in cavity-type microwave spectrometers. Our instrument operates in a configuration in which the axis of the supersonic expansion is perpendicular to the cavity axis, and it is common to find that the appearance or non-appearance of Doppler doubling is dependent upon the longitudinal cavity mode chosen. This likely results from the details of the overlap between the particle density distribution of the supersonic jet and the nodal structure of the mode, which in turn selects whether molecules with zero or non-zero transverse velocity components access regions of peak power within the cavity. Our use of a hypodermic injection needle along the axis of the expansion may also contribute. For transitions in which Doppler doubling was suspected, it was observed that the average frequency of the presumed Doppler doublet components was equal to the frequency



measured using a mode in which the doubling did not appear. Moreover, the intensity ratio of Doppler doublet components was much closer to 1:1 than that of a pair of  $0^+$  and  $0^-$  transitions, for which spin statistics dictate a 3:1 ratio. Indeed, the relative transition intensities for the  $0^+$  and  $0^-$  states alternated with the parity of  $K_{-J}$ , as expected for a pair of symmetric and antisymmetric tunneling states.

The isotopic dependence of the doubling provides definitive evidence that the motion involves both of the hydrogen bonding protons: The doubling appears in isotopologues for which both hydrogen bonds contain  $^1\text{H}$ , but disappears when one is substituted with deuterium (i.e., it is present in  $\text{HCOOH-HNO}_3$ ,  $\text{HCOOH-H}^{15}\text{NO}_3$ ,  $\text{DCOOH-HNO}_3$ , and  $\text{H}^{13}\text{COOH-HNO}_3$  but absent in  $\text{HCOOD-H}^{15}\text{NO}_3$ ,  $\text{HCOOH-DNO}_3$ , and  $\text{HCOOD-HNO}_3$ ). As observed in several carboxylic acid dimers, such an asymmetric substitution lifts the degeneracy of the configurations connected by double proton transfer and quenches the tunneling between them. Thus, we conclude that double proton transfer occurs in the ground vibrational state of  $\text{HCOOH-HNO}_3$ .<sup>143</sup>

Assignment of the spectra to either the  $0^+$  or  $0^-$  states was based on the agreement between the observed relative intensities and those predicted to arise from nuclear spin statistics. As seen in Figure 3.1, we observe an exchange of state-intensities in the  $0^+$  and  $0^-$  states with the parity of  $K_{-J}$ , a feature previously observed and described for several carboxylic acid dimers.<sup>103,106</sup> Specifically, tunneling between the two equivalent forms of the complex, followed by rotation about the a-axis interchanges the protons, leading to a 1:3 intensity ratio for the  $0^+$  and  $0^-$  state for transitions when  $K_{-J}$  is even and a 3:1 intensity ratio when  $K_{-J}$  is odd, in accord with the assignments given in the figure.

**Table 3.1 Observed Spectroscopic Constants for Isotopologues of HNO<sub>3</sub>–HCOOH Without Substitution in the H-Bonds**

Isotope	HCOOH-HNO <sub>3</sub> 0 <sup>+</sup> State	HCOOH-HNO <sub>3</sub> 0 <sup>-</sup> State	HCOOH-H <sup>15</sup> NO <sub>3</sub> 0 <sup>+</sup> State	HCOOH-H <sup>15</sup> NO <sub>3</sub> 0 <sup>-</sup> State	H <sup>13</sup> COOH- HNO <sub>3</sub> <sup>a</sup>	DCOOH- HNO <sub>3</sub> <sup>b</sup>
<i>A</i> (MHz)	6175.920(98)	6175.264(49)	6174.767(54)	6174.877(44)	6172.66(15)	6167.29(57)
<i>B</i> (MHz)	1368.84012(42)	1368.84027(74)	1360.43598(44)	1360.43597(59)	1347.9018(13)	1325.6573(34)
<i>C</i> (MHz)	1121.83870(36)	1121.83199(60)	1116.17782(40)	1116.17187(44)	1107.6852(13)	1092.5301(41)
$\Delta_{ID}$ (amu Å <sup>2</sup> )	-0.541	-0.547	-0.553	-0.549	-0.563	-0.597
<sup>14</sup> N $\chi_{aa}$ (MHz)	-0.7885(15)	-0.7872(22)	-	-	-0.805(45)	-0.777(25)
<sup>14</sup> N( $\chi_{bb}$ - $\chi_{cc}$ ) (MHz)	0.513(11)	0.440(56)	-	-	0.54(25)	0.344(92)
$\Delta_J$ (kHz)	0.3249(49)	0.2897(43)	0.2912(33)	0.2875(32)	0.255(13)	0.241(37)
$\Delta_{JK}$ (kHz)	0.820(87)	1.261(46)	1.260(54)	1.313(53)	0.820 <sup>c</sup>	3.06(49)
$\delta_J$ (kHz)	0.0634(49)	0.0760(95)	0.0507(35)	0.0646(42)	0.098(15)	0.080(46)
RMS (kHz)	2	2	2	2	4	14
<i>N</i>	39	36	18	19	14	31

(a) Transition frequencies for the 0<sup>+</sup> and 0<sup>-</sup> states were combined in a single fit. See text for discussion.

(b) Transition frequencies for the 0<sup>+</sup> and 0<sup>-</sup> states of DCOOH–HNO<sub>3</sub> were fit together, due to spectral congestion arising from two quadrupolar nuclei and proton exchange doubling, which is not quenched by substitution on the formyl hydrogen. The sign of the residuals generally alternates with that of  $K_{-J}$ , supporting the existence of tunneling in the isotopologue.

(c) Value was fixed to that of the 0<sup>+</sup> state of HCOOH–HNO<sub>3</sub> because only  $K_{-J}=0$  and 1 transitions were used in the fit.

**Table 3.2 Observed Spectroscopic Constants for Isotopologues of HNO<sub>3</sub>–HCOOH with Substitution in the H-Bonds**

Isotopologue	HCOOD-H <sup>15</sup> NO <sub>3</sub>	HCOOD-HNO <sub>3</sub>	HCOOH-DNO <sub>3</sub>
A (MHz)	6077.493(27)	6077.329(99)	6094.98(10)
B (MHz)	1355.55430(19)	1364.00473(81)	1365.3094(11)
C (MHz)	1109.69374(17)	1115.3578(10)	1116.7928(11)
$\Delta_{ID}$ (amu Å <sup>2</sup> )	-0.555	-0.560	-0.547
<sup>14</sup> N $\chi_{aa}$ (MHz)	-	-0.811(17)	-0.843(11)
<sup>14</sup> N ( $\chi_{bb}-\chi_{cc}$ ) (MHz)	-	0.460(52)	0.16(14)
HCOOD $\chi_{aa}$ (MHz) <sup>a</sup>	0.2139(14)	0.255(26)	-
DNO <sub>3</sub> $\chi_{aa}$ (MHz) <sup>a</sup>	-	-	0.1280(73)
$\Delta_J$ (kHz)	0.2845(17)	0.2543(85)	0.2637(99)
$\Delta_{JK}$ (kHz)	1.260 <sup>b</sup>	1.51(13)	1.286(94)
$\delta_J$ (kHz)	0.0508(17)	0.0656(97)	0.040(14)
RMS (kHz)	1	5	4
<i>N</i>	26	44	37

(a) ( $\chi_{bb}-\chi_{cc}$ ) was not necessary to fit the deuterium hyperfine structure.

(b) Value fixed to the HCOOH–H<sup>15</sup>NO<sub>3</sub> value because only  $K_{-1} = 0$  and 1 transitions were used in the fit.

Spectra for each isotopologue studied were fit using the A-reduced Watson Hamiltonian<sup>34</sup> (equation 1) and the SPFIT program of Pickett.<sup>144</sup>

$$\begin{aligned}
 H = & \left[ \frac{B+C}{2} - \Delta_J J^2 \right] J^2 + \left[ A - \frac{B+C}{2} - \Delta_{JK} J^2 - \Delta_K J_z^2 \right] J_z^2 \\
 & + \quad \quad \quad (1)
 \end{aligned}$$

$$\left[ \frac{B-C}{2} - 2\delta_J J^2 \right] (J_x^2 - J_y^2) - \delta_K [J_z^2 (J_x^2 - J_y^2) + (J_x^2 + J_y^2) J_z^2]$$

Here, *A*, *B*, and *C* are rotational constants, the upper and lower case deltas are quartic centrifugal distortion constants, and the *J*s are angular momentum operators. The constants  $\Delta_J$ ,  $\Delta_{JK}$ , and  $\delta_J$  were needed to fit the data within experimental uncertainty, but  $\Delta_K$  and  $\delta_K$  were not determined and were, therefore, effectively set to zero. For isotopologues where only  $K_{-1} = 0$  and 1 transitions were observed,  $\Delta_{JK}$  was locked to the value of the most closely related isotopologue for which it was experimentally

determined. For HCOOH–HNO<sub>3</sub> and HCOOH–H<sup>15</sup>N<sub>3</sub>, which exhibited a pair of states, separate fits were performed for each state. For H<sup>13</sup>COOH–HNO<sub>3</sub>, only  $K_{-J} = 0$  and 1 transitions were observed and, in many cases, only the more intense of the two states was observable due to a reduced signal-to-noise ratio. Since the intensity alternates with the sign of  $(-1)^{K-1}$ , separate fits would, therefore, have had to include only  $K_{-J} = 0$  or only  $K_{-J} = 1$  transitions. For this reason, and since the rotational constants for the two states are so similar, we opted to combine the  $K_{-J} = 0$  and 1 data into a single fit, resulting in standard errors in the rotational constants that were slightly larger than those of the parent or <sup>15</sup>N isotopologues, though still quite acceptable. Likewise, for the DCOOH–HNO<sub>3</sub> complex, the spectral congestion due to tunneling and hyperfine structure from both the <sup>14</sup>N and deuterium nuclei precluded definitive tunneling state assignments and a single fit was, therefore, also performed. Spectroscopic constants are presented in Tables 3.1 and 3.2, and complete lists of transition frequencies, assignments, and residuals are provided in Appendix C.

Nuclear electric quadrupole hyperfine structure was observed for isotopologues containing <sup>14</sup>N or deuterium and was analyzed using standard methods.<sup>34</sup> For species with only one quadrupolar nucleus (<sup>14</sup>N or D), the coupling scheme

$$\mathbf{F} = \mathbf{J} + \mathbf{I} \quad (2)$$

was used, where  $\mathbf{I}$  is the nuclear spin and  $\mathbf{F}$  is the total angular momentum. For species with two quadrupolar nuclei (viz., <sup>14</sup>N and D), a sequential coupling scheme was implemented:

$$\mathbf{F}_I = \mathbf{J} + \mathbf{I}_N \quad (3)$$

$$\mathbf{F} = \mathbf{F}_I + \mathbf{I}_D \quad (4)$$

where  $I_N = I_D = 1$  and  $\mathbf{F}$  is the total angular momentum. The hyperfine constants  $\chi_{aa}$  and  $(\chi_{bb} - \chi_{cc})$  for the <sup>14</sup>N nucleus were obtained for <sup>14</sup>N-containing species. However, for deuterated isotopologues in which hyperfine structure was resolved and analyzed, only

$\chi_{aa}$  was determinable from the data. Hyperfine constants are included in Tables 3.1 and 3.2. Deuterium hyperfine structure was not assigned for DCOOH–HNO<sub>3</sub> because, unlike the other deuterated isotopologues studied, this species retained the spectral doubling observed for the parent form, and, as noted above, the convolution of the 0<sup>+</sup> and 0<sup>-</sup> states spectra with hyperfine structure from two nuclei made the spectra too dense and complex to assign.

Double proton transfer in HCOOH–HNO<sub>3</sub> inverts the *b*-component of the dipole moment but leaves the *a*-component unchanged. Thus, it is expected that *b*-type transitions will cross the tunneling doublet,<sup>145</sup> while *a*-type transitions will not. As a result, the doubling observed in the *a*-type spectrum reflects slight differences in the rotational constants between the two tunneling states, but does not provide a direct measure of the tunneling splitting itself. The value of  $(\mu_b/\mu_a)^2$  obtained from *ab initio* calculations is 0.0061 (see next section) and thus, it was anticipated that the *b*-type spectrum would be unobservable, given the signal-to-noise ratio typical of the *a*-type spectrum. Moreover, for the H/H species, these transitions will be shifted from the rigid rotor predictions by an unknown amount due to the tunneling frequency. Nevertheless, once the fits of the *a*-type spectra were complete, attempts were made to observe *b*-type transitions. In order to eliminate the uncertainty associated with the tunneling frequency, narrow searches were conducted at the predicted frequencies for several *b*-type lines of HCOOD–H<sup>15</sup>NO<sub>3</sub>, for which the tunneling is absent. As expected, due to the small value of  $\mu_b$ , no spectra were observed and thus searches for analogous lines of the parent complex were not pursued.

An indirect method of estimating the tunneling splitting from spectra that do not cross the tunneling doublet has been successful in a number of cases.<sup>106,107</sup> This method relies on analysis of perturbations in the pure rotational spectra that arise from Coriolis interactions between the tunneling states to estimate the energy spacing. However, in HCOOH–HNO<sub>3</sub>, the observed splittings are very small and the spectra observed for each state were well fit to a Watson Hamiltonian without the inclusion of a Coriolis perturbation term. For this reason, it was anticipated that a simultaneous fit of the two tunneling states would yield no new information. Indeed, attempts to obtain a

simultaneous fit of the  $0^+$  and  $0^-$  state spectra of the parent species using a Coriolis perturbation term ( $F_{ab}$ ) and energy difference between tunneling states ( $\Delta E_{01}$ ) proved these quantities to be indeterminate. Thus, while the doubling of the  $a$ -type spectra confirms the existence of a double proton transfer process, the small value of  $\mu_b$  and the absence of observable Coriolis perturbations has precluded a measurement of the tunneling splitting itself.

### Computational Methods and Results

MP2/6-311G(2d,2p) calculations were used to determine the minimum energy structure and dipole moment components of the complex. Several basis sets were tried, including the larger 6-311++G(2df,2p) basis, but 6-311G(2d,2p) calculations produced rotational constants in closest agreement with experiment and are therefore the ones quoted here. Frequency calculations were performed to confirm that the structure was a minimum on the potential energy surface. The results of these calculations are presented in Table 3.3, where the atom numbering corresponds to that presented in Figure 3.2a. The calculated dipole moment components of the complex are 2.69, 0.21, and 0.0 D, for  $\mu_a$ ,  $\mu_b$ , and  $\mu_c$ , respectively, and the counterpoise corrected (CPC)<sup>52</sup> binding energy is 12.3 kcal/mol (16.2 kcal/mol without the counterpoise correction). The structural changes in the monomer units upon complexation were also estimated by optimizing the monomer structures and comparing the results with the internal structural parameters obtained for the complex (both with and without the counterpoise correction). Changes in bond lengths and bond angles were small, typically only a few hundredths of an angstrom or a few degrees for bond lengths and bond angles, respectively. These results are also provided as Supporting Information. The energy and geometry of the transition state associated with double exchange of the protons were calculated at the MP2/6-311G(2d,2p) level, with the results that the barrier to double proton transfer is 9.9 kcal/mol above the potential energy minimum. Structural parameters for the transition state, also obtained at the MP2/6-311G(2d,2p) level/basis are included in Table 3.3 and illustrated in Figure 3.2b.

A separate series of calculations on a number of related carboxylic acid dimers was also performed in order to make meaningful comparisons with HCOOH–HNO<sub>3</sub>. The results of these calculations, done at the MP2/6-31++G(d,p) level/basis, are presented Table 3.4. Although calculations for all of the carboxylic acid dimers included have been reported in the literature, the basis sets and level of theory have varied, making comparison difficult. The results in Table 3.4 are generally in line with those reported elsewhere, but the consistency in level of theory enables direct comparison.

**Table 3.3 Selected *Ab Initio* Structural Parameters for HCOOH–HNO<sub>3</sub>**

	Equilibrium Structure MP2/6-311G(2d,2p)	Equilibrium Structure CP-MP2/6-311G(2d,2p) <sup>a</sup>	Transition State MP2/6-311G(2d,2p)
<i>R(O5-O6)</i>	2.6671	2.7325	2.4119
<i>R(O3-O9)</i>	2.7776	2.8627	2.4119
<i>R(O5-H8)</i>	1.6827	1.7531	1.1291
<i>R(O9-H4)</i>	1.8002	1.8903	1.2871
<i>R(C1-N7)</i>	3.9461	4.0218	3.6218
< <i>(O5-H8-O6)</i>	170.3	170.5	173.1
< <i>(O3-H4-O9)</i>	176.3	174.6	173.1
< <i>(C1-O5-O6)</i>	128.3	129.8	115.7
< <i>(O5-O6-N7)</i>	112.1	111.3	120.0

(a) Bond lengths are in angstroms. Bond angles are in degrees. Atom numbering corresponds to that in Figure 3.2. “CP” indicates “counterpoise corrected”.

**Table 3.4 Comparison Between HCOOH–HNO<sub>3</sub> and Several Carboxylic Acid Dimers**

<b>Complex</b>	<b>Binding Energy (kcal/mol)</b>	<b>Barrier Height (kcal/mol)</b>	<b>O-O Distances at Minimum Energy Structure (Å)</b>	<b>O-O Distances at Transition State Structure (Å)</b>	<b>H-Bond Lengths at Minimum Energy Structure (Å)</b>	<b>H-Bond Lengths at Transition State Structure (Å)</b>
Formic Formic	17.0(14.5)	7.9	2.787/2.787	2.412/2.412	1.797/1.797	1.206/1.206
Formic Propiolic	17.2(14.6)	7.7	2.772/2.786	2.412/2.412	1.797/1.780	1.220/1.192
Formic Benzoic	18.2(15.4)	7.0	2.742/2.785	2.411/2.411	1.795/1.748	1.233/1.179
Acrylic Acrylic	18.8(15.8)	6.9	2.756/2.749	2.409/2.405	1.763/1.757	1.205/1.203
Nitric Formic	14.3(11.8)	9.2	2.753/2.946	2.427/2.427	1.975/1.763	1.312/1.119

All calculations were done at the MP2/6-31++G(d,p) level/basis. Numbers in parentheses and the structural parameters for the minimum energy structures are counterpoise corrected. Binding energies are “ $D_e$ ”, not  $D_o$ .



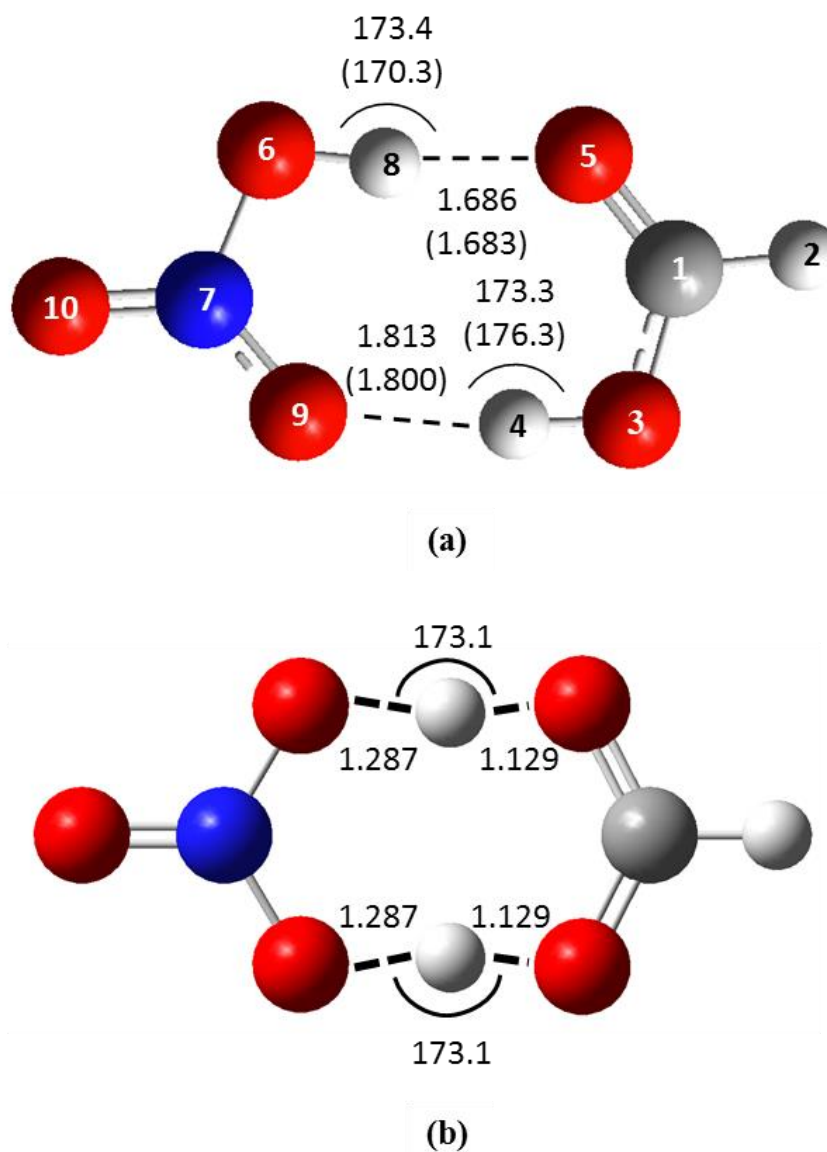


**Figure 3.2 Equilibrium and Transition State Structures of HCOOH-HNO<sub>3</sub>**

(a) The HCOOH-HNO<sub>3</sub> complex with important intermolecular structural parameters indicated. Numbers not in parentheses are experimental values for the ground vibrational state. Numbers in parentheses are theoretical values calculated at MP2/6-311g(2d,2p) level without counterpoise correction. (b) Calculated structure of the transition state, obtained at the MP2/6-311G(2d,2p) level/basis. The atom numbers (not labeled) are the same as in (a). All distances are in Å. All angles are in degrees.

## Structure Analysis

The rotational constants in Tables 3.1 and 3.2 may be used to determine the inertial defect,  $\Delta_{ID}$ , of the complex, defined by<sup>34</sup>

$$\Delta_{ID} \equiv \frac{h}{8\pi^2} \left( \frac{1}{C} - \frac{1}{A} - \frac{1}{B} \right) = -2 \sum_i m_i c_i^2 \quad (5)$$

The values obtained are also listed in the tables. The small, negative values (e.g.,  $-0.547$  amu  $\text{\AA}^2$  for the parent species) are consistent with a planar system, in agreement with *ab initio* calculations. Thus, in all subsequent analysis, the complex is assumed to be planar.

The structure of the complex was determined using previously published<sup>146</sup> analytical expressions for the components of the inertial tensor in terms of the moments of inertia of the monomers, their orientation, and their center-of-mass separation,  $R_{cm}$ . This type of analysis, while common for linear and symmetric top complexes, has been less widely used for systems containing a pair of asymmetric rotors, and it is therefore useful to outline the procedure here. An important advantage of such an analysis is that angular information from nuclear hyperfine structure is readily incorporated. We initially invoke the usual approximation that the monomer geometries are unchanged upon complexation, though the effects of this constraint will be tested and incorporated into the final results.

The components of the inertial tensor of the complex are given in an  $(X,Y,Z)$  axis system (shown in Figure 3.3a), for which the origin lies at the center of mass of the complex. In the most general formulation, the  $a$ ,  $b$ , and  $c$  axes of each monomer are initially aligned along  $Z$ ,  $X$ ,  $Y$ , respectively, and three rotations orient each monomer within in the complex. Since HCOOH–HNO<sub>3</sub> is planar, however, only a single angle is required for each monomer. This angle is designated  $\theta_i$ , (where  $i = 1$  and  $i = 2$  refer to HNO<sub>3</sub> and HCOOH, respectively) and is the angle formed between the  $a$ -axis of monomer  $i$  and  $Z$  (see Figure 3.3a).  $\theta_i$  is defined to be positive when the  $a$ -axis of monomer  $i$  is rotated counterclockwise with respect to  $Z$ . The non-zero elements of the inertial tensor of the complex in the  $(X,Y,Z)$  axis system reduce to<sup>146</sup>

$$I_{ZZ} = \sum_{i=1}^2 \left[ I_{aa}^{(i)} \cos^2 \theta_i + I_{bb}^{(i)} \sin^2 \theta_i \right] \quad (6)$$

$$I_{XX} = \mu R_{cm}^2 + \sum_{i=1}^2 \left[ I_{aa}^{(i)} \sin^2 \theta_i + I_{bb}^{(i)} \cos^2 \theta_i \right] \quad (7)$$

$$I_{YY} = \mu R_{cm}^2 + I_{cc}^{(1)} + I_{cc}^{(2)} \quad (8)$$

$$I_{XZ} = I_{ZX} = \sum_{i=1}^2 \left[ I_{aa}^{(i)} - I_{bb}^{(i)} \right] \cos \theta_i \sin \theta_i \quad (9)$$

Here,  $\mu = m(\text{HNO}_3)m(\text{HCOOH})/[m(\text{HNO}_3)+m(\text{HCOOH})]$  is the pseudo diatomic reduced mass of the complex and  $I_{gg}^{(i)}$  is the moment of inertia of monomer  $i$  about its  $g$ -inertial axis.

The coordinates of each atom in the complex in the  $(X, Y, Z)$  frame are given by<sup>146</sup>

$$X_i = a_i \sin \theta_i + b_i \cos \theta_i \quad (10)$$

$$Y_i = 0 \quad (11)$$

$$Z_i = a_i \cos \theta_i - b_i \sin \theta_i + (-1)^i R_i \quad (12)$$

where  $(a_i, b_i, c_i)$  are the coordinates of the  $i^{\text{th}}$  atom in the inertial axis system of its monomer and  $i = 1$  or  $2$ , depending on whether the atom is in  $\text{HNO}_3$  or  $\text{HCOOH}$ .  $R_1$  and  $R_2$  are the distances between the center of mass of the complex and the centers of mass of  $\text{HNO}_3$  and  $\text{HCOOH}$ , respectively, and are defined as positive quantities.

The moments of inertia of  $\text{HNO}_3$ <sup>147</sup> and  $\text{HCOOH}$ <sup>59-61</sup> were obtained from the literature rotational constants, e.g.,  $I_{aa} = h/8\pi^2 A$ , etc. Since  $I_{cc}$  of the complex is independent of the angular orientation of the monomers,  $R_{cm}$  was first determined for each isotopologue studied by determining the value that reproduced the  $C$  rotational constant. For species in

which two states were observed, the ground state rotational constants were used. The resulting values are listed in Table 3.5.

The value of  $\theta_l$  was next estimated from the  $^{14}\text{N}$  nuclear hyperfine structure. Invoking the usual assumption that the  $\text{HNO}_3$  is negligibly perturbed by a weak intermolecular interaction, the observed value of  $\chi_{aa}$  for each isotopologue was used to estimate the angle,  $\tau$ , formed between the principal axis system of the  $\text{HNO}_3$  quadrupole coupling tensor and the inertial axis system of the complex, viz.,

$$\chi_{aa} = \chi_{xx} \cos^2 \tau + \chi_{yy} \sin^2 \tau \quad (13)$$

Here,  $\chi_{xx} = 1.1468(34)$  MHz and  $\chi_{yy} = -1.0675(34)$  MHz, are eigenvalues corresponding to the in-plane eigenvectors of the  $\text{HNO}_3$  quadrupole coupling tensor, with the  $x$ -axis most closely aligned with the N–O(H) bond.<sup>148,149</sup> Using the value of  $\chi_{aa}$  listed in Table 3.1 for the parent form of the  $\text{HCOOH–HNO}_3$  gives a value of  $\tau = 69.21^\circ$ , which was also used for isotopologues involving  $\text{H}^{15}\text{NO}_3$ . For complexes containing  $\text{DNO}_3$ , the value of  $\tau = 71.26^\circ$  was obtained from  $\chi_{aa}(^{14}\text{N})$  of  $\text{DNO}_3\text{–HCOOH}$ .

The angle  $\tau$  does not exactly equal  $\theta_l$  because the principal axis system of the quadrupole coupling tensor of  $\text{HNO}_3$  does not coincide with its inertial axis system and because the  $Z$  axis does not exactly coincide with the  $a$ -axis of the complex. The relationship between these angles is indicated in Figure 3.3b.  $\psi$  is the angle between the principal axis system of the  $^{14}\text{N}$  quadrupole coupling tensor and the N–O(H) bond, and has previously been determined to be  $1.88^\circ$ .<sup>148</sup>  $\alpha$  is the angle between the  $a$ -axis of  $\text{HNO}_3$  and the N–O(H) bond, and can be obtained for any isotopologue of nitric acid from the published structure.<sup>147</sup>  $\beta$  is the angle between the  $Z$ -axis as defined in Figure 3.3 and the  $a$ -axis of the complex. From the diagram, it is clear that

$$\theta_l = \tau - \psi - \alpha - \beta \quad (14)$$

thus allowing  $\theta_1$  to be determined from the observed value of  $\tau$ . Although it is not known *a priori* whether the *a*-axis of the complex is rotated clockwise or counterclockwise with respect to *Z*, the clockwise rotation shown in Figure 3.3b turns out to be correct. Strictly speaking,  $\beta$  must be determined iteratively, since it depends on the structure of the complex which, in turn depends on  $\theta_1$  and  $\theta_2$ . However,  $\beta$  is small and its variation among isotopologues is even smaller. For the parent species, one iteration yielded a value of  $\beta = 0.89^\circ$  and this was used for all isotopic species studied. The actual values obtained from the final structures of each isotopologue are also included in Table 3.5, where it is seen that the variation is negligible.

With  $R_{cm}$  and  $\theta_1$  determined, the value of  $\theta_2$  was adjusted to reproduce either the value of *A* or the value of *B*. The two results generally agreed to within  $\sim 4^\circ$ , and the average value was used. The results for each isotopologue are also reported in Table 3.5.

Once  $R_{cm}$ ,  $\theta_1$ , and  $\theta_2$  were determined, the coordinates of each atom in the (*X,Y,Z*) axis system were obtained from equations 10 - 12, and values of all intermolecular distances and angles were readily determined. Note that these calculations require the coordinates of each atom in the inertial axis system of its monomer, which were obtained from published structures.<sup>59,61,147</sup> The entire analysis was performed for each isotopologue and the results are summarized in Table 3.5. The consistency among isotopologues is seen to be excellent and the average of the maximum and minimum values obtained for  $R(H8-O5)$ ,  $R(O9-H4)$ ,  $\angle(O5-H8-O6)$ , and  $\angle(O3-H4-O9)$  (i.e., the hydrogen bond lengths and angles) are given, with uncertainties chosen to include all values.

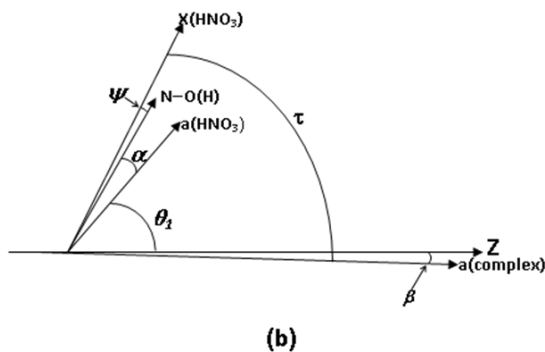
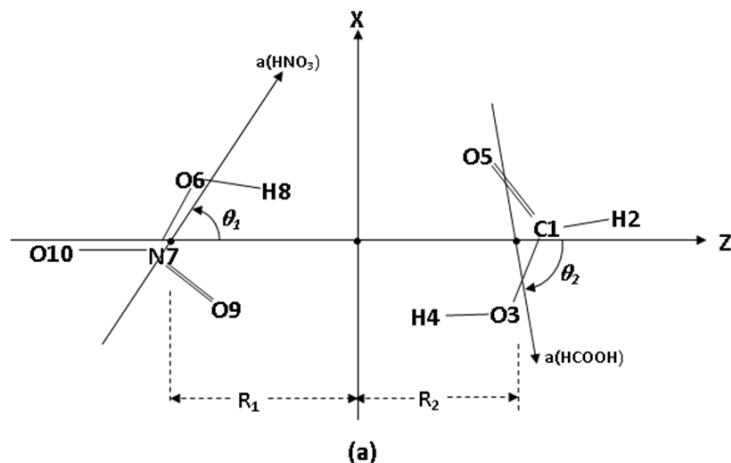


**Figure 3.3 Definitions of Structural Parameters for HCOOH-HNO<sub>3</sub>**

(a) Definition of angles to define the structure of HCOOH-HNO<sub>3</sub>. (b) Relationship between additional angles used in equation 14.

The final, recommended structural parameters were determined as follows: Because equations 6 – 9 use the moments of inertia of the free monomers to compute the moments and products of inertia of the complex, they are subject to errors resulting from slight changes in monomer geometries upon complexation. To estimate the magnitude of this effect, the structural analysis was repeated for HCOOH-H<sup>14</sup>NO<sub>3</sub> using monomer moments of inertia which were calculated by imposing the *ab initio* changes<sup>150</sup> in structure upon complexation on the experimental monomer geometries. The resulting changes in  $R(H8-O5)$ ,  $R(O9-H4)$ ,  $\angle(O5-H8-O6)$ , and  $\angle(O3-H4-O9)$  were small,

typically on the order of the error bar derived from variations among isotopologues. Thus, the isotopic average values for these quantities obtained as described above, were corrected by adding the calculated change resulting from the theoretical changes in monomer geometries for the parent species. These values are listed in Table 3.5 under “Preferred Values” and are also included in Figure 3.2a, along with the corresponding *ab initio* values in parentheses.

As a check on the structure, the program STRFIT<sup>151</sup> was also used to determine the intermolecular distances and angles. Bond lengths and bond angles of the monomers were constrained to their free-molecule values, given in the literature for HNO<sub>3</sub><sup>147</sup> and HCOOH.<sup>59,61</sup> In pursuing this approach, it soon became apparent that the results were sensitive to the starting values of the fitted parameters, particularly  $R(O5-O6)$ , which was used in these calculations as one of the defining structural parameters. With a large (yet reasonable) initial estimate of this distance, the fit converged to a structure in which  $R(H8-O5) = 2.034 \text{ \AA}$  and  $R(O9-H4) = 1.716 \text{ \AA}$ . While the standard errors and correlation coefficients suggested a high quality fit, this structure is in poor agreement with both the *ab initio* structure and the structure described above. Moreover, the structure corresponded to an angle  $\tau = 89.6^\circ$ , in rather poor agreement with the value of  $69.2^\circ$  obtained above from nuclear hyperfine structure. With a shorter initial guess for  $R(O5-O6)$ , however, the structure listed in Table 3.5 under “STRFIT” was obtained. While the standard errors and correlation coefficients from this fit were somewhat larger than those of the earlier fit, this structure gave a value of  $\tau = 71.0^\circ$ , a value within  $2^\circ$  of that derived from hyperfine structure. This structure is also in agreement with the results obtained by other methods (e.g., equations 6-14 and *ab initio* computation) and we believe it to correspond to the true global minimum on the least squares surface.<sup>152</sup> Interestingly, in an attempt to resolve this issue, a third fit was tried in which the monomer structures were adjusted based on the predicted structural changes from *ab initio* calculations. When this was done, no fit corresponding to the previously observed local-minimum could be obtained, regardless of the starting values and the results were similar to those reported in Table 3.5.

**Table 3.5 Experimental Structural Parameters for Isotopologues of HNO<sub>3</sub>–HCOOH<sup>(a)</sup>**

Complex	$R_{cm}^{(b)}$	$\alpha^{(c)}$	$\beta^{(d)}$	$\theta_1^{(e)}$	$\theta_2^{(e)}$	$R(H8-O5)$	$R(O9-H4)$	$\langle(O5-H8-O6)\rangle$	$\langle(O3-H4-O9)\rangle$
HNO <sub>3</sub> -HCOOH	3.475976	15.13	0.89	51.31	-80.40	1.6527	1.8523	166.8	172.9
H <sup>15</sup> NO <sub>3</sub> -HCOOH	3.476787	15.09	0.67	51.37	-80.42	1.6531	1.8516	166.9	172.9
H <sup>15</sup> NO <sub>3</sub> -HCOOD	3.457604	15.09	0.71	51.37	-81.77	1.6464	1.8586	166.1	173.1
HNO <sub>3</sub> -HCOOD	3.456808	15.13	0.74	52.23	-81.54	1.6572	1.8483	167.8	172.4
HNO <sub>3</sub> -H <sup>13</sup> COOH	3.484357	15.13	0.67	52.02	-80.34	1.6622	1.8435	168.3	172.3
DNO <sub>3</sub> -HCOOH	3.459116	23.26	0.67	45.24	-79.64	1.6795	1.8384	170.3	171.4
HNO <sub>3</sub> -DCOOH	3.506919	15.13	0.75	50.90	-80.60	1.6455	1.8585	166.3	172.9
Average of Maximum and Minimum Values <sup>f</sup>						1.663(17)	1.849(10)	168.2(21)	172.25(85)
Value from STRFIT						1.67	1.84	170.1	171.2
Preferred Values <sup>(g)</sup>						1.686(17)	1.813(10)	173.4(21)	173.29(85)
<i>Ab initio</i> Value <sup>(h)</sup>						1.6827	1.8002	170.3	176.3

(a) Bond lengths are in angstroms. Bond angles are in degrees.

(b) Determined for each isotopologue from the *C* rotational constant.

(c) Determined from the structure of HNO<sub>3</sub> reported in Ref. 147.

(d) The value of  $\beta = 0.89$  was used for all calculations. The final value of  $\beta$  is what is listed for each isotopologue. The variation is sufficiently small as to not warrant further iteration.

(e) The negative sign indicates clockwise rotation of the *a*-axis of formic acid with respect to *Z*. See Figure 3.3a.

(f) Uncertainty chosen to encompass maximum and minimum values.

(g) Values incorporate calculated changes in monomer geometries upon complexation. See text for discussion.

(h) Obtained at the MP2/6-311G(2d,2p) level/basis.



## Discussion

The structure of HCOOH–HNO<sub>3</sub>, as determined from both experimental rotational constants and *ab initio* calculation indicates the expected cyclic, doubly hydrogen bonded geometry, analogous to that of virtually all previously studied carboxylic acid dimers. The agreement between the experimental and theoretical intermolecular distances and angles is excellent and provides a solid measure of confidence in the reported structure. Moreover, as anticipated at the outset of this investigation, the hydrogen bond lengths and O···O distances associated with the two hydrogen bonds are significantly different. For example, in the “preferred” structure of Table 3.5, the hydrogen bond length associated with the proton of the HNO<sub>3</sub> is 0.127(27) Å shorter than that associated with the carboxylic proton of the HCOOH. It seems sensible that the shorter hydrogen bond is that involving the stronger acid as the proton donor. The corresponding O···O distances also follow this trend, with the heavy atom distance in the shorter hydrogen bond 0.163 Å shorter than that in the longer hydrogen bond.<sup>153</sup>

With a sizable difference between the two hydrogen bonds, significant structural reorganization is necessary to interconvert equivalent forms, and it is thus reasonable to ask to what extent proton exchange is an important process in this system. The primary physical manifestation of such a process is the existence of a pair of tunneling states, whose origin lies in the splitting of the degenerate states corresponding to equivalent configurations when the barrier to proton transfer is finite. As argued above, such a pair of states exists in this system, and isotopic substitution experiments indicate that the underlying process is indeed double proton transfer. The ability to observe both states at the low temperature of the supersonic jet (for which  $kT$  is approximately 1 – 2 cm<sup>-1</sup>) strongly suggests that the spacing is small. Additionally, we note that the excellent agreement between the experimentally derived average structure and the computationally determined equilibrium structure further support a picture in which the vibrational wavefunction is largely localized in one or the other of two potential wells, with little amplitude in the classically forbidden region. If the energies of the 0<sup>+</sup> and 0<sup>-</sup> states were above the barrier, the additional delocalization might be expected to render the average

hydrogen bond lengths significantly different from those at either of the equilibrium geometries.

The spectral splittings observed in the *a*-type spectrum of HCOOH–HNO<sub>3</sub> are small in comparison with those previously reported in high resolution studies of carboxylic acid dimers. For example, the splittings in the 5<sub>05</sub> – 6<sub>06</sub> transitions, calculated from published rotational constants for the 0<sup>+</sup> and 0<sup>-</sup> states of (HCOOH)<sub>2</sub>, HCCCCOOH–HCOOH, C<sub>6</sub>H<sub>5</sub>COOH–HCOOH, and (CH<sub>2</sub>CHCOOH)<sub>2</sub><sup>154</sup> are 41 MHz, 2.43 MHz, 0.987 MHz, and 2.182 MHz, respectively. These values may be compared with that of only 0.033 MHz observed for HCOOH–H<sup>15</sup>NO<sub>3</sub>. Note that since these splittings generally increase with *J*, the 5<sub>05</sub> – 6<sub>06</sub> transition has been arbitrarily chosen for this comparison, but the same conclusion is reached when comparing other rotational transitions as well. As indicated above, these splittings reflect small differences in the effective rotational constants for the two tunneling states but do not provide a measure of the tunneling splitting. It is likely that the usual factors that play into determining the tunneling splitting itself (e.g., barrier height, separation between minima, tunneling path), combined with slight differences in vibrational averaging between the 0<sup>+</sup> and 0<sup>-</sup> states and the possibility of small Coriolis interactions, conspire to produce these differences in a way that is very difficult to predict.

It is also of interest to compare a number of calculated properties of HCOOH–HNO<sub>3</sub> with those of several related carboxylic acid dimers. Referring to Table 3.4, it is seen that the calculated barrier height for the proton transfer (9.2 kcal/mol) is about 1 – 2 kcal/mol higher than those of the carboxylic acid dimers, which fall fairly consistently in the 7 – 8 kcal/mol range. Moreover, while the barrier in HCOOH–HNO<sub>3</sub> is larger, the binding energy is seen to be 3 – 4 kcal/mole smaller than that of several related carboxylic acid dimers (regardless of whether or not the counterpoise correction is applied). The smaller binding energy may be the result of geometrical constraints that preclude the two dissimilar hydrogen bonds from simultaneously acquiring their optimum geometry.

The most striking difference between HCOOH–HNO<sub>3</sub> and the carboxylic acid dimers is the value of R(O3-O9) at the minimum energy structure, which is seen to be substantially longer than all the other oxygen–oxygen distances listed. Interestingly, the value of this distance does not stand out among the complexes listed at the transition state structure. This indicates that, while the change in R(O5-O6) between the minimum energy structure and the transition state for HCOOH–HNO<sub>3</sub> is similar to that in the carboxylic acid dimers, R(O3-O9) must change by a much larger amount to reach the transition state. Note that we state this as an observation about the potential energy surface, though it is by no means clear that the optimum tunneling path passes through the saddle point geometry.

Finally, the <sup>14</sup>N nuclear quadrupole coupling constant can be used to roughly assess the degree of proton transfer in this system. As we have argued previously<sup>30,64</sup> to the extent that the electronic structure of the HNO<sub>3</sub> is unperturbed upon formation of a planar complex, the c-component of the <sup>14</sup>N nuclear quadrupole coupling tensor,  $\chi_{cc}$ , should be equal to that for free HNO<sub>3</sub> (since the complex is planar). The extent to which it does not may be used as a measure of the degree to which the acid has released its proton. Thus, comparison of  $\chi_{cc}$  of the complex with known values for free HNO<sub>3</sub> and aqueous NO<sub>3</sub><sup>−</sup> motivates the definition of a parameter,<sup>64</sup>  $Q_{PT}^A$ , which specifies where the system lies between the limits of no proton release and full proton release:

$$Q_{PT}^A = \frac{\chi_{cc}^{complex} - \chi_{cc}^{HNO_3}}{\chi_{cc}^{NO_3^-} - \chi_{cc}^{HNO_3}} \times 100\% \quad (15)$$

Using the value of  $\chi_{cc} = (-1/2)[\chi_{aa} + (\chi_{bb} - \chi_{cc})] = 0.138$  MHz for the 0<sup>+</sup> state of HCOOH–H<sup>14</sup>NO<sub>3</sub>, and the values of  $\chi_{cc} = -0.0773(51)$  MHz<sup>148</sup> for free HNO<sub>3</sub> and 0.656(5) MHz<sup>155</sup> for aqueous NO<sub>3</sub><sup>−</sup> yields the value  $Q_{PT}^A = 29\%$ . This result is similar to the 31% value determined for HNO<sub>3</sub>–(H<sub>2</sub>O)<sub>2</sub>.<sup>64,156</sup> Note that this parameter addresses a distinctly different aspect of the proton transfer problem than does the observation of

spectral splitting due to proton exchange:  $Q_{PT}^A$  is a static quantity that arises from the change in electronic structure of the  $\text{HNO}_3$  within the complex. The dynamical aspect of the problem, as revealed through manifestations of proton tunneling is related to the frequency with which the system converts between two equivalent, static structures, each of which has a value of  $\chi_{cc}$  reflective of the degree of proton release.

## Conclusion

The complex  $\text{HNO}_3\text{-HCOOH}$  has been studied by microwave spectroscopy and *ab initio* calculations. The system has a structure similar to that well known for carboxylic acid dimers, namely a cyclic, double hydrogen bonded geometry. The hydrogen bond lengths are 1.686(17) Å and 1.813(10) Å for the hydrogen bonds involving the  $\text{HNO}_3$  and  $\text{HCOOH}$  protons, respectively, and the corresponding  $\text{O}\cdots\text{O}$  separations<sup>153</sup> are 2.631 Å and 2.794 Å. These results indicate that substantial structural reorganization is necessary to accomplish the interconversion between equivalent structures. Nevertheless, a doubling is observed in the *a*-type spectrum of the complex and is attributed to a double proton transfer process on the basis of (i) its disappearance upon deuteration in one of the hydrogen bonds and (ii) relative intensities which are in accord with expectations based on nuclear spin statistics for a pair of tunneling states. The observed splitting (which is *not* the tunneling splitting) is unusually small compared with that reported in a number of high resolution studies of carboxylic acid dimers but is, itself, difficult to interpret. The calculated binding energy of the complex, (14.3 and 11.8 kcal/mol with and without counterpoise correction, respectively) is 3 – 4 kcal/mol smaller than that of several recently studied carboxylic acid dimers, and the barrier to proton transfer (potential energy minimum to transition state) is 1–2 kcal/mol larger. Structures at the potential energy minimum and at the transition state suggest that significant heavy atom motion is necessary to accomplish double proton transfer. An observation of the *b*-type rotational spectrum of the complex would be of great interest, but has not yet been possible for this system due to a rather small value of  $\mu_b$ .

**Acknowledgements**

This work was supported by the National Science Foundation (Grant Nos. CHE-0845290 and CHE-1266320), the Minnesota Supercomputer Institute, and the University of Minnesota through a Lester C. and M. Krogh graduate fellowship to R.B.M. We thank Professor Donald Truhlar for valuable communications about this work.

**Chapter 4 : Intramolecular Competition Between n-Pair and  $\pi$ -Pair  
Hydrogen Bonding: Microwave Spectrum and Internal Dynamics of the  
Pyridine – Acetylene Hydrogen-Bonded Complex**

Reproduced from R. B. Mackenzie, C. T. Dewberry, E. Clouston, G. C. Cole, A. C. Legon, D. P. Tew, and K. R. Leopold, *J. Chem. Phys.*, **143**, 104309 (2015)  
with the permission of AIP Publishing.

## Abstract

*a*-type rotational spectra of the hydrogen-bonded complex formed from pyridine and acetylene are reported. Rotational and  $^{14}\text{N}$  hyperfine constants indicate that the complex is planar with an acetylenic hydrogen directed toward the nitrogen. However, unlike the complexes of pyridine with HCl and HBr, the acetylene moiety in  $\text{HCCH-NC}_5\text{H}_5$  does not lie along the symmetry axis of the nitrogen lone pair, but rather, forms an average angle of  $46^\circ$  with the  $\text{C}_2$  axis of the pyridine. The *a*-type spectra of  $\text{HCCH-NC}_5\text{H}_5$ , and  $\text{DCCD-NC}_5\text{H}_5$  are doubled, suggesting the existence of a low lying pair of tunneling states. This doubling persists in the spectra of  $\text{HCCD-NC}_5\text{H}_5$ ,  $\text{DCCH-NC}_5\text{H}_5$ , indicating that the underlying motion does not involve interchange of the two hydrogens of the acetylene. Single  $^{13}\text{C}$  substitution in either the ortho or meta positions of the pyridine eliminates the doubling and gives rise to separate sets of spectra that are well predicted by a bent geometry with the  $^{13}\text{C}$  on either the same side (“inner”) or the opposite side (“outer”) as the acetylene. High level *ab initio* calculations are presented which indicate a binding energy of 1.2 kcal/mol and a potential energy barrier of  $44\text{ cm}^{-1}$  in the  $\text{C}_{2v}$  configuration. Taken together, these results reveal a complex with a bent hydrogen bond and large amplitude rocking of the acetylene moiety. It is likely that the bent equilibrium structure arises from a competition between a weak hydrogen bond to the nitrogen (an n-pair hydrogen bond) and a secondary interaction between the ortho hydrogens of the pyridine and the  $\pi$  electron density of the acetylene.

## Introduction

In this article, we report an investigation of eight isotopologues of the hydrogen-bonded complex formed by pyridine (py) and acetylene. Pyridine forms strong hydrogen bonds with HCl and HBr,<sup>157-159</sup> with the HX molecule lying along its C<sub>2</sub> axis in the lowest energy equilibrium conformation. The motivation for the present work was to discover what happens to the geometry of the complex when HCl and HBr are replaced by a much weaker H-bond donor molecule such as acetylene.

This study follows an extensive, systematic series of microwave spectroscopic investigations of hydrogen-bonded complexes of the type B···HX, where B is one of a number of simple Lewis bases and X = F, Cl, Br or I. An important result from that work is a set of rules<sup>160,161</sup> for predicting the angular geometries of such systems. In summary, it was shown that in the equilibrium geometry, the HX subunit lies along the symmetry axis of either a non-bonding electron (n) pair carried by B or, in the absence of n-pairs, a  $\pi$  electron pair. When both n and  $\pi$  pairs are present on B, the n-pair takes precedence. These rules were later<sup>162</sup> found to apply to halogen-bonded complexes of the type B···XY, where XY is a di-halogen molecule, either polar or nonpolar.

In the early work<sup>163-165</sup> on hydrogen-bonded complexes, it was necessary to assume a collinear arrangement of the HX moiety and the H-bond accepting center on the base because of the well-known difficulty associated with locating the H atom by deuterium substitution. This difficulty arises mainly because (i) the substituted atom necessarily lies close to the molecular center of mass, and (ii) because D for H substitution significantly attenuates the zero-point excursions of that atom, thus complicating the interpretation of the zero-point moments of inertia. Fortunately, a method<sup>166-168</sup> based on the complete halogen nuclear quadrupole coupling tensor can locate the HX internuclear axis precisely within the principal inertia axis system of a complex B···HX. If the molecule has C<sub>s</sub> symmetry, with the principal inertial plane *ab*, for example, as the symmetry plane, the



only nonzero off-diagonal element of the coupling tensor is  $\chi_{ab}(X)$ , and the angle  $\alpha_{az}$  between the principal inertia axis  $a$  and the HX axis,  $z$ , is given by

$$\alpha_{az} = \frac{1}{2} \tan^{-1} \left\{ \frac{-2\chi_{ab}(X)}{\chi_{aa}(X) - \chi_{bb}(X)} \right\} \quad (1)$$

It can be shown that the angle,  $\alpha_{az}$ , so determined is a good approximation to the *equilibrium* value even when zero-point averaged coupling constants are employed.<sup>166,167</sup>

As a result, a good approximation to the *equilibrium* value of the nonlinearity of the hydrogen bond,  $\theta$ , can be obtained. By this means, it was found that complexes  $B \cdots \text{HCl}$ <sup>167-173</sup> and  $B \cdots \text{HBr}$ <sup>166,174-178</sup> can exhibit large angular deviations from linearity, when the symmetry of B allows it. For example, when  $X = \text{Cl}$ ,  $\theta = 20.3(8)^\circ$ ,  $9.5(1)^\circ$ ,  $16.5(1)^\circ$ ,  $21.0(5)^\circ$ ,  $17.5^\circ$  and  $18.3(1)^\circ$ , for  $B =$  formaldehyde, 2,5-dihydrofuran, oxirane, thiirane, methylenecyclopropane, and vinyl fluoride, respectively. Similarly, when  $X = \text{Br}$ ,  $\theta$  is [not measured],  $10.2(1)^\circ$ ,  $17.0(1)^\circ$ ,  $19.7(1)^\circ$ ,  $18.0(2)^\circ$  and  $20.1(1)^\circ$ , for this same set of bases, respectively. Figure 4.1 illustrates the definition of  $\theta$  in the case of  $\text{H}_2\text{CO} \cdots \text{HCl}$ .

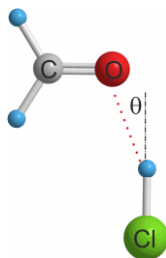


**Figure 4.1 HCl–H<sub>2</sub>CO Complex**

The HCl–H<sub>2</sub>CO complex showing the angle,  $\theta$ , which defines the nonlinearity of the hydrogen bond.

An obvious explanation for the significant magnitude of the values of  $\theta$  in these cases is a secondary interaction between the nucleophilic halogen atom of HX and an electrophilic region on B. To account for this, the rules for angular geometry for  $B \cdots \text{HX}$  need a minor modification, namely the inclusion of a (hypothetical) mechanism in which a secondary interaction involving X causes the hydrogen bond (initially along the axis of an n-pair or  $\pi$ -pair) to become nonlinear until the energetic benefit of the secondary interaction balances the energetic cost of the H-bond bend. If this hypothesis is correct, larger

nonlinearities should be observable for the corresponding complexes  $B\cdots HCCH$ , given that acetylene is known<sup>179</sup> to form weaker hydrogen bonds than HCl or HBr while still retaining the ability to form secondary hydrogen bonds via its  $\pi$  electron density.

In order to test this hypothesis, the rotational spectra of several complexes  $B\cdots HCCH$  ( $B$  = formaldehyde,<sup>180</sup> 2,5-dihydrofuran,<sup>181</sup> oxirane,<sup>182</sup> thiirane<sup>183</sup> and vinyl fluoride<sup>184</sup>) were investigated. The orientation of the HCCH moiety could not be determined using equation 1 owing to the absence of a suitable nuclear quadrupole coupling tensor. However, the larger moment of inertia of HCCH relative to that of HCl and HBr, and the correspondingly attenuated zero-point motion of HCCH allowed it to be satisfactorily located within the principal inertia axis system of the complex by conventional use of zero-point moments of inertia. The experimental result is that the order of  $\theta$  is  $B\cdots HCCH > B\cdots HCl \sim B\cdots HBr$  when  $B$  = formaldehyde, 2,5-dihydrofuran, oxirane, thiirane, methylenecyclopropane, or vinyl fluoride. For a given  $B$ , the value of  $\theta$  for  $B\cdots HCCH$  is about double those found for  $B\cdots HCl$  and  $B\cdots HBr$ .

The pyridine-acetylene complex offers a severe test of the propensity of acetylene to form nonlinear hydrogen bonds when acting as the H-bond donor. The n-pair of the nitrogen atom lies along the  $C_2$  axis of pyridine and, as noted above, forms strong hydrogen bonds with HCl and HBr. Indeed, the interaction with HBr is so strong that the complex has been shown to have significant  $pyH^+\cdots Br^-$  character.<sup>2</sup> In this light, it might be expected that a hydrogen bond between HCCH and pyridine would be more difficult to bend than the corresponding hydrogen bonds in other  $B\cdots HCCH$  complexes. On the other hand, secondary interactions involving the ortho hydrogens of pyridine have been noted in the complex pyridine- $CO_2$ .<sup>185</sup> Hence, the question addressed in this work is whether pyridine- $\cdots HCCH$  has  $C_{2v}$  symmetry at equilibrium, with the HCCH atoms lying along the pyridine  $C_2$  axis, or whether the secondary interaction of the  $\pi$  bond of HCCH with the ortho-H atoms of pyridine is sufficiently strong to lead to a bent  $N\cdots H-C\equiv$  hydrogen bond. An answer to this question, as sought through an investigation of the rotational spectrum of py- $HCCH$ , is reported here.

## Experimental

Rotational spectra of py-HCCH were recorded between 4.3 and 10.7 GHz using the pulsed-nozzle Fourier transform microwave (FTMW) spectrometers at the University of Exeter<sup>183,186</sup> and the University of Minnesota.<sup>31,49</sup> Acetylene was introduced in a ~1% argon gas mixture, which was expanded through a 0.8 mm diameter nozzle into the microwave cavity with a stagnation pressure of 1.1 atm. Initially, pyridine was added through a continuous flow line backed by argon at a pressure of 0.7 atm, described elsewhere.<sup>50,138</sup> The flow line bubbled through a small reservoir of pyridine and terminated in a needle of inner diameter 0.010", which was placed a few millimeters downstream of the nozzle orifice and bent so as to introduce the gas along the axis of the expansion. Eventually pyridine bubblers were placed on both the pulse and continuous flow lines in order to increase the amount of pyridine entering the supersonic expansion. This novel use of a continuous flow line was found to increase signal intensity by a factor of ~5. The nozzle was pulsed at a rate of 4 Hz and four free induction decay signals were collected per pulse with a data collection time of 140.8  $\mu$ s. Transition frequencies were typically accurate to ~4 kHz. Sample spectra are shown in Figure 4.2.

Rotational transitions of the parent, ortho- and meta-  $N^{13}CC_4H_5$ -HCCH species were observed in natural abundance. The deuterated species  $NC_5H_5$ -DCCD,  $NC_5H_5$ -HCCD and  $NC_5H_5$ -DCCH were observed using a ~1% mixture of deuterated acetylene in argon. Deuterated acetylene isotopologues were synthesized by reacting 3.1 g  $CaC_2$  from Sigma Aldrich with either pure  $D_2O$  or a 50/50 mixture of  $H_2O/D_2O$ .

An additional broadband spectrum of the parent complex was taken using the newly constructed chirped pulse FTMW spectrometer which operates in tandem with the cavity-type spectrometer at the University of Minnesota. This instrument employs the methodology of Pate and coworkers<sup>4</sup> and is described elsewhere.<sup>5,12</sup> The broadband spectrum was useful in determining the relative intensities of the rotational transitions which, in combination with an analysis of nuclear spin statistics, enabled assignment of ground and excited states tunneling states, as described below.

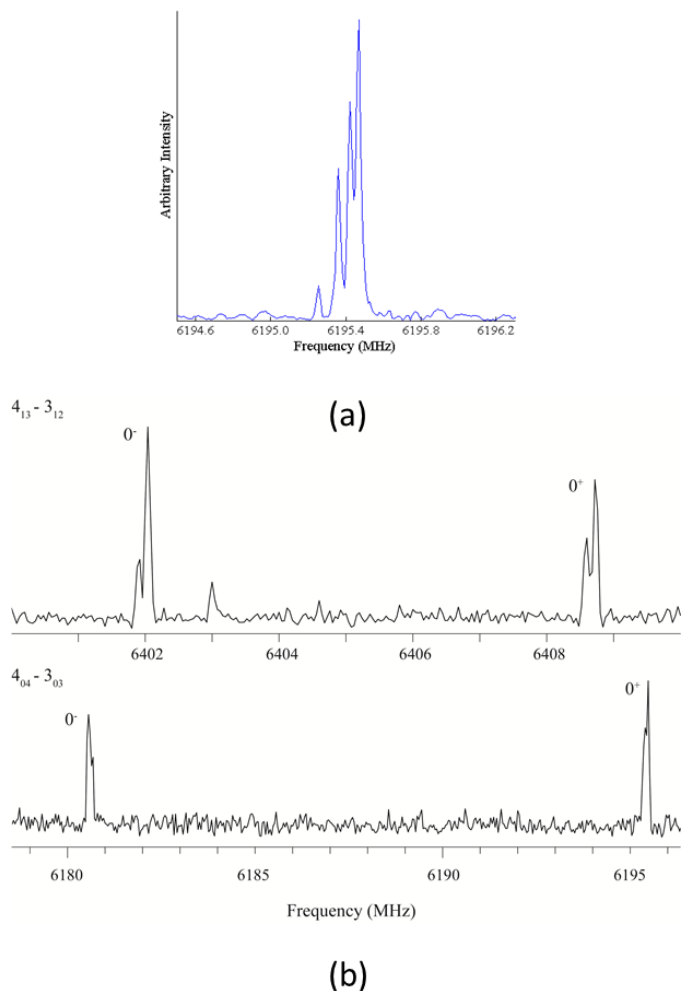


**Figure 4.2 Cavity and Chirped-Pulse Spectrum of py-HCCH**

(a) The  $4_{04} \leftarrow 3_{03}$  transition in the  $0^+$  state of py-HCCH taken with the cavity FTMW. (b) Two rotational transitions of py-HCCH taken on a chirped pulse spectrometer, showing the dependence of relative intensities on the parity of  $K_{-1}$ .

### Computational Details

High level *ab initio* predictions of the  $r_e$  geometries and energy differences were computed using the CCSD(T)(F12\*) method, that is, coupled-cluster theory with singles, doubles, and perturbative triples,<sup>187</sup> and explicit-correlation in order to approach the basis set limit.<sup>188,189</sup> The cc-pVDZ-F12 basis sets<sup>190</sup> were used without any counterpoise correction, and only valence electrons were correlated. The computed basis set limit CCSD(T) dissociation energy is 1.2 kcal/mol. For a more extensive investigation of the nature of the large amplitude motion and zero-point effects, CCSD(T)(F12\*)/cc-pVDZ-

F12 energies were computed along a 1-d curvilinear path tracing the in-plane HCCH wagging coordinate. Along the path, the HCCH and NC<sub>5</sub>H<sub>5</sub> moieties were kept fixed at the C<sub>2v</sub> optimized geometries and the HCCH unit rotated around a pivot defined by the intersection of the N-C and C-C vectors of the C<sub>s</sub> minima, with a constant N-H distance of 2.22 Å. This frozen path has a barrier to inversion of 48 cm<sup>-1</sup> compared to 44 cm<sup>-1</sup> for the fully relaxed path. These numbers are sufficiently similar so as to justify using the 1-d path to compute an approximate tunneling frequency. Zero-point and tunneling states were computed by numerically solving the 1-d Schrödinger equation in mass-weighted space, giving a tunneling frequency of 220 MHz. To provide information regarding the remaining degrees of freedom, harmonic frequencies were computed at the MP2-F12/cc-pVDZ-F12 level of theory<sup>191</sup> at the MP2-F12/cc-pVDZ-F12 C<sub>s</sub> and C<sub>2v</sub> stationary points. All electronic structure calculations were performed using the Turbomole program package.<sup>192</sup>

### **Microwave Spectrum**

*a*-type rotational transitions were initially recorded at the University of Exeter for both py-HCCH and py-DCCD. All spectra were found to be doubled, with splittings on the order of several MHz, suggesting the existence of a pair of states with sufficiently similar energies that both are populated in the supersonic jet. Moreover, the *A* rotational constants differed significantly from that of free pyridine and indeed, rotational constants and isotopic shifts from preliminary fits were in reasonable agreement with the *ab initio* structure, which is a planar C<sub>s</sub> geometry with a bent hydrogen bond. Thus, the observed spectral doubling could be indicative of a pair of tunneling states that arise due to the finite barrier at the C<sub>2v</sub> configuration. However, based on spectra of the HCCH and DCCD complexes alone, it was not possible to rule out an internal rotation that interchanges the positions of the acetylenic hydrogens, similar to that which occurs during the geared tunneling motion in (HCCH)<sub>2</sub>.<sup>193</sup> Thus, additional experiments on py-HCCD and py-DCCH were performed at the University of Minnesota. The spectra were again found to be doubled, indicating that the motion does not involve interchange of the acetylenic hydrogens and therefore most likely arises from motion along a coordinate that

connects the two equivalent potential energy minima associated with a bent hydrogen bond. *Ab initio* calculations investigating the barrier to internal rotation of the HCCH unit revealed that the HCCH moiety is not bound to pyridine when in the  $C_{2v}$  T-shaped configuration. The computed basis set limit CCSD(T) dissociation energy of 1.2 kcal/mol is sufficiently large as to provide further evidence precluding internal rotation of the HCCH unit.

The magnitude of the observed splittings provides additional insight into the nature of the motion. The splittings increase with  $J$  and, for any given rotational transition, are uniformly larger for the HCCH species than for the DCCD species. Moreover, the magnitude of the splitting depends primarily on the hydrogen isotope in the outer position, i.e., the splittings of py-HCCH and py-DCCH were nearly identical to each other as were those of py-DCCD and py-HCCD. This further suggests that the motion is dominated by the outer hydrogen of the acetylene. Thus, the geometry suggested by the isotopic substitutions is indeed a degenerate bent structure, connected by a large amplitude rocking motion that passes through the  $C_{2v}$  geometry. An illustration of the proposed motion is given in Figure 4.3.

In order to provide additional evidence for the rocking motion in Figure 4.3, the ortho- and meta-substituted  $^{13}\text{C}$  species were examined.  $^{13}\text{C}$  substitution at either the ortho- or meta- positions quenches the tunneling by breaking the symmetry of the pyridine, producing instead a pair of distinct isotopologues – one with the  $^{13}\text{C}$  on the inside of the acute angle formed between the acetylene and the pseudo- $C_2$  axis of pyridine, and one with the  $^{13}\text{C}$  on the outside. Indeed, for both the ortho- and meta-substituted species a pair of spectra was observed, the members of which were assignable to separate isotopologues whose moments of inertia were consistent with semi-rigid structures having the  $^{13}\text{C}$  in either the inner or outer positions. This observation provides further evidence for the proposed motion.

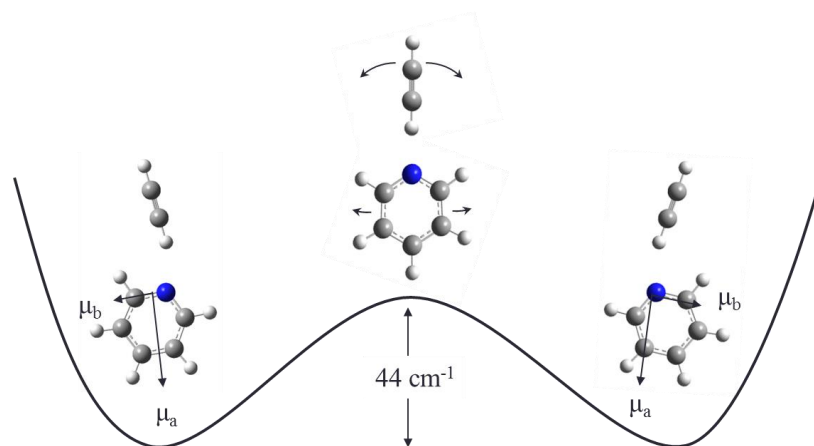


**Figure 4.3 1-Dimensional Potential Proposed for py-HCCH**

A 1-dimensional potential and the proposed tunneling motion for py-HCCH. The  $44\text{ cm}^{-1}$  barrier is the result of calculations done at the CCSD(T)(F12\*)/cc-pVDZ-F12 level/basis set along a fully relaxed path.

The *ab initio* calculations also strongly support the existence of a tunneling-assisted HCCH rocking motion and the above interpretation of the spectra. As noted above, the  $C_{2v}$  barrier between the two bent  $C_s$  structures is  $44\text{ cm}^{-1}$  and the  $0^+$  and  $0^-$  states are split by 220 MHz on the 1-d potential surface. Even acknowledging substantial errors that could arise from the use of a 1-d potential, this value is sufficiently small that both tunneling states may be expected to be populated in the jet. Moreover, repeating the 1-d vibrational calculation for the  $^{13}\text{C}$  isotopologues breaks the symmetry of the potential through the arc length in the mass weighted space, and localizes the ground and first vibrational states at one of the two minima.

The motion indicated in Figure 4.3 inverts the component of the electric dipole moment along the  $b$ -inertial axis of the complex ( $\mu_b$ ) but leaves the  $a$ -component ( $\mu_a$ ) unchanged. As a result,  $a$ -type rotational transitions occur between states of the same vibrational symmetry (i.e.,  $0^+ \leftarrow 0^+$  and  $0^- \leftarrow 0^-$ ) while  $b$ -type transitions will occur between states of opposite symmetry (i.e.,  $0^- \leftarrow 0^+$  and  $0^+ \leftarrow 0^-$ ). Thus, the observed  $a$ -type spectra are pure rotational transitions, and the observed doubling arises from small differences in rotational parameters between the  $0^+$  and  $0^-$  states. Only  $b$ -type transitions cross the tunneling doublet and provide a direct measure of the tunneling splitting (i.e., the

separation between the  $0^+$  and  $0^-$  states). Several attempts were made to locate  $b$ -type (inversion) transitions, but none were readily identified and additional experiments were not pursued. Note that  $b$ -type spectra of the  $^{13}\text{C}$  isotopologues should be uncomplicated by tunneling and therefore well predicted from the rotational constants obtained from the  $a$ -type spectrum. However, searches for them were not successful, primarily because their predicted intensities are  $\sim 10$  times smaller than those of the  $a$ -type spectra, which were themselves rather weak due to reliance on the naturally occurring  $^{13}\text{C}$ .

Assignment of the tunneling states was made on the basis of nuclear spin statistics. Since the  $0^+$  and  $0^-$  states correlate with the ground and first excited vibrational states of a  $C_{2v}$  (zero barrier) complex, the nuclear spin statistics can be analyzed for a  $C_{2v}$  system, as the symmetries will not change upon introduction of the barrier. Rotation through  $\pi$  about the  $a$ -axis of the complex interchanges *two* equivalent pairs of hydrogens and thus, the total wavefunction must be *symmetric* with respect to this operation. The electronic wavefunction,  $\psi_{el}$ , is symmetric and can be ignored, while the vibrational wavefunction,  $\psi_{vib}$ , is symmetric for the  $0^+$  state and antisymmetric for the  $0^-$  state. The rotational wavefunction,  $\psi_{rot}$ , has the parity of  $(-1)^{K_{-1}}$ , and  $\psi_{spin}$  may be written as  $\psi_{ortho}\psi_{meta}$ , the product of singlet or triplet spin functions for the pairs of ortho and meta hydrogens. Thus, writing  $\psi_{tot} = \psi_{el}\psi_{vib}\psi_{rot}\psi_{spin}$  leads to the conclusion that in the  $0^+$  state, the even  $K_{-1}$  and odd  $K_{-1}$  have statistical weights of 10 and 6, respectively, while in the  $0^-$  state the intensity ratio is reversed. This predicted alternation of intensities with the parity of  $K_{-1}$  was indeed observed (see Figure 4.2b) and allowed for the definitive assignments of the spectra.

Spectra for the  $0^+$  and  $0^-$  states were fit separately using a Watson A-reduced Hamiltonian and the SPFIT program of Pickett,<sup>144</sup> see also Appendix D for observed transitions and associated residuals.  $^{14}\text{N}$  nuclear hyperfine structure was observed and treated by standard methods,<sup>34</sup> but for the deuterated species studied, deuterium hyperfine structure was not well resolved and was, therefore, not analyzed. The observed spectra were readily assignable for transitions involving  $J$  and  $K_{-1}$  as high as 7 and 3,



respectively. However, single-state fits for the parent and deuterated-acetylene isotopologues including all observed transitions produced residuals as large as several hundred kHz, with little improvement obtained by inclusion of sextic distortion constants. After numerous attempts, satisfactory fits, with rms residuals on the order of 5–10 kHz, were obtained only when the data sets were restricted to transitions involving  $K_{-1} = 0,1$ . In light of the large amplitude motion described above, it is reasonable to suppose that the difficulties with higher  $K_{-1}$  transitions are a result of a strong Coriolis perturbation (e.g. arising from coupling of intermolecular stretching and bending modes) that is not treated in a simple one-state model. Thus, in order to minimize the effect of any untreated interactions, rotational constants for observed isotopologues containing parent pyridine are reported in Table 4.1 for the restricted fits involving only  $K_{-1} = 0,1$ . Note that, while the results obtained are generally reasonable, a few of the centrifugal distortion constants are negative.

The results of similar fits for the  $^{13}\text{C}$  substituted isotopologues are given in Table 4.2. These fits are also generally reasonable, with rms residuals of 5 kHz or less. Note that the appearance of a few negative centrifugal distortion constants persists in these  $^{13}\text{C}$  pyridine species, suggesting that large amplitude angular motion may be a pervasive feature of the system, even in the absence of tunneling between degenerate configurations. We note, however, that transitions with  $K_{-1} > 1$  were not recorded for the  $^{13}\text{C}$  isotopologues owing to their reduced intensity, thus precluding additional insight as to the behavior at higher values of  $K_{-1}$ .

As noted above, no  $b$ -type transitions were identified in this work and thus, a direct measure of the tunneling splitting is not possible. In some cases, however, an estimate of the tunneling splitting can be made from analysis of Coriolis perturbations in a combined fit of data from both the  $0^+$  and  $0^-$  states.<sup>194</sup> Thus, several attempts were made to fit the doubled  $a$ -type transitions of the parent species using a coupled, A-reduced Watson Hamiltonian from Pickett's SPFIT program:

$$H = \sum_i H_i^R + \sum_i H_i^{\text{CD}} + H^{\text{int}} \quad (2)$$

where

$$H^{int} = \Delta E_{01} + F_{ab}(P_a P_b + P_b P_a) \quad (3)$$

Here,  $i = 0, 1$  (corresponding to the two tunneling states),  $H^R$  is the rotational Hamiltonian,  $H^{CD}$  incorporates centrifugal distortion, and  $H^{int}$  represents the interaction between the ground and first excited states with a tunneling energy  $\Delta E_{01}$  and the Coriolis coupling constant,  $F_{ab}$ .<sup>195</sup> These fits, however, were met with limited success. While  $K_{-1} = 0, 1, 2,$  and  $3$  transitions for both  $0^+$  and  $0^-$  states were fit with an average residual of 5 kHz, several features of the results were of concern. First, the standard errors of the rotational constants were 340 kHz, 110 kHz, and 2 kHz for  $A, B,$  and  $C$  respectively, with the value for  $B$  being most startling. Second, the resulting inertial defect for the combined fits, defined as<sup>34</sup>

$$\Delta_{ID} = \frac{h}{8\pi^2} \left( \frac{1}{C} - \frac{1}{A} - \frac{1}{B} \right) = -2 \sum_i m_i c_i^2 \quad (4)$$

was typically  $\sim 25 \text{ amu } \text{\AA}^2$ , in sharp contrast with both the experimental results (Tables 4.1 and 4.2) and *ab initio* calculations, which indicate a planar system, for which a negative, near-zero value is anticipated. Finally, consistent with the large standard errors associated with the rotational constants, the fits did not appear unique and indeed,  $\Delta E_{01}$  was occasionally negative (depending on starting parameters). Thus, we conclude that while the perturbations in this system are large enough to observe, they are not large enough to extract meaningful, uncorrelated constants from analysis of Coriolis perturbations alone. Consequently, we settled on the single-state fits described above.

**Table 4.1 Spectroscopic Constants for H<sub>5</sub>C<sub>5</sub>N-HCCH and -DCCD**

Constant	H <sub>5</sub> C <sub>5</sub> N-HCCH 0 <sup>+</sup> State	H <sub>5</sub> C <sub>5</sub> N-HCCH 0 <sup>-</sup> State	H <sub>5</sub> C <sub>5</sub> N-DCCD 0 <sup>+</sup> State	H <sub>5</sub> C <sub>5</sub> N-DCCD 0 <sup>-</sup> State
<i>A</i> (MHz)	5866.41(65)	5866.4(14)	5832.2(17)	5840.2(21)
<i>B</i> (MHz)	826.54924(62)	826.6813(14)	783.3767(18)	783.4782(18)
<i>C</i> (MHz)	726.14279(55)	722.4005(13)	691.7321(17)	688.9347(18)
$\Delta_{\text{ID}}$ (amu $\text{\AA}^2$ )	-1.60	2.10	-1.18	1.99
<sup>14</sup> N $\chi_{aa}$ (MHz)	-3.9168(33)	-3.8807(73)	-3.95(21)	-3.94(20)
<sup>14</sup> N( $\chi_{bb}-\chi_{cc}$ ) (MHz)	-2.6796(84)	-2.670(19)	-1.52(40)	-1.72(44)
$\Delta_J$ (kHz)	1.8659(60)	-0.925(14)	1.375(14)	-0.452(13)
$\Delta_{JK}$ (kHz)	-46.39(38)	-49.10(91)	-22.2(11)	-29.5(12)
$\delta_J$ (kHz)	-0.9050(43)	1.099(10)	-0.6088(99)	0.7539(96)
RMS (kHz)	4	10	5	5
<i>N</i>	54	48	20	18

**Table 4.2 Spectroscopic Constants for H<sub>5</sub>C<sub>5</sub>N-DCCH, and -HCCD**

Constant	H <sub>5</sub> C <sub>5</sub> N-DCCH 0 <sup>+</sup> State	H <sub>5</sub> C <sub>5</sub> N-DCCH 0 <sup>-</sup> State	H <sub>5</sub> C <sub>5</sub> N-HCCD 0 <sup>+</sup> State	H <sub>5</sub> C <sub>5</sub> N-HCCD 0 <sup>-</sup> State
A (MHz)	5841.5(11)	5843.0(17)	5854.2(12)	5852.7(24)
B (MHz)	820.01502(82)	820.1534(12)	789.03291(76)	789.1358(16)
C (MHz)	720.88215(77)	717.0641(11)	696.37277(68)	693.6136(14)
$\Delta_{ID}$ (amuÅ <sup>2</sup> )	-1.76	2.10	-1.10	1.85
<sup>14</sup> N $\chi_{aa}$ (MHz)	-3.907(39)	-3.905(61)	-3.903(27)	-3.877(65)
<sup>14</sup> N( $\chi_{bb}-\chi_{cc}$ ) (MHz)	-2.71(12)	-2.70(18)	-2.744(84)	-2.70(19)
$\Delta_J$ (kHz)	1.7936(82)	-0.973(12)	1.413(10)	-0.552(20)
$\Delta_{JK}$ (kHz)	-51.11(57)	-54.60(89)	-18.92(45)	-20.35(97)
$\delta_J$ (kHz)	-0.8847(58)	1.1187(92)	-0.6157(81)	0.789(15)
RMS (kHz)	4	6	3	6
<i>N</i>	29	31	26	29

**Table 4.3 Spectroscopic Constants for H<sub>5</sub>C<sub>5</sub>N–HCCH with <sup>13</sup>C-pyridine substitutions**

Constant	inner - ortho <sup>13</sup> C	outer – ortho <sup>13</sup> C	inner – meta <sup>13</sup> C	outer – meta <sup>13</sup> C
	H <sub>5</sub> C <sub>5</sub> N - HCCH	H <sub>5</sub> C <sub>5</sub> N – HCCH	H <sub>5</sub> C <sub>5</sub> N – HCCH	H <sub>5</sub> C <sub>5</sub> N – HCCH
<i>A</i> (MHz)	5831.0(14)	5731.1(20)	5692.2(24)	5805.1(22)
<i>B</i> (MHz)	826.60497(81)	825.2940(11)	823.6956(14)	819.2898(11)
<i>C</i> (MHz)	724.00857(76)	721.0322(11)	719.7943(13)	718.2006(11)
$\Delta_{ID}$ (amu $\text{\AA}^2$ )	-0.033	0.366	-0.219	-0.234
<sup>14</sup> N $\chi_{aa}$ (MHz)	-3.906(27)	-3.916(39)	-3.921(47)	-3.886(39)
<sup>14</sup> N( $\chi_{bb}$ - $\chi_{cc}$ ) (MHz)	-2.640(84)	-2.64(12)	-2.63(15)	-2.58(12)
$\Delta_J$ (kHz)	1.330(11)	-0.514(15)	-0.539(19)	1.047(16)
$\Delta_{JK}$ (kHz)	-49.33(55)	-39.57(80)	-54.08(99)	-51.01(81)
$\delta_J$ (kHz)	-0.5979(79)	0.871(11)	0.669(14)	-0.235(11)
RMS (kHz)	3	4	5	4
<i>N</i>	25	26	25	25

## Structure Analysis

The structure of the complex was determined using two separate methods, one involving analytical expressions for the components of the inertial tensor described previously,<sup>146</sup> and the other involving Kisiel's fitting program STRFIT.<sup>151</sup> In both cases, the structures of free pyridine and acetylene were assumed to be unchanged upon complexation and rotational constants from the single state fits were used rather than those of the combined fit discussed above.

First, analytical expressions for the inertial tensor components of the complex were applied. A similar analysis has been recently described for HNO<sub>3</sub>-HCOOH.<sup>14</sup> Briefly, the inertial tensor components of the complex are written in an  $X, Y, Z$  axis system, in which the origin corresponds to the center of mass of the complex. The  $a, b,$  and  $c$  inertial axes of each monomer are initially oriented along the  $Z, X, Y$  axes, respectively, and rotation matrices are applied to bring each monomer to its correct orientation within the complex. Assuming a planar structure for py-HCCH, (which is supported by both the small inertial defect and the *ab initio* results) only the angle between the  $Z$ -axis and the  $a$ -axis of each monomer,  $\theta_n$ , is needed to specify their relative orientation. Thus, the structure of the complex is fully defined by  $R_{cm}$ ,  $\theta_1$  (pyridine), and  $\theta_2$  (acetylene), as depicted in Figure 4.4a, which also defines the atom numbering used. The general equations for the inertial tensor components reduce to

$$I_{ZZ} = \sum_{i=1}^2 \left[ I_{aa}^{(i)} \cos^2 \theta_i + I_{bb}^{(i)} \sin^2 \theta_i \right] \quad (5)$$

$$I_{XX} = \mu R_{cm}^2 + \sum_{i=1}^2 \left[ I_{aa}^{(i)} \sin^2 \theta_i + I_{bb}^{(i)} \cos^2 \theta_i \right] \quad (6)$$

$$I_{YY} = \mu R_{cm}^2 + I_{cc}^{(1)} + I_{cc}^{(2)} \quad (7)$$

$$I_{XZ} = I_{ZX} = \sum_{i=1}^2 \left[ I_{aa}^{(i)} - I_{bb}^{(i)} \right] \cos \theta_i \sin \theta_i \quad (8)$$

Here,  $I_{gg}^{(i)}$  is the moment of inertia of the monomer  $i$  about its  $g$ -inertial axis and  $\mu$  is the pseudodiatom reduced mass of the complex. For acetylene,  $I_{aa} = 0$ . The remaining moments of inertia were obtained from literature rotational constants for pyridine<sup>196</sup> and acetylene.<sup>197</sup>

For each state and each isotopologue studied,  $R_{cm}$  was first determined from the  $C$  rotational constant of the complex, which is independent of the angular orientation of the monomers. The results are listed in the third column of Table 4.3. Next, using the observed  $\chi_{aa}({}^{14}\text{N})$ , the angle between the principal axis of the pyridine quadrupole coupling tensor and the  $a$ -axis of the complex,  $\tau$ , was estimated from the tensor projection formula

$$\chi_{aa} = \chi_{xx} \cos^2 \tau + \chi_{yy} (1 - \cos^2 \tau) \quad (9)$$

Here,  $\chi_{xx}$  and  $\chi_{yy}$  are eigenvalues of the coupling tensor of free pyridine with values of  $-4.908$  MHz and  $1.434$  MHz, respectively.<sup>198</sup> Since the parent form of pyridine has  $C_{2v}$  symmetry,  $x$  and  $y$  coincide with its  $a$ - and  $b$ -inertial axes, respectively. Thus, assuming that the average position of the  $a$ -axis of the complex coincides with  $Z$  (which is a very good approximation for this complex),  $\tau = \theta_1$ . Although equation (9) admits both positive and negative values of  $\tau$ , the positive value is taken without loss of generality.<sup>199</sup> For complexes with  ${}^{13}\text{C}$  substitution at the ortho or meta positions of pyridine, the  $a$ -axis is rotated off the N11-C5 axis, so that  $\tau$  and  $\theta_1$  are no longer equal. However, the orientation of the principal axis system of the quadrupole coupling tensor with respect to the molecular frame does not change upon isotopic substitution and thus,  $\tau$  was corrected for the angle between the  $a$ -axis of the pyridine and the N11-C5 axis,  $\alpha$ , calculated from the published structure. The relationship between  $\theta_1$ ,  $\alpha$ , and  $\tau$  is depicted in Figure 4b for the inner  ${}^{13}\text{C}$  ortho substituted complex. As noted in the figure, a small adjustment should be made to account for  $\beta$ , the angle between the  $a$ - and  $Z$ - axes of the complex. However, as noted above,  $\beta$  turns out to be  $\sim 0.5^\circ$  and is small enough to ignore.

With  $R_{\text{cm}}$  and  $\theta_1$  determined,  $\theta_2$  was left to be obtained from either the  $A$  or  $B$  rotational constants of the complex. Slightly different values were required to reproduce the observed  $A$  and  $B$ , but these values generally differed by only a few degrees and thus, the average value was taken. More significantly, with  $\tau$ , and hence  $\theta_1$  chosen to be positive, the observed values of  $A$  and  $B$  could each be reproduced by either a positive or a negative value of  $\theta_2$ . The pairs of positive and negative angles obtained from this analysis are summarized in Table 4.3 for each isotopologue studied and for each state of complexes in which spectral doubling was observed. Averages of the maximum and minimum values obtained are given separately for the  $0^+$  states, the  $0^-$  states, and the  $^{13}\text{C}$  substituted isotopologues, with error bars chosen to encompass all values obtained for each subgroup.

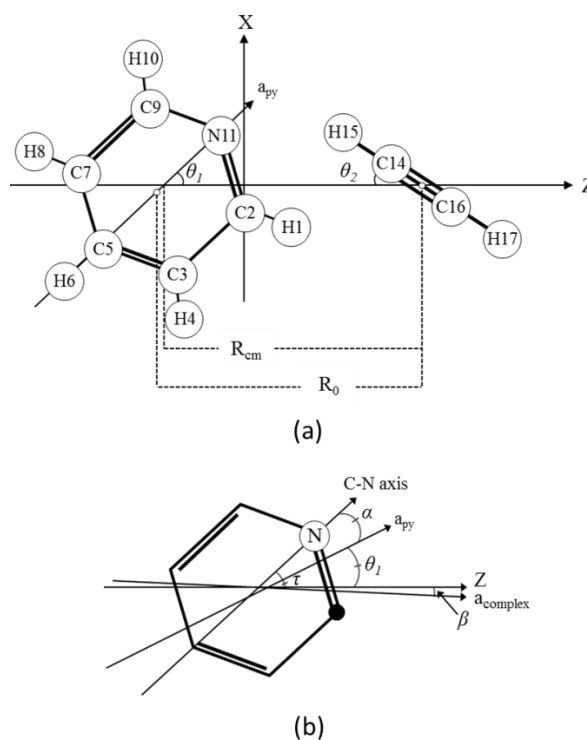


#### Figure 4.4 Structure Parameters of the py-HCCH Complex

(a) Diagram is for the parent species and specification of atom numbering. (b) Angle definitions for one of the meta-substituted  $^{13}\text{C}$  pyridine species, in which the  $a$ -axis of pyridine does not coincide with its pseudo- $C_2$  axis. Note that the center of mass of pyridine does not lie on the C5-N11 axis.



Together with the constraint of planarity noted above, the values obtained for  $R_{\text{cm}}$ ,  $\theta_1$ , and  $\theta_2$ , in principle, fully specify the geometry of the complex. However, some criterion is needed to choose the sign of  $\theta_2$ . Normally, such a choice can be made by comparing interatomic distances obtained from each structure and choosing the configuration that is most isotopically invariant. In this case, the logical choice is the intermolecular N11-H15 distance (i.e., the hydrogen bond length), and these values, calculated from  $R_{\text{cm}}$ ,  $\theta_1$ , and  $\theta_2$ , are also listed in Table 4.3. Comparison of the range of values of  $R(\text{N11-H15})$  obtained for positive and negative values of  $\theta_2$  show somewhat smaller variations among the sets of negative values, thus favoring the configuration drawn in Figure 4.4. That a hydrogen of the acetylene is directed toward the nitrogen of pyridine is the chemically intuitive structure. Note that this orientation of the HCCH moiety shown in the figure indeed corresponds to a negative value of  $\theta_2$ , since this angle is defined to be positive when the acetylene is rotated *counterclockwise* from the  $Z$  axis to its orientation in the complex.<sup>146</sup>

While the negative choice of  $\theta_2$  gives somewhat more isotopically consistent values of the hydrogen bond length, in absolute terms, the variation is unusually large. For example, the average values for the  $0^+$  and the  $^{13}\text{C}$  substituted species differ by 0.082 Å. This is perhaps not surprising, given the large amplitude motion inferred from the spectroscopic data above. In this light, an alternate geometrical parameter, less subject to the effects of large amplitude zero point oscillations may be desirable and for this purpose, the distance between the midpoint of the C5-N11 line segment (i.e., the “center” of the pyridine ring) and the midpoint of the  $\text{C}\equiv\text{C}$  bond in acetylene, was chosen. This distance is also shown in Figure 4.4a and is denoted by  $R_o$ . Values of  $R_o$  corresponding to positive and negative values of  $\theta_2$  are also listed in Table 4.3, where it is apparent that the variation among states and isotopologues is about an order of magnitude smaller than that observed for  $R(\text{N11-H15})$ . Moreover, values corresponding to the positive and negative values of  $\theta_2$  typically agree to within  $10^{-5} - 10^{-4}$  Å. Thus, the notion of a hydrogen bond length is only approximate in this system, and it is better to think of the complex in terms of a fixed average separation between the centers of the pyridine ring and the center of

the C≡C bond, with large amplitude angular oscillations that render the “hydrogen bond length” somewhat variable from state to state and isotopologue to isotopologue.

Finally, despite ambiguities associated with defining the complex in terms of atom-atom distances and bond angles, the above analysis was checked using Kisiel’s STRFIT program.<sup>151</sup> To implement the program, the geometry was defined by three parameters  $R_o$ ,  $\angle(\text{HCCH})$ , and  $\angle(\text{py})$ , the latter two defined as the angle that  $R_o$  forms with the HCCH axis and the  $C_2$  (or pseudo  $C_2$ ) axis of the pyridine (or  $^{13}\text{C}$  pyridine), respectively. Dummy atoms (“C<sub>pyr12</sub>” and “C<sub>cc13</sub>”) were used to define the endpoints of  $R_o$ . Several fits were run with a combination of the  $B$  and  $C$  rotational constants from the  $0^+$  and  $0^-$  states, and the  $^{13}\text{C}$ -pyridine isotopologues. Fits using only the rotational constants from either the  $0^+$  or the  $0^-$  states yielded values of  $R_o$  similar to those determined above, but the value of  $\angle(\text{py})$  was indeterminate.<sup>200</sup> A fit using only data for the  $^{13}\text{C}$ -substituted pyridine complexes, which are presumably more localized in a single potential well, was better behaved and also gave acceptable agreement with the results of the above analysis. The results of this fit are also included in Table 4.3. In order to enable direct comparison with the results of STRFIT (given below),  $R_{\text{cm}}$ ,  $\theta_1$ , and  $\theta_2$  were used to determine  $\angle(\text{HCCH})$ , and  $\angle(\text{py})$ , and this comparison is also provided in the table. Using the average values of  $\angle(\text{py})$  and  $\angle(\text{HCCH})$  obtained for the  $^{13}\text{C}$  species, we calculate that the average angle formed between the HCCH axis and the pseudo- $C_2$  axis of the pyridine is  $46^\circ$ .

The final, recommended structural parameters of the complex are given in the last line of Table 4.3. Since values obtained for  $0^+$  and  $0^-$  states of complexes containing the parent form of pyridine are subject to ambiguities related to tunneling between potential wells, we have chosen to use the values obtained from the  $^{13}\text{C}$  isotopologues for this purpose. They are generally in good agreement with the results of the STRFIT analysis and, moreover, in most cases, lie between those separately obtained for the  $0^+$  and  $0^-$  states. Only for  $\angle(\text{py})$  do the  $^{13}\text{C}$  results lie outside the range defined by the  $0^+$  and  $0^-$  state fits, but the difference is only a few degrees. We note, of course, that given the dynamical

complexity of this system, a variety of criteria could be used to assess the “best” structural parameters and thus, the full set of results presented in Table 4.3 can be used to provide a variety of perspectives as needed. The recommended structure is shown in Figure 4.5 and the *ab initio* results are included in the table for comparison. While the experimental and theoretical numbers represent zero-point and equilibrium values, respectively, the agreement is seen to be quite good.

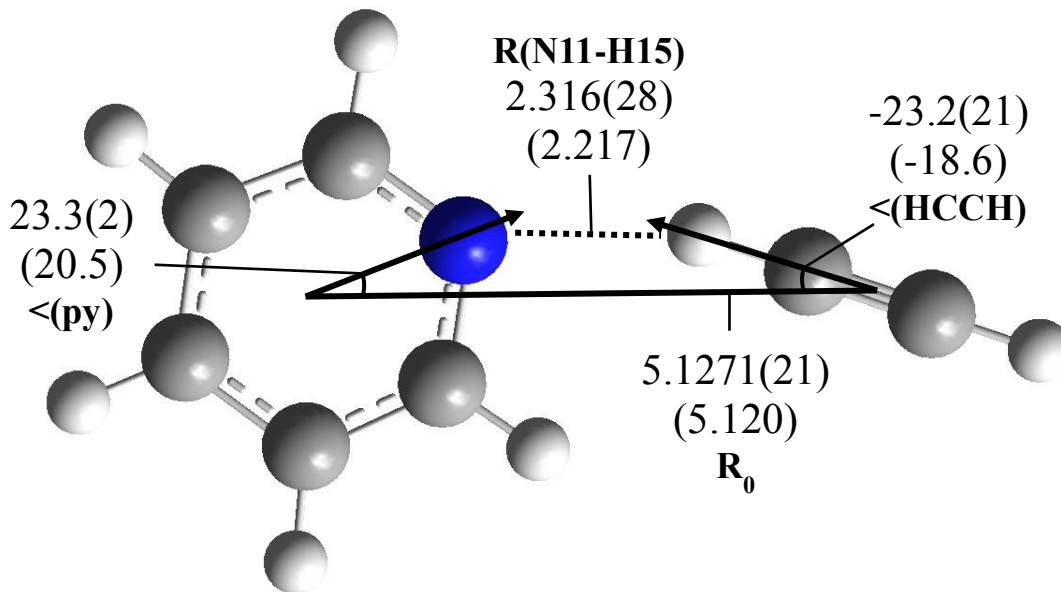


**Figure 4.5 Recommended Experimental Structure for py-HCCH**

The numbers in parentheses are CCSD(T)(F12\*)/cc-pVDZ-F12 values and correspond to the calculated equilibrium geometry.

**Table 4.4 Experimental Structural Parameters for Py-HCCH**

State	Isotope	$R_{cm}$	$\theta_1^a$	$\theta_2^b$	$R(N11-H15)^b$	$R_o^b$	$\langle(Py)^b$	$\langle(HCCH)^b$
$0^-$	Parent	5.12683	23.7	-26.8 [27.1]	2.37631 [2.71350]	5.13603 [5.13603]	23.7 [23.7]	-26.8 [27.1]
	Py-DCCH	5.06692	23.4	-26.1 [26.4]	2.35727 [2.67392]	5.13177 [5.13167]	23.7 [23.0]	-25.8 [26.0]
	Py-HCCD	5.18237	23.8	-24.9 [25.2]	2.35082 [2.68260]	5.13553 [5.13562]	23.5 [24.0]	-25.2 [25.4]
	Py-DCCD	5.12234	23.0	-24.1 [24.4]	2.32775 [2.63268]	5.13159 [5.13159]	23.0 [23.0]	-24.1 [24.4]
<b>Average<sup>c</sup></b>					<b>2.352(24) [2.673(40)]</b>	<b>5.1338(22) [5.1338(22)]</b>	<b>23.35(35) [23.50(50)]</b>	<b>-25.5(13) [25.8(14)]</b>
$0^+$	Parent	5.10884	23.3	-15.0 [15.3]	2.22827 [2.43706]	5.11807 [5.11807]	23.3 [23.3]	-15.0 [15.3]
	Py-DCCH	5.04860	23.4	-15.8 [16.1]	2.23451 [2.44597]	5.11738 [5.11732]	23.5 [23.2]	-15.7 [15.9]
	Py-HCCD	5.16852	23.5	-17.3 [17.6]	2.24648 [2.49310]	5.11870 [5.11877]	23.2 [23.7]	-17.6 [17.8]
	Py-DCCD	5.10832	22.9	-17.7 [18.0]	2.24300 [2.40099]	5.11758 [5.11758]	22.9 [22.9]	-17.7 [18.0]
<b>Average<sup>c</sup></b>					<b>2.2374(91) [2.465(28)]</b>	<b>5.11804(66) [5.11805(73)]</b>	<b>23.20(30) [23.30(40)]</b>	<b>-16.4(14) [16.7(14)]</b>
	Inner-o- <sup>13</sup> C	5.10233	8.2	-21.1 [21.2]	2.28789 [2.56707]	5.12526 [5.12526]	23.4 [23.4]	-21.0 [21.3]
	Outer-o- <sup>13</sup> C	5.11669	38.5	-24.5 [24.8]	2.33365 [2.63756]	5.12833 [5.12833]	23.1 [23.1]	-24.7 [24.6]
	Inner-m- <sup>13</sup> C	5.12200	39.7	-25.4 [25.7]	2.34391 [2.67317]	5.12916 [5.12916]	23.4 [23.4]	-25.3 [25.8]
	Outer-m- <sup>13</sup> C	5.12974	7.2	-22.3 [22.4]	2.30467 [2.58987]	5.12497 [5.12497]	23.5 [23.5]	-22.5 [22.2]
<b>Average<sup>c</sup></b>					<b>2.316(28) [2.620(53)]</b>	<b>5.1271(21) [5.1271(21)]</b>	<b>23.3(2) [23.3(2)]</b>	<b>-23.2(21) [23.6(23)]</b>
<b>STRFIT<sup>d</sup></b>					<b>2.33168<sup>e</sup></b>	<b>5.12985(82)</b>	<b>21.1(22)</b>	<b>-25.5(12)</b>
<b><i>Ab Initio</i><sup>f</sup></b>					<b>2.217</b>	<b>5.120</b>	<b>20.5</b>	<b>-18.6</b>
<b>RECOMMENDED<sup>g</sup></b>					<b>2.316(28)</b>	<b>5.1271(21)</b>	<b>23.2(2)</b>	<b>-23.2(21)</b>

(a)  $\theta_1$  is defined to be positive without loss of generality. (b) Numbers not in square brackets correspond to the negative choice of  $\theta_2$  and represent the geometry shown in Figure 4.4. Numbers in brackets correspond to the positive choice of  $\theta_2$ , for which the acetylene subunits is rotated counterclockwise about its center of mass. See text for discussion. (c) Average of the maximum and minimum values for the  $0^-$  or  $0^+$  states, or <sup>13</sup>C derivatives. Uncertainly (in parentheses) is half the range, i.e., half the difference between the maximum and minimum values, so as to encompass all values obtained. (d) Results using <sup>13</sup>C data only. See text for discussion. (e) No uncertainty is given because this was not a fitted parameter in STRFIT. (f) *Ab initio* (equilibrium) values obtained at the CCSD(T)(F12\*)/cc-pVDZ-F12 level/basis. (g) Average of the experimental (zero point) values obtained for <sup>13</sup>C species with the negative choice of  $\theta_2$ . See text for discussion.

## Discussion

As noted in the Introduction, the goal of this work was to determine whether acetylene forms a linear hydrogen bond with pyridine, or whether competing interactions between the ortho hydrogens on the ring and the  $\pi$  electrons of the acetylene give rise to a bent hydrogen bond. The arguments presented above provide strong evidence for the existence of a bent hydrogen bond. In comparison with pyridine–HCl and pyridine–HBr, we may infer that the weaker acidity of acetylene diminishes the importance of the linear interaction and renders the bent configuration more energetically competitive. It is interesting to note that the secondary hydrogen bond involving the ortho hydrogens of the pyridine is quite long and nonlinear: If Z represents the center of the  $C\equiv C$  bond, the  $H1\cdots Z$  distance is 3.42 Å and the  $C2-H1\cdots Z$  angle is  $122^\circ$ .<sup>201</sup> Yet, the interaction is of sufficient importance to move the acetylene axis  $46^\circ$  away from the axis of the nitrogen lone pair. Note that although no detailed quantum chemical calculations of the electron density have been performed for this system, the existence of such a secondary interaction is the most chemically intuitive explanation for the observed non-linearity. Moreover, the 3.42 Å distance is reasonably commensurate with that in other complexes which appear to exhibit secondary hydrogen bonding interactions.<sup>166a</sup> For example, the  $r(H\cdots X)$  distances are 3.226, 3.278, and 3.283 Å, with corresponding angles of 107.1, 110.9, and 125.7 degrees for  $B\cdots HCl$  complexes, where B = formaldehyde, oxirane, and 2,5-dihydrofuran, respectively. The influence of a similarly long (3.09 Å) and nonlinear ( $103^\circ$ ) secondary hydrogen bond has been noted in the complex  $py-CO_2$ .<sup>185</sup>  $Py-HCCH$  also differs from the complexes  $H_3N-HCCH$ <sup>202</sup> and  $(CH_3)_3N-HCCH$ ,<sup>203</sup> which form linearly hydrogen bonds due to the absence of sufficiently proximate competitive binding sites on the base.

The nonlinear geometry of the complex, compounded by the relatively small moment of inertia of acetylene, produces a dynamically complex system. Spectroscopic evidence is consistent with a tunneling motion through a barrier at the  $C_{2v}$  configuration and this, in itself, is associated with vibrational motion of substantial amplitude. The inability to

satisfactorily fit transitions with  $K_{-l} > 1$ , together with the appearance of several negative centrifugal distortion constants even for the  $^{13}\text{C}$  isotopologues, is suggestive of additional large amplitude motion not directly related to the tunneling. Indeed, there are five computed intermolecular modes with low harmonic frequencies:  $22\text{ cm}^{-1}$  (in-phase, out-of-plane intermolecular bending),  $30\text{ cm}^{-1}$  (in-phase, in-plane intermolecular bending, corresponding to the tunneling coordinate in Figure 4.3),  $105\text{ cm}^{-1}$  (intermolecular stretching),  $115\text{ cm}^{-1}$  (out-of-phase, out-of-plane intermolecular bending), and  $155\text{ cm}^{-1}$  (out-of-phase, in-plane intermolecular bending).<sup>204</sup> As a consequence, an isotopically invariant value of the H–N distance is not well defined, as the zero point averaging is expected to strongly depend on the moment of inertia of the acetylene moiety. This is further manifested in the N $\cdots$ H hydrogen bond length of  $2.32\text{ \AA}$ , which is somewhat larger than that in py-HF ( $2.2\text{ \AA}$ )<sup>205</sup> and consistent with the low binding energy of  $1.2\text{ kcal/mol}$ . Interestingly, however, the hydrogen bond length is quite similar to the  $2.33\text{ \AA}$  value reported for HCCH–NH<sub>3</sub>.<sup>202</sup> Py-HCCH is an excellent example of a system for which structure and dynamics are inextricably entwined, and thus for which the specification of the potential energy minimum alone provides an inadequate description of even the ground vibrational state. Such may often be the case when competing binding sites are separated by a small barrier and a relatively short path to interconversion.

## Conclusion

The weakly bound complex formed from pyridine and acetylene has been investigated in order to study the competition between n-pair and  $\pi$ -pair hydrogen bonding. Compared with the previously studied complexes py-HCl and py-HBr in which the HX axis aligns with the  $C_2$  axis of the pyridine, py-HCCH is bent, with the acetylene axis leaning  $\sim 46^\circ$  away from the axis of the nitrogen lone pair. This tilt is presumably indicative of  $\pi$ -pair hydrogen bonding with the ortho hydrogens of the pyridine, which assumes greater importance relative to that of the linear hydrogen bond owing to the weaker acidity of HCCH relative to that of HCl or HBr. *Ab initio* calculations of the intermolecular potential energy surface at the CCSD(T)(F12\*)/cc-pVDZ-F12 level reveal a small ( $44\text{ cm}^{-1}$ ) barrier at the  $C_{2v}$  configuration and spectroscopic evidence indicates that the

system tunnels between the two equivalent potential minima associated with the two ortho hydrogens. The N...H hydrogen bond length is 2.32(3) Å, but because of its dynamic complexity, the complex is best described by the distance between the center of the pyridine ring and the center of the C≡C bond of acetylene (the former defined as the midpoint between the nitrogen and the para carbon of pyridine). This system is an excellent example of one in which large amplitude zero-point motion renders conventional descriptions of molecular structure in terms of isotopically invariant bond lengths and bond angles only approximate. Such a situation may not be uncommon in the presence of competitive binding sites with geometrical proximity and a small barrier to interconversion.

### **Acknowledgement**

ACL acknowledges the Engineering and Physical Sciences Research Council (EPSRC) for a Senior Fellowship and the University of Bristol for a Senior Research Fellowship. Work at the University of Minnesota was supported by the National Science Foundation (Grant # CHE-1266320). GCC received support via an EPSRC Research Studentship and support for RBM was made available through a University of Minnesota Lester C. and Joan M. Krogh graduate fellowship. DPT thanks the Royal Society for a University Research Fellowship.

## **Chapter 5 : Multidimensional Large Amplitude Dynamics in the Pyridine – Water Complex**

Rebecca B. Mackenzie, Christopher T. Dewberry, Ryan D. Cornelius,  
Christopher J. Smith, and Kenneth R. Leopold



### Abstract

Aqueous pyridine plays an important role in a variety of catalytic processes aimed at harnessing solar energy. In this work, the pyridine-water interaction is studied by microwave spectroscopy and DFT calculations. Water forms a hydrogen bond to the nitrogen with the oxygen tilted slightly toward either of the ortho hydrogens of the pyridine, and a tunneling motion involving in-plane rocking of the water interconverts the resulting equivalent structures. A pair of tunneling states with severely perturbed rotational structure is identified and their energy separation,  $\Delta E$ , is inferred from the perturbations and confirmed by direct measurement. Values of  $\Delta E$  are 10404.45 MHz and 13566.94 MHz for the H<sub>2</sub>O and D<sub>2</sub>O complexes, respectively, revealing a curious increase upon deuteration. Small splittings in some transitions suggest an additional internal motion making this complex an interesting test case for theoretical treatments of large amplitude motion.

## Introduction

The interaction of pyridine (py) and water underlies a variety of topics in sustainable energy research. The py-H<sub>2</sub>O complex, for example, has been investigated for its possible role in photo-induced bond cleavage of water<sup>206</sup> and both pyridine and pyridinium are prominent in studies on photoelectrochemical mechanisms for CO<sub>2</sub> reduction.<sup>207</sup> Solvent-solute interactions play an important role in the photophysics of pyridine solutions<sup>208</sup> and calculations indicate that n- $\pi^*$  excitation induces significant structural rearrangement of the py-H<sub>2</sub>O complex.<sup>209</sup> Detailed information about the pyridine-water interaction should be a valuable part of our understanding of a variety of environmentally friendly photochemical processes.

Nearly 20 years ago, Caminati *et al.* reported microwave spectra of the three diazine-water complexes.<sup>210-212</sup> In each case, the primary interaction is an N $\cdots$ HO hydrogen bond that is rendered nonlinear, presumably by a secondary attraction between the oxygen and an available ortho-hydrogen. Moreover, in the case of pyrazine, which has C<sub>2v</sub> symmetry and two available ortho hydrogens, the complex with water has two degenerate minimum energy configurations, and these researchers were able to determine the tunneling frequency for their interconversion.<sup>210</sup> Curiously, however, analogous studies of the py-H<sub>2</sub>O complex have not been reported. Low resolution gas phase infrared spectra have been published,<sup>213</sup> and some microwave spectra have been collected,<sup>214</sup> but the latter appear to have been too complex to assign at the time. With the aid of modern, broadband chirped-pulse spectroscopy,<sup>4</sup> we have investigated both the H<sub>2</sub>O and D<sub>2</sub>O isotopologues of the system. The spectra reveal an interaction rich with internal dynamics that perturb the spectra so strongly that they would have been difficult, if not impossible, to unravel using older methods alone.

## Computational

Prior to experimentation, density functional theory (DFT) was used to predict the minimum energy structure of py-H<sub>2</sub>O.<sup>215</sup> As with the diazine-H<sub>2</sub>O complexes, and in accord with previous computational work,<sup>216</sup> the system exhibits a nonlinear hydrogen

bond (Figure 5.1). The transition state connecting the two degenerate bent configurations is a symmetric, linearly hydrogen bonded structure and the associated imaginary frequency corresponds to an in-plane rocking motion with a barrier of 0.33 kcal/mol (Figure 5.2a). This motion is similar to that described for pyrazine–H<sub>2</sub>O<sup>210</sup> and to that recently observed for py–HCCH.<sup>15</sup> The binding energy is 7.0 kcal/mol.

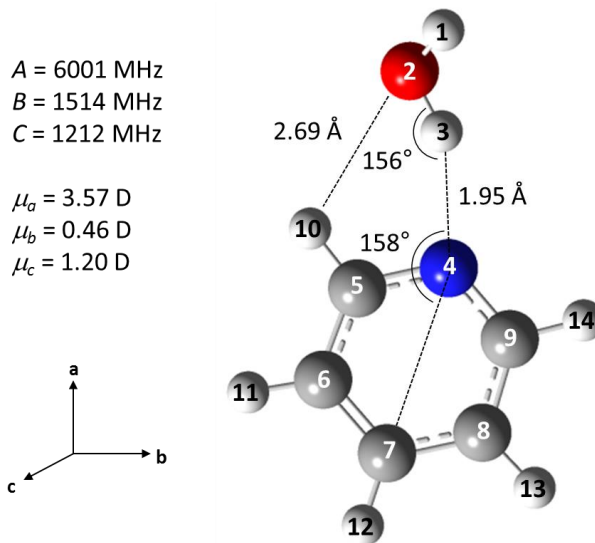


**Figure 5.1 Theoretical Results for the py–H<sub>2</sub>O Complex**

Calculations were done using M06-2X/611++G(3df,3pd). (*a,b,c*) are the inertial axes.

The spectroscopic consequence of the finite barrier in Figure 5.2a is a lifting of the degeneracy associated with the two equivalent configurations, producing a closely spaced pair of tunneling states. Moreover, the motion shown inverts  $\mu_b$ , but not  $\mu_a$  or  $\mu_c$ , where  $\mu_g$  is the dipole moment component along the *g*-inertial axis (see Figure 5.1). Thus, we anticipate that *a*- and *c*-type rotational transitions occur within a tunneling state, producing a doubling of their spectra (one set for each state). Conversely, the *b*-type transitions cross from the ground to the excited tunneling state and provide a direct measure of the tunneling splitting.

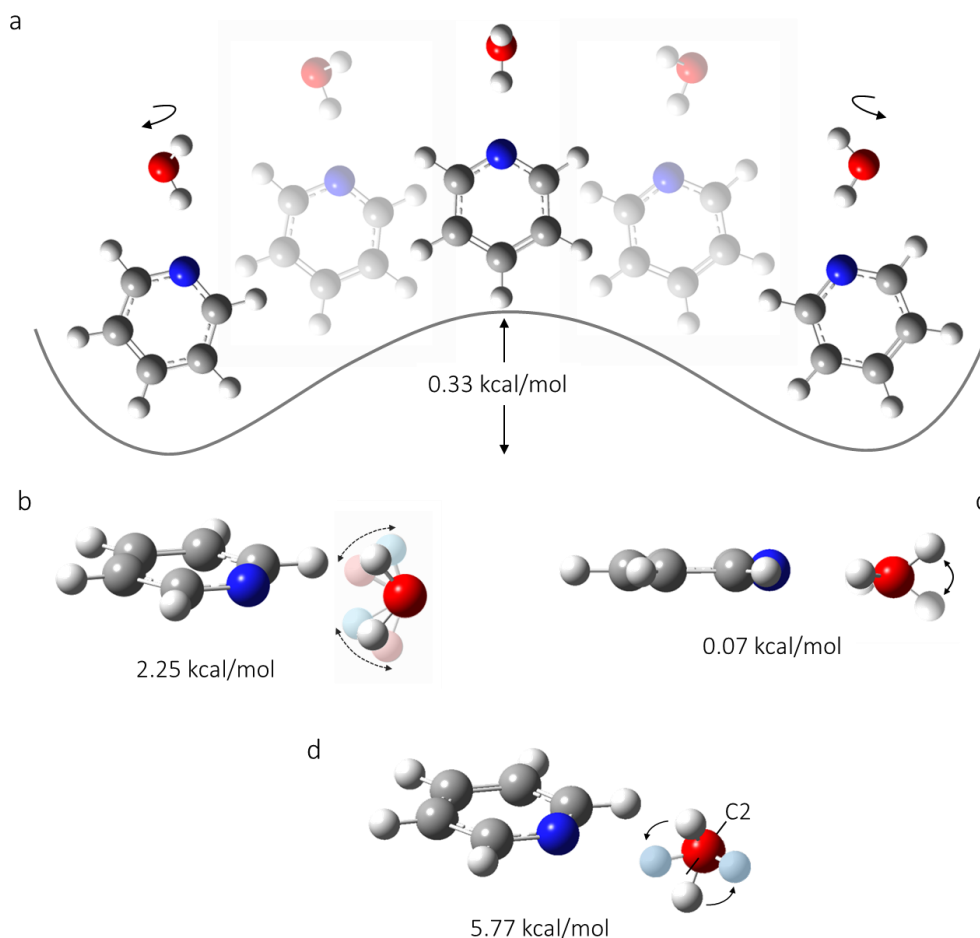


### Figure 5.2 Depiction of Possible py-H<sub>2</sub>O Internal Motions

(a) Depiction of the in-plane rocking motion in py-H<sub>2</sub>O from M06-2X/6-311++G(3df,3pd) calculations. (b,c,d) Possible water-centered motions. Calculated barrier heights are reported for each motion.

### Experimental

The vapor above a 5:1 mixture of py:H<sub>2</sub>O was entrained in Ar and expanded at a stagnation pressure of 2 atm into our tandem chirped-pulse, cavity Fourier transform microwave spectrometer.<sup>31</sup> A 3D-printed slit nozzle<sup>5</sup> (0.0085" x 1.25") was used to increase the signal-to-noise ratio. Chirped-pulse spectra between 6 and 18 GHz were taken in 3 GHz segments and line frequencies were measured to ~40 kHz. Subsequently, high resolution cavity measurements were made, which had a spectral resolution of ~4 kHz.

### Microwave Spectrum

Initially, a chirped-pulse spectrum from 6-18 GHz permitted the assignment of a series of R-branch  $a$ -type  $K_{-1} = 0$  transitions belonging to the ground state, but despite substantial efforts, no additional transitions could be identified based on a semi-rigid rotor model. An analogous  $K_{-1} = 0$  fit was obtained for py-D<sub>2</sub>O. Eventually, a comparison of the <sup>14</sup>N nuclear hyperfine structure obtained by re-measuring transitions on the cavity spectrometer provided the key for identifying transitions involving  $K_{-1} = 1$  for both isotopologues, Figure 5.3. These transitions were far removed from predictions based on a semi-rigid rotor Hamiltonian, sometimes by hundreds of MHz, indicating that the spectra were highly perturbed. Such perturbations between tunneling states are common, though their severity in this case was extraordinary.

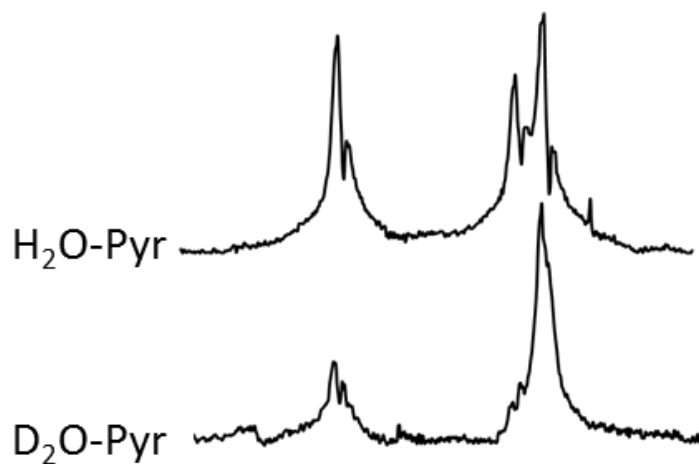


**Figure 5.3 Comparison of the  $3_{13} - 2_{12}$  Transitions for H<sub>2</sub>O – and D<sub>2</sub>O – pyridine**

Cavity spectra of the  $3_{13}$ - $2_{12}$  transitions for H<sub>2</sub>O – and D<sub>2</sub>O – pyridine complexes. While the exact hyperfine structure is not identical, the general pattern was similar enough to identify them as the same transition. The extra splitting in the H<sub>2</sub>O spectrum is discussed further on in the chapter.

Further analysis of the chirped-pulse spectrum led to the identification of transitions belonging to the excited tunneling state. The severity of the perturbation is illustrated in Figure 5.4, where it is seen that the relative positions of the ground and excited state

transitions is a strong function of the rotational quantum number,  $J$ . Nonetheless, the spectra were readily fit using Pickett's SPFIT program<sup>144</sup> to a Hamiltonian of the form

$$H = H_{Rot} + H_{CD} + H_{Int} + H_{Tun} + H_{hfs} \quad (1)$$

where

$$H_{Int} = F_{ab}(P_a P_b + P_b P_a) \quad (2)$$

$H_{Rot}$  and  $H_{CD}$  are the rigid rotor and Watson A-reduced centrifugal distortion Hamiltonians, respectively and  $H_{Int}$  is the interaction term between the two states with the Coriolis coupling constant  $F_{ab}$ .  $H_{Tun}$  is the energy separation between the states,  $\Delta E$ , and is added only for the upper state.  $H_{hfs}$  describes the  $^{14}\text{N}$  nuclear hyperfine structure. The resulting constants provided accurate predictions for transitions involving  $K_{-J} = 2$  of both tunneling states as well as three  $b$ -type transitions that cross between the tunneling states.  $c$ -type transitions were not observed despite the large calculated value of  $\mu_c$  (1.2 D). A number of py- $\text{H}_2\text{O}$  transitions, particularly those involving  $K_{-J} > 0$  in the excited state, showed a small doubling, typically between 20 and 500 kHz, as illustrated in Figure 5.5. For those lines, the most intense set of components was selected for analysis. In the final fit of all assigned lines,<sup>215</sup> a small distortion term,  $-F_{abJ} \times J(J+1)$ , was added to  $F_{ab}$ . The rms residuals were excellent, 15 and 20 kHz for the  $\text{H}_2\text{O}$  and  $\text{D}_2\text{O}$  fits, respectively, though a few residuals were as large as 52 and 84 kHz for the  $\text{H}_2\text{O}$  and  $\text{D}_2\text{O}$  fits, respectively. Spectroscopic constants are given in Table 5.1. The fitted rotational constants are seen to be in good agreement with DFT results, though the inertial defects are somewhat large.

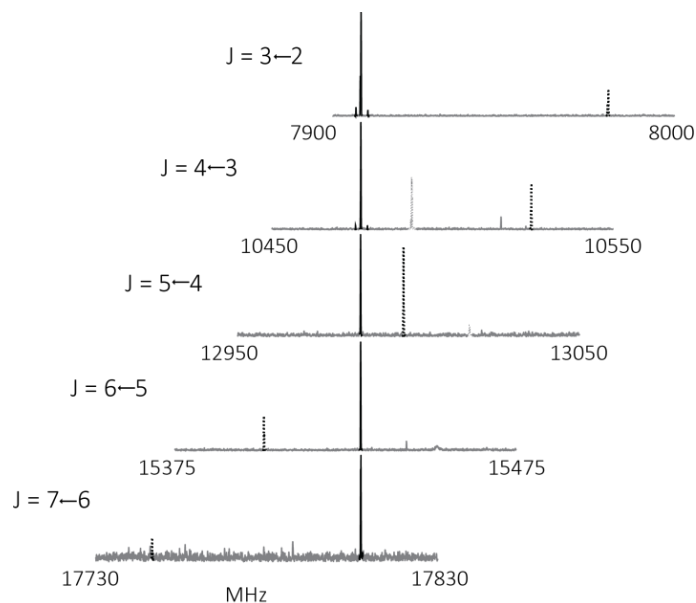


### Figure 5.4 Chirped-Pulse Spectra of py-H<sub>2</sub>O *K*=0 Transitions

Five 100 MHz segments of the py-H<sub>2</sub>O chirped-pulse spectrum showing the *a*-type *K*=0 rotational transitions for the ground (black) and excited (black dotted) states. The *K*=0 ground state intensities were normalized to facilitate comparison of relative intensities. Dotted gray transitions were assigned to other py-H<sub>2</sub>O rotational transitions.

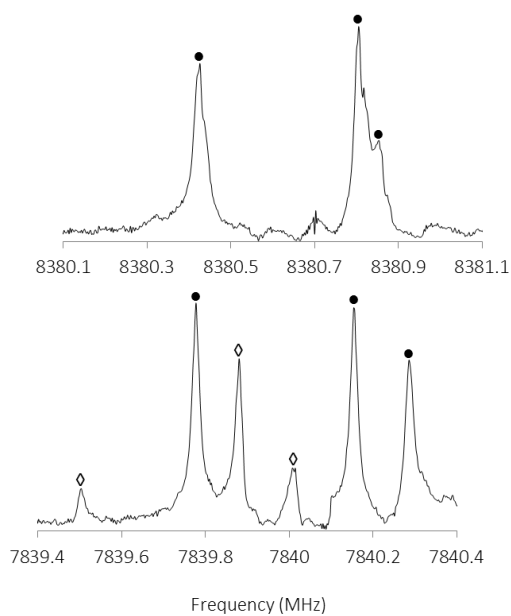


### Figure 5.5 Cavity Spectra of py - H<sub>2</sub>O

Cavity spectra of the  $3_{12} \leftarrow 2_{11}$  transition for the ground (upper) and excited (lower) states. <sup>14</sup>N hyperfine structure is evident. The excited state clearly displays a second set of transitions, marked with  $\diamond$  and offset by 270 kHz from the more intense set of transitions marked with  $\bullet$ . Similar structure in the ground state appears as barely resolved shoulders.

**Table 5.1 Spectroscopic Constants for Py–H<sub>2</sub>O and Py–D<sub>2</sub>O<sup>a</sup>**

	Py–H <sub>2</sub> O <sup>b</sup>	Py–D <sub>2</sub> O <sup>b,c</sup>	Theoretical Py–H <sub>2</sub> O <sup>d</sup>
$A''/\text{MHz}$	5932.09(12)	5906.45(12)	6001 (1.2)
$B''/\text{MHz}$	1495.6117(57)	1403.7800(60)	1514 (1.2)
$C''/\text{MHz}$	1171.4302(57)	1115.6702(64)	1212 (3.5)
$\Delta_{ID}/\text{amu}\cdot\text{\AA}^2$ <sup>e</sup>	8.3	7.4	-1.0
$A'/\text{MHz}$	5912.50(38)	5868.68(34)	
$B'/\text{MHz}$	1498.5063(77)	1407.1414(73)	
$C'/\text{MHz}$	1172.2425(69)	1116.6034(62)	
$^{14}\text{N } \chi_{aa}''/\text{MHz}$	-4.352(11)	-4.401(15)	
$^{14}\text{N } (\chi_{bb} - \chi_{cc})''/\text{MHz}$	-1.787(31)	-1.900(88)	
$^{14}\text{N } \chi_{aa}'/\text{MHz}$	-4.525(17)	-4.511(37)	
$^{14}\text{N } (\chi_{bb} - \chi_{cc})'/\text{MHz}$	-1.81(14)	-1.81(19)	
$\Delta_J''/\text{kHz}$	1.275(33)	1.074(32)	
$\Delta_J'/\text{kHz}$	1.107(29)	0.917(29)	
$\delta_J''/\text{kHz}$	0.399(19)	0.335(17)	
$\delta_J'/\text{kHz}$	0.357(30)	0.278(27)	
$\Delta_{JK}''/\text{kHz}$	12.2(11)	10.54(91)	
$\Delta_{JK}'/\text{kHz}$	45.9(16)	46.7(14)	
$\delta_K''/\text{kHz}$	9.6(28)	8.0(30)	
$\delta_K'/\text{kHz}$	28.4(36)	23.9(30)	
$\Delta E/\text{MHz}$	10404.45(12)	13566.94(12)	
$F_{ab}/\text{MHz}$	417.1488(70)	383.1749(75)	
$F_{abJ}/\text{kHz}$	-7.91(18)	-7.01(17)	
RMS/kHz	15	20	
$N$	133	123	

(a) Double and single primes refer to the lower and upper states, respectively.

(b) For rotational transitions with additional doubling, the most intense set of components was selected.

(c) Deuterium hyperfine structure was too collapsed to analyze.

(d) The values in parentheses are the percent change from the experimental ground state values.

(e)  $\Delta_{ID} = \frac{h}{8\pi^2} \left( \frac{1}{C} - \frac{1}{A} - \frac{1}{B} \right)$



The observed *b*-type transitions provide direct, unambiguous measures of  $\Delta E$ . Remarkably, however,  $\Delta E$  increases upon deuteration, counter to expectation were it purely the tunneling energy associated with the motion of Figure 5.2a. A clue to the origin of this anomaly may lie in the additional doubling of some of the spectra noted above, as these “extra” splittings reveal the existence of tunneling states associated with another pair of equivalent configurations. The absence of *c*-type transitions at their rigid rotor locations suggests a motion that inverts  $\mu_c$ , causing either the average of  $\mu_c$  (and hence the corresponding intensities) to vanish or requiring the *c*-type transitions to cross an associated tunneling doublet, thus displacing them from their predicted positions by an unknown amount. Two possible motions are a cross-plane wag of the free water hydrogen or a rotation of the water about an axis perpendicular to its plane that interchanges the bound and free hydrogens (Figure 5.2b and 5.2c). Further DFT calculations revealed 0.07 and 2.23 kcal/mol barriers for these motions, respectively. However, if the equilibrium geometry is planar, the vibrationally averaged  $\mu_c$  would be zero, presenting a third scenario in which the second pair of tunneling states arises from an exchange of the hydrogens by a rotation of the water about its  $C_2$  axis (Figure 5.2d). In any case, the existence of a second motion is supported by the second set of splittings, a few abnormally large residuals, and the rather high inertial defect.

Figure 5.6 illustrates how a second large amplitude motion could produce the anomalous isotopic dependence of  $\Delta E$ . Two splittings are shown:  $\Delta E_1$  arises from motion along the coordinate of Figure 5.2a;  $\Delta E_2$  and  $\Delta E_2'$  arise from the water-centered internal motion and may differ for the upper and lower states of the rocking motion. The  $\Delta E$  determined in this work is a composite quantity, viz.  $\Delta E = \Delta E_1 + (\Delta E_2 - \Delta E_2')/2$ . While  $\Delta E_1$ ,  $\Delta E_2$ , and  $\Delta E_2'$  should all decrease slightly upon deuteration,  $\Delta E_2$  and  $\Delta E_2'$  will be more sensitive and may change by different amounts. If the change in  $(\Delta E_2 - \Delta E_2')/2$  offsets that in  $\Delta E_1$ , an anomalous isotope dependence can be realized. While quantitative details of the diagram remain to be clarified, it serves to illustrate the complexity than can pervade systems with multiple large amplitude motions.

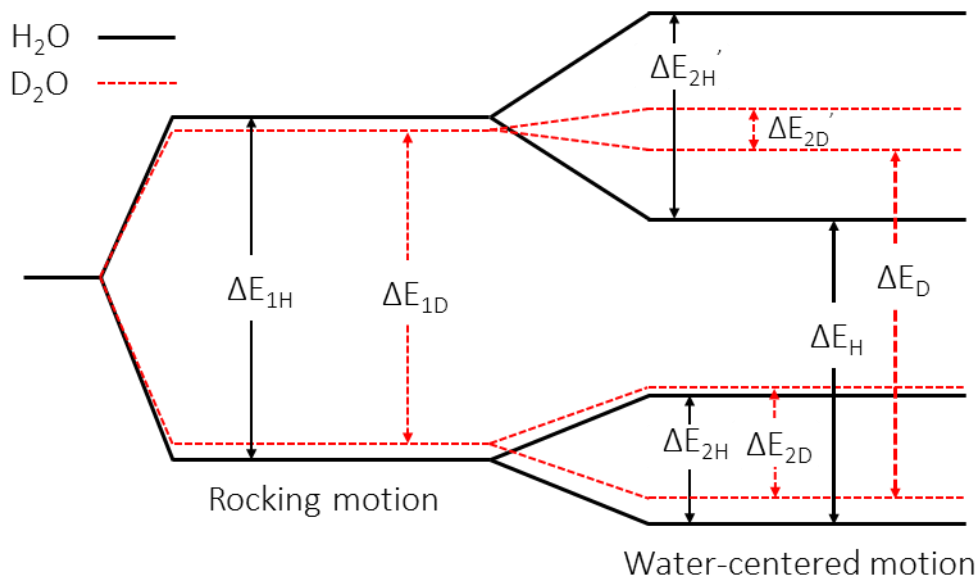


**Figure 5.6 Qualitative Energy Diagram Resulting from Multiple Internal Motions**

Qualitative energy diagram illustrating the effect of a second, water-centered tunneling motion on the observed value of  $\Delta E$ . Tunneling energies are only labeled for the  $\text{H}_2\text{O}$  species.  $\Delta E$  measured in this work is between the ground and excited rocking states with no change from ground to excited water-related levels.

### Conclusion

In summary, the  $\text{py-H}_2\text{O}$  complex has been studied by microwave spectroscopy and density functional theory. The system has a nonlinear  $\text{N}\cdots\text{HO}$  hydrogen bond and a binding energy of 7.0 kcal/mol. Unusually strong perturbations in the spectrum reveal complex internal dynamics that include a rocking between equivalent configurations in the heavy atom plane. Cross-plane wagging of the free water hydrogen and/or a hydrogen-exchanging internal rotation of the water unit are also implicated. Two pairs of tunneling states are observed and the compound motions likely give rise to an unexpected isotope dependence of measured tunneling energies. This feature should provide a challenging test case for theoretical treatments of multidimensional large amplitude dynamics. Future work should focus on accessing additional tunneling states (Figure 5.6) to further define the water-centered motion, and on elucidating the effects of the double well potential and facile tunneling dynamics on the photophysics of aqueous pyridine.

## **Acknowledgments**

This work was supported by the National Science Foundation, Grant Nos. CHE-1266320 and CHE-1563324, a UMN Doctoral Dissertation Fellowship awarded to R.B.M., the Minnesota Supercomputer Institute, and a Lando Summer Undergraduate Research Fellowship awarded to R.D.C. through the University of Minnesota. We thank Prof. Renee Frontiera for bringing this problem to our attention.

## **Chapter 6 : Effects of a Remote Binding Partner on the Electric Field and Electric Field Gradient at an Atom in a Weakly Bound Trimer**

Reproduced from R. B. Mackenzie, B. A. Timp, Y. Mo, and K. R. Leopold,  
*J. Chem. Phys.*, **139**, 034320 (2013)  
with the permission of AIP Publishing.

## Abstract

Microwave spectra are reported for the  $C_{3v}$  symmetric complexes  $\text{Kr-SO}_3$  and  $\text{Kr-SO}_3\text{-CO}$ . The S-C distance in the trimer, 2.871(9) Å, is the same as that previously determined for  $\text{SO}_3\text{-CO}$  to within the estimated uncertainties. The Kr-S distances are 3.438(3) Å and 3.488(6) Å in  $\text{Kr-SO}_3$  and  $\text{Kr-SO}_3\text{-CO}$ , respectively, indicating that the addition of CO to  $\text{Kr-SO}_3$  increases the Kr-S distance by 0.050(9) Å. Measurements of the  $^{83}\text{Kr}$  nuclear quadrupole coupling constants provide direct probes of the electric field gradient at the Kr nucleus, and a comparison between the two systems reflects the degree to which the CO influences the electronic structure of the krypton atom. Although the Kr and CO in the trimer are on opposite sides of the  $\text{SO}_3$  and thus are not in direct contact, the addition of CO to  $\text{Kr-SO}_3$  reduces the electric field gradient at the Kr nucleus by 18%. Calculations using the Block Localized Wavefunction decomposition method are used to understand the physical origins of this change. While the magnitudes of both the electric field and the electric field gradient at the Kr nucleus decrease upon addition of the CO to  $\text{Kr-SO}_3$ , the changes are shown to arise from rather complex combinations of geometrical distortion, electrostatic, polarization, and electron transfer effects. For the electric field, the electrostatic term accounts for the largest portion of the reduction, while for the electric field gradient, polarization and structural change of the  $\text{Kr-SO}_3$  moiety make the primary contributions. Despite significant changes in the electronic environment at the Kr nucleus, calculated binding energies indicate that the interactions are largely additive, with the binding energy of the trimer very nearly equal to the sum of the  $\text{Kr-SO}_3$  and  $\text{SO}_3\text{-CO}$  binding energies.

## Introduction

Understanding how the properties of isolated molecules evolve into those of condensed matter is an important goal of cluster science.<sup>217,218</sup> While studies of dimers directly probe pairwise interactions, investigations involving trimers and larger clusters contain information about many-body interactions. Experiments that compare the properties of a trimer with those of its constituent dimers speak directly to the role of cooperative interactions in clusters and as such, provide information that is, at least in principle, transferrable to detailed descriptions of liquids, solids, and solutions.

In this work, we explore the influence of a remote binding partner on the interaction between two moieties in a weakly bound trimer. Specifically we investigate the effect of an added CO molecule on the Kr atom in the complex Kr–SO<sub>3</sub>. The CO is “remote” in this context in that, as shown below, the trimer has the C<sub>3v</sub> symmetric structure Kr–SO<sub>3</sub>–CO. Thus, the CO is on the side of the SO<sub>3</sub> opposite the krypton and is not in direct contact with it. We examine the effect of the CO on the Kr–S interaction using microwave spectroscopy to determine both the Kr–S distance and the <sup>83</sup>Kr nuclear quadrupole coupling constant. The latter is directly proportional to the electric field gradient at the krypton nucleus and thus provides a sensitive measure of the changes in its electronic environment that occur upon complexation. The experimental work is complemented with a theoretical study using the Block Localized Wavefunction method,<sup>219-221</sup> which permits the quadrupole coupling constant to be decomposed into physically meaningful contributions. In particular, we examine both the electric field and electric field gradient at the Kr nucleus through a series of calculations which partition these quantities into contributions from geometric distortion, electrostatic interactions, polarization, and electron transfer. The dimer Kr–SO<sub>3</sub> is also studied in this work, both experimentally and theoretically, in order to provide a basis for comparison. While the dipole moment of Kr–SO<sub>3</sub> has been measured (0.369 D),<sup>222</sup> the Kr–S bond length and <sup>83</sup>Kr quadrupole coupling constant have not been previously determined and thus, this work adds to our knowledge of that complex as well.

Our choice of these somewhat exotic clusters follows from a series of prior studies performed in our laboratory which have focused on simple complexes of  $\text{SO}_3$  and  $\text{BF}_3$ . We have shown that, with a series of suitably chosen bases, the interactions of these simple Lewis acids can span the entire range between van der Waals and chemical bonding.<sup>223,224</sup> Moreover, the structure and bonding of such systems are extraordinarily sensitive to near-neighbor interactions,<sup>223,224</sup> and indeed several of our prior reports have investigated the effects of adding both highly polar and weakly polar neighbors such as HCN, CO, and Ar on the properties of  $\text{SO}_3$  and  $\text{BF}_3$  containing dimers. Examples include the complexes  $\text{Ar-SO}_3\text{-CO}$ ,<sup>225</sup>  $\text{Ar-SO}_3\text{-HCN}$ ,<sup>226</sup>  $\text{HCN-SO}_3\text{-CO}$ ,<sup>226</sup>  $\text{HCN-HCN-SO}_3$ ,<sup>227</sup> and  $\text{HCN-HCN-BF}_3$ .<sup>228</sup> To get the most information about these types of systems, however, we would like to fully exploit the nuclear quadrupole interactions described above as a probe of electronic structure. While the  $^{14}\text{N}$  in these systems does exhibit nuclear quadrupole interactions, the values of the observed coupling constants are convoluted with the effects of large amplitude angular vibrational motion of the HCN. Moreover, there are no common isotopes of argon with the nuclear spin necessary to produce nuclear quadrupole coupling. The use of atomic  $^{83}\text{Kr}$ , with nuclear spin of 9/2 and a natural abundance of 11.6%, alleviates both of these difficulties by permitting the observation of nuclear quadrupole coupling without the accompanying complications of large amplitude motion. Thus, this study provides an unambiguous probe of electronic structure which has not been available for other related systems.

### Experimental and Results

Spectra were recorded between 3.2 and 5.7 GHz using the pulsed-nozzle Fourier transform microwave spectrometer described elsewhere.<sup>31,49</sup>  $\text{Kr-SO}_3$  was produced from a mixture of 12 % Kr in Ar that had been passed over a sample of polymerized  $\text{SO}_3$  at 0 °C and expanded through a 0.8 mm diameter nozzle at a stagnation pressure of 2.7 atm. To produce  $\text{Kr-SO}_3\text{-CO}$ , CO at a concentration of ~1% was added to the mixture and the optimum stagnation pressure was found to be 3.4 atm. The nozzle was pulsed at a rate of 4 Hz, and four free induction decay signals were collected per pulse. Spectra were easily located using rotational constants estimated on the basis of standard van der Waals radii

of Ar and Kr, and the known weak bond distances in Ar–SO<sub>3</sub> (3.350 Å)<sup>229</sup> and SO<sub>3</sub>–CO (2.854 Å).<sup>225</sup> Observed transition frequencies and their assignments are provided in Appendix F and a sample spectrum of the trimer is shown in Figure 6.1.

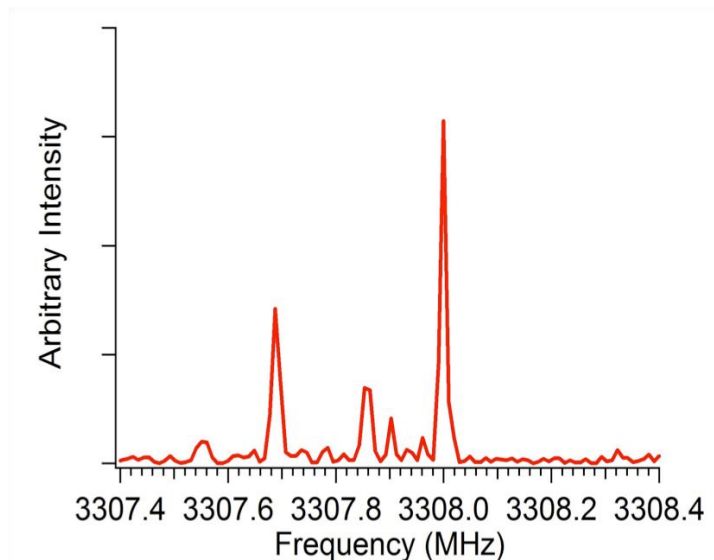


**Figure 6.1 Cavity Spectrum of <sup>83</sup>Kr-SO<sub>3</sub>-CO**

A portion of the spectrum of <sup>83</sup>Kr–SO<sub>3</sub>–CO, showing hyperfine structure in the J = 3 → 4, K = 0 transition. F assignments are from left to right 13/2 → 15/2, 15/2 → 17/2, and 11/2 → 13/2. The natural abundance of <sup>83</sup>Kr is 11.6%. This spectrum represents 1000 seconds of signal averaging time. The large feature at 3308.0 MHz is an instrumental artifact at the cavity frequency.

Observed spectra of both complexes were those of a symmetric top, but because the oxygens have a nuclear spin of zero, only K = 0, ±3, ±6, etc. exist.<sup>230</sup> Moreover, only K = 0 and ±3 states were observed in this work due to the range of J values observed and due to cooling of the higher K states in the supersonic jet. Using estimated isotope shifts and known natural abundances of the Kr isotopes, the different Kr isotopologues of each complex were readily identified. <sup>34</sup>S spectra were measured in natural abundance, and <sup>13</sup>CO spectra were obtained with an isotopically enriched sample (Cambridge Isotope Laboratories, 99 atom percent <sup>13</sup>C). Spectra were fit for each isotopologue to a symmetric top energy expression,

$$E = BJ(J + 1) - D_J J^2(J + 1)^2 - D_{JK} J(J + 1)K^2 + \Delta E_Q \quad (1)$$



using the SPFIT program of Pickett.<sup>144</sup> Here,  $\Delta E_Q$  is the energy associated with the nuclear quadrupole interaction, and was only included for species containing  $^{83}\text{Kr}$ . Other symbols in equation 1 have their usual meanings.<sup>230</sup> The resulting spectroscopic constants are given in Table 6.1 and the residuals from the fits are also included in Appendix F.

**Table 6.1 Spectroscopic Constants of Kr-SO<sub>3</sub> and Kr-SO<sub>3</sub>-CO**

Isotope	$B$ , MHz	$D_J$ , kHz	$D_{JK}$ , kHz <sup>a</sup>	$eQq$ ( $^{83}\text{Kr}$ ), MHz
$^{82}\text{Kr}-^{32}\text{SO}_3^{\text{b}}$	956.59017(46)	1.833(26)		
$^{83}\text{Kr}-^{32}\text{SO}_3$	951.43967(30)	1.846(18)		20.2229(45)
$^{84}\text{Kr}-^{32}\text{SO}_3^{\text{b}}$	946.42217(21)	1.833(12)		
$^{84}\text{Kr}-^{34}\text{SO}_3^{\text{b}}$	935.76595(20)	1.775(11)		
$^{86}\text{Kr}-^{32}\text{SO}_3^{\text{b}}$	936.69977(31)	1.783(18)		
$^{86}\text{Kr}-^{34}\text{SO}_3^{\text{b}}$	926.01973(91)	1.717(56)		
$^{82}\text{Kr}-^{32}\text{SO}_3-^{12}\text{CO}$	415.60982(15)	0.1696(25)	1.8460(90)	
$^{83}\text{Kr}-^{32}\text{SO}_3-^{12}\text{CO}$	413.50359(11)	0.1696 <sup>c</sup>		16.646(57)
$^{84}\text{Kr}-^{32}\text{SO}_3-^{12}\text{CO}$	411.44689(39)	0.17090(49)	1.7950(25)	
$^{86}\text{Kr}-^{32}\text{SO}_3-^{12}\text{CO}$	407.44753(37)	0.1658(61)	1.776(21)	
$^{82}\text{Kr}-^{32}\text{SO}_3-^{13}\text{CO}$	410.61632(22)	0.1665(36)	1.744(13)	
$^{83}\text{Kr}-^{32}\text{SO}_3-^{13}\text{CO}$	408.52718(24)	0.1665 <sup>d</sup>		16.79(17)
$^{84}\text{Kr}-^{32}\text{SO}_3-^{13}\text{CO}$	406.48650(17)	0.1668(21)	1.752(11)	
$^{86}\text{Kr}-^{32}\text{SO}_3-^{13}\text{CO}$	402.51967(30)	0.1758(51)	1.727(18)	

(a)  $D_{JK}$  was determined for isotopologues where more than one  $K$  state was observed.

(b) Constants for these isotopologues were calculated by hand because only two transitions were determined. Error was propagated from the error in the transition frequencies.

(c) Held fixed at the  $^{82}\text{Kr}-^{32}\text{SO}_3-^{12}\text{CO}$  value.

(d) Held fixed at the  $^{82}\text{Kr}-^{32}\text{SO}_3-^{13}\text{CO}$  value.

### Structural Analysis

The coordinates used to specify the structures of Kr-SO<sub>3</sub> and Kr-SO<sub>3</sub>-CO are defined in Figure 6.2. As in our previous work on SO<sub>3</sub>-CO and Ar-SO<sub>3</sub>-CO,<sup>225</sup> the geometry of the SO<sub>3</sub> was assumed to be unchanged upon complexation. The C<sub>3</sub> axis of the SO<sub>3</sub> was allowed to undergo large amplitude vibrational motion through an angle,  $\chi$ , and the CO (when present) was assumed to undergo similar motion through the angle  $\gamma$ . Since both complexes are symmetric tops,  $\langle\chi\rangle = \langle\gamma\rangle = 0$ . Large amplitude, out-of-plane motion along

an azimuthal angular coordinate is also possible, but drops out of the problem for a symmetric top upon vibrational averaging.<sup>146</sup> For each isotopologue of each complex, the zero-point, vibrationally averaged moment of inertia,  $\langle I_{bb} \rangle$ , was estimated from its observed rotational constant with the usual neglect of vibrational averaging, viz,  $\langle I_{bb} \rangle \approx h/8\pi^2 B$ , and related to the structural parameters of the complex.

For Kr-SO<sub>3</sub>,  $\langle I_{bb} \rangle$  may be written<sup>146,231</sup>

$$\langle I_{bb} \rangle = \mu \langle R_{cm}^2 \rangle + \left( \frac{1}{2} \right) I_{bb}^{(SO_3)} \left[ 1 + \langle \cos^2 \chi \rangle \right] + \left( \frac{1}{2} \right) I_{cc}^{(SO_3)} \langle \sin^2 \chi \rangle \quad (2)$$

where  $R_{cm}$  is the center-of-mass distance (equal to the Kr-S distance),  $\mu$  is the pseudodiatom reduced mass, equal to  $M_{Kr} M_{SO_3} / M_{Kr-SO_3}$ ,  $I_{gg}^{(SO_3)}$  is the moment of inertia of SO<sub>3</sub> about its *g*-inertial axis, and the angular brackets denote vibrational averages. Thus, using values of  $I_{gg}^{(SO_3)}$  obtained from the observed rotational constants of free SO<sub>3</sub>,<sup>232,233</sup> values of  $\langle R_{cm}^2 \rangle^{1/2} \equiv R_{Kr-S}$  can be obtained from equation 2 once estimates of the angular vibrational amplitudes are made. For Ar-<sup>33</sup>SO<sub>3</sub>, the effective angle,  $\chi_{eff} \equiv \cos^{-1} \left( \langle \cos^2 \chi \rangle^{1/2} \right)$ , was determined<sup>234</sup> from nuclear hyperfine structure to be 15.6(+3.3/-4.8)°. Since the <sup>33</sup>S species were not observed in this work,  $\chi_{eff}$  for Kr-SO<sub>3</sub> cannot be obtained from the data but it is likely to be similar to that in Ar-SO<sub>3</sub>. Thus, the value of  $R_{Kr-S}$  was obtained from a series of nonlinear least squares fits of all the isotopic moments of inertia, with  $\chi_{eff}$  held fixed at values of 10.8°, 15.6°, and 18.9° (the range spanned by the uncertainties above). The reported value, 3.438(3) Å, is the average of the high and low values that resulted, with a quoted uncertainty representing the spread of the values obtained.

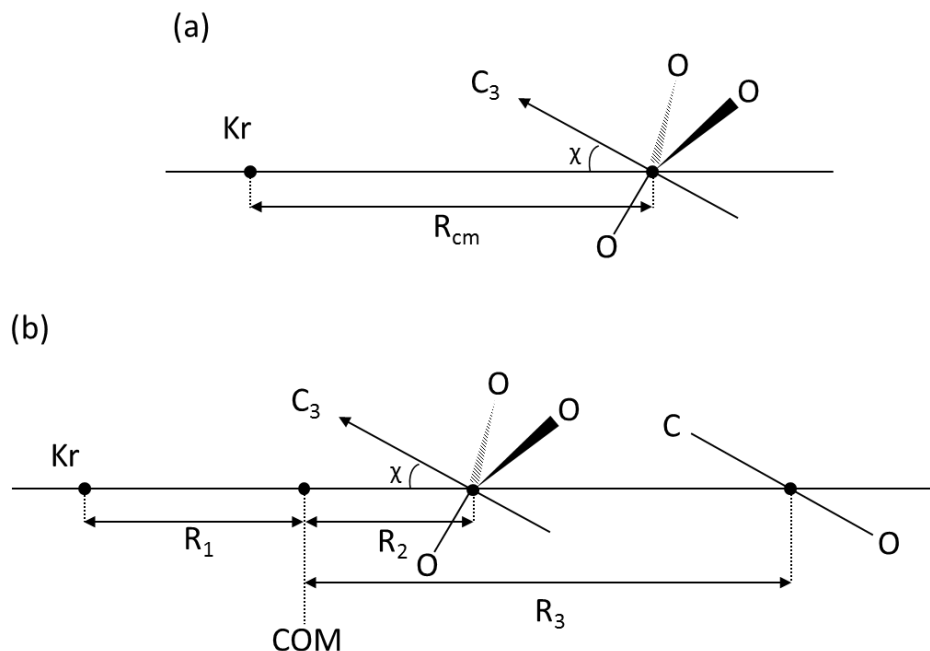


**Figure 6.2 Definition of Structural Coordinates for Kr-SO<sub>3</sub> and Kr-SO<sub>3</sub>-CO**

For Kr-SO<sub>3</sub>-CO, the vibrationally averaged moments of inertia,  $\langle I_{bb} \rangle = \langle I_{cc} \rangle$  can also be written in terms of the coordinates defined in Figure 6.2, though the expressions are somewhat more complicated:

$$\begin{aligned} \langle I_{bb} \rangle = & M_{Kr} R_1^2 + M_{SO_3} R_2^2 + M_{CO} R_3^2 + \left(\frac{1}{2}\right) I_{bb}^{(CO)} [1 + \langle \cos^2 \gamma \rangle] + \\ & \left(\frac{1}{2}\right) I_{bb}^{(SO_3)} [1 + \langle \cos^2 \chi \rangle] + \left(\frac{1}{2}\right) I_{cc}^{(SO_3)} [\langle \sin^2 \chi \rangle] \end{aligned} \quad (3)$$

$R_1$ ,  $R_2$ , and  $R_3$  are related to the Kr-S and S-C distances as follows,

$$R_1 = R_{Kr-S} - R_2 \quad (4)$$

$$R_2 = \frac{1}{M} [M_{Kr} R_{Kr-S} - M_{CO} (R_{C-S} + r_1)] \quad (5)$$

$$R_3 = R_{C-S} + R_2 + r_1 \quad (6)$$

and  $M_{Kr}$ ,  $M_{CO}$ , and  $M$  are the mass of the krypton atom, the mass of CO, and the total mass of the complex, respectively. For SO<sub>3</sub>-CO, the values of  $\chi_{eff}$  and  $\gamma_{eff}$  have been estimated to be 11.4(+4.4/-10.1)<sup>o</sup> and 6.5(1.5)<sup>o</sup>, respectively.<sup>225</sup> Using these values and

ranges, substitution of equations 4 – 6 into equation 3 allows the best values of  $R_{Kr-S}$  and  $R_{S-C}$  to be determined via a nonlinear least squares analysis of the moments of inertia for the isotopic species observed. The results are  $R_{Kr-S} = 3.488(6) \text{ \AA}$  and  $R_{C-S} = 2.871(9) \text{ \AA}$ , where the quoted uncertainties are the standard errors in the least squares analysis which, in this case, exceeded the uncertainty introduced by the ranges in the estimated values of  $\gamma_{eff}$  and  $\chi_{eff}$ . Note that the successful inclusion of  $^{13}\text{C}$  substitution data in the fit confirms that the carbon of the CO, not the oxygen, is directed toward the  $\text{SO}_3$ . The structural results for both complexes are summarized in Table 6.2, where it may be seen that the addition of CO to  $\text{Kr-SO}_3$  lengthens the  $\text{Kr-S}$  distance by  $0.050(9) \text{ \AA}$ . The structures are illustrated in Figure 6.3, which also indicates the observed values of the  $^{83}\text{Kr}$  quadrupole coupling constants.

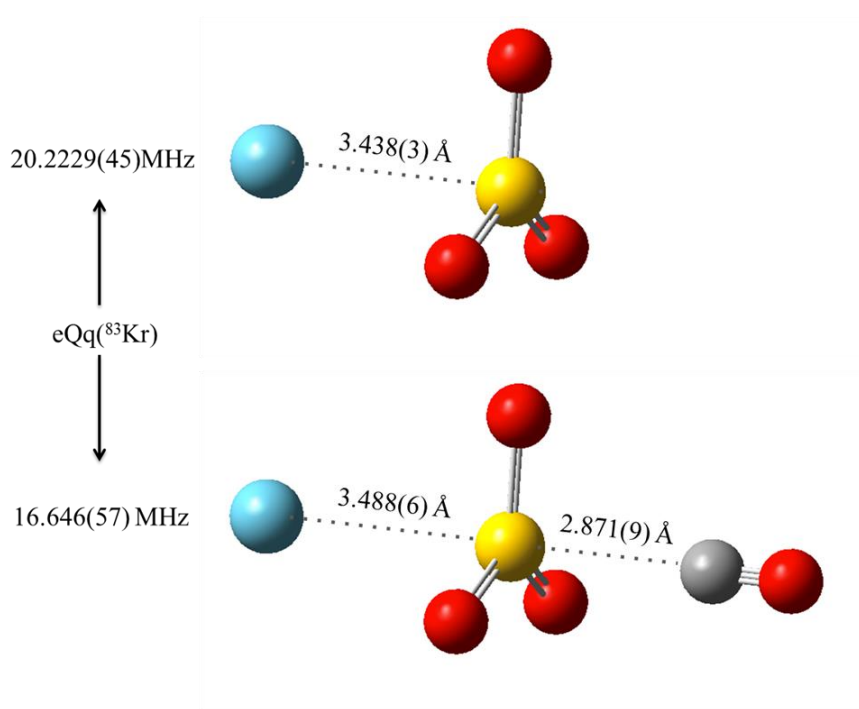


**Figure 6.3 Structural Results for  $\text{Kr-SO}_3$  and  $\text{Kr-SO}_3\text{-CO}$**

Structural results for  $\text{Kr-SO}_3$  and  $\text{Kr-SO}_3\text{-CO}$  determined from observed rotational constants, with observed  $^{83}\text{Kr}$  nuclear quadrupole coupling constants also indicated.

**Table 6.2 Experimental Structural Parameters for Kr-SO<sub>3</sub> and Kr-SO<sub>3</sub>-CO**

Structural Parameter	Kr-SO <sub>3</sub>	Kr-SO <sub>3</sub> -CO
$R_{Kr-S}$ [Å]	3.438(3)	3.488(6)
$R_{S-C}$ [Å]	–	2.871(9)
$\chi$ [deg] <sup>a</sup>	15.6(+3.3/–4.8)	11.4(+4.4/–10.1)
$\gamma$ [deg] <sup>a</sup>	–	6.5(15)

(a) Assumed value. See text for discussion.

### Theoretical Methods and Results

A striking result from Table 6.2, one which forms an important focus of this paper, is that the <sup>83</sup>Kr nuclear quadrupole coupling constant in Kr-SO<sub>3</sub> reduced by 18% upon addition of the CO to the opposite side of the SO<sub>3</sub>. In order to gain a better understanding of the origins of this effect, a series of theoretical calculations was performed using the GAMESS package of programs.<sup>235</sup> First, the geometries of both Kr-SO<sub>3</sub> and Kr-SO<sub>3</sub>-CO were optimized using density functional theory (DFT) with the M06-2X functional<sup>236</sup> and cc-pVTZ basis set. For comparison, the PBE-D<sup>237,238</sup> functional was also used with the same basis set. The important results, including van der Waals bond lengths, binding energies, and electric fields and field gradients along  $z$  at the Kr nucleus,  $E_z$  and  $q$ , respectively, are summarized in Table 6.3. The latter quantity is the  $zz$  component of the electric field gradient tensor,  $(\nabla E)_{zz}$ , where throughout this work, the positive  $z$ -axis is taken to be along the C<sub>3</sub> axis of the complex, in the direction from sulfur to krypton. Note that the measured values of “ $eQq$ ” are, in fact,  $eQq_{aa}$ , where “ $a$ ” refers to the  $a$ -inertial axis of the complex. However, since these complexes are prolate symmetric tops, and  $a$ -axis is the same as the  $z$ -axis used in the DFT calculations and thus,  $q = q_{zz} = q_{aa}$ . Therefore, theoretical values of the <sup>83</sup>Kr nuclear quadrupole constants were readily obtained by multiplying the calculated values of  $q_{zz}$ , by  $eQ$  (where  $e$  is the charge of an electron and  $Q = 0.259 \text{ b}^{239}$  is the nuclear quadrupole moment of <sup>83</sup>Kr), and converting to MHz. The binding energies in Table 6.3 were calculated with and without the counterpoise (CP) correction<sup>52</sup> for basis set superposition error (BSSE). Complete sets of Cartesian coordinates at the optimized geometries are provided in Appendix F.

**Table 6.3 Properties of Kr-SO<sub>3</sub> and Kr-SO<sub>3</sub>-CO**

<b>Kr-SO<sub>3</sub></b>					
Parameter	M06-2X/ cc-pVTZ <sup>a</sup>	%Error	PBE-D/ cc-pVTZ <sup>b</sup>	%Error	Experiment
$R_{Kr-S}$ (Å)	3.298	-4.1%	3.495	+1.7%	3.438(3)
BE (kcal/mol) <sup>c</sup>	1.30(1.57)		1.38(1.61)		
$E_z$ (au) <sup>d</sup>	0.002895		0.001935		
$q$ (au) <sup>d</sup>	-0.459282		-0.360867		
$eQq$ (MHz) <sup>e</sup>	27.95	+38%	21.96	+8.6%	20.2229(45)
<b>Kr-SO<sub>3</sub>-CO</b>					
$R_{Kr-S}$ (Å)	3.341	-4.2%	3.572	+2.4%	3.488(6)
$R_{S-C}$ (Å)	2.834	-1.3%	2.742	-4.5%	2.871(9)
BE (kcal/mol) <sup>c</sup>	4.06(4.46)		3.80(4.40)		
$E_z$ (au) <sup>d</sup>	0.002412		0.001336		
$q$ (au) <sup>d</sup>	-0.387885		-0.257832		
$eQq$ (MHz) <sup>e</sup>	23.61	+42%	15.69	-5.7%	16.646(57)

(a) Calculated at the DFT level with the M06-2X functional and cc-pVTZ basis set.

(b) Calculated at the PBE-D functional and cc-pVTZ basis set.

(c) The binding energy for Kr-SO<sub>3</sub> is relative to Kr + SO<sub>3</sub>. The binding energy for Kr-SO<sub>3</sub>-CO is relative to Kr-SO<sub>3</sub> + CO. Values not in parentheses are CP corrected. Values in parentheses are uncorrected for basis set superposition error.

(d) Electric fields and electric field gradients are at the Kr nucleus. The positive  $z$  direction is along a vector from S to Kr.  $q$  is equal to the  $zz$  component of the electric field gradient tensor.

(e) Nuclear quadrupole coupling constant for the <sup>83</sup>Kr isotopologues was calculated using a <sup>83</sup>Kr nuclear quadrupole moment of 0.259 b [Ref. 239].

Although not included in Table 6.3, the binding energy of SO<sub>3</sub>-CO was also determined for later use in assessing the degree to which the constituent dimer bond energies are additive. Using the M06-2X and PBE-D functionals, with corrections for BSSE, the binding energies of CO-SO<sub>3</sub> relative to CO + SO<sub>3</sub> are 4.16 kcal/mol and 4.00 kcal/mole, respectively. These are in good agreement with the 3.92 kcal/mol value previously obtained from CP-corrected MP2/aug-cc-pVTZ calculations.<sup>225</sup> The calculated S-C weak bond distances are 2.834 Å and 2.742 Å with the M06-2X and PBE-D functionals, respectively, both in reasonable agreement with the experimental value of 2.854(12) Å.<sup>225</sup>

Examination of Table 6.3 reveals that overall, the PBE-D functional performs better for Kr-SO<sub>3</sub> and Kr-SO<sub>3</sub>-CO in terms of reproducing the experimentally determined quantities (i.e., weak bond lengths and nuclear quadrupole coupling constants). For

example, the Kr–S bond distances obtained using the PBE-D functional are within 2.5% of the experimental values for Kr–SO<sub>3</sub> and Kr–SO<sub>3</sub>–CO, respectively, while those obtained from the M06-2X are both smaller than the experimental values by about 4%.<sup>240</sup> Only the S–C distance in Kr–SO<sub>3</sub>–CO is better reproduced by the M06-2X functional. For the <sup>83</sup>Kr quadrupole coupling constants, the M06-2X results are 38-42% too large, while those obtained with the PBE-D function are within ~9% of the experimental values (9% high for the dimer and 6% low for the trimer).

The reduction in  $eQq$  of the <sup>83</sup>Kr upon addition of CO is consistent with the observed lengthening of the Kr–S bond since it is clear that in the limit of infinite separation, the krypton atom is spherically symmetric and thus the electric field gradient at the nucleus is identically zero. In order to provide a more detailed physical description of this effect, block-localized wavefunction (BLW) computations were performed. The BLW method is the most efficient variant of the *ab initio* valence bond (VB) theory<sup>219-221</sup> and can define electron localized states self-consistently. Further, the intermolecular interaction can be decomposed into a few physically meaningful contributions from geometric distortion, electrostatic interactions (including Pauli exchange), polarization, and electron transfer effects.<sup>241,242</sup> Calculations were done using both the M06-2X and PBE-D functionals, but in light of the superior performance of the latter in reproducing the observed quadrupole coupling constants, only the PBE-D results are reported here. The results with the M06-2X functional, though quantitatively somewhat different, were qualitatively very similar to those described below.

Detailed descriptions of the BLW method and its implementation are given elsewhere.<sup>219-221,241-243</sup> Briefly, the formation of a complex is envisioned as taking place via a sequence of well-defined steps. First, calculations are performed for the isolated moieties at their optimized geometries in the complex. Any changes in physical properties relative to those of the fully optimized moieties provide a measure of the components of the overall interaction that are due to geometrical distortion of the individual moieties upon complexation. Next, the moieties are brought together without disturbing their individual electron densities, and an initial block-localized wavefunction is constructed. Here, any

change in the energy, electric field, or electric field gradient is attributed to the mutual electrostatic interaction (including Pauli repulsion). In a third step, electron distributions of the individual moieties are allowed to relax in response to the electric field of the interacting partner, but without electron transfer between them, and the resulting changes correspond to the contributions from polarization. Finally, electrons are allowed to flow freely between the interacting species, yielding a final state in which molecular orbitals are delocalized over the entire system. The changes in calculated properties incurred in this step correspond to the contributions from electron transfer.

Of interest for Kr–SO<sub>3</sub> and Kr–SO<sub>3</sub>–CO are values of the z-components of the electric field,  $E_z$ , and electric field gradient,  $q$ , at the Kr nucleus. As noted above, the positive z-axis is defined here to be along the vector pointing from S to Kr and, for a free krypton atom, the values of  $E_z$  and  $q$  are identically zero. Upon formation of a complex, no structural change is possible in the Kr and thus, any changes in the Kr–SO<sub>3</sub> attributable to geometrical distortion can only arise from deformation of the SO<sub>3</sub>. For Kr–SO<sub>3</sub>, however, these turn out to be negligible. Thus, the first significant step in the decomposition corresponds to bringing the two moieties together and determining the electrostatic term. The remaining contributions to  $E_z$  and  $q$  from polarization and electron transfer were calculated as described above, and the results are given in Table 6.4. Also included in the table are the energetic changes which occur at each step of the BLW decomposition, as well as the <sup>83</sup>Kr nuclear quadrupole coupling constants.

For Kr–SO<sub>3</sub>–CO, the isolated moieties correspond to Kr–SO<sub>3</sub> and CO, and the resulting decomposition provides a description of the effect of the CO on the Kr–SO<sub>3</sub>. Here, geometry change within the Kr–SO<sub>3</sub> unit is more significant, and largely corresponds to the lengthening of the Kr–S van der Waals bond length which is both observed experimentally and reproduced theoretically. The results of the BLW decomposition are also given in Table 6.4.

BLW calculations on the SO<sub>3</sub>–CO complex were also performed for completeness. The complex does not contain quadrupolar nuclei and thus electric fields and electric field



gradients were not determined. However, a decomposition of the binding energy is meaningful. The contributions to the overall binding energy of the complex at the PBE-D/cc-pVTZ level are as follows: Geometry change (0.17 kcal/mol); Electrostatic/Pauli (4.22 kcal/mol); Polarization (−1.44 kcal/mol); Electron transfer (−6.95 kcal/mol). With the largest contributions arising from the electrostatic/Pauli and electron transfer terms, these values sum to the overall binding energy of −4.00 kcal/mol value given above. Note that this value is the result of significant cancellation among contributing terms.

**Table 6.4 BLW Decomposition Results for Kr-SO<sub>3</sub> and Kr-SO<sub>3</sub>-CO<sup>a</sup>**

	$E_z$ (a.u.) <sup>b</sup>	$q$ (a.u.) <sup>b</sup>	$eQq$ (MHz)	Energy Change (kcal/mol) <sup>c</sup>
<b>Kr-SO<sub>3</sub></b>				
Isolated Kr	0	0	0	
Geometry Change <sup>d</sup>	0	0	0	0.00
Electrostatic/Pauli <sup>e</sup>	0.005885	0.080789	−4.92	−0.11
Polarization <sup>f</sup>	0.001537	−0.167596	10.20	−0.20
Electron transfer <sup>g</sup>	0.001935	−0.360867	21.96	−1.07
<b>Kr-SO<sub>3</sub>-CO</b>				
Optimized Kr-SO <sub>3</sub>	0.001935	−0.360867	21.96	
Geometry Change <sup>h</sup>	0.001745	−0.310417	18.89	0.18
Electrostatic/Pauli <sup>i</sup>	0.001303	−0.306393	18.65	3.72
Polarization <sup>f</sup>	0.001459	−0.269893	16.42	−1.30
Electron transfer <sup>g</sup>	0.001336	−0.257832	15.69	−6.40

(a) Calculated at the DFT level with the PBE-D functional and cc-pVTZ basis set.

(b) Electric fields and electric field gradients are at the Kr nucleus. The positive  $z$  direction is from S to Kr.

(c) Change relative to previous row.

(d) Separated Kr and SO<sub>3</sub> with SO<sub>3</sub> at its geometry in the Kr-SO<sub>3</sub> dimer.

(e) Kr and SO<sub>3</sub> brought together at the Kr-SO<sub>3</sub> geometry without perturbation of the individual moieties' electron densities.

(f) Polarization allowed, but no electron transfer.

(g) Electron transfer between moieties permitted.

(h) Separated Kr-SO<sub>3</sub> and CO at their geometries in the Kr-SO<sub>3</sub>-CO trimer.

(i) Kr-SO<sub>3</sub> and CO brought together at the Kr-SO<sub>3</sub>-CO geometry without perturbation of their individual electron densities.

Both the polarization and electron transfer effects can be visualized by electron density difference (EDD) maps, which are shown in Figure 6.4. Figures 6.4a and 6.4b depict changes occurring when the Kr-SO<sub>3</sub> complex is formed. Figures 6.4c and 6.4d show the

changes in Kr–SO<sub>3</sub> and CO resulting from their union to form the trimer. The red and blue regions of the maps refer to gain and loss of electron density, respectively. It is apparent that both polarization and electron transfer cause significant redistribution of electron density on the krypton atom upon formation of Kr–SO<sub>3</sub>. On the other hand, upon addition of CO to Kr–SO<sub>3</sub>, polarization produces much larger changes in the electron density on krypton than does electron transfer, which is not even visible on the diagram. However, significant changes can be seen on the SO<sub>3</sub> and CO moieties from both polarization and electron transfer.

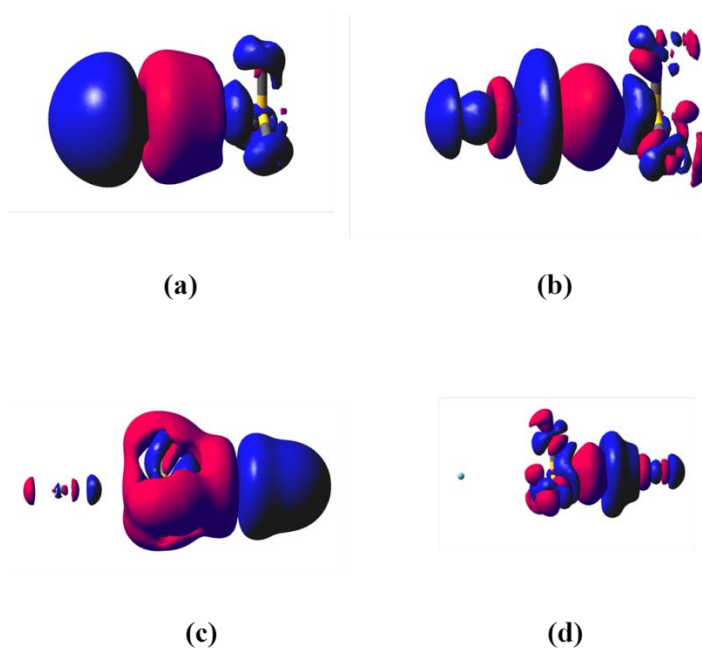


**Figure 6.4 Electron Density Difference (EDD) maps**

Electron density difference (EDD) maps showing the electron density changes due to polarization (left) and electron transfer (right). (a,b) represent Kr + SO<sub>3</sub>; (c,d) represent Kr–SO<sub>3</sub> + CO. The isovalue in all plots is 0.0001 a.u.

### Discussion

The basic structural features of Kr–SO<sub>3</sub> and Kr–SO<sub>3</sub>–CO are in accord with expectation. The rare gas – sulfur distance in Kr–SO<sub>3</sub> is longer than that in Ar–SO<sub>3</sub><sup>229</sup> by about 0.088(4) Å, an amount that lies well within the range of expectation based on standard tables of van der Waals radii.<sup>244</sup> Moreover, as in the case of Ar–SO<sub>3</sub>, the rare gas – sulfur distance increases slightly upon addition of the CO (0.061 ± 0.012 Å for Ar–SO<sub>3</sub> vs.

0.050 ± 0.009 Å for Kr–SO<sub>3</sub>) while S–C distance shows no change within the estimated uncertainty upon addition of either Ar or Kr. As we have noted previously,<sup>225</sup> it is sensible that the weak interaction of the SO<sub>3</sub> with a rare gas would have negligible effect on the SO<sub>3</sub>–CO interaction, while the more strongly interacting CO would compete with, and therefore weaken, the rare gas–SO<sub>3</sub> interaction. Still, however, the observed changes are small and to a large extent, the two sides of the trimer show evidence of only very minor structural perturbation resulting from the presence of a binding partner on the other side.

Comparison of the calculated binding energies also shows that the two halves of the dimer are essentially independent. Using the PBE-D functional with a cc-pVTZ basis set, CP-corrected the binding energy of Kr–SO<sub>3</sub>–CO relative to Kr + SO<sub>3</sub> + CO is 5.18 kcal/mol, which is just 0.20 kcal/mol smaller than the sum of the binding energies for Kr–SO<sub>3</sub> (1.38 kcal/mol) and SO<sub>3</sub>–CO (4.00 kcal/mol). At the M06-2X/cc-pVTZ level, the additivity is even better, with the CP-corrected binding energy of the trimer (5.36 kcal/mol) only 0.10 kcal/mol less than the sum of the Kr–SO<sub>3</sub> and SO<sub>3</sub>–CO binding energies at the same level (1.30 and 4.16 kcal/mol, respectively). Thus, to a very good approximation, the binding energies are additive.

While the structures and binding energies appear to indicate negligible communication between Kr and CO across the SO<sub>3</sub> moiety, the <sup>83</sup>Kr quadrupole coupling constants offer a distinctly different picture. In particular, the addition of CO to <sup>83</sup>Kr–SO<sub>3</sub> produces a reduction of 18% in the nuclear quadrupole coupling constant. Since Kr is an atom, this reduction must arise solely from electronic effects (i.e., real changes in the electric field gradient at the Kr), as it can have no projective contributions due to changes in vibrational bending amplitude. Moreover, since the electric field gradient is identically zero in the free atom, the quadrupole coupling constants fully represent the changes that take place upon complexation. Note that the large change in the coupling constant is not inconsistent with the small bond length change and additive binding energies noted above. Rather, it reflects an exquisite sensitivity of the quadrupole coupling constants to subtle changes in the electron distribution, measured against what is, in effect, a “zero-

background” (i.e., the zero value of the quadrupole coupling constant of a free  $^{83}\text{Kr}$  atom).

Some perspective on the absolute magnitude of the  $^{83}\text{Kr}$  quadrupole coupling constants in  $\text{Kr-SO}_3$  and  $\text{Kr-SO}_3\text{-CO}$  can be gained by comparison with quadrupole coupling data obtained by Gerry and coworkers for a series of metal-halide containing systems. Complexes of Kr with  $\text{CuF}$ ,<sup>245</sup>  $\text{AgF}$ ,<sup>246</sup>  $\text{AuF}$ <sup>246</sup>, for example, have been examined, and convincing arguments based on bond lengths, stretching force constants, and quadrupole coupling constants, have led to the remarkable conclusion that the Kr – metal bonds in these systems are best described as weak *chemical* bonds. The  $^{83}\text{Kr}$  quadrupole coupling constants are 128.79 MHz, 105.401 MHz, and 189.97 MHz in  $^{83}\text{KrCuF}$ ,  $^{83}\text{KrAgF}$ , and  $^{83}\text{KrAuF}$ , respectively, values which are significantly larger than those observed here. This underscores the conclusion from both binding energies and bond lengths that  $\text{Kr-SO}_3$  and  $\text{Kr-SO}_3\text{-CO}$  are “weakly bound”. Still, however, the perturbation of the electronic environment at the Kr in these complexes is not insignificant, amounting to 9 – 19% of that observed in the case of the Kr-metal bonds. In contrast, the  $^{83}\text{Kr}$  quadrupole coupling constant in  $\text{Kr-HCl}$ <sup>247</sup> is only 5.2 MHz, or about 3 – 5% of the values in the Kr-metal bonds.

The remaining question to be answered from this work concerns the physical origins of the observed coupling constants and here, the BLW decomposition is most useful. Figures 6.5 and 6.6 graphically display the physical contributions to  $E_z$  and  $q$  (plotted as  $eQq$ ) that are given in Table 6.4. For  $\text{Kr-SO}_3$ ,  $E_z$  contains a large, positive contribution from the electrostatic/Pauli repulsion term, which is then substantially reduced by polarization. Electron transfer increases the field somewhat, but only slightly. The quadrupole coupling constant, on the other hand, has a moderate, negative contribution from the electrostatic/Pauli term, which is then rendered positive by large contributions from both polarization and electron transfer.

The addition of CO to  $\text{Kr-SO}_3$  decreases both the electric field and the quadrupole coupling constant at the krypton nucleus, but for somewhat different reasons. The

reduction in  $E_z$  at Kr upon addition of CO is seen to arise predominantly from a combination of distortion (i.e., lengthening of the Kr–S bond) and electrostatic terms, with polarization and electron transfer producing smaller contributions which almost exactly cancel. For the quadrupole coupling constant, all four terms work in concert to reduce the value relative to that in Kr–SO<sub>3</sub>. However, the dominant contributions come from geometrical distortion and polarization, with much smaller electrostatic and electron transfer terms.

It is clear that the individual physical effects described above combine in a rather complicated way to produce the observed quadrupole coupling constants and the calculated electric field strengths. Thus, a simple picture based on the action of the SO<sub>3</sub> quadrupole moment and/or the SO<sub>3</sub>–CO dipole moment on a polarizable krypton atom is insufficient to understand the observed coupling constants. This is in contrast with the complexes Kr–HCl and Kr–HCN, for which the <sup>83</sup>Kr coupling constants were directly proportional to the electric field gradient at the Kr nucleus calculated from electric multipole moments of the binding partners.<sup>247</sup> It is interesting to note that, while a direct relationship between electron transfer and binding energy is not necessarily guaranteed,<sup>248,249</sup> the electron transfer is a major contributor to the overall binding energies of both Kr–SO<sub>3</sub> and Kr–SO<sub>3</sub>–CO (Table 6.4). In contrast, however, while it plays a significant role in determining the electric field *gradient* at the Kr, it is only a minor contributor to the electric field itself, as well as to the changes incurred by addition of CO to the dimer.

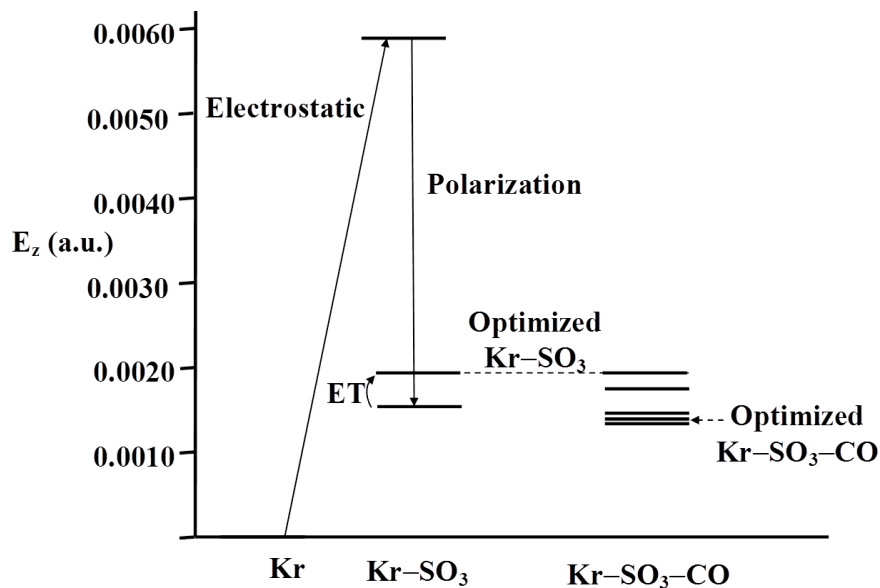


**Figure 6.5 Summary of the BLW Decomposition of  $E_z$  at the Kr Nucleus**

Diagram summarizing the BLW decomposition of the  $z$ -component of the electric field at the Kr nucleus. The arrows depict the sequence of electric field values computed at successive stages of the BLW decomposition, starting from Kr and proceeding to Kr-SO<sub>3</sub> and Kr-SO<sub>3</sub>-CO. The various physical components are labeled, except for Kr-SO<sub>3</sub>-CO in the top half of the diagram. The bottom half is an expanded view of the Kr-SO<sub>3</sub>-CO diagram which provides space for clear labeling.

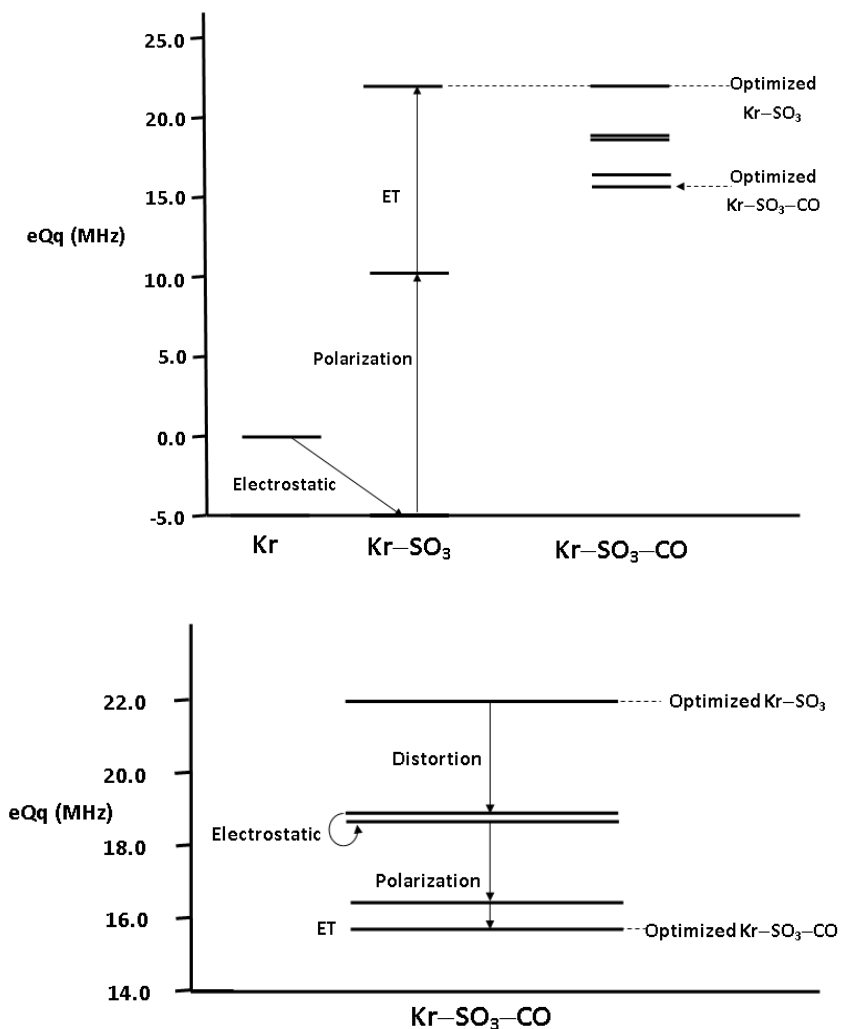


**Figure 6.6 Summary of the BLW Decomposition of  $eQq$  of  $^{83}\text{Kr}$**

Diagram summarizing the BLW decomposition of the  $zz$ -component of the  $^{83}\text{Kr}$  nuclear quadrupole coupling constant, obtained from computed values of  $q$ . The arrows depict the sequence of values computed at successive stages of the BLW decomposition, starting from Kr and proceeding to Kr-SO<sub>3</sub> and Kr-SO<sub>3</sub>-CO. The various physical components are labeled, except for Kr-SO<sub>3</sub>-CO in the top half of the diagram. The bottom half is an expanded view of the Kr-SO<sub>3</sub>-CO diagram which provides space for clear labeling.

## Conclusion

The complexes Kr-SO<sub>3</sub> and Kr-SO<sub>3</sub>-CO have been studied experimentally by rotational spectroscopy and theoretically by the Block Localized Wavefunction (BLW) decomposition method. In Kr-SO<sub>3</sub>-CO, the Kr and the CO approach the SO<sub>3</sub> from opposite sides, forming a C<sub>3v</sub> symmetric complex. The Kr-S and S-C distances are very similar to those in Kr-SO<sub>3</sub> and SO<sub>3</sub>-CO, respectively, and the binding energy of the trimer is very nearly equal to the sum of the binding energies for Kr-SO<sub>3</sub> and SO<sub>3</sub>-CO. Thus, from both structural and energetic perspectives, the interactions on the two sides of the SO<sub>3</sub> appear to be independent. Measurements of the <sup>83</sup>Kr nuclear quadrupole coupling constants, however, demonstrate that the electric field gradient at the Kr in Kr-SO<sub>3</sub> is reduced by 18% upon addition of the CO to the other side of the SO<sub>3</sub>. Theoretical calculations indicate that both the electric field and the electric field gradient at the Kr are reduced by the presence of CO but that the reductions occur for different reasons. For the electric field, the effect is mainly electrostatic, accounting for ~75% of the reduction. For the electric field gradient, polarization and lengthening of the Kr-S bond make the primary contributions.

## Acknowledgement

This work was supported by the National Science Foundation, grant Nos. CHE 0845290 and CHE 1055310 .



## References

---

1. Leopold, K. R. Hydrated Acid Clusters. *Annu. Rev. Phys. Chem.* **2011**, *62*, 327.
2. Pradzynski, C. C.; Forck, R. M.; Zeuch, T.; Slaviček, P.; Buck, U. A fully size-resolved perspective on the crystallization of water clusters. *Science* **2012**, *337*, 1529.
3. Balle, T. J.; Flygare, W. H. Fabry–Perot Cavity Pulsed Fourier Transform Microwave Spectrometer with a Pulsed Nozzle Particle Source. *Rev. Sci. Instrum.* **1981**, *52*, 33.
4. Brown, G. G.; Dian, B. C.; Douglass, K. O.; Geyer, S. M.; Shipman, S. T.; Pate, B. H. A Broadband Fourier Transform Microwave Spectrometer Based on Chirped Pulse Excitation. *Rev. Sci. Instrum.* **2008**, *79*, 053103.
5. Dewberry, C. T.; Mackenzie, R. B.; Green, S.; Leopold, K. R. 3D-Printed Slit Nozzles for Fourier Transform Microwave Spectroscopy. *Rev. Sci. Instrum.* **2015**, *86*, 065107.
6. Kulmala, M.; Petäjä, T.; Ehn, M.; Thornton, J.; Sipilä, M.; Worsnop, D. R.; Kerminen, V.-M. Chemistry of Atmospheric Nucleation: On the Recent Advances on Precursor Characterization and Atmospheric Cluster Composition in Connection with Atmospheric New Particle Formation. *Annu. Rev. Phys. Chem.* **2014**, *65*, 21–37.
7. IPCC, Contribution of Working Group I to the Fourth Assessment Report of the Intergovernmental Panel on Climate Change, S. Solomon *et al.*, Eds. (Cambridge Univ. Press, Cambridge, UK), [www.ipcc.ch/ipccreports/ar4-wg1.htm](http://www.ipcc.ch/ipccreports/ar4-wg1.htm) (2007).
8. Morokuma, K.; Muguruma, C. Ab Initio Molecular Orbital Study of the Mechanism of the Gas Phase Reaction  $\text{SO}_3 + \text{H}_2\text{O}$ : Importance of the Second Water Molecule. *J. Am. Chem. Soc.* **1994**, *116*, 10316–10317.
9. Zhang, R.; Suh, I.; Zhao, J.; Zhang, D.; Fortner, E. C.; Tie, X.; Molina, L. T.; Molina, M. J. Atmospheric New Particle Formation Enhanced by Organic Acids. *Science* **2004**, *304*, 1487–1490.
10. Barsanti, K. C.; McMurry, P. H.; Smith, J. N. The Potential Contribution of Organic Salts to New Particle Growth. *Atmos. Chem. Phys.* **2009**, *9*, 2949–2957.
11. Smith, J. N.; Barsanti, K. C.; Friedli, H. R.; Ehn, M.; Kulmala, M.; Collins, D. R.; Jacob, H. Observations of Ammonium Salts in Atmospheric Nanoparticles and Possible Climatic Implications. *Proc. Natl. Acad. Sci. U. S. A.* **2010**, *107*, 6634–6639.
12. Mackenzie, R. B.; Dewberry, C. T.; Leopold, K. R. Gas Phase Observation and Microwave Spectroscopic Characterization of Formic Sulfuric Anhydride. *Science* **2015**, *349*, 58–61.

- 
13. Mackenzie, R. B.; Dewberry, C. T.; Leopold, K. R. The Trimethylamine-Formic Acid Complex: Microwave Characterization of a Prototype for Potential Precursors to Atmospheric Aerosol. *J. Phys. Chem. A* **2016**, *120*, 2268–2273.
  14. Mackenzie, R. B.; Dewberry, C. T.; Leopold, K. R. The Formic Acid-Nitric Acid Complex: Microwave Spectrum, Structure, and Proton Transfer. *J. Phys. Chem. A* **2014**, *118*, 7975–7985.
  15. Mackenzie, R. B.; Dewberry, C. T.; Coulston, E.; Cole, G. C.; Legon, A. C.; Tew, D. P.; Leopold, K. R. Intramolecular Competition between n-Pair and  $\pi$ -Pair Hydrogen Bonding: Microwave Spectrum and Internal Dynamics of the Pyridine-Acetylene Hydrogen-Bonded Complex. *J. Chem. Phys.* **2015**, *143*, 104309.
  16. Bentley, R.; Chasteen, T. G. Environmental VOSCs--Formation and Degradation of Dimethyl Sulfide, Methanethiol and Related Materials. *Chemosphere* **2004**, *55*, 291–317.
  17. Kolb, C. E.; Jayne, J. T.; Worsnop, D. R.; Molina, M. J.; Meads, R. F.; Viggiano, A. A. Gas Phase Reaction of Sulfur Trioxide with Water Vapor. *J. Am. Chem. Soc.* **1994**, *116*, 10314–10315.
  18. Hazra, M. K.; Sinha, A. Formic Acid Catalyzed Hydrolysis of SO<sub>3</sub> in the Gas Phase : A Barrierless Mechanism for Sulfuric Acid Production of Potential Atmospheric Importance. *J. Am. Chem. Soc.* **2011**, *133*, 17444–17453.
  19. O'Dowd, C. D.; Aalto, P.; Hämeri, K.; Kulmala, M.; Hoffmann, T. Atmospheric Particles from Organic Vapours. *Nature* **2002**, *416*, 497–498.
  20. Elm, J.; Kurte, T.; Bilde, M.; Mikkelsen, K. V. Molecular Interaction of Pinic Acid with Sulfuric Acid : Exploring the Thermodynamic Landscape of Cluster Growth. *J. Phys. Chem. A* **2014**, *118*, 7892–7900.
  21. Nadykto, A. B.; Yu, F. Strong Hydrogen Bonding between Atmospheric Nucleation Precursors and Common Organics. *Chem. Phys. Lett.* **2007**, *435*, 14–18.
  22. Zhang, R.; Wang, L.; Khalizov, A. F.; Zhao, J.; Zheng, J.; McGraw, R. L.; Molina, L. T. Formation of Nanoparticles of Blue Haze Enhanced by Anthropogenic Pollution. *Proc. Natl. Acad. Sci. U. S. A.* **2009**, *106*, 17650–17654.
  23. Metzger, A.; Verheggen, B.; Dommen, J.; Duplissy, J.; Prevot, A. S. H.; Weingartner, E.; Riipinen, I.; Kulmala, M.; Spracklen, D. V.; Carslaw, K. S.; et al. Evidence for the Role of Organics in Aerosol Particle Formation under Atmospheric Conditions. *Proc. Natl. Acad. Sci. U. S. A.* **2010**, *107*, 6646–6651.

- 
24. Paasonen, P.; Nieminen, T.; Asmi, E.; Manninen, H. E.; Petäjä, T.; Plass-Dülmer, C.; Flentje, H.; Birmili, W.; Wiedensohler, a.; Hörrak, U.; et al. On the Roles of Sulphuric Acid and Low-Volatility Organic Vapours in the Initial Steps of Atmospheric New Particle Formation. *Atmos. Chem. Phys.* **2010**, *10*, 11223–11242.
25. Riipinen, I.; Yli-Juuti, T.; Pierce, J. R.; Petäjä, T.; Worsnop, D. R.; Kulmala, M.; Donahue, N. M. The Contribution of Organics to Atmospheric Nanoparticle Growth. *Nat. Geosci.* **2012**, *5*, 453–458.
26. Schobesberger, S.; Junninen, H.; Bianchi, F.; Lönn, G.; Ehn, M.; Lehtipalo, K.; Dommen, J.; Ehrhart, S.; Ortega, I. K.; Franchin, A.; et al. Molecular Understanding of Atmospheric Particle Formation from Sulfuric Acid and Large Oxidized Organic Molecules. *Proc. Natl. Acad. Sci. U. S. A.* **2013**, *110*, 17223–17228.
27. Finlayson-Pitts, B. J.; Pitts, J. N. J. *Chemistry of the Upper and Lower Atmosphere*; 6th ed.; Academic Press: San Diego, California, 2000.
28. Phillips, J. A.; Goodfriend, H.; Leopold, K. R.; Canagaratna, M. Microwave Detection of a Key Intermediate in the Formation of Atmospheric Sulfuric Acid: The Structure of H<sub>2</sub>O-SO<sub>3</sub>. *J. Phys. Chem.* **1995**, *99*, 501–504.
29. Fiacco, D. L.; Hunt, S. W.; Leopold, K. R. Microwave Investigation of Sulfuric Acid Monohydrate. *J. Am. Chem. Soc.* **2002**, *124*, 4504–4511.
30. Sedo, G.; Doran, J. L.; Leopold, K. R. Partial Proton Transfer in the Nitric Acid Trihydrate Complex. *J. Phys. Chem. A* **2009**, *113*, 11301–11310 and references therein.
31. Phillips, J. A.; Canagaratna, M.; Goodfriend, H.; Grushow, A.; Almlöf, J.; Leopold, K. R. Microwave and Ab Initio Investigation of HF-BF<sub>3</sub>. *J. Am. Chem. Soc.* **1995**, *117*, 12549–12556.
32. Methods and materials are provided in Appendix A.
33. We note that since formic acid inevitably contains water, experiments do not definitively establish whether the transformation of SO<sub>3</sub> + HCOOH occurs directly or whether an additional water molecule participates. However, the theoretical results of this work suggest that the reaction is possible without such assistance.
34. Gordy, W.; Cook, R. L. *Microwave Molecular Spectra*; Third.; John Wiley & Sons: New York, 1984.
35. van Peski, A.J.; Sur les Anhydrides Mixtes D'Acide Sulfurique et de Carboacides. *Rec. Trav. Chim.* **1921**, *40*, 103-118.

- 
36. Russell, J.; Cameron, A. E. Acidity Measurements with the Hydrogen Electrode in Mixtures of Acetic Acid and Acetic Anhydride. *J. Am. Chem. Soc.* **1938**, *60*, 1345–1348.
37. Tanghe, L. J.; Brewer, R. J. Equilibrium between Sulfuric and Acetylsulfuric Acids. *Anal. Chem.* **1968**, *40*, 350–353.
38. Burdick, D.C. *Process for the Preparation of Isoflavones*, World Intellectual Property Organization, International Bureau, International Publication Number WO 02/085881 A1 (2002).
39. Neese, F.; Valeev, E. F. Revisiting the Atomic Natural Orbital Approach for Basis Sets: Robust Systematic Basis Sets for Explicitly Correlated and Conventional Correlated Ab Initio Methods. *J. Chem. Theory Comput.* **2011**, *7*, 33–43.
40. Keller, J. W.; Harrod, B. L.; Chowdhury, S. A. Theoretical Study of Formic Acid - Sulfur Dioxide Dimers. *J. Phys. Chem. A* **2010**, *114*, 13182–13188.
41. Benkovic, S. J.; Hevey, R. C. Studies in Sulfate Esters. V. The Mechanism of Hydrolysis of Phenyl Phosphosulfate, a Model System for 3'-Phosphoadenosine 5'-Phosphosulfate. *J. Am. Chem. Soc.* **1970**, *92*, 4971–4977.
42. Ehn, M.; Thornton, J. A.; Kleist, E.; Sipilä, M.; Junninen, H.; Pullinen, I.; Springer, M.; Rubach, F.; Tillmann, R.; Lee, B.; et al. A Large Source of Low-Volatility Secondary Organic Aerosol. *Nature* **2014**, *506*, 476–479.
43. Berndt, T.; Stratmann, F.; Brüsel, S.; Heintzenber, J.; Laaksonen, A.; Kulmala, M. SO<sub>2</sub> Oxidation Products Other than H<sub>2</sub>SO<sub>4</sub> as a Trigger of New Particle Formation . Part 1 : Laboratory Investigations. *Atmos. Chem. Phys.* **2008**, *8*, 6365–6374.
44. Smith, J. N.; Dunn, M. J.; VanReken, T. M.; Iida, K.; Stolzenburg, M. R.; McMurry, P. H.; Huey, L. G. Chemical Composition of Atmospheric Nanoparticles Formed from Nucleation in Tecamac, Mexico: Evidence for an Important Role for Organic Species in Nanoparticle Growth. *Geophys. Res. Lett.* **2008**, *35*, L04808.
45. Angelino, S.; Suess, D. T.; Prather, K. A. Formation of Aerosol Particles from Reactions of Secondary and Tertiary Alkylamines: Characterization by Aerosol Time-of-Flight Mass Spectrometry. *Environ. Sci. Technol.* **2001**, *35*, 3130–3138.
46. Chebbi, A.; Carlier, P. Carboxylic Acids in the Troposphere, Occurrence, Sources, and Sinks: A Review. *Atmos. Environ.* **1996**, *30*, 4233–4249.
47. Chen, M.; Titcombe, M.; Jiang, J.; Jen, C.; Kuang, C.; Fischer, M. L.; Eisele, F. L.; Siepmann, J. I.; Hanson, D. R.; Zhao, J.; et al. Acid-Base Chemical Reaction Model for

- 
- Nucleation Rates in the Polluted Atmospheric Boundary Layer. *Proc. Natl. Acad. Sci. U. S. A.* **2012**, *109*, 18713–18718.
48. Yli-Juuti, T.; Barsanti, K.; Hildebrandt Ruiz, L.; Kieloaho, a.-J.; Makkonen, U.; Petäjä, T.; Ruuskanen, T.; Kulmala, M.; Riipinen, I. Model for Acid-Base Chemistry in Nanoparticle Growth (MABNAG). *Atmos. Chem. Phys.* **2013**, *13*, 12507–12524.
49. Phillips, J. A. *Structure and Dynamics of Partially Bound Molecular Complexes*. Ph. D. Thesis. University of Minnesota, Minneapolis, MN; 1996.
50. Canagaratna, M.; Phillips, J. A.; Goodfriend, H.; Leopold, K. R. Structure and Bonding of the Sulfamic Acid Zwitterion: Microwave Spectrum Of  $^+H_3N-SO_3^-$ . *J. Am. Chem. Soc.* **1996**, *118*, 5290–5295.
51. Liljefors, T.; Norrby, P. An Ab Initio Study of the Trimethylamine - Formic Acid and the Trimethylammonium Ion - Formate Anion Complexes , Their Monohydrates , and Continuum Solvation. **1997**, 7863, 1052–1058.
52. Boys, S.F.; Bernardi, F. The Calculation of Small Molecular Interactions by the Differences of Separate Total Energies. Some Procedures with Reduced Errors. *Mol. Phys.* **1970**, *19*, 553-566.
53. Computationally derived geometries reported in this paper are corrected for basis set superposition error.
54. Lide, D. R.; Mann, D. E. Microwave Spectra of Molecules Exhibiting Internal Rotation. III. Trimethylamine. *J. Chem. Phys.* **1958**, *28*, 572.
55. Weber, W. H.; Maker, P. D.; Johns, J. W. C.; Weinberger, E. Sub-Doppler Laser-Stark and High-Resolution Fourier Transform Spectroscopy of the  $\nu_3$  Band of Formic Acid. *J. Mol. Spectrosc.* **1987**, *121*, 243–260.
56. Fits including only the cavity spectra gave smaller rms residuals and essentially the same spectroscopic constants. The results of fits including both cavity and chirped-pulse data are presented here to illustrate the full set of  $J$  and  $K_{-J}$  values that were successfully analyzed.
57. Wollrab, J. E.; Laurie, V. W. Structure and Conformation of Trimethylamine. *J. Chem. Phys.* **1969**, *51*, 1580.
58. Li, X. L.; Bocquet, R.; Petitpres, D.; Boucher, D.; Poteau, L.; Demaison, J. The Rotational Spectrum of Trimethylamine Measured by Microwave and Millimeter-Wave Fourier-Transform Spectroscopies and by Sideband Laser Spectroscopy. *J. Mol. Spectrosc.* **1995**, *172*, 449–455.

- 
59. Winnewisser, M.; Winnewisser, B. P.; Stein, M.; Birk, M.; Wagner, G.; Winnewisser, G.; Yamada, K. M. T.; Belov, S. P.; Baskakov, O. I. Rotational Spectra of Cis-HCOOH, Trans-HCOOH, and Trans-H<sup>13</sup>COOH. *J. Mol. Spectrosc.* **2002**, *216*, 259–265.
60. Davis, R. W.; Robiette, A. G.; Gerry, M. C. L.; Bjarnov, E.; Winnewisser, G. Microwave Spectra and Centrifugal Distortion Constants of Formic Acid Containing <sup>13</sup>C and <sup>18</sup>O: Refinement of the Harmonic Force Field and the Molecular Structure. *J. Mol. Spectrosc.* **1980**, *81*, 93–109.
61. Cazzoli, G.; Puzzarini, C.; Stopkowicz, S.; Gauss, J. Precise Laboratory Measurements of Trans-DCOOH and Trans-HCOOD for Astrophysical Observations. *Astrophys. J. Suppl. Ser.* **2011**, *196*, 10.
62. The uncertainty arising from the rotational constants is on the order of 10<sup>-7</sup> Å, which is unreasonably small, as it is likely that more substantial error is incurred when rotational constants are inverted to obtain moments of inertia, e.g., by via the approximation that  $\langle 1/I_{cc} \rangle \approx \langle I_{cc} \rangle^{-1}$ . The magnitude of this uncertainty, however, is difficult to assess.
63. Kraitchman, J. Determination of Molecular Structure from Microwave Spectroscopic Data. *Am. J. Phys.* **1953**, *21*, 17–24.
64. Sedo, G.; Leopold, K. R. Partial Proton Transfer in a Molecular Complex: Assessments from Both the Donor and Acceptor Points of View. *J. Phys. Chem. A* **2011**, *115*, 1787–1794
65. Rego, C. A.; Batten, R. C.; Legon, A. C. The Properties of the Hydrogen-Bonded Dimer (CH<sub>3</sub>)<sub>3</sub>N⋯HCN from an Investigation of its Rotational Spectrum. *J. Chem. Phys.* **1988**, *89*, 696–702.
66. Domene, C.; Fowler, P. W.; Legon, A. C. <sup>14</sup>N Electric Field Gradient in Trimethylamine Complexes as a Diagnostic for Formation of Ion Pairs. *Chem. Phys. Lett.* **1999**, *309*, 463–470
67. Recognizing the  $\chi_{aa} + \chi_{bb} + \chi_{cc} = 0$ , the value of  $\chi_{cc} = -(1/2) [\chi_{aa} + (\chi_{bb} - \chi_{cc})]$  is determined from the measured values of  $\chi_{aa}$  and  $(\chi_{bb} - \chi_{cc})$ .
68. Legon, A. C.; Rego, C. A. Rotational Spectrum of the Trimethylamine – Hydrogen Iodide Dimer: An Ion Pair (CH<sub>3</sub>)<sub>3</sub>NH<sup>+</sup>⋯I<sup>-</sup> in the Gas Phase. *J. Chem. Phys.* **1993**, *99*, 1463–1468.

- 
69. Tubergen, M. J.; Kuczkowski, R. L. Microwave Spectroscopic Characterization of a Strong Hydrogen Bond: Trimethylamine – Water. *J. Am. Chem. Soc.* **1993**, *115*, 9263–9266.
70. Linstrom, P. J., Mallard, W. G., Eds. *NIST Chemistry WebBook*; NIST Standard Reference Data Base, Number 69; National Institute of Standards and Technology: Gaithersburg, MD, <http://webbook.nist.gov>, (retrieved January 8, 2016).
71. Hynes, J.T.; Klinman, J.P.; Limbach, H.-H.; Schowen, R.L., Eds., *Hydrogen Transfer Reactions*, Vol. 1, Wiley-VCH: Weinheim 2007 and references therein.
72. Bell, R.P., *The Proton in Chemistry*, Methuen & Co. Ltd.: London, 1959 and references therein.
73. Hynes, J.T.; Klinman, J.P.; Limbach, H.-H.; Schowen, R.L., Eds. *Hydrogen Transfer Reactions*, Vol. 3 Wiley-VCH: Weinheim 2007 and references therein.
74. Nagel, Z.D.; Klinman, J.P. Update 1 of: Tunneling and Dynamics in Enzymatic Hydride Transfer. *Chem. Rev.* **2010**, *110*, PR41-PR67.
75. Brönsted, J.N. Some Remarks on the Concept of Acids and Bases. *Recueil des Travaux Chimiques des Pays-Bas et de la Belgique* **1923**, *42*, 718-728.
76. Lowry, T.M. The Electronic Theory of Valency. Part I. Intramolecular Ionisation. *Trans. Farad. Soc.* **1923**, *18*, 285-295.
77. See, for example, Hammes-Schiffer, S. Proton-Coupled Electron Transfer: Theoretical Formulation and Applications in Hynes, J.T.; Klinman, J.P.; Limbach, H.-H.; Schowen, R.L., Eds., *Hydrogen Transfer Reactions*, Vol. 2, Wiley-VCH: Weinheim 2007, pp. 479-502.
78. Hammes-Schiffer, S. Theoretical Perspectives on Proton-Coupled Electron Transfer Reactions. *Acc. Chem. Res.* **2001**, *34*, 273-281.
79. See, for example, Scheiner, S. Theoretical Studies of Excited State Proton Transfer in Small Model Systems. *J. Phys. Chem. A* **2000**, *104*, 5898-5909.
80. See, for example, Remer, L.C.; Jensen, J.H. Theoretical Studies of Excited State Proton Transfer in Small Model Systems. *J. Phys. Chem. A* **2000**, *104*, 9266-9275.
81. Löwdin, P.-O., *Rev. Mod. Phys.* Proton Tunneling in DNA and its Biological Implications. **1963**, *35*, 724-732.

- 
82. Kryachko, E.S. The Origin of Spontaneous Point Mutations in DNA via Löwdin Mechanism of Proton Tunneling in DNA Base Pairs: Cure with Covalent Base Pairing. *Int. J. Quant. Chem.* **2002**, *90*, 910-923.
83. Brovarets, O.O.; Hovorun, D.M. Can Tautomerization of the A·T Watson-Crick Base Pair via Double Proton Transfer Provoke Point Mutations During DNA Replication? A Comprehensive QM and QTAIM Analysis. *J. Biomol. Struct. and Dynam.* **2013**, DOI:10.1080/07391102.2012.755795.
84. Lin, Y.; Wang, H.; Wu, Y.; Gao, S.; Schaefer, III, H.F. Proton-Transfer in Hydrogenated Guanine-Cytosine Trimer Neutral Species, Cations, and Anions Embedded in B-Form DNA. *Phys. Chem. Chem. Phys.* **2014**, *16*, 6717-6725.
85. Waluk, J. Tautomerization of Porphycenes. pp.245-272 in Reference 1.
86. Braun, J.; Schlabach, M.; Wehrle, B.; Köcher, M.; Vogel, E.; Limbach, H.-H. NMR Study of the Tautomerism of Porphyrin Including the Kinetic HH/HD/DD Isotope Effects in the Liquid and the Solid State. *J. Am. Chem. Soc.* **1994**, *116*, 6593-6604.
87. Smedarchina, Z.; Shibl, M.F.; Kühn, O.; Fernández-Ramos, A. The Tautomerization Dynamics of Porphycene and Its Isotopomers – Concerted versus Stepwise Mechanisms. *Chem. Phys. Lett.* **2007**, *436*, 314-321.
88. Benderskii, V.A.; Makarov, D.E.; Wight, C.A., Eds., *Advances in Chemical Physics: Chemical Dynamics at Low Temperatures*, Vol. 88, **2007**.
89. Hancock, G.C.; Truhlar, D.G. Reaction-Path Analysis of the Effect of Monomer Excitation on the Tunneling Splitting of the Hydrogen Fluoride Dimer. *J. Chem. Phys.* **1989**, *90*, 3498-3505.
90. Volobuev, Y.; Necochea, W.C.; Truhlar, D.G. Tunneling Splittings in Predissociated HF Dimer. *J. Phys. Chem. A* **1997**, *101*, 3045-3048.
91. Kim, Y. Dynamics and Kinetic Isotope Effect for the Double Proton Transfer in Formamidine Monohydrated Complex Using Direct Semiempirical Dynamics Calculation. *J. Phys. Chem. A* **1998**, *102*, 3025-3036.
92. Kim, Y.; Hwang, H.J. Dynamics and Kinetic Isotope Effects for the Intramolecular Double Proton Transfer in Oxalamidine Using Direct Semiempirical Dynamics Calculation. *J. Am. Chem. Soc.* **1999**, *121*, 4669-4676.
93. Kamarchik, E.; Wang, Y.; Bowman, J. Reduced-Dimensional Quantum Approach to Tunneling Splittings Using Saddle-Point Normal Coordinates. *J. Phys. Chem. A* **2009**, *113*, 7556-7562.



- 
94. Ushiyama, H.; Takatsuka, K. Successive Mechanism of Double-Proton Transfer in Formic Acid Dimer: A Classical Study. *J. Chem. Phys.* **2001**, *115*, 5903-5912.
95. Matanović, I.; Došlić, N.; Johnson, B.R. Generalized Approximation to the Reaction Path: The Formic Acid Dimer Case. *J. Chem. Phys.* **2008**, *128*, 084103-1-10.
96. See, for example, Redington, R.L. Coherent Proton Tunneling in Hydrogen Bonds of Isolated Molecules: Malonaldehyde and Tropolone, in Ref.[71], pp. 3-31.
97. Shida, N.; Barbara, P.F.; Almlöf, J.A Reaction Surface Hamiltonian Treatment of the Double Proton Transfer of Formic Acid Dimer. *J. Chem. Phys.* **1991**, *94*, 3633-3643.
98. Kohanoff, J.; Koval, S.; Estrin, D.A.; Laria, D.; Abashkin, Y. Concertedness and Solvent Effects in Multiple Proton Transfer Reactions: The Formic Acid Dimer in Solution. *J. Chem. Phys.* **2000**, *112*, 9498-9508.
99. Smedarchina, Z.; Siebrand, W.; Fernández-Ramos, A.; Meana-Pañeda, R. Mechanisms of Double Proton Transfer. Theory and Applications. *Z. Physik. Chem.* **2008**, *222*, 1291-1309.
100. Limbach, H.-H.; Schowen, K.B.; Schowen, R.L. Heavy Atom Motions and Tunneling in Hydrogen Transfer Reactions: The Importance of the Pre-Tunneling State. *J. Phys. Org. Chem.* **2010**, *23*, 586-605.
101. Costain, C.C.; Srivastava Microwave Rotation Spectrum of CF<sub>3</sub>COOH-HCOOH. *G.P. J. Chem Phys.* **1961**, *35*, 1903-1904.
102. Bellott, E.M.; Wilson, E.B. Hydrogen Bonded Bimolecular Complexes of Carboxylic Acids in the Vapor Phase. Observation and Characterization by Low Resolution Microwave Spectroscopy. *Tetrahedron* **1975**, *31*, 2896-2898.
103. Daly, A.M.; Douglass, K.O.; Sarkozy, L.C.; Neill, J.L.; Muckle, M.T.; Zaleski, D.P.; Pate, B.H.; Kukolich, S.G. Microwave Measurements of Proton Tunneling and Structural Parameters for the Propiolic Acid-Formic Acid Dimer. *J. Chem. Phys.* **2011**, *135*, 154304-1-12.
104. Sun, M.; Wang, Y.; Carey, S.J.; Mitchell, E.G.; Bowman, J.; Kukolich, S.G. Calculations and Measurements of the Deuterium Tunneling Frequency in the Propiolic Acid-Formic Acid Dimer and Description of a Newly Constructed Fourier Transform Microwave Spectrometer. *J. Chem. Phys.* **2013**, *139*, 084316-1-7.
105. Kukolich, S.G.; Mitchell, E.G.; Carey, S.J.; Sun, M.; Sargus, B.A. Microwave Structure for the Propiolic Acid-Formic Acid Complex. *J. Phys. Chem. A* **2013**, *117*, 9525-9530.

- 
106. Evangelisti, L.; Écija, P.; Cocinero, E.J.; Castaño, F.; Lesarri, A.; Caminati, W.; Meyer, R. Proton Tunneling in Heterodimers of Carboxylic Acids: A Rotational Study of the Benzoic Acid-Formic Acid Bimolecule. *J. Phys. Chem. Lett.* **2012**, *3*, 3770-3775.
107. Tayler, M.C.D.; Ouyang, B.; Howard, B.J. Unraveling the Spectroscopy of Coupled Intramolecular Tunneling Modes: A Study of Double Proton Transfer in the Formic-Acetic Acid Complex. *J. Chem. Phys.* **2011**, *134*, 054316-1-9.
108. Martinache, L.; Kresa, W.; Wegener, M.; Vonmont, U.; Bauder, A. Microwave Spectra and Partial Substitution Structure of Carboxylic Acid Bimolecules. *Chem. Phys.* **1990**, *148*, 129-140.
109. Antolínez, S.; Dreizler, H.; Storm, V.; Sutter, D.H.; Alonso, J.L. The Microwave Spectrum of the Bimolecule Trifluoroacetic Acid...Cyclopropanecarboxylic Acid. *Z. Naturforsch.* **1997**, *52a*, 803-806.
110. Feng, G.; Gou, Q.; Evangelisti, L.; Caminati, W. Frontiers in Rotational spectroscopy: Shapes and Tunneling Dynamics of the Four Conformers of the Acrylic Acid – Difluoroacetic Acid Adduct. *Angew. Chemie.* **2014**, *53*, 530-534.
111. Feng, G.; Gou, Q.; Evangelisti, L.; Xia, Z.; Caminati, W. Conformational Equilibria in Carboxylic Acid Bimolecules: A Rotational Study of Acrylic Acid-Formic Acid. *Phys. Chem. Chem. Phys.* **2013**, *15*, 2917-2922.
112. Feng, G.; Favero, L.B.; Maris, A.; Vigorito, A.; Caminati, W. Proton Transfer in Homodimers of Carboxylic Acids: The Rotational Spectrum of the Dimer of Acrylic Acid. Meyer, R., *J. Am. Chem. Soc.* **2012**, *134*, 19281-19286.
113. Birer, Ö.; Havenith, M. High-Resolution Infrared Spectroscopy of the Formic Acid Dimer. *Annu. Rev. Phys. Chem.* **2009**, *60*, 263-275.
114. Xue, Z.; Suhm, M.A. Probing the Stiffness of the Simplest Double Hydrogen Bond: The Symmetric Hydrogen Bond Modes of Jet-Cooled Formic Acid Dimer. *J. Chem. Phys.* **2009**, *131*, 054301-1-14.
115. Keller, J.W. The Formic Acid-Trifluoroacetic Acid Bimolecule. Gas-Phase Infrared Spectrum and Computational Studies. *J. Phys. Chem. A* **2004**, *108*, 4610-4618.
116. Florio, G.M.; Sibert, III, E.L.; Zwier, T.S. Fluorescence-Dip IR Spectra of Jet-Cooled Benzoic Acid Dimer in Its Ground and First Excited Singlet States. *J. Chem. Soc. Farad. Trans.* **2001**, *118*, 315-330.

- 
117. Georges, R.; Freytes, M.; Hurtmans, D.; Kleiner, I.; Auwera, J.V.; Herman, M. Jet-Cooled and Room Temperature FTIR Spectra of the Dimer of Formic Acid in the Gas Phase. *Chem. Phys.* **2004**, *305*, 187-196.
118. Ito, F. Jet-Cooled Infrared spectra of the Formic Acid Dimer by Cavity Ring-Down Spectroscopy: Observation of the C-O Stretching Region and Vibrational Analysis of the Fermi-Triad System. *Chem. Phys. Lett.* **2007**, *447*, 202-207.
119. Ito, F.; Nakanaga, T. Jet-Cooled Infrared Spectra of the Formic Acid Dimer by Cavity Ring-Down Spectroscopy: Observation of the O-H Stretching Region. *Chem. Phys.* **2002**, *277*, 163-169.
120. Shipman, S.T.; Douglass, P.C.; Yoo, H.S. Hinkle, C.E.; Mierzejewski, E.L. Pate, B.H., Vibrational Dynamics of Carboxylic Acid Dimers in Gas and Dilute Solution. *Phys.Chem.Chem.Phys.* **2007**, *9*, 4572-4586.
121. Ortlieb, M.; Havenith, M. Proton Transfer in (HCOOH)<sub>2</sub>: An IR High-Resolution Study of the Antisymmetric C–O Stretch. *J. Phys. Chem. A* **2007**, *111*, 7355-7363.
122. Madeja, F.; Havenith, M. High Resolution Spectroscopy of Carboxylic Acid in the Gas Phase: Observation of Proton Transfer in (DCOOH)<sub>2</sub>. *J. Chem. Phys.* **2002**, *117*, 7162-7168.
123. Riehn, C.; Matylitsky, V.V.; Gelin, M.F.; Brutschy, B. Double Hydrogen Bonding of Acetic Acid Studied by Femtosecond Degenerate Four-Wave Mixing. *Mol. Phys.* **2005**, *103*, 1615-1623.
124. Matylitsky, V.V.; Riehn, C.; Gelin, M.F.; Brutschy, B. The Formic Acid Dimer (HCOOH)<sub>2</sub> Probed by Time-Resolved Structure Selective Spectroscopy. *J. Chem. Phys.* **2003**, *119*, 10553-10562.
125. Derissen, J.L. A Reinvestigation of the Molecular Structure of Acetic Acid Monomer and Dimer by Gas Electron Diffraction. *J. Mol. Struct.* **1971**, *7*, 67-80.
126. Derissen, J.L. An Investigation of the Structure of Propionic Acid Monomer and Dimer by Gas Electron Diffraction. *J. Mol. Struct.* **1971**, *7*, 81-88.
127. Almenningen, A.; Bastiansen, O.; Motzfeldt, T. A Reinvestigation of the Structure of Monomer and Dimer Formic Acid by Gas Electron Diffraction Technique. *Acta Chemica. Scand.* **1969**, *23*, 2848-2864.
128. Kim, Y. Direct Dynamics Calculation for the Double Proton Transfer in Formic Acid Dimer. *J. Am. Chem. Soc.* **1996**, *118*, 1522-1528.

- 
129. Tautermann, C.S.; Voegelé, A.F.; Loerting, T.; Liedl, K.R. An Accurate Semiclassical Method to Predict Ground-State Tunneling Splittings. *J. Chem. Phys.* **2002**, *117*, 1967-1974.
130. Tautermann, C.S.; Voegelé, A.F.; Liedl, K.R. The Ground-State Tunneling Splitting of Various Carboxylic Acid Dimers. *J. Chem. Phys.* **2004**, *120*, 631-637.
131. Smedarchina, Z.; Fernández-Ramos, A.; Siebrand, W. Tunneling Dynamics of Double Proton Transfer in Formic Acid and Benzoic Acid Dimers. *J. Chem. Phys.* **2005**, *122*, 134309-1-12.
132. Markwick, P.R.L.; Doltsinis, N.L.; Marx, D. Targeted Car-Parrinello Molecular Dynamics: Elucidating Double Proton Transfer in Formic Acid Dimer. *J. Chem. Phys.* **2005**, *122*, 054112-1-8.
133. Mil'nikov, G.V.; Kühn, O.; Nakamura, H. Ground-State and Vibrationally Assisted Tunneling in the Formic Acid Dimer. *J. Chem. Phys.* **2005**, *123*, 074308-1-9.
134. Luckhaus, D. Concerted Hydrogen Exchange Tunneling in Formic Acid Dimer. *J. Phys. Chem. A* **2006**, *110*, 3151-3158.
135. Matanović, I.; Došlić, N.; Kühn, O. Ground and Asymmetric CO-Stretch Excited State Tunneling Splittings in the Formic Acid Dimer. *J. Chem. Phys.* **2007**, *127*, 014309-1-7.
136. Barnes, G.L.; Squires, S.M.; Sibert, III Symmetric Double Proton Tunneling in Formic Acid Dimer: A Diabatic Basis Approach. *J. Phys. Chem. B* **2008**, *112*, 595-603.
137. Fillaux, F. Quantum Entanglement and Nonlocal Proton Transfer Dynamics in Dimers of Formic Acid and Analogues. *Chem. Phys. Lett.* **2005**, *408*, 302-306.
138. Legon, A.C.; Wallwork, A.L.; Rego, C.A. The Rotational Spectrum and Nature of the Heterodimer in Trimethylammonium Bromide Vapor. *J. Chem. Phys.* **1990**, *92*, 6397-6407.
139. Gillies, C.W.; Gillies, J.Z.; Suenram, R.D.; Lovas, F.J.; Kraka, E.; Cremer, D. Van der Waals Complexes in 1,3-Dipolar Cycloaddition Reactions: Ozone-Ethylene. *J. Am. Chem. Soc.* **1991**, *113*, 2412-2421.
140. Gutowsky, H.S.; Chen, J.; Hajduk, P.J.; Keen, J.D.; Emilsson, T. The Silicon-Carbon Double Bond: Theory Takes a Round. *J. Am. Chem. Soc.* **1989**, *111*, 1901-1902.

- 
141. Emilsson, T.; Klots, T.D.; Ruoff, R.S.; Gutowsky, H.S. Rotational Spectra and Structures of the OC– and H<sub>3</sub>N–HCN–HF Trimers: Coaxial Mixing Nozzle for Reactive Species. *J. Chem. Phys.* **1990**, *93*, 6971-6976.
142. Chilton, T.H. *Strong Water Nitric Acid: Sources, Methods of Manufacture, and Uses*; MIT Press: Cambridge, MA 1968, p. 166.
143. No attempts to record the spectra of HCOOD–DNO<sub>3</sub> were made because the already small splittings of the parent species were expected to be reduced still further and become so highly convoluted with hyperfine structure from the nitrogen and two deuterium nuclei that no further information would be recovered.
144. Pickett, H.M. The Fitting and Prediction of Vibration-Rotation Spectra with spin Interactions. *J. Mol. Spectrosc.* **1991**, *148*, 371-377.
145. An easy way to see this is as follows: For a molecule with separable rotational and vibrational coordinates, such that  $\psi(\mathbf{Q};\theta,\phi) = \psi_v(\mathbf{Q})\psi_R(\theta,\phi)$ , the transition moment,
- $$\langle \psi''(\mathbf{Q};\theta,\phi) | \mu_z | \psi'(\mathbf{Q};\theta,\phi) \rangle = \langle \psi_v''(\mathbf{Q}) | \mu_z | \psi_v'(\mathbf{Q}) \rangle \cdot \langle \psi_R''(\theta,\phi) | \mu_z | \psi_R'(\theta,\phi) \rangle .$$
- If  $\mu_c = 0$  (as in HNO<sub>3</sub>–HCOOH), then  $\mu_z = \mu_a(\mathbf{Q})\cos(\theta_{az}) + \mu_b(\mathbf{Q})\cos(\theta_{bz})$  and thus
- $$\langle \psi''(\mathbf{Q};\theta,\phi) | \mu_z | \psi'(\mathbf{Q};\theta,\phi) \rangle = \langle \psi_v''(\mathbf{Q}) | \mu_a(\mathbf{Q}) | \psi_v'(\mathbf{Q}) \rangle \cdot \langle \psi_R''(\theta,\phi) | \cos(\theta_{az}) | \psi_R'(\theta,\phi) \rangle +$$
- $$\langle \psi_v''(\mathbf{Q}) | \mu_b(\mathbf{Q}) | \psi_v'(\mathbf{Q}) \rangle \cdot \langle \psi_R''(\theta,\phi) | \cos(\theta_{bz}) | \psi_R'(\theta,\phi) \rangle$$
- where  $\psi_v''$  and  $\psi_v'$  represent the symmetric and antisymmetric tunneling states, respectively. In HNO<sub>3</sub>–HCOOH,  $\mu_a$  is symmetric with respect to the tunneling coordinate and  $\mu_b$  is antisymmetric. As a result, the first term is non-vanishing only when  $\psi_v''$  and  $\psi_v'$  are of the same symmetry, i.e. when  $\psi_v'' = \psi_v'$ , and thus transitions within each member of the tunneling doublet obey *a*-type selection rules. Conversely, the second term is non-vanishing only when  $\psi_v''$  and  $\psi_v'$  are of opposite symmetry, and thus transitions that cross the tunneling doublet obey *b*-type selection rules.
146. Leopold, K.R. Generalized Equations for the Inertial Tensor of a Weakly Bound Complex. *J. Mol. Spectrosc.* **2012**, *278*, 27-30. E: *J. Mol. Spectrosc.* **2013**, *293*, 60.
147. Cox., A.P.; Ellis, M.C.; Attfield, C.J.; Ferris, A.C. Microwave Spectrum of DNO<sub>3</sub>, and Average Structures of Nitric and Nitrous Acids. *J. Mol. Struct.* **1994**, *320*, 91-106.
148. Ott, M.E.; Craddock, M.B.; Leopold, K.R. Nuclear Quadrupole Coupling Constants for Rare-Isotopic Forms of Nitric Acid. *J. Mol. Spectrosc.* **2005**, *229*, 286-289.

- 
149. Equation 13 differs from the usual projection formula  $\chi_{aa}^{complex} = \chi_{aa}^{monomer} \langle (3\cos^2 \tau - 1)/2 \rangle$  which is strictly applicable only for a linear molecule or symmetric top and is approximately valid for an asymmetric top when  $\tau$  is small. In the case of HCOOH–HNO<sub>3</sub>, these conditions are not necessarily met and the more accurate form expressed in equation 13 was used.
150. CPC corrected values obtained at the MP2/6-311G(2d,2p) level/basis were used for this correction.
151. Kisiel, Z. Least-Squares Mass-Dependence Molecular Structures for Selected Weakly Bound Intermolecular Clusters. *J. Mol. Spectrosc.* **2003**, *218*, 58-67.
152. This is a complex fitting problem and, as aptly noted by Kisiel<sup>151</sup> care must be taken to avoid least squares convergence in local minima. In this case, auxiliary information from nuclear hyperfine structure is used to distinguish between correct and incorrect structures. This information is built into the analysis based on analytical expressions for inertial tensor components.
153. The method of determining the “preferred” structure is not readily amenable to determining the O···O distances. Therefore, this difference corresponds to the structure listed as “Average of Maximum and Minimum Values” in Table 3.5. Without the use of the *ab initio* – corrected monomer geometries, the O···O distances are 2.578 Å and 2.819 Å for the hydrogen bonds involving the HNO<sub>3</sub> and HCOOH protons, respectively, corresponding to a difference of 0.241 Å.
154. For diacrylic acid, the *a*-type spectra cross the tunneling doublet, whereas the *b*-type spectra do not. The 2.182 MHz value corresponds to a hypothetical pair of 5<sub>05</sub>–6<sub>06</sub> transitions, each within one of the tunneling states, and is given to provide the most direct comparison with the other systems listed. The splitting between the 5<sub>05</sub>–6<sub>16</sub> transitions in the 0<sup>+</sup> and 0<sup>-</sup> states is 4.706 MHz.
155. Adachi, A.; Kiyoyama, H.; Nakahara, M.; Masuda, Y.; Yamatera, H.; Shimizu, A.; Taniguchi Y. Raman and Nuclear Magnetic Resonance Studies on the Concentration Dependence of Orientational Relaxation Times of the Nitrate Ion in Dilute Aqueous Solution. *J. Chem. Phys.* **1988**, *90*, 392-399.
156. Craddock, M.B.; Brauer, C.S.; Leopold, K.R. Microwave Spectrum, Structure, and Internal Dynamics of the Nitric Acid Dihydrate Complex. *J. Phys. Chem. A* **2008**, *112*, 488-496.
157. Cooke, S. A.; Corlett, G. K.; Lister, D. G.; Legon, A. C. Is Pyridinium Hydrochloride a Simple Hydrogen-Bonded Complex C<sub>5</sub>H<sub>5</sub>N-HCl or an Ion Pair

- 
- $C_5H_5NH^+-Cl^-$  in the Gas Phase? An Answer from Its Rotational Spectrum. *J. Chem. Soc., Faraday Trans.* **1998**, *94*, 837–834.
158. Cole, G. C.; Legon, A. C. The Nature of the Complex Formed between Pyridine and Hydrogen Bromide in the Gas Phase: An Experimental Approach Using Rotational Spectroscopy. *J. Chem. Phys.* **2004**, *121*, 10467–10473.
159. Bene, J. E. Del; Szczepaniak, K.; Chabrier, P.; Person, W. B.; Uni, V.; Gaines, V. Resolving Discrepancies between Theory and Experiment : IR Spectrum of the Proton-Shared  $HBr \cdots Pyridine$  Complex. *J. Phys. Chem. A* **1997**, *101*, 15–17.
160. Legon, A. C.; Millen, D. J. Determination of Properties of Hydrogen-Bonded Dimers by Rotational Spectroscopy and a Classification of Dimer Geometries. *Faraday Discuss. Chem. Soc.* **1982**, *73*, 71.
161. Legon, A. C.; Millen, D. J. Interpretation of the Success of the Electron-Pair Model. *Chem. Soc. Rev.* **1987**, *16*, 467–498.
162. Legon, A. C. Prereactive Complexes of Dihalogens XY with Lewis Bases B in the Gas Phase: A Systematic Case for the Halogen Analogue  $B \cdots XY$  of the Hydrogen Bond  $B-HX$ . *Angew. Chemie Int. Ed.* **1999**, *38*, 2686–2714.
163. Georgiou, A. S.; Legon, A. C.; Millen, D. J. Spectroscopic Investigations of Hydrogen Bonding Interactions in the Gas Phase. V. The Identification and Determination of the Geometry and Electric Dipole Moment of the Hydrogen Bonded Heterodimer Formed Between Oxirane and Hydrogen Fluoride,  $(CH_2)_2O \cdots HF$ , by Infrared and Microwave Spectroscopy. *Proc. R. Soc. London. Ser. A, Math. Phys. Eng. Sci.* **1981**, *373*, 511–526.
164. Georgiou, A. S.; Legon, A. C.; Millen, D. J. Spectroscopic Investigations of Hydrogen Bonding Interactions in the Gas Phase. Part VI. A Microwave Spectroscopic Determination of Geometry for the Heterodimer  $(CH_2)_3O \cdots HF$  Formed between Oxetane and Hydrogen Fluoride: Hydrogen Bonding as a Probe for Lone Pairs. *J. Mol. Struct.* **1980**, *69*, 69–78.
165. Kisiel, Z.; Legon, A. C.; Millen, D. J. Spectroscopic Investigations of Hydrogen Bonding Interactions in the Gas Phase. VII. The Equilibrium Conformation and Out-of-Plane Bending Potential Energy Function of the Hydrogen-Bonded Heterodimer  $H_2O \cdots HF$  Determined from Its Microwave Rotational Spectrum. *Proc. R. Soc. A Math. Phys. Eng. Sci.* **1982**, *381*, 419–442.
166. Legon, A. C. Non-Linear Hydrogen Bonds and Rotational Spectroscopy: Measurement and Rationalisation of the Deviation from Linearity. *Faraday Discuss.* **1994**, *97*, 19.

- 
167. Legon, A. C.; Thorn, J. C. Can the Nonlinearity of Hydrogen Bonds  $B\cdots HX$  Be Measured Precisely? A Method from Rotational Spectroscopy and Its Application to 2,5-dihydrofuran $\cdots HCl$ . **1994**, *277*, 472-479.
168. Hill, J. G.; Legon, A. C. On the Directionality and Non-Linearity of Halogen and Hydrogen Bonds. *Phys. Chem. Chem. Phys.* **2015**, *17*, 858-867.
169. Legon, A. C. The Rotational Constant  $A_0$  and Planarity of the Hydrogen-Bonded Complex  $H_2CO\cdots HCl$ . *J. Chem. Soc., Faraday Trans.* **1996**, *92*, 2677-2679.
170. Legon, A. C.; Rego, C. A.; Wallwork, A. L. Rotational Spectrum of a Short-Lived Dimer of Oxirane and Hydrogen Chloride: Evidence for a Bent Hydrogen Bond. *J. Chem. Phys.* **1992**, *97*, 3050.
171. Evans, C. M.; Legon, A. C. Pre-Chemical Interactions in a Pulsed Jet : The Angular Geometry of Thiirane $\cdots HCl$  and the Nonlinearity of Its Hydrogen Bond from Rotational Spectroscopy. *Chem. Phys.* **1995**, *198*, 119-131.
172. Kisiel, Z.; Fowler, P. W.; Legon, A. C. Investigation of the Rotational Spectrum of the Hydrogen-Bonded Dimer Formed between Methylene cyclopropane and  $HCl$ . *J. Chem. Phys.* **1994**, *101*, 4635.
173. Kisiel, Z.; Fowler, P. W.; Legon, A. C. Rotational Spectrum, Structure, and Chlorine Nuclear Quadrupole Tensor of the Vinyl Fluoride $\cdots HCl$  Dimer. *J. Chem. Phys.* **1990**, *93*, 3054.
174. Cooke, S. A.; Corlett, G. K.; Evans, C. M.; Legon, A. C. The Rotational Spectrum of the Complex 2,5-Dihydrofuran $\cdots HBr$  and the Non Linearity of the  $O\cdots H-Br$  Hydrogen Bond. *J. Chem. Soc., Faraday Trans.* **1997**, *93*, 2973-2976.
175. Legon, A. C.; Wallwork, A. L. Non-Reactive Interaction of Oxirane and Hydrogen Bromide: Isolation of an Oxirane $\cdots$ Hydrogen Bromide Dimer in a Supersonic Jet and Its Characterisation by Microwave Spectroscopy. *J. Chem. Soc., Faraday Trans.* **1990**, *86*, 3975-3982.
176. Legon, A. C.; Wallwork, A. L.; Warner, H. E. Rotational Spectroscopy of a Mixture of Thiirane and Hydrogen Bromide: Detection and Characterization of a Short-Lived Complex  $(CH_2)_2S\cdots HBr$  in a Pulsed Jet. *J. Chem. Soc., Faraday Trans.* **1991**, *87*, 3327-3334.
177. Legon, A. C.; Lister, D. G. Nonlinear Hydrogen Bonds of the Type  $(CH_2)_2Z\cdots HY$ : The Rotational Spectrum of a Complex of Methylene cyclopropane and Hydrogen Bromide. *Phys. Chem. Chem. Phys.* **1999**, *1*, 4175-4180.



- 
178. Legon, A. C.; Ottaviani, P. A Non-Linear Hydrogen Bond F $\cdots$ H–Br in Vinyl Fluoride  $\cdots$ HBr Characterised by Rotational Spectroscopy. *Phys. Chem. Chem. Phys.* **2002**, *4*, 4103–4108.
179. Legon, A. C.; Millen, D. J. Hydrogen Bonding as a Probe of Electron Densities: Limiting Gas-Phase Nucleophilicities and Electrophilicities of B and HX. *J. Am. Chem. Soc.* **1987**, *109*, 356–358.
180. Howard, N. W.; Legon, A. C. Nature, Geometry, and Binding Strength of the Ammonia–Hydrogen Chloride Dimer Determined from the Rotational Spectrum of Ammonium Chloride Vapor. *J. Chem. Phys.* **1988**, *88*, 4694.
181. Cole, G. C.; Hughes, R. A.; Legon, A. C. Rotational Spectrum, Inversion, and Geometry of 2,5-Dihydrofuran...ethyne and a Generalization about Z...H-C Hydrogen Bonds. *J. Chem. Phys.* **2005**, *122*, 134311.
182. Legon, A. C. Nonlinear Hydrogen Bonds O $\cdots$ H-C and the Role of Secondary Interactions. The Rotational Spectrum of the Oxirane-Acetylene Complex. *Chem. Phys. Lett.* **1995**, *2614*, 24–31.
183. Batten, R. C.; Cole, G. C.; Legon, A. C. Rotational Spectroscopy of a Weak Complex of Thiirane and Ethyne: The Identification and Properties of a Highly Nonlinear S $\cdots$ H–C Hydrogen Bond. *J. Chem. Phys.* **2003**, *119*, 7903.
184. Cole, G. C.; Legon, A. C. Non-Linearity of Weak B $\cdots$ H–C Hydrogen Bonds: An Investigation of a Complex of Vinyl Fluoride and Ethyne by Rotational Spectroscopy. *Chem. Phys. Lett.* **2003**, *369*, 31–40.
185. Doran, J. L.; Hon, B.; Leopold, K. R. Rotational Spectrum and Structure of the Pyridine-CO<sub>2</sub> van Der Waals Complex. *J. Mol. Struct.* **2012**.
186. Legon, A.C. in *Atomic and Molecular Beams*, Vol. 2, G. Scoles Ed., Chapter 9, p. 289, Oxford University Press, 1992.
187. Raghavachari, K.; Trucks, G. W.; Pople, J. A.; Head-Gordon, M. A Fifth-Order Perturbation Comparison of Electron Correlation Theories. *Chem. Phys. Lett.* **1989**, *157*, 479–483.
188. Hättig, C.; Tew, D. P.; Köhn, A. Communications: Accurate and Efficient Approximations to Explicitly Correlated Coupled-Cluster Singles and Doubles, CCSD-F12. *J. Chem. Phys.* **2010**, *132*, 231102.
189. Hättig, C.; Klopper, W.; Köhn, A.; Tew, D. P. Explicitly Correlated Electrons in Molecules. *Chem. Rev.* **2012**, *112*, 4–74.

- 
190. Peterson, K. A.; Adler, T. B.; Werner, H.-J. Systematically Convergent Basis Sets for Explicitly Correlated Wavefunctions: The Atoms H, He, B-Ne, and Al-Ar. *J. Chem. Phys.* **2008**, *128*, 084102.
191. Bachorz, R. A.; Bischoff, F. A.; Glöß, A.; Hättig, C.; Höfener, S.; Klopper, W. I. M.; Tew, D. P. Software News and Updates The MP2-F12 Method in the Turbomole Program Package. *J. Comput. Chem.* **2011**, *32*, 2492–2513.
192. TURBOMOLE v6.5, for further information see <http://www.turbomole.com>.
193. Ohshima, Y.; Matsumoto, Y.; Takami, M.; Kuchitsu, K. The Structure and Tunneling Motion of Acetylene Dimer Studied by Free-Jet Infrared Absorption Spectroscopy in the 14  $\mu\text{m}$  Region. *Chem. Phys. Lett.* **1988**, *147*, 2–7.
194. See, for example, reference 106
195. Fits involving  $F_{ac}$  and  $F_{bc}$  were also tried but were unsuccessful.
196. Mata, F.; Quintana, M. J.; Sørensen, G. O. Microwave Spectra of Pyridine and Monodeuterated Pyridines. Revised Molecular Structure of Pyridine. *J. Mol. Struct.* **1977**, *42*, 1–5.
197. Herman, M.; Campargue, A.; El Idrissi, M. I.; Vander Auwera, J. Vibrational Spectroscopic Database on Acetylene. *J. Phys. Chem. Ref. Data* **2003**, *32*, 921.
198. Heineking, N.; Dreizler, H.; Schwarz, R. Nitrogen and Deuterium Hyperfine Structure in the Rotational Spectra of Pyridine and 4-D Pyridine. *Z. Naturforsch* **2015**, *1213*, 1210–1213.
199. Obtuse values of  $\theta_1$  can also be obtained from equation 9, but these were rejected on the basis that they are both chemically unreasonable and inconsistent with the basic geometry predicted theoretically.
200. Fitting the  $0^+$  states did not yield a converged value of  $\angle(\text{py})$  while fitting the  $0^-$  states gave a value of  $65(11)^\circ$ . This value is so far from that returned by any of the other fits or by the analysis based on analytical expressions that we believe it to be a computational artifact arising from its indeterminacy. The large value obtained produces a correspondingly anomalous hydrogen bond length of 3.07 Å.
201. This value is calculated for the  $0^+$  state of the parent species. The value obtained for the  $0^-$  state is  $130^\circ$ . The H1...Z distances for the two states are 3.4165 Å and 3.4186 Å for the  $0^+$  and  $0^-$  states, respectively.

- 
202. Fraser, G. T.; Leopold, K. R.; Klemperer, W. The Structure of  $\text{NH}_3$ -acetylene. *J. Chem. Phys.* **1984**, *80*, 1423.
203. Legon, A. C.; Rego, C. A. Microwave Rotational Spectrum and Properties of a Hydrogen-Bonded Dimer Formed by Trimethylamine and Acetylene. *J. Mol. Struct.* **1988**, *189*, 137–152.
204. Here, “in-phase” and “out-of-phase” refer to motions in which the nitrogen atom and the hydrogen-bonded hydrogen atom move in the same and in opposite directions, respectively, over the course of a vibrational cycle. “Bending” vibrational motion is about the monomer centers of mass.
205. Cooke, S. A.; Corlett, G. K.; Legon, A. C. The Rotational Spectrum of the Pyridine-HF Complex. *J. Mol. Struct.* **1998**, *448*, 107–114.
206. Liu, X.; Sobolewski, A. L.; Domcke, W. Photoinduced Oxidation of Water in the Pyridine-Water Complex: Comparison of the Singlet and Triplet Photochemistries. *J. Phys. Chem. A* **2014**, *118*, 7788–7795.
207. White, J. L.; Baruch, M. F.; Pander III, J. E.; Hu, Y.; Fortmeyer, I. C.; Park, J. E.; Zhang, T.; Liao, K.; Gu, J.; Yan, Y.; et al. Light-Driven Heterogeneous Reduction of Carbon Dioxide: Photocatalysts and Photoelectrodes. *Chem. Rev.* **2015**, *115*, 12888–12935.
208. Chachisvilis, M.; Zewail, A. H. Femtosecond Dynamics of Pyridine in the Condensed Phase: Valence Isomerization by Conical Intersections. *J. Phys. Chem. A* **1999**, *103*, 7408–7418.
209. Reimers, J. R.; Cai, Z.-L. Hydrogen Bonding and Reactivity of Water to Azines in Their  $S_1$  ( $n, \pi^*$ ) Electronic Excited States in the Gas Phase and in Solution. *Phys. Chem. Chem. Phys.* **2012**, *14*, 8791–8802.
210. Caminati, W.; Favero, L. B.; Favero, P. G.; Maris, A.; Melandri, S. Intermolecular Hydrogen Bonding between Water and Pyrazine. *Angew. Chemie Int. Ed.* **1998**, *37*, 792–795.
211. Melandri, S.; Sanz, M. E.; Caminati, W.; Favero, P. G.; Kisiel, Z. The Hydrogen Bond between Water and Aromatic Bases of Biological Interest: An Experimental and Theoretical Study of the 1:1 Complex of Pyrimidine with Water. *J. Am. Chem. Soc.* **1998**, *120*, 11504–11509.
212. Caminati, W.; Moreschini, P.; Favero, P. G. The Hydrogen Bond between Water and Aromatic Bases of Biological Interest: Rotational Spectrum of Pyridazine - Water. **1998**, *5639*, 8097–8100.

- 
213. Millen, D. J.; Mines, G. W. Hydrogen Bonding in the Gas Phase. Part 5. Infrared Spectroscopic Investigation of O-H...N Complexes Formed by Water: Ammonia Monohydrate and Amine and Pyridine Monohydrates. *J. Chem. Soc., Faraday Trans. 2* **1976**, *73*, 369.
214. Kuczkowski R.L. in *Microwave Information Letters XXXVIII*. P.37, Ed. F.J. Lovas, Ed. **1995**.
215. Computational details, as well as observed line frequencies, assignments, and residuals are available in Appendix E.
216. Sicilia, M. C.; Muñoz-Caro, C.; Niño, A. Theoretical Analysis of Pyridine Protonation in Water Clusters of Increasing Size. *ChemPhysChem* **2005**, *6*, 139–147.
217. Sanov, A.; Lineberger, W. C. Cluster Anions: Structure, Interactions, and Dynamics in the Sub-Nanoscale Regime. *Phys. Chem. Chem. Phys.* **2004**, *6* (9), 2018.
218. Castleman, A. W.; Bowen, K. H. Clusters: Structure, Energetics, and Dynamics of Intermediate States of Matter. *J. Phys. Chem.* **1996**, *3654*, 12911–12944.
219. Mo, Y. Geometrical Optimization for Strictly Localized Structures Geometrical Optimization for Strictly Localized Structures. *J. Chem. Phys.* **2003**, *119*, 1300–1306.
220. Mo, Y.; Peyerimhoff, S. D. Theoretical Analysis of Electronic Delocalization. *J. Chem. Phys.* **1998**, *109* (5), 1687.
221. Mo, Y.; Song, L.; Lin, Y. Block-Localized Wavefunction (BLW) Method at the Density Functional Theory (DFT) Level. *J. Phys. Chem. A* **2007**, *111* (34), 8291–8301.
222. Leopold, K. R.; Bowen, K. H.; Klemperer, W. Electric Dipole Moment of KrSO<sub>3</sub>. *J. Chem. Phys.* **1981**, *74*, 4211–4212.
223. Leopold, K. R.; Canagaratna, M.; Phillips, J. A. Partially Bonded Molecules from the Solid State to the Stratosphere. *Acc. Chem. Res.* **1997**, *30* (2), 57–64.
224. Leopold, K. R. In *Advances in Molecular Structure Research*; Hargittai, M., Hargittai, I., Eds.; JAI Press: Greenwich, CT, 1996; p 103.
225. Craddock, M. B.; Brauer, C. S.; Higgins, K. J.; Leopold, K. R. A Microwave and Ab Initio Investigation of N<sub>2</sub>-SO<sub>3</sub>, OC-SO<sub>3</sub>, and OC-SO<sub>3</sub>-Ar. *J. Mol. Spectrosc.* **2003**, *222* (1), 63–73.
226. Brauer, C. S.; Craddock, M. B.; Higgins, K. J.; Leopold, K. R. Microsolvation of a Partially Bonded Complex by Non-Polar and Weakly Polar Microsolvents: A

- 
- Microwave and Ab Initio Study of HCN–SO<sub>3</sub>–Ar and HCN–SO<sub>3</sub>–CO. *Mol. Phys.* **2007**, *105*, 613–625.
227. Fiacco, D. L.; Hunt, S. W.; Leopold, K. R. Structural Change at the Onset of Microsolvation: Rotational Spectroscopy of HCN···HCN–SO<sub>3</sub>. *J. Phys. Chem. A* **2000**, *104*, 8323.
228. Fiacco, D. L.; Leopold, K. R. Partially Bound Systems as Sensitive Probes of Microsolvation: A Microwave and Ab Initio Study of HCN···HCN–BF<sub>3</sub>. *J. Phys. Chem. A* **2003**, *107*, 2808–2814.
229. Bowen, K. H.; Leopold, K. R.; Chance, K. V.; Klemperer, W. Weakly Bound Complexes of Sulfur Trioxide: The Structure of ArSO<sub>3</sub> and the Dipole Moment of N<sub>2</sub>SO<sub>3</sub>. *J. Chem. Phys.* **1980**, *73*, 137–141.
230. Townes, C.H.; Schawlow, A. *Microwave Spectroscopy*, Dover: New York, 1975.
231. See for examples references 65 and 202.
232. Meyer, V.; Sutter, D. H.; Dreizler, H. The Centrifugally Induced Pure Rotational Spectrum and the Structure of Sulfur Trioxide. A Microwave Fourier Transform Study of a Nonpolar Molecule. *Z. Naturforsch* **1991**, *46a*, 710–714.
233. Sharpe, S. W.; Blake, T. A.; Sams, R. L.; Maki, A.; Masiello, T.; Barber, J.; Vulpanovici, N.; Nibler, J. W.; Weber, A. The  $\nu_3$  and  $2\nu_3$  Bands of <sup>32</sup>S<sup>16</sup>O<sub>3</sub>, <sup>32</sup>S<sup>18</sup>O<sub>3</sub>, <sup>34</sup>S<sup>16</sup>O<sub>3</sub>, and <sup>34</sup>S<sup>18</sup>O<sub>3</sub>. *J. Mol. Spectrosc.* **2003**, *222* (2), 142–152.
234. Fiacco, D. L.; Kirchner, B.; Burns, W. A.; Leopold, K. R. Quadrupole Coupling Constants for <sup>33</sup>SO<sub>3</sub>: Microwave Measurements for Ar-<sup>33</sup>SO<sub>3</sub> and *ab Initio* Results for the <sup>33</sup>SO<sub>3</sub> Monomer. *J. Mol. Spectrosc.* **1998**, *191*, 389–391.
235. Schmidt, M. W.; Baldrige, K. K.; Boatz, J. A.; Elbert, S. T.; Gordon, M. S.; Jensen, J. H.; Koseki, S.; Matsunaga, N.; Ngyuyen, K. A.; Su, S.; et al. General Atomic and Molecular Electronic Structure System. *J. Comput. Chem.* **1993**, *14*, 1347–1363.
236. Zhao, Y.; Truhlar, D. G. The M06 Suite of Density Functionals for Main Group Thermochemistry , Thermochemical Kinetics , Noncovalent Interactions , Excited States , and Transition Elements: Two New Functionals and Systematic Testing of Four M06-Class Functionals and 12 Other Functionals. *Theor. Chem. Accounts* **2008**, *120*, 215–241.
237. Grimme, S. Accurate Description of van der Waals Complexes by Density Functional Theory Including Empirical Corrections. *J. Comput. Chem.* **2004**, *25*, 1463–1473.

- 
238. Perdew, J. P.; Burke, K.; Ernzerhof, M. Generalized Gradient Approximation Made Simple. *Phys. Rev. Lett.* **1996**, *77* (18), 3865–3868.
239. Stone, N. J. Table of Nuclear Magnetic Dipole and Electric Quadrupole Moments. *At. Data Nucl. Data Tables* **2005**, *90* (1), 75–176.
240. While the difference between the experimental and theoretical values could arise from the difference between the (calculated) equilibrium structures and (measured) vibrationally averaged structures, these differences seem too large. For example, in HF–BF<sub>3</sub>, which is a much lighter system, the estimated anharmonic extension of the weak (H)F–B bond was only 0.0097 Å. See reference 31. However, it is possible that a portion of the observed discrepancies could be accounted for on this basis.
241. Mo, Y.; Bao, P.; Gao, J. Energy Decomposition Analysis Based on a Block-Localized Wavefunction and Multistate Density Functional Theory. *Phys. Chem. Chem. Phys.* **2011**, *13* (15), 6760–6775.
242. Mo, Y.; Gao, J.; Peyerimhoff, S. D. Energy Decomposition Analysis of Intermolecular Interactions Using a Block-Localized Wave Function Approach. *J. Chem. Phys.* **2000**, *112* (13), 5530.
243. Brauer, C. S.; Craddock, M. B.; Kilian, J.; Grumstrup, E. M.; Orilall, M. C.; Mo, Y.; Gao, J.; Leopold, K. R. Amine-Hydrogen Halide Complexes: Experimental Electric Dipole Moments and a Theoretical Decomposition of Dipole Moments and Binding Energies. *J. Phys. Chem. A* **2006**, *110*, 10025–10034.
244. Cotton, F.A.; Wilkinson, G., *Advanced Inorganic Chemistry. A Comprehensive Text*, 3rd Edition, Wiley, NY, 1972.
245. Michaud, J. M.; Cooke, S. A.; Gerry, M. C. L. Rotational Spectra, Structures, Hyperfine Constants, and the Nature of the Bonding of KrCuF and KrCuCl. *Inorg. Chem.* **2004**, *43* (13), 3871–3881.
246. Thomas, J. M.; Walker, N. R.; Cooke, S. A.; Gerry, M. C. L. Microwave Spectra and Structures of KrAuF, KrAgF, and KrAgBr; <sup>83</sup>Kr Nuclear Quadrupole Coupling and the Nature of Noble Gas–Noble Metal Halide Bonding. *J. Am. Chem. Soc.* **2004**, *126* (4), 1235–1246.
247. Campbell, E. J.; Buxton, L. W.; Keenan, M. R.; Flygare, W. H. <sup>83</sup>Kr and <sup>131</sup>Xe Nuclear Quadrupole Coupling and Quadrupolar Shielding in KrHCl and XeDCl. *Phys. Rev. A* **1981**, *24* (2), 812–821.

- 
248. Jonas, V.; Frenking, G.; Reetz, M. T. Comparative Theoretical-Study of Lewis Acid-Base Complexes of BH<sub>3</sub>, BF<sub>3</sub>, BCl<sub>3</sub>, AlCl<sub>3</sub>, and SO<sub>2</sub>. *J. Am. Chem. Soc.* **1994**, *116*, 8741–8753.
249. Mo, Y.; Gao, J. Polarization and Charge-Transfer Effects in Lewis Acid-Base Complexes. *J. Phys. Chem. A* **2001**, *105* (26), 6530–6536.
250. Elm, J.; Bilde, M.; Mikkelsen, K. V. Assessment of Density Functional Theory in Predicting Structures and Free Energies of Reaction of Atmospheric Prenucleation Clusters. *J. Chem. Theory Comput.* **2012**, *8* (6), 2071–2077.
251. Gaussian 09, Revision D.01, M. J. Frisch, G. W. Trucks, H. B. Schlegel, G. E. Scuseria, M. A. Robb, J. R. Cheeseman, G. Scalmani, V. Barone, B. Mennucci, G. A. Petersson, H. Nakatsuji, M. Caricato, X. Li, H. P. Hratchian, A. F. Izmaylov, J. Bloino, G. Zheng, J. L. Sonnenberg, M. Hada, M. Ehara, K. Toyota, R. Fukuda, J. Hasegawa, M. Ishida, T. Nakajima, Y. Honda, O. Kitao, H. Nakai, T. Vreven, J. A. Montgomery, Jr., J. E. Peralta, F. Ogliaro, M. Bearpark, J. J. Heyd, E. Brothers, K. N. Kudin, V. N. Staroverov, R. Kobayashi, J. Normand, K. Raghavachari, A. Rendell, J. C. Burant, S. S. Iyengar, J. Tomasi, M. Cossi, N. Rega, J. M. Millam, M. Klene, J. E. Knox, J. B. Cross, V. Bakken, C. Adamo, J. Jaramillo, R. Gomperts, R. E. Stratmann, O. Yazyev, A. J. Austin, R. Cammi, C. Pomelli, J. W. Ochterski, R. L. Martin, K. Morokuma, V. G. Zakrzewski, G. A. Voth, P. Salvador, J. J. Dannenberg, S. Dapprich, A. D. Daniels, Ö. Farkas, J. B. Foresman, J. V. Ortiz, J. Cioslowski, and D. J. Fox, Gaussian, Inc., Wallingford CT, 2009.
252. Neese, F. The ORCA Program System. *Comput. Mol. Sci.* **2012**, *2* (1), 73–78.

## Appendices



## Appendix A : Supplemental Material for Chapter 1

### Experimental Conditions

SO<sub>3</sub> was pulsed into the microwave cavity through a 0.8 mm nozzle with an Ar stagnation pressure of 1.3 atm. Formic acid (~12% water) was added separately with Ar at 0.7 atm through a continuous flowline needle with an ID of 0.016" that terminated a few mm downstream of the expansion orifice. For cavity experiments, the nozzle was pulsed at a rate of 4 Hz, and four free induction decay signals were collected per pulse with a data collection time of 140.8 μs. Typically, ~2,000 fids were averaged for each cavity run. For chirp experiments, ~50,000 fids were averaged.

### Computational Details

Two separate protocols were used to generate the potential energy surface for the H<sub>2</sub>O, SO<sub>3</sub>, and HCOOH complexes. For the DFT protocol, equilibrium geometries and transition state structures were evaluated using the M06-2X density functional, which has previously been shown to perform well for small pre-nucleation clusters.<sup>250</sup> The M06-2X calculations were performed with the 6-311++G(3df,3pd) basis set and an ultrafine integration grid was used. Analytic vibrational frequencies were determined to verify the authenticity of stationary points and were subsequently used for the molecular partition functions necessary to compute the zero point vibrational energies, Figure A.3. The DFT potential energy surface was then validated with a highly accurate wave function protocol. In the WF protocol, geometries were optimized using MP2/6-311++G(3df,3pd) and single point electronic energies were computed using CCSD(T) with the complete basis set extrapolation of Neese and Valeev between the ANO-pVDZ and AND-pTZV basis sets.<sup>39</sup> Zero point vibrational energies from the MP2 calculations were used to adjust the CCSD(T) single point energies, Figure 1.2. The DFT and high accuracy WF protocol potential energy surfaces are in strong agreement for the formation of FSA, further emphasizing the reliability of the former calculations. All subsequent calculations were done using the DFT protocol. All DFT and MP2 geometry optimizations and frequency calculations were performed using the Gaussian09 Rev D.01 software package.<sup>251</sup> All CCSD(T) calculations were performed using the ORCA 3.0.3 software package.<sup>252</sup>

Since previous theoretical work has been done on H<sub>2</sub>SO<sub>4</sub>···HCOOH,<sup>18</sup> no new geometries were tested and a calculation on the global minimum was done for computational consistency. However, because the SO<sub>3</sub>···HCOOH complex has not been previously considered, a few starting geometries were tested to find the global minimum. Four minima were found, two for both the trans- and cis- geometries of the HCOOH monomer. These geometries, along with their associated energies, are in Figure A.4. An isomer of FSA was also considered, in part to access if it might account for some of the unassigned transitions in the chirp spectrum. The acidic proton was rotated away from

the formic tail and a minimum was found with the proton hovering over one of the sulfur-oxygens. This geometry, along with its energy relative to the FSA minimum, is in Figure A.5.

Further computational work was done on some larger carboxylic acids to confirm that the reaction between  $\text{SO}_3$  and a carboxylic acid is viable when the carbon tail is significantly larger. This was tested with benzoic and pinic acid, two acids recently implicated in nucleation schemes.<sup>20-22</sup> The results, Figure A.6, suggest that any carboxylic acid can undergo such a reaction in the gas phase and that the associated barrier is fairly small (less than 1 kcal/mol when including zero point energy corrections).

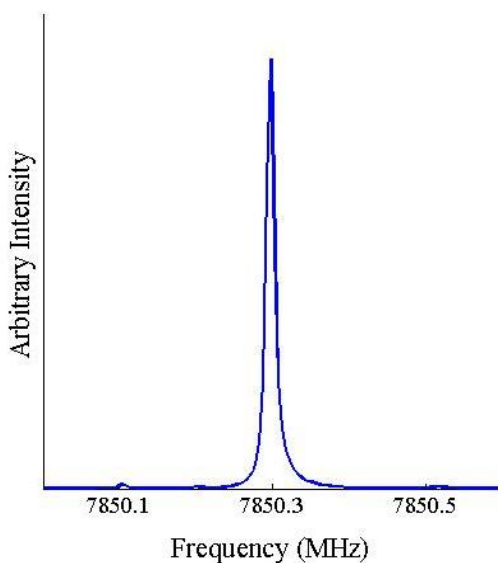


**Figure A.1 Cavity Spectrum of FSA Rotational Transition**

Cavity spectrum of the  $2_{02} \leftarrow 1_{01}$  transition for FSA (the parent isotopologue). This spectrum is an average of 500 pulses at 140.8  $\mu\text{s}$  span time.

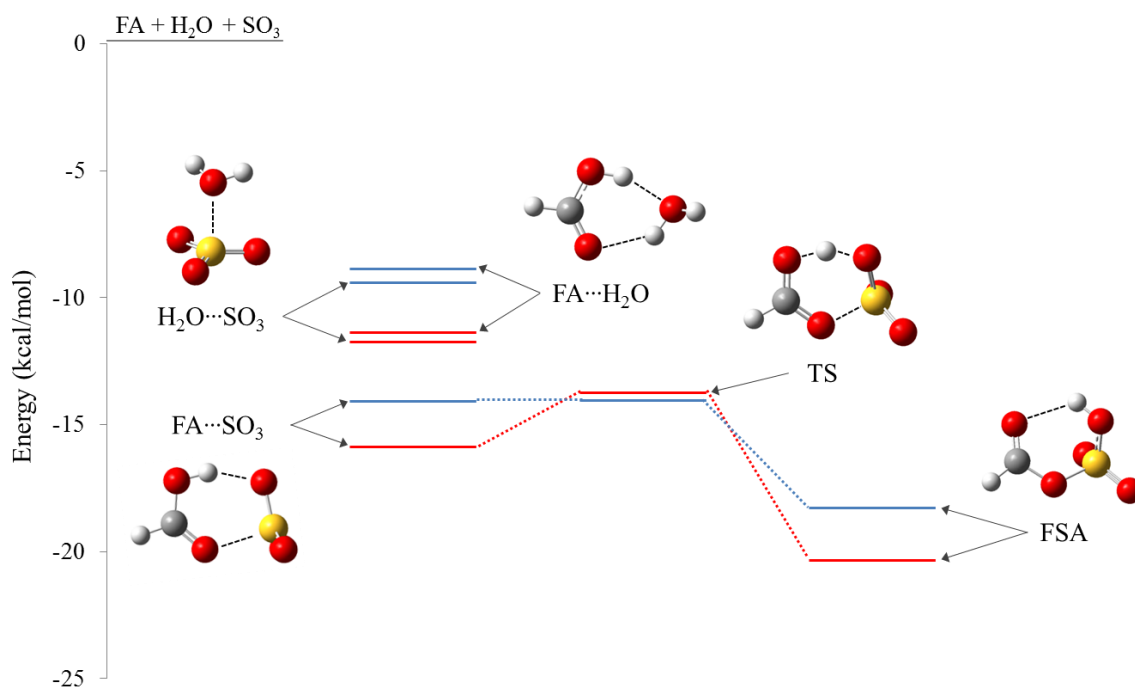


**Figure A.2 DFT Potential Energy Landscape of H<sub>2</sub>O, SO<sub>3</sub>, and HCOOH**

Potential energy landscape of the complexes formed between H<sub>2</sub>O, SO<sub>3</sub>, and HCOOH done at the M06-2X/6-311++G(3df,3pd) level of theory. The red and blue traces are ZPE uncorrected and corrected, respectively. Zero is defined for both as the sum of the monomer energies. The barrier to conversion from the complex to FSA is 2.1 kcal/mol without ZPE corrections and 0.04 kcal/mol with ZPE corrections. These values are in good agreement with the results from the single point CCSD(T) calculations reported in Fig. 2, (2.2 and 0.2 kcal/mol, respectively). Although, while the SO<sub>3</sub>···HCOOH, TS, and FSA calculations are in good agreement between the DFT and WF protocol, the energetic ordering of the HCOOH···H<sub>2</sub>O and SO<sub>3</sub>···H<sub>2</sub>O is reversed. However, in both protocols, these complexes are always 3-4 kcal/mol higher in energy than the HCOOH···SO<sub>3</sub> complex.

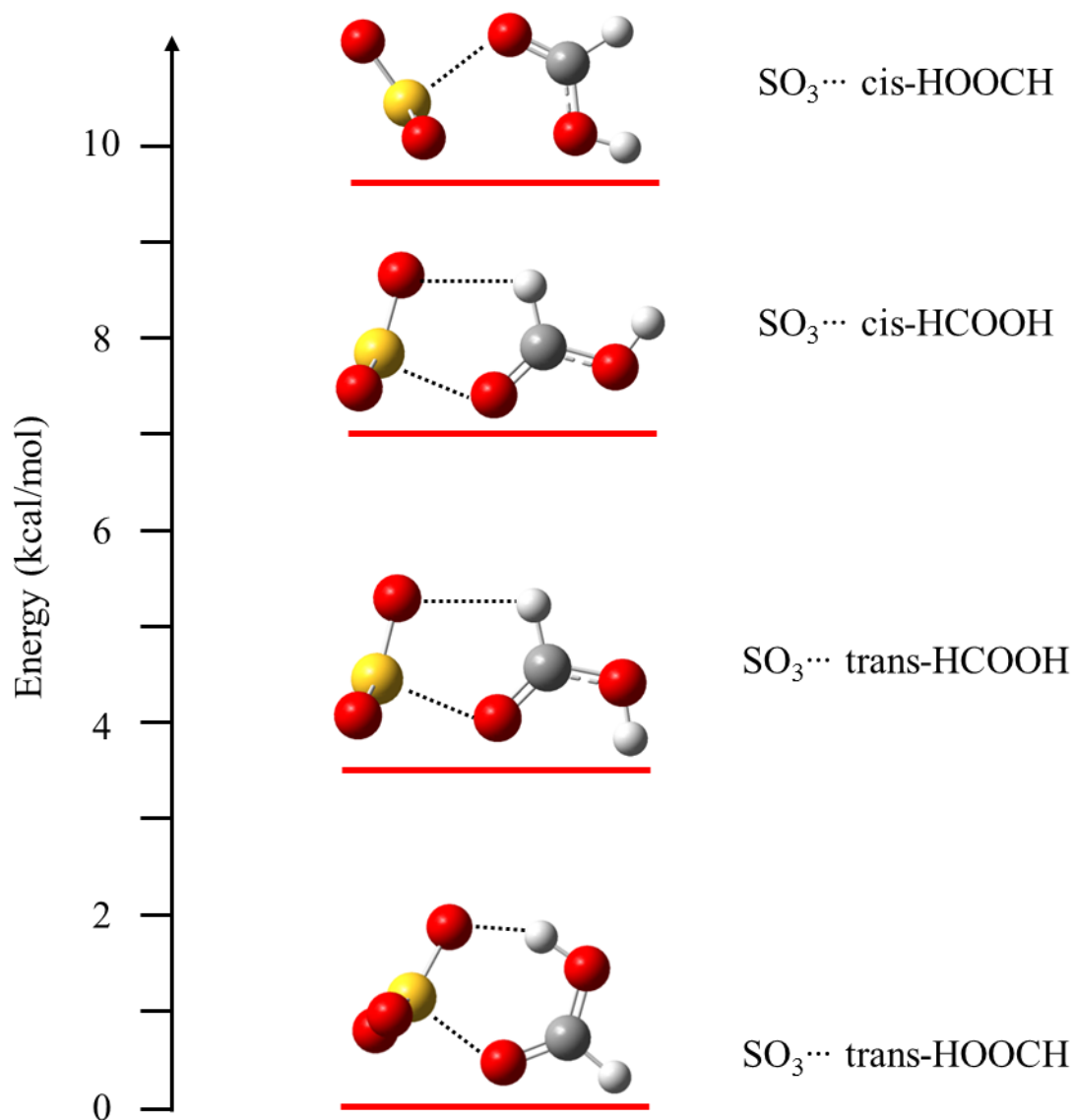


**Figure A.3 Energy Comparison of  $\text{SO}_3$ -HCOOH Isomers**

Energy comparison of the four investigated isomers for the  $\text{SO}_3 \cdots \text{HCOOH}$  van der Waals complex done at M06-2X/6-311++G(3df,3pd). The energies, as compared to the global minimum  $\text{SO}_3 \cdots \text{trans-HOOCH}$ , are 3.4, 7.1, and 9.6 kcal/mol for  $\text{SO}_3 \cdots \text{trans-HCOOH}$ ,  $\text{SO}_3 \cdots \text{cis-HCOOH}$ , and  $\text{SO}_3 \cdots \text{cis-HOOCH}$ , respectively.

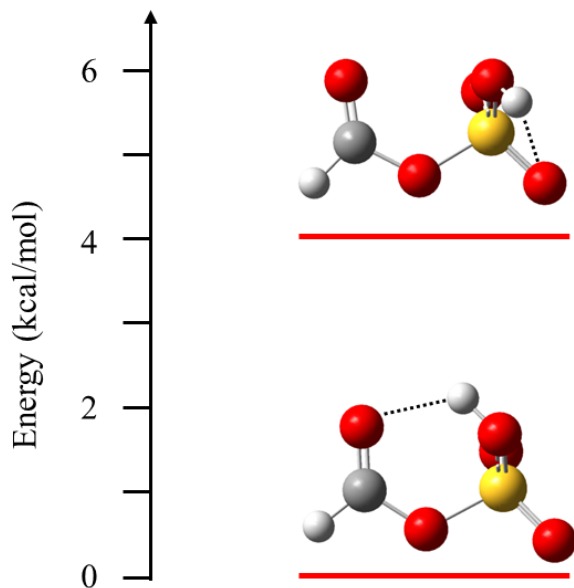


**Figure A.4 Energy Comparison of FSA Isomers**

Energy comparison of FSA and its isomer done with the M06-2X functional and the 6-311++G(3df,3pd) basis set. In the high energy isomer, the acidic proton is bent away from the formic oxygen and hydrogen bonds with the sulfuric oxygen. This configuration is 4.0 kcal/mol higher in energy and is unlikely to be the carrier of any unassigned lines in the spectrum.

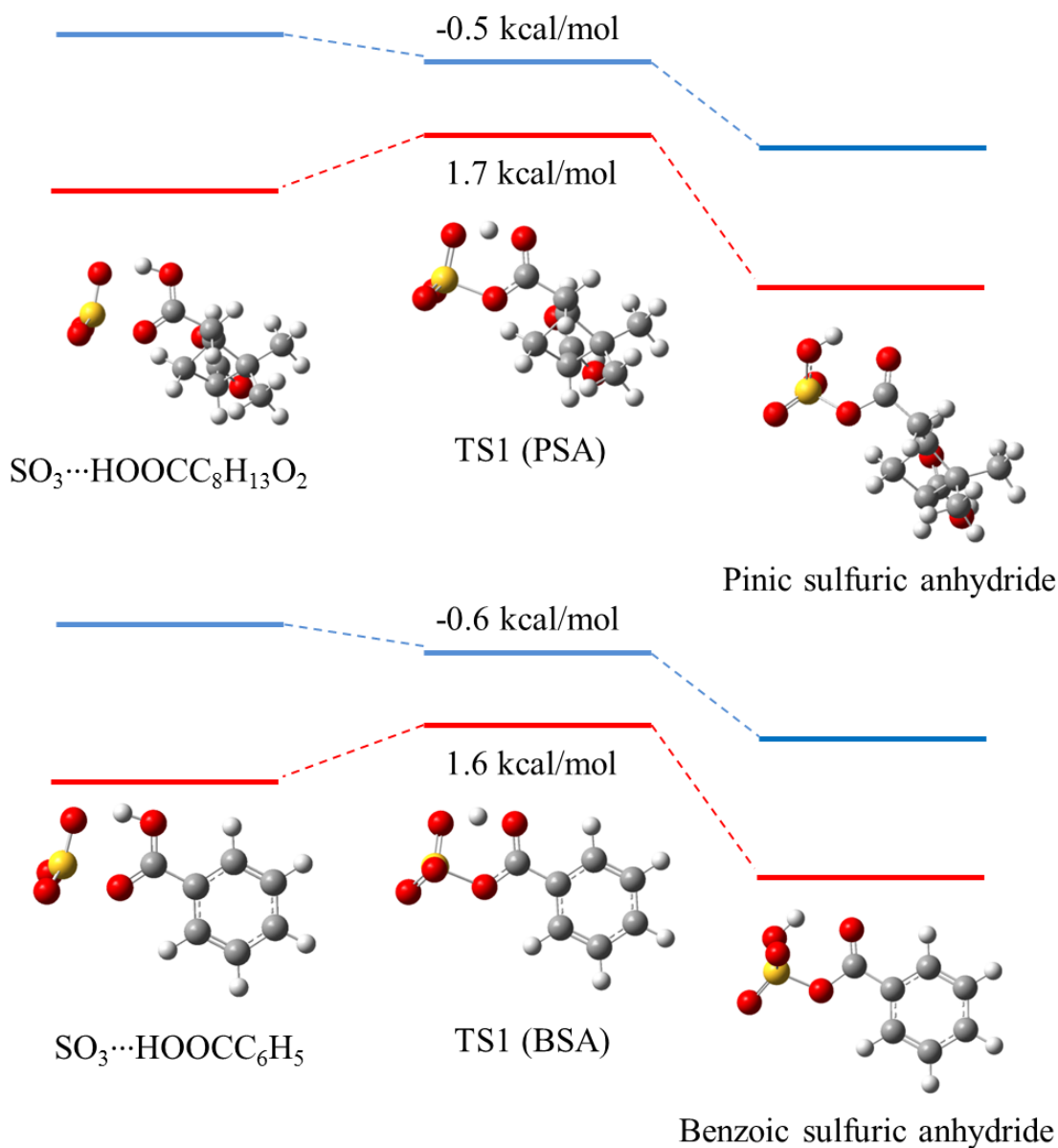


**Figure A.5 Potential Energy Surface for the Formation of FSA Analogues**

Uncorrected (red trace) and ZPE corrected (blue trace) potential energy surfaces for the conversion of the benzoic acid -  $\text{SO}_3$  and pinic acid -  $\text{SO}_3$  van der Waals complexes to benzoic sulfuric anhydride (BSA) and pinic sulfuric anhydride (PSA), respectively, the analogous species' to FSA. The calculations were done at M06-2X/6-311++G(3df,3pd). The uncorrected barrier to conversion is 1.6 and 1.7 kcal/mol for BSA and PSA, respectively. With ZPE corrections, the "barrier" is -0.6 and -0.5 kcal/mol for BSA and PSA, respectively, suggesting that the conversion is barrierless and that the mechanism can be extended to any carboxylic acid.

**Table A.1 Comparison of Theoretical Rotational Constants with Experimental Results and Predicted Dipole Moment Components**

Constant	Experimental FSA	FSA*	H <sub>2</sub> SO <sub>4</sub> ··· HCOOH*	SO <sub>3</sub> ···trans-HOOCH (global minimum)*	SO <sub>3</sub> ···trans- HCOOH*	SO <sub>3</sub> ···cis- HCOOH*	SO <sub>3</sub> ···cis- HOOCH*
<i>A</i> (MHz)	4510.1155(12)	4541.675	3626.473	4420.316	5007.035	5029.402	4232.445
<i>B</i> (MHz)	2013.28751(13)	2026.871	1020.113	1802.583	1327.441	1335.975	1684.916
<i>C</i> (MHz)	1913.33629(13)	1926.747	945.728	1693.684	1310.392	1320.575	1561.256
μ <sub>a</sub> (D)	-	3.1882	1.9400	4.3548	4.8972	5.7736	6.5246
μ <sub>b</sub> (D)	-	0.4768	1.0393	0.4498	0.0201	2.7437	0.1960
μ <sub>c</sub> (D)	-	0.9728	2.1014	0.0427	0.0000	0.0001	0.0002

Observed rotational constants for O<sub>2</sub>S(OH)OCHO (FSA) and the theoretical constants for FSA, SO<sub>3</sub>···HCOOH, and H<sub>2</sub>SO<sub>4</sub>···HCOOH as well as their calculated dipole moments.

\*All calculations were done using the M06-2X functional with the 6-311++G(3df,3pd) basis set.

**Table A.2 Theoretical Predictions for SO<sub>3</sub>, H<sub>2</sub>O, and HCOOH complexes**

Species	M06-2X/6-311++G(3df,3pd)*		MP2/6-311++G(3df,3pd)*		CCSD(T)/CBS// MP2/6-311++G(3df,3pd)*	
	E <sub>total</sub>	E <sub>total</sub> (ZPE)	E <sub>total</sub>	E <sub>total</sub> (ZPE)	E <sub>total</sub>	E <sub>total</sub> (ZPE) <sup>‡</sup>
SO <sub>3</sub>	-623.8177049	-623.8047711	-623.0496879	-623.0372518	-623.2305211	-623.218085
H <sub>2</sub> O	-76.42703067	-76.40538884	-76.3242865	-76.30268139	-76.37767678	-76.35607167
HCOOH	-189.7636041	-189.7292355	-189.4756223	-189.4415729	-189.5997181	-189.5656688
H <sub>2</sub> O⋯HCOOH	-266.2087762	-266.1487544	-265.8166871	-265.7569836	-265.994682	-265.9349785
H <sub>2</sub> O⋯SO <sub>3</sub>	-700.2634612	-700.2251554	-699.3889206	-699.3516275	-699.6235215	-699.5862284
HCOOH⋯SO <sub>3</sub>	-813.6066029	-813.5564534	-812.5458667	-812.4964042	-812.8522249	-812.8027625
TS1 <sup>†</sup>	-813.6031907	-813.5563822	-812.5388411	-812.4925303	-812.8487521	-812.8024414
FSA	-813.6137183	-813.5631431	-812.5474222	-812.4976261	-812.8593028	-812.8095067

\* All values in hartrees.

<sup>†</sup> Transition state for HCOOH⋯SO<sub>3</sub> → FSA. The imaginary frequencies ( $\nu_{im}$ ) of the transition state (TS) at M06-2X/6-311++G(3df,3pd) and MP2/6-311++G(3df,3pd) are  $-877.46i$  cm<sup>-1</sup> and  $-861.89i$  cm<sup>-1</sup>, respectively.

<sup>‡</sup> The MP2/6-311++G(3df,3pd) zero point energy corrections were used to augment the CCSD(T) single point energies.



**Table A.3 Selected FSA Structural Parameters from M06-2X and MP2 Calculations**

Parameter* †	M06-2X/6-311++G(3df,3pd)	MP2/6-311++G(3df,3pd)
C1-H2	1.0920	1.0905
C1-O3	1.1887	1.2011
C1-O4	1.3563	1.3603
O4-S5	1.6352	1.6534
S5-O6	1.4032	1.4100
S5-O7	1.4109	1.4180
S5-O8	1.5550	1.5616
O8-H9	0.9745	0.9764
O3...H9	2.0811	2.0167
∠(O3-C1-H2)	125.8	125.6
∠(O3-C1-O4)	125.0	125.6
∠(C1-O4-O5)	119.6	118.4
∠(O4-S5-O8)	101.2	101.0
∠(S5-O8-H9)	108.8	106.9
∠(O4-S5-O6)	104.6	104.3
∠(O4-S5-O7)	106.7	106.5
∠(O3...H9-O8)	121.8	126.2

\*All distances in Å.

† All angles in degrees.

**Table A.4 Cartesian Coordinates for Previously Unstudied Species from Theory**

HCOOH...SO <sub>3</sub>						
Atomic Number	M06-2X/6-311++G(3df,3pd)			MP2/6-311++G(3df,3pd)		
	X	Y	Z	X	Y	Z
16	-0.906180	0.111857	0.006211	-0.977336	0.122764	0.000657
8	-1.550743	-0.477744	-1.100341	-1.458205	-0.406860	-1.228588
8	-0.229560	1.364497	-0.204401	-0.294950	1.394138	-0.019996
8	-1.296051	-0.203942	1.325475	-1.433915	-0.379464	1.250634
6	1.882888	-0.614280	-0.002741	1.977040	-0.592408	-0.000322
8	0.734444	-1.054458	-0.028774	0.852356	-1.083467	-0.002915
1	2.718654	-1.312599	0.019173	2.860548	-1.228432	0.001973
8	2.226256	0.624188	0.001233	2.270661	0.679633	0.000073
1	1.408119	1.188244	-0.047637	1.427000	1.186827	-0.004215

TS [HCOOH...SO <sub>3</sub> → FSA]						
Atomic Number	M06-2X/6-311++G(3df,3pd)			MP2/6-311++G(3df,3pd)		
	X	Y	Z	X	Y	Z
16	-0.803983	0.067553	0.020278	-0.807968	0.069475	0.025697
8	-1.659242	-0.442750	-0.973519	-1.706697	-0.478736	-0.919705
8	-0.096451	1.314715	-0.361614	-0.103536	1.300758	-0.442758
8	-1.123970	-0.025486	1.391487	-1.061351	0.033101	1.422094
6	1.784294	-0.623020	-0.011945	1.788823	-0.621012	-0.013340
8	0.582365	-1.056355	-0.084401	0.590839	-1.083747	-0.093471
1	2.549863	-1.396440	0.021694	2.564423	-1.382032	0.024197
8	2.111460	0.572114	0.011303	2.102881	0.585515	0.011305
1	1.094793	1.155818	-0.140519	1.053046	1.141387	-0.175019

FSA						
Atomic Number	M06-2X/6-311++G(3df,3pd)			MP2/6-311++G(3df,3pd)		
	X	Y	Z	X	Y	Z
16	-0.730897	-0.000421	0.082485	-0.735471	0.004988	0.084759
8	-1.858725	-0.668491	-0.418129	-1.868999	-0.661886	-0.423694
8	-0.374055	1.140781	-0.911670	-0.359537	1.134957	-0.925424
8	-0.617724	0.449950	1.414800	-0.616179	0.465071	1.420764
6	1.784698	-0.595383	-0.056131	1.782320	-0.601415	-0.050010
8	0.507645	-1.038253	-0.168325	0.506114	-1.059836	-0.156957
1	2.465732	-1.448049	-0.094961	2.464980	-1.451325	-0.078898
8	2.104614	0.544866	0.046467	2.106008	0.551810	0.038739
1	0.426400	1.596256	-0.593163	0.469380	1.539078	-0.604611

**Table A.5 Observed Transitions for the Parent Isotopologue of FSA (HOSO<sub>3</sub>CHO)**

J'	K <sub>a</sub> '	K <sub>c</sub> '	J''	K <sub>a</sub> ''	K <sub>c</sub> ''	Observed Frequency (MHz)	Calculated Frequency (MHz)	Obs-Calc (MHz)
1	0	1	0	0	0	3926.623	3926.623	0.000
2	1	2	1	1	1	7753.281	7753.281	0.000
2	0	2	1	0	1	7850.296	7850.297	-0.001
2	1	1	1	1	0	7953.184	7953.183	0.001
3	1	3	2	1	2	11628.094	11628.091	0.003
3	0	3	2	0	2	11768.091	11768.091	0.000
3	2	2	2	2	1	11779.804	11779.804	-0.000
3	2	1	2	2	0	11791.554	11791.552	0.002
3	1	2	2	1	1	11927.889	11927.891	-0.002
4	1	4	3	1	3	15500.786	15500.780	0.006
4	0	4	3	0	3	15677.160	15677.158	0.002
4	2	3	3	2	2	15704.082	15704.084	-0.002
4	3	2	3	3	1	15712.037	15712.038	-0.001
4	3	1	3	3	0	15712.361	15712.363	-0.002
4	2	2	3	2	1	15733.341	15733.342	-0.001
4	1	3	3	1	2	15900.257	15900.261	-0.004
4	0	4	3	1	3	13417.348	13417.348	-0.000
1	1	1	0	0	0	6423.447	6423.448	-0.001
2	1	2	1	0	1	10250.110	10250.106	0.004
3	1	3	2	0	2	14027.904	14027.901	0.003
1	1	0	0	0	0	6523.398	6523.399	-0.001
2	1	1	1	0	1	10549.958	10549.960	-0.002
3	1	2	2	0	2	14627.550	14627.554	-0.004

**Table A.6 Observed Transitions for the  $^{34}\text{S}$  Isotopologue of FSA ( $\text{HO}^{34}\text{SO}_3\text{CHO}$ )**

$J'$	$K_a'$	$K_c'$	$J''$	$K_a''$	$K_c''$	Observed Frequency (MHz)	Calculated Frequency (MHz)	Obs-Calc (MHz)
2	1	2	1	1	1	7723.881	7723.885	-0.004
2	0	2	1	0	1	7820.106	7820.106	0.000
2	1	1	1	1	0	7922.086	7922.089	-0.003
3	1	3	2	1	2	11584.028	11584.031	-0.003
3	0	3	2	0	2	11722.950	11722.950	0.000
3	1	2	2	1	1	11881.286	11881.284	0.002
4	1	4	3	1	3	15442.095	15442.092	0.003
4	0	4	3	0	3	15617.234	15617.237	-0.003
4	1	3	3	1	2	15838.185	15838.186	-0.001

**Table A.7 Observed Transitions for the  $^{13}\text{C}$  Isotopologue of FSA ( $\text{HOSO}_3^{13}\text{CHO}$ )**

$J'$	$K_a'$	$K_c'$	$J''$	$K_a''$	$K_c''$	Observed Frequency (MHz)	Calculated Frequency (MHz)	Obs-Calc (MHz)
2	1	2	1	1	1	7650.413	7650.417	-0.004
2	0	2	1	0	1	7747.739	7747.739	0.000
3	1	3	2	1	2	11473.785	11473.783	0.002
3	0	3	2	0	2	11614.233	11614.233	-0.000
3	1	2	2	1	1	11774.533	11774.534	-0.001
4	0	4	3	0	3	15471.983	15471.976	0.007

**Table A.8 Observed Transitions of DOSO<sub>3</sub>CHO**

J'	K <sub>a</sub> '	K <sub>c</sub> '	F'	J''	K <sub>a</sub> ''	K <sub>c</sub> ''	F''	Observed Frequency (MHz)	Calculated Frequency (MHz)	Obs-Calc (MHz)
1	0	1	0	0	0	0	1	3903.509	3903.512	-0.003
1	0	1	2	0	0	0	1	3903.568	3903.568	-0.000
1	0	1	1	0	0	0	1	3903.605	3903.605	-0.000
2	1	2	3	1	1	1	2	7693.439	7693.439	0.000
2	1	2	2	1	1	1	1	7693.475	7693.478	-0.003
2	0	2	1	1	0	1	1	7803.126	7803.125	0.001
2	0	2	3	1	0	1	2	7803.180	7803.185	-0.005
2	0	2	2	1	0	1	1	7803.186	7803.187	-0.001
2	1	1	1	1	1	0	0	7920.778	7920.779	-0.001
2	1	1	3	1	1	0	2	7920.819	7920.818	0.001
2	1	1	2	1	1	0	1	7920.852	7920.857	-0.005
3	1	3	2	2	1	2	2	11537.688	11537.688	0.000
3	1	3	4	2	1	2	3	11537.714	11537.718	-0.004
3	1	3	3	2	1	2	2	11537.732	11537.730	0.002
3	0	3	4	2	0	2	3	11694.905	11694.907	-0.002
3	2	2	2	2	2	1	1	11710.619	11710.632	-0.013
3	2	2	4	2	2	1	3	11710.654	11710.654	0.000
3	2	2	3	2	2	1	2	11710.684	11710.694	-0.010
3	2	1	2	2	2	0	1	11726.429	11726.417	0.012
3	2	1	4	2	2	0	3	11726.447	11726.439	0.008
3	2	1	3	2	2	0	2	11726.486	11726.479	0.007
3	1	2	4	2	1	1	3	11878.707	11878.702	0.005
3	1	2	3	2	1	1	2	11878.720	11878.713	0.007
4	1	4	5	3	1	3	4	15379.171	15379.176	-0.005
4	1	4	4	3	1	3	3	15379.189	15379.181	0.008
4	0	4	5	3	0	3	4	15574.959	15574.967	-0.008
4	0	4	3	3	0	3	2	15574.978	15574.971	0.007
4	2	3	3	3	2	2	2	15611.081	15611.098	-0.017
4	2	3	5	3	2	2	4	15611.102	15611.102	-0.000
4	2	3	4	3	2	2	3	15611.127	15611.119	0.008
4	2	2	3	3	2	1	2	15650.343	15650.353	-0.010
4	2	2	5	3	2	1	4	15650.361	15650.358	0.003
4	2	2	4	3	2	1	3	15650.386	15650.375	0.011
4	1	3	5	3	1	2	4	15833.410	15833.420	-0.010
4	1	3	4	3	1	2	3	15833.431	15833.425	0.006
1	1	1	1	0	0	0	1	6297.308	6297.309	-0.001
1	1	1	2	0	0	0	1	6297.329	6297.328	0.001
3	1	2	3	2	0	2	2	14503.768	14503.776	-0.008
3	1	2	4	2	0	2	3	14503.789	14503.785	0.004

**Table A.8 continued...**

J'	K <sub>a</sub> '	K <sub>c</sub> '	F'	J''	K <sub>a</sub> ''	K <sub>c</sub> ''	F''	Observed Frequency (MHz)	Calculated Frequency (MHz)	Obs-Calc (MHz)
2	1	1	3	1	0	1	2	10428.269	10428.268	0.001
2	1	1	1	1	0	1	0	10428.314	10428.313	0.001
3	1	3	2	2	0	2	2	13821.695	13821.682	0.013
3	1	3	4	2	0	2	3	13821.726	13821.732	-0.006
2	1	2	2	1	0	1	1	10087.179	10087.181	-0.002
2	1	2	3	1	0	1	2	10087.197	10087.199	-0.002
3	0	3	4	2	1	2	3	9410.893	9410.893	-0.000
3	0	3	3	2	1	2	2	9410.917	9410.915	0.002

**Table A.9 Observed Transitions of HOSO<sub>3</sub>CDO**

J'	K <sub>a</sub> '	K <sub>c</sub> '	F'	J''	K <sub>a</sub> ''	K <sub>c</sub> ''	F''	Observed Frequency (MHz)	Calculated Frequency (MHz)	Obs-Calc (MHz)
1	0	1	2	0	0	0	1	3820.432	3820.432	0.000
2	1	2	3	1	1	1	2	7530.713	7530.716	-0.003
2	1	2	2	1	1	1	2	7530.753	7530.752	0.001
2	0	2	3	1	0	1	2	7637.244	7637.242	0.002
2	1	1	1	1	1	0	0	7750.952	7750.952	-0.000
2	1	1	3	1	1	0	2	7750.994	7750.989	0.005
3	1	3	4	2	1	2	3	11293.836	11293.836	0.000
3	0	3	4	2	0	2	3	11446.830	11446.831	-0.001
3	2	2	4	2	2	1	3	11461.236	11461.238	-0.002
3	2	1	4	2	2	0	3	11475.679	11475.679	0.000
3	1	2	4	2	1	1	3	11624.166	11624.168	-0.002
3	1	3	3	2	0	2	2	13646.774	13646.773	0.001
4	1	4	5	3	1	3	4	15054.369	15054.366	0.003
4	0	4	5	3	0	3	4	15245.730	15245.729	0.001
4	2	3	5	3	2	2	4	15278.804	15278.806	-0.002
4	3	2	5	3	3	1	4	15288.581	15288.580	0.001
4	3	1	5	3	3	0	4	15289.026	15289.026	0.000
4	2	2	5	3	2	1	4	15314.739	15314.739	0.000
4	1	3	5	3	1	2	4	15494.459	15494.462	-0.003
2	1	2	3	1	0	1	2	9990.149	9990.151	-0.002
2	1	2	2	1	0	1	1	9990.176	9990.177	-0.001
2	1	1	3	1	0	1	2	10320.569	10320.569	-0.000
3	1	2	3	2	0	2	2	14307.463	14307.460	0.003
3	1	2	4	2	0	2	3	14307.494	14307.495	-0.001
3	1	2	2	2	0	2	1	14307.510	14307.510	0.000
3	1	3	4	2	0	2	3	13646.743	13646.744	-0.001
3	1	3	3	2	0	2	2	13646.774	13646.773	0.001



**Table A.10 Spectroscopic Constants for Observed Isotopologues of FSA**

Constant	HOSO <sub>3</sub> CHO	HO <sup>34</sup> SO <sub>3</sub> CHO*	HOSO <sub>3</sub> <sup>13</sup> CHO*	DOSO <sub>3</sub> CHO <sup>†</sup>	HOSO <sub>3</sub> CDO
<b>A (MHz)</b>	4510.1155(12)	4511.41(28)	4496.4(11)	4402.3855(21)	4424.72510(82)
<b>B (MHz)</b>	2013.28751(13)	2005.30074(47)	1987.8089(13)	2008.63262(62)	1965.28477(27)
<b>C (MHz)</b>	1913.33629(13)	1906.19874(47)	1887.5407(13)	1894.94290(67)	1855.14994(29)
<b><math>\Delta_{ID}</math> (amu<math>\text{\AA}^2</math>)</b>	-98.9	-98.9	-98.9	-99.7	-99.0
<b>D <math>\chi_{aa}</math> (MHz)</b>	-	-	-	0.1243(56)	0.0347(56)
<b>D (<math>\chi_{bb}-\chi_{cc}</math>) (MHz)</b>	-	-	-	-	0.1924(72)
<b><math>\Delta_J</math> (kHz)</b>	0.3030(55)	0.363(12)	0.444(55)	0.303(21)	0.2940(98)
<b><math>\Delta_{JK}</math> (kHz)</b>	1.427(29)	-	-	1.29(11)	1.341(27)
<b>RMS (kHz)</b>	2	3	3	6	2
<b>N</b>	23	9	6	47	27

\* For isotopologues where transitions with  $K > 1$  were not observed,  $\Delta_{JK}$  was not fit.

<sup>†</sup> ( $\chi_{bb}-\chi_{cc}$ ) was not necessary to fit the deuterium hyperfine transitions and is likely  $\sim 0$ .

## Appendix B : Supplemental Material for Chapter 2

**Table B.1 Observed Transitions for TMA-HCOOH**

J'	K <sub>a</sub> '	K <sub>c</sub> '	F'	J''	K <sub>a</sub> ''	K <sub>c</sub> ''	F''	Observed Frequency (MHz)	Calculated Frequency (MHz)	Obs-Calc (MHz)	Estimated Error (MHz)
2	1	2	2	1	1	1	1	5449.647	5449.649	-0.002	0.002
2	1	2	2	1	1	1	2	5449.813	5449.814	-0.001	0.002
2	1	2	3	1	1	1	2	5450.542	5450.544	-0.002	0.002
2	1	2	1	1	1	1	1	5450.782	5450.785	-0.003	0.003
2	1	2	1	1	1	1	0	5451.194	5451.196	-0.002	0.002
2	0	2	2	1	0	1	2	5557.370	5557.370	-0.000	0.002
2	0	2	2	1	0	1	1	5558.216	5558.216	-0.000	0.003
2	0	2	3	1	0	1	2	5558.288	5558.288	-0.000	0.003
2	0	2	1	1	0	1	1	5559.645	5559.644	0.001	0.003
2	1	1	2	1	1	0	1	5673.061	5673.058	0.003	0.004
2	1	1	1	1	1	0	1	5673.337	5673.332	0.005	0.006
2	1	1	2	1	1	0	2	5673.745	5673.739	0.006	0.004
2	1	1	3	1	1	0	2	5673.918	5673.915	0.003	0.002
2	1	1	1	1	1	0	0	5675.036	5675.035	0.001	0.004
3	1	3	3	2	1	2	3	8172.226	8172.228	-0.002	0.004
3	1	3	3	2	1	2	2	8172.958	8172.958	0.000	0.002
3	1	3	2	2	1	2	1	8173.172	8173.166	0.006	0.004
3	1	3	4	2	1	2	3	8173.221	8173.223	-0.002	0.008
3	0	3	2	2	0	2	1	8327.595	8327.602	-0.007	0.008
3	0	3	3	2	0	2	2	8327.718	8327.720	-0.002	0.005
3	0	3	4	2	0	2	3	8327.772	8327.772	0.000	0.002
3	1	2	3	2	1	1	2	8507.989	8507.987	0.002	0.003
3	1	2	4	2	1	1	3	8508.234	8508.233	0.001	0.005
3	1	2	2	2	1	1	1	8508.281	8508.282	-0.001	0.003
4	1	4	4	3	1	3	3	10893.086	10893.086	0.000	0.002
4	1	4	3	3	1	3	2	10893.151	10893.150	0.001	0.002
4	1	4	5	3	1	3	4	10893.212	10893.210	0.002	0.002
4	0	4	3	3	0	3	2	11085.844	11085.841	0.003	0.004
4	0	4	4	3	0	3	3	11085.871	11085.872	-0.001	0.002
4	0	4	5	3	0	3	4	11085.919	11085.919	0.000	0.002
4	2	3	4	3	2	2	3	11120.692	11120.691	0.001	0.002
4	2	3	5	3	2	2	4	11121.079	11121.079	0.000	0.002
4	2	3	3	3	2	2	2	11121.177	11121.178	-0.001	0.002
4	1	3	4	3	1	2	3	11339.400	11339.407	-0.007	0.006
4	1	3	5	3	1	2	4	11339.510	11339.519	-0.009	0.005
5	1	5	6	4	1	4	5	13609.733	13609.724	0.009	0.044
5	0	5	5	4	0	4	4	13829.439	13829.436	0.003	0.005
5	0	5	6	4	0	4	5	13829.484	13829.482	0.002	0.005
5	2	4	5	4	2	3	4	13896.149	13896.174	-0.025	0.042
5	2	4	6	4	2	3	5	13896.357	13896.380	-0.023	0.042
5	2	3	5	4	2	2	4	13971.623	13971.652	-0.029	0.042
5	2	3	6	4	2	2	5	13971.811	13971.826	-0.015	0.042
5	1	4	6	4	1	3	5	14166.438	14166.506	-0.068	0.065
6	1	6	6	5	1	5	5	16322.120	16322.118	0.002	0.090
6	1	6	7	5	1	5	6	16322.181	16322.168	0.013	0.090

**Table B.1 continued...**

J'	K <sub>a</sub> '	K <sub>c</sub> '	F'	J''	K <sub>a</sub> ''	K <sub>c</sub> ''	F''	Observed Frequency (MHz)	Calculated Frequency (MHz)	Obs-Calc (MHz)	Estimated Error (MHz)
6	0	6	7	5	0	5	6	16556.069	16556.117	-0.048	0.040
6	2	5	6	5	2	4	5	16668.281	16668.320	-0.039	0.044
6	2	5	7	5	2	4	6	16668.408	16668.446	-0.038	0.045
6	3	4	6	5	3	3	5	16704.262	16704.259	0.003	0.045
6	3	4	7	5	3	3	6	16704.494	16704.509	-0.015	0.045
6	3	3	6	5	3	2	5	16708.862	16708.860	0.002	0.043
6	2	4	7	5	2	3	6	16797.997	16798.047	-0.050	0.060
6	1	5	7	5	1	4	6	16987.739	16987.787	-0.048	0.038

**Table B.2 Observed Transitions for TMA-DCOOH**

J'	K <sub>a</sub> '	K <sub>c</sub> '	F'	J''	K <sub>a</sub> ''	K <sub>c</sub> ''	F''	Observed Frequency (MHz)	Calculated Frequency (MHz)	Obs-Calc (MHz)	Estimated Error (MHz)
4	1	4	4	3	1	3	3	10583.804	10583.803	0.001	0.004
4	1	4	3	3	1	3	2	10583.868	10583.870	-0.002	0.004
4	1	4	5	3	1	3	4	10583.932	10583.929	0.003	0.004
4	0	4	3	3	0	3	2	10770.225	10770.226	-0.001	0.004
4	0	4	4	3	0	3	3	10770.257	10770.264	-0.007	0.004
4	0	4	5	3	0	3	4	10770.303	10770.307	-0.004	0.004
4	1	3	4	3	1	2	3	11012.090	11012.087	0.003	0.004
4	1	3	5	3	1	2	4	11012.206	11012.203	0.003	0.004
5	1	5	6	4	1	4	5	13223.694	13223.685	0.009	0.080
5	0	5	5	4	0	4	4	13437.309	13437.308	0.001	0.002
5	0	5	6	4	0	4	5	13437.351	13437.350	0.001	0.002
5	1	4	6	4	1	3	5	13758.059	13758.072	-0.013	0.053
6	1	6	7	5	1	5	6	15859.691	15859.690	0.001	0.065
6	0	6	7	5	0	5	6	16088.785	16088.769	0.016	0.065
6	2	5	7	5	2	4	6	16191.512	16191.490	0.022	0.044
6	2	4	7	5	2	3	6	16309.991	16309.956	0.035	0.060
6	1	5	6	5	1	4	5	16498.730	16498.728	0.002	0.004
6	1	5	5	5	1	4	4	16498.753	16498.759	-0.006	0.004
6	1	5	7	5	1	4	6	16498.775	16498.774	0.001	0.004

**Table B.3 Observed Transitions for TMA(<sup>13</sup>C11)-HCOOH**

Transitions for this isotopologue were all collected with the cavity, thus all estimated errors were set to 4 kHz, the typical error for transitions measured on the cavity.

J'	K <sub>a</sub> '	K <sub>c</sub> '	F'	J''	K <sub>a</sub> ''	K <sub>c</sub> ''	F''	Observed Frequency (MHz)	Calculated Frequency (MHz)	Obs- Calc (MHz)
3	1	3	3	2	1	2	2	8125.740	8125.741	-0.001
3	1	3	2	2	1	2	1	8125.960	8125.959	0.001
3	1	3	4	2	1	2	3	8126.008	8126.010	-0.002
3	0	3	3	2	0	2	2	8275.015	8275.014	0.001
3	0	3	4	2	0	2	3	8275.064	8275.065	-0.001
3	1	2	3	2	1	1	2	8448.427	8448.421	0.006
3	1	2	4	2	1	1	3	8448.676	8448.671	0.005
3	1	2	2	2	1	1	1	8448.722	8448.714	0.008
4	1	4	4	3	1	3	3	10830.356	10830.355	0.001
4	1	4	3	3	1	3	2	10830.420	10830.422	-0.002
4	1	4	5	3	1	3	4	10830.481	10830.480	0.001
4	0	4	3	3	0	3	2	11016.492	11016.488	0.004
4	0	4	4	3	0	3	3	11016.521	11016.524	-0.003
4	0	4	5	3	0	3	4	11016.569	11016.568	0.001
4	2	3	4	3	2	2	3	11049.495	11049.492	0.003
4	2	3	5	3	2	2	4	11049.885	11049.886	-0.001
4	2	3	3	3	2	2	2	11049.986	11049.987	-0.001
4	1	3	4	3	1	2	3	11260.235	11260.236	-0.001
4	1	3	3	3	1	2	2	11260.334	11260.335	-0.001
4	1	3	5	3	1	2	4	11260.350	11260.350	0.000
5	0	5	5	4	0	4	4	13744.187	13744.186	0.001
5	0	5	6	4	0	4	5	13744.230	13744.228	0.002

**Table B.4 Theoretical Atomic Cartesian Coordinates for the Complex**  
M06-2X/6-311++G(3df,3pd) with counterpoise correction

	<i>x</i>	<i>y</i>	<i>z</i>
<b>C2</b>	-2.28651	-0.28468	-3.2E-05
<b>O3</b>	-2.0792	0.901323	-5.4E-05
<b>O4</b>	-1.37019	-1.22348	-9.8E-05
<b>H1</b>	-3.29877	-0.7087	0.000073
<b>H5</b>	-0.43709	-0.79172	-0.00011
<b>N6</b>	1.001323	-0.04027	0.000008
<b>C7</b>	1.004397	0.792272	-1.19913
<b>H8</b>	0.968167	0.156668	-2.08247
<b>H9</b>	0.124225	1.431656	-1.18742
<b>H10</b>	1.907209	1.413542	-1.24821
<b>C11</b>	2.124978	-0.96728	-0.00028
<b>H12</b>	2.077895	-1.60001	0.884137
<b>H12</b>	2.077397	-1.60005	-0.88465
<b>H13</b>	3.08408	-0.43409	-0.00058
<b>C7</b>	1.004343	0.79171	1.199551
<b>H9</b>	0.123624	1.430353	1.188604
<b>H8</b>	0.969186	0.15563	2.082594
<b>H10</b>	1.90666	1.413721	1.248495

## Appendix C : Supplemental Material for Chapter 3

**Table C.1 Observed Transitions for HCOOH-HNO<sub>3</sub> 0<sup>+</sup> State**

J'	K <sub>a</sub> '	K <sub>c</sub> '	F'	J''	K <sub>a</sub> ''	K <sub>c</sub> ''	F''	Observed Frequency (MHz)	Calculated Frequency (MHz)	Obs-Calc (MHz)
2	1	2	2	1	1	1	1	4734.146	4734.147	-0.001
2	1	2	3	1	1	1	2	4734.385	4734.387	-0.002
2	1	2	1	1	1	1	0	4734.704	4734.704	0.000
2	0	2	2	1	0	1	2	4971.837	4971.838	-0.001
2	0	2	1	1	0	1	0	4971.872	4971.871	0.001
2	0	2	3	1	0	1	2	4972.088	4972.087	0.001
2	0	2	1	1	0	1	1	4972.463	4972.462	0.001
2	1	1	2	1	1	0	1	5228.143	5228.146	-0.003
2	1	1	3	1	1	0	2	5228.394	5228.397	-0.003
2	1	1	1	1	1	0	0	5228.574	5228.575	-0.001
3	1	3	3	2	1	2	2	7095.759	7095.761	-0.002
3	1	3	4	2	1	2	3	7095.827	7095.827	0.000
3	1	3	2	2	1	2	1	7095.843	7095.841	0.002
3	0	3	3	2	0	2	3	7434.743	7434.741	0.002
3	0	3	4	2	0	2	3	7434.996	7434.993	0.003
3	0	3	2	2	0	2	2	7435.330	7435.330	0.000
3	2	1	3	2	2	0	2	7508.793	7508.795	-0.002
3	2	1	4	2	2	0	3	7509.054	7509.056	-0.002
3	1	2	3	2	1	1	3	7836.326	7836.324	0.002
3	1	2	3	2	1	1	2	7836.532	7836.533	-0.001
3	1	2	2	2	1	1	1	7836.583	7836.588	-0.005
3	1	2	4	2	1	1	3	7836.605	7836.605	0.000
4	1	4	4	3	1	3	3	9450.710	9450.706	0.004
4	1	4	5	3	1	3	4	9450.734	9450.734	0.000
4	0	4	5	3	0	3	4	9870.657	9870.659	-0.002
4	2	2	4	3	2	1	3	10047.278	10047.276	0.002
4	2	2	4	3	2	1	3	10047.278	10047.276	0.002
4	2	2	5	3	2	1	4	10047.393	10047.392	0.001
4	2	2	5	3	2	1	4	10047.393	10047.392	0.001
4	1	3	4	3	1	2	3	10437.373	10437.374	-0.001
4	1	3	3	3	1	2	2	10437.388	10437.386	0.002
4	1	3	5	3	1	2	4	10437.408	10437.405	0.003
5	1	5	5	4	1	4	4	11797.386	11797.390	-0.004
5	1	5	6	4	1	4	5	11797.403	11797.403	0.000
5	0	5	6	4	0	4	5	12271.562	12271.561	0.001

**Table C.1 continued...**

J'	K <sub>a</sub> '	K <sub>c</sub> '	F'	J''	K <sub>a</sub> ''	K <sub>c</sub> ''	F''	Observed Frequency (MHz)	Calculated Frequency (MHz)	Obs-Calc (MHz)
5	2	4	6	4	2	3	5	12432.606	12432.606	0.000
5	1	4	5	4	1	3	4	13027.769	13027.771	-0.002
5	1	4	4	4	1	3	3	13027.773	13027.773	0.000
5	1	4	6	4	1	3	5	13027.785	13027.787	-0.002

**Table C.2 Observed Transitions for HCOOH-HNO<sub>3</sub> 0<sup>-</sup> State**

J'	K <sub>a</sub> '	K <sub>c</sub> '	F'	J''	K <sub>a</sub> ''	K <sub>c</sub> ''	F''	Observed Frequency (MHz)	Calculated Frequency (MHz)	Obs-Calc (MHz)
2	1	2	2	1	1	1	1	4734.129	4734.128	0.001
2	1	2	3	1	1	1	2	4734.366	4734.368	-0.001
2	0	2	2	1	1	1	2	4971.825	4971.824	0.001
2	0	2	1	1	1	1	0	4971.859	4971.858	0.001
2	0	2	2	1	1	1	1	4972.060	4972.061	-0.001
2	0	2	3	1	1	1	2	4972.076	4972.074	0.002
2	0	2	1	1	1	1	1	4972.449	4972.448	0.001
3	1	3	4	2	2	2	3	7095.802	7095.799	0.003
3	0	3	3	2	2	2	3	7434.717	7434.718	-0.001
3	0	3	2	2	2	2	1	7434.924	7434.921	0.004
3	0	3	4	2	2	2	3	7434.970	7434.971	-0.001
3	0	3	2	2	2	2	2	7435.308	7435.308	0.000
3	2	2	3	2	2	1	2	7471.756	7471.758	-0.002
3	2	2	4	2	2	1	3	7472.010	7472.011	-0.001
3	2	2	2	2	2	1	1	7472.151	7472.152	-0.001
3	2	1	3	2	2	0	2	7508.774	7508.777	-0.003
3	2	1	4	2	2	0	3	7509.035	7509.036	-0.001
3	2	1	2	2	2	0	1	7509.176	7509.178	-0.002
4	0	4	3	3	3	3	2	9870.598	9870.602	-0.004
4	0	4	5	3	3	3	4	9870.628	9870.626	0.002
4	2	3	4	3	3	2	3	9955.278	9955.278	0.000
4	2	3	5	3	3	2	4	9955.385	9955.385	0.000
4	2	3	3	3	3	2	2	9955.414	9955.412	0.002
4	2	2	4	3	3	1	3	10047.259	10047.261	-0.002
4	2	2	5	3	3	1	4	10047.374	10047.375	-0.001
4	2	2	3	3	3	1	2	10047.405	10047.404	0.001
4	1	3	4	3	3	2	3	10437.359	10437.359	-0.001
5	1	5	4	4	4	4	3	11797.362	11797.362	0.000
5	0	5	4	4	4	4	3	12271.497	12271.501	-0.004
5	0	5	6	4	4	4	5	12271.514	12271.515	-0.001
5	2	4	5	4	4	3	4	12432.518	12432.515	0.003
5	2	4	6	4	4	3	5	12432.571	12432.569	0.002
5	2	4	4	4	4	3	3	12432.578	12432.575	0.003
5	2	3	5	4	4	2	4	12614.177	12614.176	0.001
5	2	3	6	4	4	2	5	12614.239	12614.241	-0.002
5	2	3	4	4	4	2	3	12614.246	12614.247	-0.001



**Table C.3 Observed Transitions for HCOOH-H<sup>15</sup>NO<sub>3</sub> 0<sup>+</sup> State**

J'	K <sub>a</sub> '	K <sub>c</sub> '	J''	K <sub>a</sub> ''	K <sub>c</sub> ''	Observed Frequency (MHz)	Calculated Frequency (MHz)	Obs-Calc (MHz)
2	1	2	1	1	1	4708.955	4708.957	-0.002
2	0	2	1	0	1	4944.159	4944.158	0.001
2	1	1	1	1	0	5197.468	5197.470	-0.002
3	1	3	2	1	2	7057.858	7057.859	-0.001
3	0	3	2	0	2	7393.654	7393.652	0.002
3	2	2	2	2	1	7429.779	7429.780	-0.001
3	1	2	2	1	1	7790.412	7790.413	-0.001
4	1	4	3	1	3	9400.361	9400.362	-0.001
4	0	4	3	0	3	9816.527	9816.523	0.004
4	2	3	3	2	2	9899.291	9899.291	0.000
4	1	3	3	1	2	10376.107	10376.108	-0.001
5	1	5	4	1	4	11734.800	11734.802	-0.002
5	0	5	4	0	4	12205.384	12205.383	0.001
5	2	4	4	2	3	12362.744	12362.742	0.002
5	1	4	4	1	3	12951.640	12951.640	0.000
6	1	6	5	1	5	14059.898	14059.897	0.002
6	0	6	5	0	5	14555.254	14555.256	-0.002
6	1	5	5	1	4	15513.658	15513.658	0.000

**Table C.4 Observed Transitions for HCOOH-H<sup>15</sup>NO<sub>3</sub> 0<sup>-</sup> State**

J'	K <sub>a</sub> '	K <sub>c</sub> '	J''	K <sub>a</sub> ''	K <sub>c</sub> ''	Observed Frequency (MHz)	Calculated Frequency (MHz)	Obs-Calc (MHz)
2	1	2	1	1	1	4708.936	4708.939	-0.003
2	0	2	1	0	1	4944.146	4944.146	0.000
3	1	3	2	1	2	7057.834	7057.834	0.000
3	0	3	2	0	2	7393.635	7393.634	0.001
3	2	2	2	2	1	7429.759	7429.761	-0.002
3	2	1	2	2	0	7465.917	7465.920	-0.003
4	1	4	3	1	3	9400.332	9400.330	0.002
4	0	4	3	0	3	9816.498	9816.499	-0.001
4	2	3	3	2	2	9899.268	9899.267	0.002
4	2	2	3	2	1	9989.120	9989.121	-0.001
4	1	3	3	1	2	10376.094	10376.093	0.001
5	1	5	4	1	4	11734.766	11734.765	0.001
5	0	5	4	0	4	12205.354	12205.353	0.001
5	2	4	4	2	3	12362.715	12362.712	0.003
5	2	3	4	2	2	12540.221	12540.222	-0.001
5	1	4	4	1	3	12951.620	12951.619	0.001
6	1	6	5	1	5	14059.857	14059.857	0.000
6	0	6	5	0	5	14555.221	14555.223	-0.002
6	1	5	5	1	4	15513.630	15513.631	-0.001

**Table C.5 Observed Transitions for HCOOD-HNO<sub>3</sub>**

J'	K <sub>a</sub> '	K <sub>c</sub> '	F <sub>1</sub> '	F'	J''	K <sub>a</sub> ''	K <sub>c</sub> ''	F <sub>1</sub> ''	F''	Observed Frequency (MHz)	Calculated Frequency (MHz)	Obs-Calc (MHz)
2	1	2	2	3	1	1	1	1	2	4709.869	4709.859	0.010
2	1	2	1	2	1	1	1	1	2	4709.949	4709.955	-0.006
2	1	2	3	4	1	1	1	2	3	4710.100	4710.095	0.005
2	1	2	3	3	1	1	1	2	2	4710.157	4710.163	-0.006
2	0	2	2	3	1	0	1	1	2	4949.119	4949.126	-0.007
2	0	2	3	4	1	0	1	2	3	4949.150	4949.148	0.002
2	0	2	1	2	1	0	1	1	2	4949.530	4949.534	-0.004
2	1	1	2	3	1	1	0	1	2	5207.153	5207.147	0.006
2	1	1	3	2	1	1	0	2	1	5207.380	5207.381	-0.001
2	1	1	3	4	1	1	0	2	3	5207.399	5207.394	0.005
2	1	1	3	3	1	1	0	2	2	5207.455	5207.464	-0.009
3	1	3	3	4	2	1	2	2	3	7059.163	7059.155	0.008
3	1	3	4	3	2	1	2	3	2	7059.210	7059.217	-0.007
3	1	3	4	5	2	1	2	3	4	7059.224	7059.223	0.001
3	1	3	4	4	2	1	2	3	3	7059.244	7059.246	-0.002
3	0	3	4	5	2	0	2	3	4	7399.842	7399.839	0.003
3	1	2	3	4	2	1	1	2	3	7804.854	7804.850	0.004
3	1	2	2	3	2	1	1	1	2	7804.897	7804.907	-0.010
3	1	2	4	5	2	1	1	3	4	7804.924	7804.924	0.000
3	1	2	4	4	2	1	1	3	3	7804.955	7804.948	0.007
4	1	4	4	4	3	1	3	3	3	9401.601	9401.604	-0.003
4	1	4	5	6	3	1	3	4	5	9401.619	9401.616	0.003
4	0	4	3	4	3	0	3	2	3	9822.398	9822.406	-0.008
4	0	4	5	6	3	0	3	4	5	9822.431	9822.434	-0.003
4	0	4	4	4	3	0	3	3	3	9822.449	9822.447	0.002
4	2	3	4	5	3	2	2	3	4	9909.796	9909.794	0.002
4	2	3	4	4	3	2	2	3	3	9909.825	9909.823	0.002
4	2	3	5	6	3	2	2	4	5	9909.904	9909.903	0.001
4	2	3	5	5	3	2	2	4	4	9909.933	9909.936	-0.003
4	2	2	4	3	3	2	1	3	2	10004.718	10004.728	-0.010
4	2	2	4	5	3	2	1	3	4	10004.736	10004.736	0.000
4	2	2	4	4	3	2	1	3	3	10004.763	10004.764	-0.001
4	2	2	5	4	3	2	1	4	4	10004.835	10004.847	-0.012
4	2	2	5	6	3	2	1	4	5	10004.858	10004.853	0.005
4	2	2	5	5	3	2	1	4	4	10004.883	10004.887	-0.004
4	1	3	4	5	3	1	2	3	4	10394.750	10394.757	-0.007
4	1	3	4	4	3	1	2	3	3	10394.773	10394.773	0.000
4	1	3	5	6	3	1	2	4	5	10394.795	10394.790	0.005

**Table C.5 continued...**

J'	K <sub>a</sub> '	K <sub>c</sub> '	F <sub>1</sub> '	F'	J''	K <sub>a</sub> ''	K <sub>c</sub> ''	F <sub>1</sub> ''	F''	Observed Frequency (MHz)	Calculated Frequency (MHz)	Obs-Calc (MHz)
5	1	5	5	6	4	1	4	4	5	11735.516	11735.520	-0.004
5	1	5	6	7	4	1	4	5	6	11735.538	11735.535	0.003
5	0	5	4	5	4	0	4	3	4	12209.235	12209.237	-0.002
5	0	5	5	6	4	0	4	4	5	12209.260	12209.259	0.001
5	1	4	5	6	4	1	3	4	5	12973.853	12973.855	-0.002
5	1	4	6	7	4	1	3	5	6	12973.875	12973.872	0.003

**Table C.6 Observed Transitions for HCOOD-H<sup>15</sup>NO<sub>3</sub>**

J'	K <sub>a</sub> '	K <sub>c</sub> '	F'	J''	K <sub>a</sub> ''	K <sub>c</sub> ''	F''	Observed Frequency (MHz)	Calculated Frequency (MHz)	Obs-Calc (MHz)
2	1	2	1	1	1	1	0	4684.544	4684.543	0.001
2	1	2	3	1	1	1	2	4684.609	4684.610	-0.001
2	1	2	2	1	1	1	2	4684.646	4684.644	0.002
2	1	2	2	1	1	1	1	4684.675	4684.676	-0.001
2	0	2	1	1	0	1	1	4921.027	4921.027	0.000
2	0	2	3	1	0	1	2	4921.130	4921.130	0.000
2	0	2	1	1	0	1	0	4921.186	4921.188	-0.002
2	1	1	1	1	1	0	0	5176.259	5176.261	-0.002
2	1	1	3	1	1	0	2	5176.328	5176.328	0.000
2	1	1	2	1	1	0	1	5176.394	5176.394	0.000
3	1	3	4	2	1	2	3	7021.175	7021.177	-0.002
3	1	3	3	2	1	2	2	7021.198	7021.196	0.002
3	0	3	4	2	0	2	3	7358.390	7358.390	0.000
3	0	3	2	2	0	2	1	7358.404	7358.403	0.001
3	1	2	4	2	1	1	3	7758.524	7758.525	-0.001
3	1	2	3	2	1	1	2	7758.545	7758.544	0.001
4	1	4	5	3	1	3	4	9351.141	9351.143	-0.002
4	1	4	4	3	1	3	3	9351.151	9351.151	0.000
4	0	4	5	3	0	3	4	9768.198	9768.198	0.000
4	1	3	5	3	1	2	4	10333.225	10333.225	0.000
5	1	5	6	4	1	4	5	11672.814	11672.813	0.001
5	0	5	6	4	0	4	5	12143.012	12143.012	0.000
5	1	4	6	4	1	3	5	12897.406	12897.405	0.001
6	1	6	7	5	1	5	6	13984.887	13984.887	0.000
6	0	6	7	5	0	5	6	14477.887	14477.887	0.000
6	1	5	7	5	1	4	6	15447.579	15447.580	-0.001

**Table C.7 Observed Transitions for H<sup>13</sup>COOH-HNO<sub>3</sub>**

J'	Ka'	Kc'	F'	J''	Ka''	Kc''	F''	Observed Frequency (MHz)	Calculated Frequency (MHz)	Obs-Calc (MHz)
2	0	2	3	1	0	1	2	4902.430	4902.434	-0.004
3	1	3	3	2	1	2	2	7000.997	7000.994	0.003
3	1	3	4	2	1	2	3	7001.064	7001.061	0.003
3	0	3	4	2	0	2	3	7331.821	7331.827	-0.006
3	1	2	3	2	1	1	2	7721.422	7721.423	-0.001
3	1	2	4	2	1	1	3	7721.501	7721.497	0.004
4	0	4	5	3	0	3	4	9735.499	9735.502	-0.003
4	1	3	4	3	1	2	3	10284.557	10284.559	-0.002
4	1	3	5	3	1	2	4	10284.595	10284.591	0.004
5	1	5	5	4	1	4	4	11641.063	11641.067	-0.004
5	1	5	6	4	1	4	5	11641.082	11641.080	0.002
5	0	5	4	4	0	4	3	12106.259	12106.256	0.003
5	0	5	5	4	0	4	4	12106.278	12106.278	0.000
5	1	4	6	4	1	3	5	12837.893	12837.895	-0.002

**Table C.8 Observed Transitions for HCOOH-DNO<sub>3</sub>**

J'	Ka'	Kc'	F <sub>1</sub> '	F'	J''	Ka''	Kc''	F <sub>1</sub> ''	F''	Observed Frequency (MHz)	Calculated Frequency (MHz)	Obs-Calc (MHz)
2	0	2	2	3	1	0	1	1	2	4954.653	4954.653	0.000
2	0	2	3	4	1	0	1	2	3	4954.675	4954.673	0.002
2	0	2	2	2	1	0	1	1	1	4954.690	4954.694	-0.004
2	1	1	3	4	1	1	0	2	3	5212.753	5212.751	0.002
3	1	3	3	3	2	1	2	2	2	7067.605	7067.604	0.001
3	1	3	4	5	2	1	2	3	4	7067.664	7067.668	-0.004
3	1	3	2	2	2	1	2	1	1	7067.687	7067.683	0.004
3	0	3	4	5	2	0	2	3	4	7408.226	7408.227	-0.001
3	2	2	4	5	2	2	1	3	4	7446.299	7446.298	0.001
3	2	2	4	4	2	2	1	3	3	7446.342	7446.335	0.007
3	2	2	2	3	2	2	1	1	2	7446.447	7446.455	-0.008
3	2	2	2	2	2	2	1	1	1	7446.480	7446.475	0.005
3	2	1	4	3	2	2	0	3	2	7484.339	7484.346	-0.007
3	2	1	4	5	2	2	0	3	4	7484.360	7484.358	0.002
3	2	1	4	4	2	2	0	3	3	7484.404	7484.396	0.008
3	2	1	2	3	2	2	0	1	2	7484.512	7484.515	-0.003
3	2	1	2	2	2	2	0	1	1	7484.541	7484.536	0.005
3	1	2	3	4	2	1	1	2	3	7812.907	7812.904	0.003
3	1	2	4	5	2	1	1	3	4	7812.983	7812.981	0.002
4	1	4	4	5	3	1	3	3	4	9412.876	9412.880	-0.004
4	1	4	5	6	3	1	3	4	5	9412.920	9412.911	0.009
4	0	4	5	6	3	0	3	4	5	9833.805	9833.803	0.002
4	2	3	4	5	3	2	2	3	4	9920.792	9920.792	0.000
4	2	3	5	6	3	2	2	4	5	9920.901	9920.905	-0.004
4	2	3	3	4	3	2	2	2	3	9920.932	9920.935	-0.003
4	2	2	4	5	3	2	1	3	4	10015.327	10015.327	0.000
4	2	2	5	6	3	2	1	4	5	10015.445	10015.445	0.000
4	2	2	3	4	3	2	1	2	3	10015.474	10015.475	-0.001
4	1	3	4	5	3	1	2	3	4	10405.545	10405.551	-0.006
4	1	3	5	6	3	1	2	4	5	10405.590	10405.585	0.005
5	1	5	6	7	4	1	4	5	6	11749.708	11749.711	-0.003
5	0	5	6	7	4	0	4	5	6	12223.740	12223.737	0.003
5	2	4	5	6	4	2	3	4	5	12389.100	12389.091	0.009
5	2	4	6	7	4	2	3	5	6	12389.150	12389.150	0.000
5	2	3	5	6	4	2	2	4	5	12575.695	12575.695	0.000
5	2	3	6	7	4	2	2	5	6	12575.762	12575.760	0.002
5	1	4	5	6	4	1	3	4	5	12987.440	12987.442	-0.002

**Table C.9 Observed Transitions for DCOOH-HNO<sub>3</sub>**

J'	Ka'	Kc'	F'	J''	Ka''	Kc''	F''	Observed Frequency (MHz)	Calculated Frequency (MHz)	Obs-Calc (MHz)
2	1	2	3	1	1	1	2	4603.287	4603.274	0.013
2	0	2	2	1	0	1	1	4828.126	4828.152	-0.026
2	0	2	3	1	0	1	2	4828.150	4828.166	-0.016
2	1	1	2	1	1	0	1	5069.304	5069.285	0.019
2	1	1	2	1	1	0	2	5069.351	5069.351	0.000
2	1	1	3	1	1	0	2	5069.519	5069.530	-0.011
2	1	1	1	1	1	0	0	5069.730	5069.728	0.002
3	0	3	4	2	0	2	3	7221.726	7221.743	-0.017
3	2	2	3	2	2	1	2	7254.280	7254.269	0.011
3	2	2	4	2	2	1	3	7254.527	7254.518	0.009
3	2	2	2	2	2	1	1	7254.675	7254.657	0.018
3	2	1	3	2	2	0	2	7287.062	7287.067	-0.005
3	2	1	4	2	2	0	3	7287.318	7287.321	-0.003
3	1	2	3	2	1	1	2	7598.943	7598.923	0.020
3	1	2	2	2	1	1	1	7598.982	7598.981	0.001
3	1	2	4	2	1	1	3	7599.010	7598.993	0.017
4	1	4	4	3	1	3	3	9190.502	9190.507	-0.005
4	1	4	5	3	1	3	4	9190.550	9190.535	0.015
4	1	4	3	3	1	3	2	9190.557	9190.530	0.027
4	0	4	3	3	0	3	2	9591.086	9591.107	-0.021
4	0	4	5	3	0	3	4	9591.124	9591.130	-0.006
4	2	2	4	3	2	1	3	9747.655	9747.675	-0.020
4	2	2	5	3	2	1	4	9747.770	9747.786	-0.016
4	2	2	3	3	2	1	2	9747.800	9747.814	-0.014
4	1	3	4	3	1	2	3	10121.875	10121.889	-0.014
4	1	3	5	3	1	2	4	10121.928	10121.920	0.008
5	1	5	6	4	1	4	5	11473.928	11473.919	0.009
5	0	5	4	4	0	4	3	11929.458	11929.471	-0.013
5	0	5	6	4	0	4	5	11929.480	11929.485	-0.005
5	1	4	5	4	1	3	4	12635.674	12635.666	0.008
5	1	4	6	4	1	3	5	12635.696	12635.682	0.014



## Appendix D : Supplemental Material for Chapter 4

The frequencies of transitions observed in Ken Leopold's lab are marked with an \*. Transitions without an \* were observed in Tony Legon's lab.

Transitions marked with † have  $K_{-1} > 1$  and were not used in the final fit reported in the chapter. The attempted fits including these lines had rms greater than 150 kHz. The residuals listed with these transitions are from the fits reported in the chapter.

**Table D.1 Observed Transitions for  $\text{H}_5\text{C}_5\text{N-HCCH } 0^+$  State**

$J'$	$K_a'$	$K_c'$	$F'$	$J''$	$K_a''$	$K_c''$	$F''$	Observed Frequency (MHz)	Calculated Frequency (MHz)	Obs-Calc (MHz)
3	1	3	3	2	1	2	3	4505.214*	4505.216	-0.002
3	1	3	3	2	1	2	2	4506.278*	4506.276	0.002
3	1	3	2	2	1	2	1	4506.554*	4506.555	-0.001
3	1	3	4	2	1	2	3	4506.645*	4506.645	0.000
3	1	2	3	2	1	1	2	4807.677*	4807.677	0.000
3	1	2	4	2	1	1	3	4808.015*	4808.014	0.001
3	1	2	2	2	1	1	1	4808.092*	4808.090	0.002
3	0	3	3	2	0	2	3	4650.656*	4650.653	0.003
3	0	3	2	2	0	2	1	4651.744*	4651.741	0.003
3	0	3	3	2	0	2	2	4651.925*	4651.921	0.004
3	0	3	4	2	0	2	3	4651.983*	4651.980	0.003
3	0	3	2	2	0	2	2	4653.714*	4653.712	0.002
4	1	4	4	3	1	3	3	6006.583*	6006.582	0.001
4	1	4	3	3	1	3	2	6006.663*	6006.663	0.000
4	1	4	5	3	1	3	4	6006.752*	6006.752	0.000
4	0	4	4	3	0	3	4	6194.095*	6194.094	0.001
4	0	4	3	3	0	3	2	6195.360*	6195.358	0.002
4	0	4	4	3	0	3	3	6195.423*	6195.421	0.002
4	0	4	5	3	0	3	4	6195.469*	6195.469	0.000
4	0	4	3	3	0	3	3	6197.151*	6197.150	0.001
4	1	3	4	3	1	2	3	6408.588*	6408.588	0.000
4	1	3	3	3	1	2	2	6408.720*	6408.727	-0.007
4	1	3	5	3	1	2	4	6408.742*	6408.738	0.004
5	0	5	5	4	0	4	5	7731.457	7731.458	-0.001
5	0	5	5	4	0	4	4	7732.838	7732.832	0.006
5	0	5	6	4	0	4	5	7732.871	7732.876	-0.005
5	0	5	4	4	0	4	3	7732.804	7732.811	-0.007
5	0	5	4	4	0	4	4	7734.534	7734.540	-0.006
5	1	5	5	4	1	4	5	7503.507	7503.501	0.006
5	1	5	6	4	1	4	5	7505.194	7505.197	-0.003

**Table D.1 continued...**

J'	K <sub>a</sub> '	K <sub>c</sub> '	F'	J''	K <sub>a</sub> ''	K <sub>c</sub> ''	F''	Observed Frequency (MHz)	Calculated Frequency (MHz)	Obs-Calc (MHz)
5	1	5	5	4	1	4	4	7505.105	7505.100	0.005
5	1	5	4	4	1	4	4	7507.144	7507.142	0.002
5	1	4	5	4	1	3	5	8007.064	8007.062	0.002
5	1	4	6	4	1	3	5	8007.840	8007.832	0.008
5	1	4	5	4	1	3	4	8007.747	8007.747	0.000
5	1	4	4	4	1	3	3	8007.804	8007.812	-0.008
5	1	4	4	4	1	3	4	8008.673	8008.674	-0.001
6	1	6	6	5	1	5	6	8999.820	8999.826	-0.006
6	1	6	6	5	1	5	5	9001.512	9001.522	-0.010
6	1	6	5	5	1	5	4	9001.545	9001.538	0.007
6	1	6	7	5	1	5	6	9001.582	9001.587	-0.005
6	0	6	5	5	0	5	4	9262.716	9262.715	0.001
6	0	6	7	5	0	5	6	9262.750	9262.757	-0.007
6	0	6	6	5	0	5	6	9261.295	9261.297	-0.002
6	1	5	6	5	1	4	6	9603.981	9603.983	-0.002
6	1	5	6	5	1	4	5	9604.756	9604.753	0.003
6	1	5	5	5	1	4	4	9604.780	9604.790	-0.010
6	1	5	7	5	1	4	6	9604.814	9604.807	0.007
6	1	5	5	5	1	4	5	9605.720	9605.716	0.004
7	1	7	7	6	1	6	6	10495.523	10495.520	0.003
7	0	7	7	6	0	6	6	10783.760	10783.753	0.007
7	0	7	8	6	0	6	7	10783.799	10783.796	0.003
5	2	4	5	4	2	3	5	7758.395 †	7760.341	-1.946
5	2	4	5	4	2	3	4	7758.937 †	7760.877	-1.940
5	2	4	6	4	2	3	5	7759.219 †	7761.159	-1.940
5	2	4	4	4	2	3	4	7759.917 †	7761.863	-1.946
5	2	3	5	4	2	2	5	7787.713 †	7790.074	-2.361
5	2	3	5	4	2	2	4	7788.217 †	7790.571	-2.354
5	2	3	6	4	2	2	5	7788.477 †	7790.831	-2.354
5	2	3	4	4	2	2	4	7789.125 †	7791.482	-2.357
6	2	5	6	5	2	4	6	9306.883 †	9309.129	-2.246
6	2	5	6	5	2	4	5	9307.699 †	9309.948	-2.249
6	2	5	7	5	2	4	6	9307.866 †	9310.118	-2.252
6	2	5	5	5	2	4	5	9308.857 †	9311.104	-2.247
6	2	4	6	5	2	3	6	9358.068 †	9361.013	-2.945
6	2	4	6	5	2	3	5	9358.825 †	9361.769	-2.944
6	2	4	7	5	2	3	6	9358.957 †	9361.912	-2.955
6	2	4	5	5	2	3	5	9359.875 †	9362.820	-2.945

**Table D.1 continued...**

J'	K <sub>a</sub> '	K <sub>c</sub> '	F'	J''	K <sub>a</sub> ''	K <sub>c</sub> ''	F''	Observed Frequency (MHz)	Calculated Frequency (MHz)	Obs-Calc (MHz)
7	2	6	7	6	2	5	6	10854.703 †	10857.209	-2.506
7	2	6	8	6	2	5	7	10854.810 †	10857.322	-2.512
7	2	5	7	6	2	4	6	10936.159 †	10939.728	-3.569
7	2	5	8	6	2	4	7	10936.247 †	10939.809	-3.562

**Table D.2 Observed Transitions for H<sub>5</sub>C<sub>5</sub>N-HCCH 0<sup>-</sup> State**

J'	K <sub>a</sub> '	K <sub>c</sub> '	F'	J''	K <sub>a</sub> ''	K <sub>c</sub> ''	F''	Observed Frequency (MHz)	Calculated Frequency (MHz)	Obs-Calc (MHz)
3	1	3	2	2	1	2	1	4490.360*	4490.377	-0.017
3	1	3	4	2	1	2	3	4490.446*	4490.466	-0.020
3	1	2	3	2	1	1	2	4802.688*	4802.690	-0.002
3	1	2	4	2	1	1	3	4803.024*	4803.024	0.000
3	1	2	2	2	1	1	1	4803.102*	4803.100	0.002
3	0	3	3	2	0	2	3	4639.676*	4639.684	-0.008
3	0	3	2	2	0	2	1	4640.754*	4640.762	-0.008
3	0	3	3	2	0	2	2	4640.931*	4640.940	-0.009
3	0	3	4	2	0	2	3	4640.990*	4641.000	-0.010
3	0	3	2	2	0	2	2	4642.706*	4642.716	-0.010
4	1	4	4	3	1	3	3	5985.416*	5985.426	-0.010
4	1	4	3	3	1	3	2	5985.498*	5985.506	-0.008
4	1	4	5	3	1	3	4	5985.585*	5985.595	-0.010
4	0	4	3	3	0	3	2	6180.532*	6180.532	0.000
4	0	4	4	3	0	3	3	6180.593*	6180.594	-0.001
4	0	4	5	3	0	3	4	6180.639*	6180.642	-0.003
4	1	3	4	3	1	2	3	6401.896*	6401.894	0.002
4	1	3	3	3	1	2	2	6402.030*	6402.032	-0.002
4	1	3	5	3	1	2	4	6402.049*	6402.043	0.006
5	0	5	5	4	0	4	5	7712.692	7712.685	0.007
5	0	5	5	4	0	4	4	7714.062	7714.049	0.013
5	0	5	6	4	0	4	5	7714.098	7714.093	0.005
5	0	5	4	4	0	4	3	7714.025	7714.029	-0.004
5	0	5	4	4	0	4	4	7715.750	7715.743	0.007
5	1	5	5	4	1	4	5	7477.754	7477.747	0.076
5	1	5	6	4	1	4	5	7479.436	7479.431	0.005
5	1	5	5	4	1	4	4	7479.353	7479.334	0.019
5	1	5	4	4	1	4	4	7481.364	7481.360	0.004
5	1	4	5	4	1	3	5	7998.641	7998.640	0.001
5	1	4	6	4	1	3	5	7999.407	7999.400	0.007
5	1	4	4	4	1	3	3	7999.372	7999.381	-0.009
5	1	4	4	4	1	3	4	8000.232	8000.232	0.000
6	1	6	6	5	1	5	6	8969.950	8969.943	0.007
6	1	6	6	5	1	5	5	8971.626	8971.627	-0.001
6	1	6	5	5	1	5	4	8971.662	8971.643	0.019
6	1	6	7	5	1	5	6	8971.700	8971.691	0.009
6	1	6	5	5	1	5	5	8973.678	8973.670	0.008

Table D.2 continued...

J'	K <sub>a</sub> '	K <sub>c</sub> '	F'	J''	K <sub>a</sub> ''	K <sub>c</sub> ''	F''	Observed Frequency (MHz)	Calculated Frequency (MHz)	Obs-Calc (MHz)
6	0	6	5	5	0	5	5	9241.613	9241.604	0.009
6	0	6	6	5	0	5	5	9239.919	9239.908	0.011
6	0	6	7	5	0	5	6	9239.955	9239.951	0.004
6	0	6	6	5	0	5	6	9238.507	9238.501	0.006
6	1	5	6	5	1	4	5	9594.565	9594.557	0.008
6	1	5	7	5	1	4	6	9594.615	9594.612	0.003
6	1	5	5	5	1	4	5	9595.504	9595.510	-0.006
7	1	7	8	6	1	6	7	10462.114	10462.143	-0.029
7	0	7	7	6	0	6	6	10756.938	10756.949	-0.011
7	0	7	8	6	0	6	7	10756.977	10756.992	-0.015
3	2	2	3	2	2	1	2	4646.237‡	4647.554	-1.317
3	2	2	4	2	2	1	3	4647.487 ‡	4648.801	-1.314
3	2	2	2	2	2	1	1	4648.184 ‡	4649.494	-1.310
3	2	1	3	2	2	0	2	4652.676 ‡	4653.960	-1.284
3	2	1	4	2	2	0	3	4653.912 ‡	4655.193	-1.281
3	2	1	2	2	2	0	1	4654.606 ‡	4655.884	-1.278
4	2	3	4	3	2	2	3	6194.722 ‡	6196.502	-1.780
4	2	3	5	3	2	2	4	6195.253 ‡	6197.034	-1.781
4	3	2	4	3	3	1	3	6197.969 ‡	6202.380	-4.411
4	3	1	4	3	3	0	3	6198.064 ‡	6202.473	-4.409
4	3	2	5	3	3	1	4	6199.122 ‡	6203.530	-4.408
4	3	1	5	3	3	0	4	6199.217 ‡	6203.622	-4.405
4	3	2	3	3	3	1	2	6199.571 ‡	6203.976	-4.405
4	3	1	3	3	3	0	2	6199.664 ‡	6204.068	-4.404
5	2	4	5	4	2	3	5	7741.288 ‡	7743.560	-2.272
5	2	4	5	4	2	3	4	7741.817 ‡	7744.091	-2.274
5	2	4	6	4	2	3	5	7742.109 ‡	7744.372	-2.263
5	2	4	4	4	2	3	3	7742.127 ‡	7744.400	-2.273
5	2	4	4	4	2	3	4	7742.792 ‡	7745.068	-2.276
5	3	3	5	4	3	2	4	7749.657 ‡	7755.184	-5.527
5	3	2	5	4	3	1	4	7749.987 ‡	7755.505	-5.518
5	3	3	6	4	3	2	5	7750.248 ‡	7755.777	-5.529
5	3	3	4	4	3	2	3	7750.400 ‡	7755.923	-5.523
5	3	2	6	4	3	1	5	7750.582 ‡	7756.098	-5.516
5	3	2	4	4	3	1	3	7750.728 ‡	7756.244	-5.516
5	2	3	5	4	2	2	5	7773.180 ‡	7775.423	-2.243
5	2	3	5	4	2	2	4	7773.809 ‡	7775.913	-2.104

**Table D.2 continued...**

J'	K <sub>a</sub> '	K <sub>c</sub> '	F'	J''	K <sub>a</sub> ''	K <sub>c</sub> ''	F''	Observed Frequency (MHz)	Calculated Frequency (MHz)	Obs-Calc (MHz)
5	2	3	6	4	2	2	5	7774.068 †	7776.170	-2.102
5	2	3	4	4	2	2	3	7774.102 †	7776.196	-2.094
5	2	3	4	4	2	2	4	7774.708 †	7776.813	-2.105
6	2	5	6	5	2	4	6	9286.741 †	9289.549	-2.808
6	2	5	6	5	2	4	5	9287.557 †	9290.361	-2.804
6	2	5	7	5	2	4	6	9287.725 †	9290.529	-2.804
6	2	5	5	5	2	4	5	9288.699 †	9291.507	-2.808
6	2	4	6	5	2	3	6	9342.490 †	9344.992	-2.502
6	2	4	6	5	2	3	5	9343.238 †	9345.739	-2.501
6	2	4	7	5	2	3	6	9343.380 †	9345.879	-2.499
6	2	4	5	5	2	3	5	9344.281 †	9346.776	-2.495
7	2	6	7	6	2	5	6	10831.762 †	10835.148	-3.386
7	2	6	8	6	2	5	7	10831.869 †	10835.259	-3.390

**Table D.3 Observed Transitions for H<sub>5</sub>C<sub>5</sub>N-DCCD 0<sup>+</sup> State**

J'	K <sub>a</sub> '	K <sub>c</sub> '	F'	J''	K <sub>a</sub> ''	K <sub>c</sub> ''	F''	Observed Frequency (MHz)	Calculated Frequency (MHz)	Obs-Calc (MHz)
4	0	4	3	3	0	3	2	5887.645*	5887.640	0.005
4	0	4	4	3	0	3	3	5887.709*	5887.714	-0.005
4	0	4	5	3	0	3	4	5887.755*	5887.753	0.002
5	1	4	5	4	1	3	4	7598.917	7598.917	0.000
5	1	4	4	4	1	3	3	7598.973	7598.971	0.002
5	1	4	6	4	1	3	5	7599.008	7599.002	0.006
6	1	6	6	5	1	5	5	8564.610	8564.619	-0.009
6	1	6	5	5	1	5	4	8564.644	8564.636	0.008
6	1	6	7	5	1	5	6	8564.680	8564.679	0.001
6	0	6	6	5	0	5	5	8806.316	8806.322	-0.006
6	0	6	7	5	0	5	6	8806.351	8806.351	0.000
6	1	5	6	5	1	4	5	9114.951	9114.953	-0.002
6	1	5	5	5	1	4	4	9114.971	9114.982	-0.011
6	1	5	7	5	1	4	6	9115.009	9115.007	0.002
7	1	7	7	6	1	6	6	9986.954	9986.948	0.006
7	1	7	8	6	1	6	7	9986.984	9986.990	-0.006
7	0	7	7	6	0	6	6	10255.119	10255.120	-0.001
7	0	7	8	6	0	6	7	10255.151	10255.148	0.003
7	1	6	7	6	1	5	6	10628.818	10628.813	0.005
7	1	6	8	6	1	5	7	10628.851	10628.851	0.000

**Table D.4 Observed Transitions for H<sub>5</sub>C<sub>5</sub>N-DCCD 0<sup>-</sup> State**

J'	K <sub>a</sub> '	K <sub>c</sub> '	F'	J''	K <sub>a</sub> ''	K <sub>c</sub> ''	F''	Observed Frequency (MHz)	Calculated Frequency (MHz)	Obs-Calc (MHz)
4	0	4	3	3	0	3	2	5876.597*	5876.591	0.006
4	0	4	4	3	0	3	3	5876.654*	5876.663	-0.009
4	0	4	5	3	0	3	4	5876.706*	5876.703	0.003
5	1	4	5	4	1	3	4	7592.662	7592.663	-0.001
5	1	4	4	4	1	3	3	7592.720	7592.719	0.001
5	1	4	6	4	1	3	5	7592.751	7592.748	-0.003
6	1	6	6	5	1	5	5	8542.048	8542.057	-0.009
6	1	6	5	5	1	5	4	8542.081	8542.074	0.007
6	1	6	7	5	1	5	6	8542.118	8542.117	0.001
6	0	6	6	5	0	5	5	8789.336	8789.337	-0.001
6	0	6	7	5	0	5	6	8789.369	8789.368	0.001
6	1	5	6	5	1	4	5	9107.381	9107.380	0.001
6	1	5	5	5	1	4	4	9107.402	9107.410	-0.008
6	1	5	7	5	1	4	6	9107.439	9107.434	0.005
7	1	7	7	6	1	6	6	9961.588	9961.585	0.003
7	1	7	8	6	1	6	7	9961.625	9961.628	-0.003
7	1	6	7	6	1	5	6	10619.898	10619.896	0.002
7	1	6	8	6	1	5	7	10619.934	10619.934	-0.000



**Table D.5 Observed Transitions for H<sub>5</sub>C<sub>5</sub>N-DCCH 0<sup>+</sup> State**

J'	K <sub>a</sub> '	K <sub>c</sub> '	F'	J''	K <sub>a</sub> ''	K <sub>c</sub> ''	F''	Observed Frequency (MHz)	Calculated Frequency (MHz)	Obs-Calc (MHz)
3	1	3	3	2	1	2	2	4472.857*	4472.861	-0.004
3	1	3	2	2	1	2	1	4473.137*	4473.138	-0.001
3	1	3	4	2	1	2	3	4473.225*	4473.229	-0.004
3	0	3	3	2	0	2	2	4616.668*	4616.672	-0.004
3	0	3	4	2	0	2	3	4616.734*	4616.732	0.002
3	1	2	3	2	1	1	2	4770.435*	4770.437	-0.002
3	1	2	4	2	1	1	3	4770.772*	4770.773	-0.001
3	1	2	2	2	1	1	1	4770.850*	4770.850	0.000
4	1	4	4	3	1	3	3	5962.076*	5962.074	0.002
4	1	4	3	3	1	3	2	5962.157*	5962.155	0.002
4	1	4	5	3	1	3	4	5962.245*	5962.244	0.001
4	0	4	3	3	0	3	2	6148.520*	6148.518	0.002
4	0	4	4	3	0	3	3	6148.584*	6148.581	0.003
4	0	4	5	3	0	3	4	6148.628*	6148.628	0.000
4	1	3	4	3	1	2	3	6358.978*	6358.979	-0.001
4	1	3	5	3	1	2	4	6359.135*	6359.128	0.007
5	1	5	5	4	1	4	4	7449.546*	7449.539	0.007
5	1	5	6	4	1	4	5	7449.638*	7449.637	0.001
5	0	5	5	4	0	4	4	7674.529*	7674.534	-0.005
5	0	5	6	4	0	4	5	7674.577*	7674.577	0.000
5	1	4	5	4	1	3	4	7945.813*	7945.808	0.005
5	1	4	6	4	1	3	5	7945.882*	7945.892	-0.010
6	1	6	6	5	1	5	5	8934.952*	8934.957	-0.005
6	1	6	5	5	1	5	4	8934.978*	8934.973	0.005
6	1	6	7	5	1	5	6	8935.017*	8935.021	-0.004
6	0	6	6	5	0	5	5	9193.123*	9193.123	0.000
6	0	6	7	5	0	5	6	9193.167*	9193.165	0.002
6	1	5	6	5	1	4	5	9530.540*	9530.534	0.006
6	1	5	7	5	1	4	6	9530.584*	9530.589	-0.005

**Table D.6 Observed Transitions for H<sub>5</sub>C<sub>5</sub>N-DCCH 0<sup>-</sup> State**

J'	K <sub>a</sub> '	K <sub>c</sub> '	F'	J''	K <sub>a</sub> ''	K <sub>c</sub> ''	F''	Observed Frequency (MHz)	Calculated Frequency (MHz)	Obs-Calc (MHz)
3	1	3	3	2	1	2	2	4456.343*	4456.353	-0.010
3	1	3	2	2	1	2	1	4456.623*	4456.630	-0.007
3	1	3	4	2	1	2	3	4456.709*	4456.720	-0.011
3	0	3	3	2	0	2	2	4605.466*	4605.475	-0.009
3	0	3	4	2	0	2	3	4605.531*	4605.536	-0.005
3	1	2	3	2	1	1	2	4765.359*	4765.364	-0.005
3	1	2	4	2	1	1	3	4765.694*	4765.699	-0.005
3	1	2	2	2	1	1	1	4765.773*	4765.776	-0.003
4	1	4	4	3	1	3	3	5940.475*	5940.473	0.002
4	1	4	3	3	1	3	2	5940.555*	5940.553	0.002
4	1	4	5	3	1	3	4	5940.644*	5940.642	0.002
4	0	4	3	3	0	3	2	6133.398*	6133.395	0.003
4	0	4	4	3	0	3	3	6133.461*	6133.458	0.003
4	0	4	5	3	0	3	4	6133.506*	6133.506	0.000
4	1	3	4	3	1	2	3	6352.171*	6352.167	0.004
4	1	3	5	3	1	2	4	6352.323*	6352.317	0.006
5	1	5	5	4	1	4	4	7423.215*	7423.210	0.005
5	1	5	4	4	1	4	3	7423.259*	7423.242	0.017
5	1	5	6	4	1	4	5	7423.318*	7423.308	0.010
5	0	5	4	4	0	4	3	7655.353*	7655.348	0.005
5	0	5	5	4	0	4	4	7655.372*	7655.368	0.004
5	0	5	6	4	0	4	5	7655.416*	7655.412	0.004
5	1	4	5	4	1	3	4	7937.228*	7937.225	0.003
5	1	4	6	4	1	3	5	7937.313*	7937.309	0.004
6	1	6	6	5	1	5	5	8904.367*	8904.376	-0.009
6	1	6	5	5	1	5	4	8904.393*	8904.392	0.001
6	1	6	7	5	1	5	6	8904.433*	8904.441	-0.008
6	0	6	6	5	0	5	5	9169.835*	9169.838	-0.003
6	0	6	7	5	0	5	6	9169.877*	9169.881	-0.004
6	1	5	6	5	1	4	5	9520.145*	9520.147	-0.002
6	1	5	7	5	1	4	6	9520.199*	9520.202	-0.003

**Table D.7 Observed Transitions for H<sub>5</sub>C<sub>5</sub>N-HCCD 0<sup>+</sup> State**

J'	K <sub>a</sub> '	K <sub>c</sub> '	F'	J''	K <sub>a</sub> ''	K <sub>c</sub> ''	F''	Observed Frequency (MHz)	Calculated Frequency (MHz)	Obs-Calc (MHz)
3	1	3	3	2	1	2	2	4316.093*	4316.093	0.000
3	1	3	2	2	1	2	1	4316.368*	4316.369	-0.001
3	1	3	4	2	1	2	3	4316.459*	4316.460	-0.001
3	0	3	3	2	0	2	2	4451.008*	4451.015	-0.007
3	0	3	4	2	0	2	3	4451.076*	4451.074	0.002
3	1	2	3	2	1	1	2	4594.195*	4594.196	-0.001
3	1	2	4	2	1	1	3	4594.529*	4594.530	-0.001
3	1	2	2	2	1	1	1	4594.610*	4594.609	0.001
4	1	4	4	3	1	3	3	5753.345*	5753.344	0.001
4	1	4	3	3	1	3	2	5753.425*	5753.424	0.001
4	1	4	5	3	1	3	4	5753.514*	5753.513	0.001
4	0	4	3	3	0	3	2	5928.590*	5928.587	0.003
4	0	4	4	3	0	3	3	5928.656*	5928.651	0.005
4	0	4	5	3	0	3	4	5928.696*	5928.697	-0.001
4	1	3	4	3	1	2	3	6124.232*	6124.235	-0.003
4	1	3	5	3	1	2	4	6124.388*	6124.384	0.004
5	1	5	5	4	1	4	4	7189.094*	7189.091	0.003
5	1	5	4	4	1	4	3	7189.120*	7189.122	-0.002
5	1	5	6	4	1	4	5	7189.187*	7189.188	-0.001
5	0	5	4	4	0	4	3	7401.109*	7401.114	-0.005
5	0	5	5	4	0	4	4	7401.139*	7401.136	0.003
5	0	5	6	4	0	4	5	7401.176*	7401.178	-0.002
5	1	4	5	4	1	3	4	7652.783*	7652.782	0.001
5	1	4	6	4	1	3	5	7652.864*	7652.865	-0.001
6	0	6	6	5	0	5	5	8867.246*	8867.244	0.002
6	0	6	7	5	0	5	6	8867.284*	8867.285	-0.001

**Table D.8 Observed Transitions for H<sub>5</sub>C<sub>5</sub>N-HCCD 0<sup>-</sup> State**

J'	K <sub>a</sub> '	K <sub>c</sub> '	F'	J''	K <sub>a</sub> ''	K <sub>c</sub> ''	F''	Observed Frequency (MHz)	Calculated Frequency (MHz)	Obs-Calc (MHz)
3	1	3	3	2	1	2	2	4304.151*	4304.158	-0.007
3	1	3	2	2	1	2	1	4304.425*	4304.432	-0.007
3	1	3	4	2	1	2	3	4304.516*	4304.522	-0.006
3	0	3	3	2	0	2	2	4442.941*	4442.950	-0.009
3	0	3	4	2	0	2	3	4443.006*	4443.009	-0.003
3	1	2	3	2	1	1	2	4590.540*	4590.542	-0.002
3	1	2	4	2	1	1	3	4590.872*	4590.875	-0.003
3	1	2	2	2	1	1	1	4590.953*	4590.952	0.001
4	1	4	4	3	1	3	3	5737.722*	5737.721	0.001
4	1	4	3	3	1	3	2	5737.803*	5737.801	0.002
4	1	4	5	3	1	3	4	5737.893*	5737.890	0.003
4	0	4	3	3	0	3	2	5917.719*	5917.714	0.005
4	0	4	4	3	0	3	3	5917.781*	5917.777	0.004
4	0	4	5	3	0	3	4	5917.823*	5917.824	-0.001
4	1	3	4	3	1	2	3	6119.335*	6119.336	-0.001
4	1	3	5	3	1	2	4	6119.490*	6119.484	0.006
5	1	5	5	4	1	4	4	7170.047*	7170.043	0.004
5	1	5	4	4	1	4	3	7170.086*	7170.074	0.012
5	1	5	6	4	1	4	5	7170.142*	7170.139	0.003
5	0	5	4	4	0	4	3	7387.359*	7387.360	-0.001
5	0	5	5	4	0	4	4	7387.391*	7387.382	0.009
5	0	5	6	4	0	4	5	7387.423*	7387.424	-0.001
5	1	4	5	4	1	3	4	7646.618*	7646.619	-0.001
5	1	4	6	4	1	3	5	7646.701*	7646.702	-0.001
6	1	6	6	5	1	5	5	8600.943*	8600.953	-0.010
6	1	6	5	5	1	5	4	8600.983*	8600.968	0.015
6	1	6	7	5	1	5	6	8601.001*	8601.016	-0.015
6	0	6	6	5	0	5	5	8850.562*	8850.562	0.000
6	0	6	7	5	0	5	6	8850.598*	8850.603	-0.005

**Table D.9 Observed Transitions for Inner-meta  $^{13}\text{C}$ -  $\text{H}_5\text{C}_5\text{N}$ -HCCH**

J'	K <sub>a</sub> '	K <sub>c</sub> '	F'	J''	K <sub>a</sub> ''	K <sub>c</sub> ''	F''	Observed Frequency (MHz)	Calculated Frequency (MHz)	Obs-Calc (MHz)
3	1	3	3	2	1	2	2	4473.803*	4473.806	-0.003
3	1	3	2	2	1	2	1	4474.080*	4474.087	-0.007
3	1	3	4	2	1	2	3	4474.172*	4474.175	-0.003
3	0	3	2	2	0	2	1	4623.762*	4623.766	-0.004
3	0	3	3	2	0	2	2	4623.938*	4623.945	-0.007
3	0	3	4	2	0	2	3	4624.002*	4624.005	-0.003
3	1	2	3	2	1	1	2	4785.348*	4785.349	-0.001
3	1	2	4	2	1	1	3	4785.685*	4785.687	-0.002
3	1	2	2	2	1	1	1	4785.760*	4785.762	-0.002
4	1	4	4	3	1	3	3	5963.564*	5963.560	0.004
4	1	4	5	3	1	3	4	5963.736*	5963.730	0.006
4	0	4	3	3	0	3	2	6157.626*	6157.618	0.008
4	0	4	4	3	0	3	3	6157.685*	6157.680	0.005
4	0	4	5	3	0	3	4	6157.735*	6157.729	0.006
4	1	3	4	3	1	2	3	6378.728*	6378.725	0.003
4	1	3	5	3	1	2	4	6378.880*	6378.876	0.004
5	1	5	5	4	1	4	4	7451.771*	7451.775	-0.004
5	1	5	6	4	1	4	5	7451.867*	7451.873	-0.006
5	0	5	5	4	0	4	4	7684.992*	7684.997	-0.005
5	0	5	6	4	0	4	5	7685.039*	7685.041	-0.002
5	1	4	5	4	1	3	4	7970.272*	7970.272	0.000
5	1	4	6	4	1	3	5	7970.362*	7970.356	0.006
4	1	4	3	3	1	3	2	5963.649*	5963.642	0.007
5	1	5	4	4	1	4	3	7451.811*	7451.807	0.004
5	1	4	4	4	1	3	3	7970.327*	7970.336	-0.009

**Table D.10 Observed Transitions for Outer-meta  $^{13}\text{C}$ -  $\text{H}_5\text{C}_5\text{N}$ -HCCH**

J'	K <sub>a</sub> '	K <sub>c</sub> '	F'	J''	K <sub>a</sub> ''	K <sub>c</sub> ''	F''	Observed Frequency (MHz)	Calculated Frequency (MHz)	Obs-Calc (MHz)
3	1	3	3	2	1	2	2	4459.823*	4459.816	0.007
3	1	3	2	2	1	2	1	4460.097*	4460.095	0.002
3	1	3	4	2	1	2	3	4460.188*	4460.181	0.007
3	0	3	2	2	0	2	1	4606.085*	4606.085	0.000
3	0	3	3	2	0	2	2	4606.265*	4606.264	0.001
3	0	3	4	2	0	2	3	4606.324*	4606.323	0.001
3	1	2	3	2	1	1	2	4763.119*	4763.120	-0.001
3	1	2	4	2	1	1	3	4763.453*	4763.454	-0.001
3	1	2	2	2	1	1	1	4763.531*	4763.528	0.003
4	1	4	4	3	1	3	3	5944.755*	5944.762	-0.007
4	1	4	3	3	1	3	2	5944.836*	5944.843	-0.007
4	1	4	5	3	1	3	4	5944.923*	5944.930	-0.007
4	0	4	3	3	0	3	2	6134.419*	6134.419	0.000
4	0	4	4	3	0	3	3	6134.480*	6134.482	-0.002
4	0	4	5	3	0	3	4	6134.527*	6134.529	-0.002
4	1	3	4	3	1	2	3	6349.150*	6349.153	-0.003
4	1	3	5	3	1	2	4	6349.303*	6349.302	0.001
5	1	5	5	4	1	4	4	7428.038*	7428.035	0.003
5	1	5	4	4	1	4	3	7428.073*	7428.068	0.005
5	1	5	6	4	1	4	5	7428.131*	7428.132	-0.001
5	0	5	5	4	0	4	4	7656.577*	7656.573	0.004
5	0	5	6	4	0	4	5	7656.614*	7656.616	-0.002
5	1	4	5	4	1	3	4	7933.418*	7933.415	0.003
5	1	4	6	4	1	3	5	7933.503*	7933.499	0.004
5	1	4	4	4	1	3	3	7933.472*	7933.479	-0.007

**Table D.11 Observed Transitions for Inner-ortho  $^{13}\text{C}$ -  $\text{H}_5\text{C}_5\text{N}$ -HCCH**

J'	K <sub>a</sub> '	K <sub>c</sub> '	F'	J''	K <sub>a</sub> ''	K <sub>c</sub> ''	F''	Observed Frequency (MHz)	Calculated Frequency (MHz)	Obs-Calc (MHz)
3	1	3	3	2	1	2	2	4496.820*	4496.819	0.001
3	1	3	2	2	1	2	1	4497.097*	4497.098	-0.001
3	1	3	4	2	1	2	3	4497.188*	4497.186	0.002
3	0	3	2	2	0	2	1	4645.261*	4645.262	-0.001
3	0	3	3	2	0	2	2	4645.441*	4645.441	0.000
3	0	3	4	2	0	2	3	4645.500*	4645.501	-0.001
3	1	2	3	2	1	1	2	4804.721*	4804.722	-0.001
3	1	2	4	2	1	1	3	4805.058*	4805.058	0.000
3	1	2	2	2	1	1	1	4805.136*	4805.133	0.003
4	1	4	4	3	1	3	3	5993.981*	5993.981	0.000
4	1	4	3	3	1	3	2	5994.060*	5994.062	-0.002
4	1	4	5	3	1	3	4	5994.148*	5994.150	-0.002
4	0	4	3	3	0	3	2	6186.435*	6186.432	0.003
4	0	4	4	3	0	3	3	6186.497*	6186.495	0.002
4	0	4	5	3	0	3	4	6186.539*	6186.543	-0.004
4	1	3	4	3	1	2	3	6404.581*	6404.583	-0.002
4	1	3	5	3	1	2	4	6404.732*	6404.733	-0.001
5	1	5	5	4	1	4	4	7489.369*	7489.368	0.001
5	1	5	4	4	1	4	3	7489.404*	7489.400	0.004
5	1	5	6	4	1	4	5	7489.461*	7489.465	-0.004
5	0	5	5	4	0	4	4	7721.225*	7721.225	0.000
5	0	5	6	4	0	4	5	7721.267*	7721.268	-0.001
5	1	4	5	4	1	3	4	8002.637*	8002.635	0.002
5	1	4	4	4	1	3	3	8002.692*	8002.699	-0.007
5	1	4	6	4	1	3	5	8002.725*	8002.719	0.006

**Table D.12 Observed Transitions for Outer-ortho  $^{13}\text{C}$ -  $\text{H}_5\text{C}_5\text{N}$ -HCCH**

J'	K <sub>a</sub> '	K <sub>c</sub> '	F'	J''	K <sub>a</sub> ''	K <sub>c</sub> ''	F''	Observed Frequency (MHz)	Calculated Frequency (MHz)	Obs-Calc (MHz)
3	1	3	3	2	1	2	2	4481.705*	4481.707	-0.002
3	1	3	2	2	1	2	1	4481.984*	4481.987	-0.003
3	1	3	4	2	1	2	3	4482.074*	4482.076	-0.002
3	0	3	2	2	0	2	1	4632.276*	4632.277	-0.001
3	0	3	3	2	0	2	2	4632.454*	4632.456	-0.002
3	0	3	4	2	0	2	3	4632.513*	4632.517	-0.004
3	1	2	3	2	1	1	2	4794.288*	4794.288	-0.000
3	1	2	4	2	1	1	3	4794.623*	4794.625	-0.002
3	1	2	2	2	1	1	1	4794.702*	4794.700	0.002
4	1	4	4	3	1	3	3	5974.119*	5974.116	0.003
4	1	4	3	3	1	3	2	5974.202*	5974.198	0.004
4	1	4	5	3	1	3	4	5974.289*	5974.286	0.003
4	0	4	3	3	0	3	2	6168.975*	6168.972	0.003
4	0	4	4	3	0	3	3	6169.038*	6169.034	0.004
4	0	4	5	3	0	3	4	6169.085*	6169.083	0.002
4	1	3	4	3	1	2	3	6390.622*	6390.620	0.002
4	1	3	3	3	1	2	2	6390.756*	6390.759	-0.003
4	1	3	5	3	1	2	4	6390.773*	6390.771	0.002
5	0	5	5	4	0	4	4	7699.192*	7699.200	-0.008
5	0	5	6	4	0	4	5	7699.250*	7699.245	0.005
5	1	5	5	4	1	4	4	7465.003*	7465.005	-0.002
5	1	5	6	4	1	4	5	7465.096*	7465.103	-0.007
5	1	4	5	4	1	3	4	7985.104*	7985.104	0.000
5	1	4	6	4	1	3	5	7985.195*	7985.188	0.007
5	1	4	4	4	1	3	3	7985.161*	7985.168	-0.007
5	1	5	4	4	1	4	3	7465.044*	7465.038	0.006



## Appendix E : Supplemental Material for Chapter 5

**Table E.1 H<sub>2</sub>O - Pyridine Transitions**

$v'$	$v''$	$J'$	$K_1'$	$K_1'$	$J''$	$K_1''$	$K_1''$	$F'$	$F''$	Observed Frequency (MHz)	Obs-Calc (MHz)
0	0	1	0	1	0	0	0	1	1	2654.210	-0.010
0	0	1	0	1	0	0	0	2	1	2655.529	0.005
0	0	1	0	1	0	0	0	0	1	2657.497	0.016
1	1	1	0	1	0	0	0	1	1	2698.605	-0.012
1	1	1	0	1	0	0	0	2	1	2699.969	0.003
1	1	1	0	1	0	0	0	0	1	2701.999	0.009
0	1	4	1	4	3	0	3	3	2	2747.557	-0.006
0	1	4	1	4	3	0	3	4	3	2747.706	-0.003
0	1	4	1	4	3	0	3	5	4	2747.725	0.017
0	1	5	1	5	4	0	4	4	3	4554.778	0.001
0	1	5	1	5	4	0	4	5	4	4554.828	-0.003
0	1	5	1	5	4	0	4	6	5	4554.858	-0.001
1	1	2	1	2	1	1	1	2	1	4654.768	-0.021
1	1	2	1	2	1	1	1	3	2	4656.007	-0.013
*	0	2	1	2	1	1	1	2	1	<b>4899.613</b> 4899.638	-0.006
*	0	2	1	2	1	1	1	2	2	4900.022 4900.045	0.027
*	0	2	1	2	1	1	1	3	2	<b>4900.976</b> 4900.996	-0.002
*	0	2	1	2	1	1	1	1	0	4902.115 4902.137	0.026
*	0	2	0	2	1	0	1	1	0	5295.234	-0.008
	0	2	0	2	1	0	1	2	1	5296.302	-0.001
	0	2	0	2	1	0	1	3	2	5296.415	0.002
	0	2	0	2	1	0	1	1	2	5297.209	0.010
	0	2	0	2	1	0	1	1	1	5298.519	0.016
*	1	2	0	2	1	0	1	2	2	5366.142 <b>5366.161</b>	-0.009
*	1	2	0	2	1	0	1	1	0	5366.406 <b>5366.420</b>	-0.014
*	1	2	0	2	1	0	1	2	1	5367.506 5367.521	0.002
*	1	2	0	2	1	0	1	3	2	5367.619 <b>5367.636</b>	-0.005
*	1	2	0	2	1	0	1	1	1	5369.636 <b>5369.815</b>	0.008

Table E.1 continued...

$v'$	$v''$	$J'$	$K_1'$	$K_1'$	$J''$	$K_1''$	$K_1''$	$F'$	$F''$	Observed Frequency (MHz)	Obs- Calc (MHz)
0	0	2	1	1	1	1	0	2	1	5590.988	0.01
0	0	2	1	1	1	1	0	3	2	5592.318	0.003
0	0	2	1	1	1	1	0	1	0	5593.941	0.019
0	1	6	1	6	5	0	5	5	4	6361.116	0.005
0	1	6	1	6	5	0	5	6	5	6361.127	-0.012
0	1	6	1	6	5	0	5	7	6	6361.168	0.002
*										7122.265	
	1	3	1	3	2	1	2	3	2	<b>7122.388</b>	0.015
*										7122.667	
	1	3	1	3	2	1	2	4	3	<b>7122.789</b>	0.001
*	0	3	1	3	2	1	2	3	3	7370.853	0.019
*										7370.874	
	0	3	1	3	2	1	2	3	2	<b>7371.806</b>	-0.011
*										7371.826	
	0	3	1	3	2	1	2	2	1	7372.153	0.005
*	0	3	1	3	2	1	2	4	3	<b>7372.206</b>	-0.007
*										7372.225	
	0	3	1	3	2	1	2	2	2	<b>7373.631</b>	-0.047
*										7373.652	
*										7839.502	
	1	3	1	2	2	1	1	3	2	<b>7839.777</b>	0.014
*										7839.880	
	1	3	1	2	2	1	1	4	3	<b>7840.155</b>	-0.09
*										7840.012	
	1	3	1	2	2	1	1	2	1	<b>7840.286</b>	0.026
	0	3	0	3	2	0	2	3	3	7906.807	-0.011
	0	3	0	3	2	0	2	2	1	7908.046	0.000
	0	3	0	3	2	0	2	3	2	7908.233	0.001
	0	3	0	3	2	0	2	4	3	7908.311	0.001
	0	3	0	3	2	0	2	2	2	7910.268	0.022
	1	3	0	3	2	0	2	2	1	7980.324	-0.014
	1	3	0	3	2	0	2	3	2	7980.521	0.001
	1	3	0	3	2	0	2	4	3	7980.604	-0.005
*	0	3	2	1	2	2	0	3	2	<b>8280.821</b>	0.024
*										8280.954	
	0	3	2	1	2	2	0	4	3	<b>8282.177</b>	0.013
*										8282.304	
	0	3	2	1	2	2	0	2	1	<b>8282.867</b>	-0.027
*										8283.001	

Table E.1 continued...

$v'$	$v''$	$J'$	$K_1'$	$K_1'$	$J''$	$K_1''$	$K_1''$	$F'$	$F''$	Observed Frequency (MHz)	Obs- Calc (MHz)
0	0	3	1	2	2	1	1	3	3	8380.052	0.033
0	0	3	1	2	2	1	1	3	2	8380.425	0.000
0	0	3	1	2	2	1	1	4	3	8380.805	-0.002
0	0	3	1	2	2	1	1	2	1	8380.855	-0.002
0	0	3	1	2	2	1	1	2	2	8381.438	-0.052
		3	2	2	2	2	1	3	2	8448.419	0.007
*										8448.707	
		3	2	2	2	2	1	4	3	8448.809	0.010
*										8450.093	
		3	2	2	2	2	1	2	1	8450.495	-0.031
*										8450.779	
	1	4	1	4	3	1	3	4	3	9636.320	0.002
	1	4	1	4	3	1	3	5	4	9636.537	0.008
	0	4	1	4	3	1	3	4	3	9852.538	-0.011
	0	4	1	4	3	1	3	3	2	9852.652	0.004
	0	4	1	4	3	1	3	5	4	9852.726	-0.004
*										10143.832	
	1	4	2	3	3	2	2	4	3	<b>10142.929</b>	0.033
*										10144.378	
	1	4	2	3	3	2	2	5	4	<b>10144.477</b>	-0.016
	1	4	2	3	3	2	2	3	2	10144.627	-0.025
*										10306.578	
	1	4	2	2	3	2	1	4	3	<b>10306.673</b>	0.034
*										10307.087	
	1	4	2	2	3	2	1	5	4	<b>10307.182</b>	-0.019
	1	4	2	2	3	2	1	3	2	10307.334	-0.020
	0	4	0	4	3	0	3	4	4	10474.508	-0.019
	0	4	0	4	3	0	3	3	2	10475.971	0.005
	0	4	0	4	3	0	3	4	3	10476.023	0.004
	0	4	0	4	3	0	3	5	4	10476.090	0.003
	0	4	0	4	3	0	3	3	3	10478.006	0.025
*										10490.596	
	1	4	1	3	3	1	2	4	3	<b>10490.852</b>	-0.013
	1	4	1	3	3	1	2	5	4	10491.088	0.001
	1	4	0	4	3	0	3	3	2	10525.872	-0.005
	1	4	0	4	3	0	3	4	3	10525.927	0.002
	1	4	0	4	3	0	3	5	4	10525.998	-0.004

Table E.1 continued...

	$v'$	$v''$	$J'$	$K_1'$	$K_1'$	$J''$	$K_1''$	$K_1''$	$F'$	$F''$	Observed Frequency (MHz)	Obs- Calc (MHz)
	1	1	4	1	4	3	1	3	4	3	9636.320	0.002
	1	1	4	1	4	3	1	3	5	4	9636.537	0.008
	0	0	4	1	4	3	1	3	4	3	9852.538	-0.011
	0	0	4	1	4	3	1	3	3	2	9852.652	0.004
	0	0	4	1	4	3	1	3	5	4	9852.726	-0.004
*											10143.832	
	1	1	4	2	3	3	2	2	4	3	<b>10142.929</b>	0.033
*											10144.378	
	1	1	4	2	3	3	2	2	5	4	<b>10144.477</b>	-0.016
	1	1	4	2	3	3	2	2	3	2	10144.627	-0.025
*											10306.578	
	1	1	4	2	2	3	2	1	4	3	<b>10306.673</b>	0.034
*											10307.087	
	1	1	4	2	2	3	2	1	5	4	<b>10307.182</b>	-0.019
	1	1	4	2	2	3	2	1	3	2	10307.334	-0.020
	0	0	4	0	4	3	0	3	4	4	10474.508	-0.019
	0	0	4	0	4	3	0	3	3	2	10475.971	0.005
	0	0	4	0	4	3	0	3	4	3	10476.023	0.004
	0	0	4	0	4	3	0	3	5	4	10476.090	0.003
	0	0	4	0	4	3	0	3	3	3	10478.006	0.025
*											10490.596	
	1	1	4	1	3	3	1	2	4	3	<b>10490.852</b>	-0.013
	1	1	4	1	3	3	1	2	5	4	10491.088	0.001
	1	1	4	0	4	3	0	3	3	2	10525.872	-0.005
	1	1	4	0	4	3	0	3	4	3	10525.927	0.002
	1	1	4	0	4	3	0	3	5	4	10525.998	-0.004
*	0	0	4	2	2	3	2	1	4	3	<b>10942.369</b>	0.029
											10942.431	
*	0	0	4	2	2	3	2	1	5	4	<b>10942.880</b>	-0.001
											10942.935	
*	0	0	4	2	2	3	2	1	3	2	<b>10942.989</b>	-0.018
											10943.045	
	0	0	4	1	3	3	1	2	4	3	11159.730	-0.007
	0	0	4	1	3	3	1	2	3	2	11159.871	-0.012
	0	0	4	1	3	3	1	2	5	4	11159.916	0.005
*	0	0	4	2	3	3	2	2	4	3	<b>11196.733</b>	0.024
											11197.014	
*	0	0	4	2	3	3	2	2	5	4	<b>11197.258</b>	-0.004
*											11197.535	

Table E.1 continued...

	$v'$	$v''$	$J'$	$K_1'$	$K_1'$	$J''$	$K_1''$	$K_1''$	$F'$	$F''$	Observed Frequency (MHz)	Obs- Calc (MHz)
*	0	0	4	2	3	3	2	2	3	2	<b>11197.356</b> 11197.636	-0.029
	1	1	5	1	5	4	1	4	5	4	12171.529	-0.008
	1	1	5	1	5	4	1	4	4	3	12171.637	0.022
	1	1	5	1	5	4	1	4	6	5	12171.682	0.016
	0	0	5	1	5	4	1	4	5	5	12331.493	0.004
	0	0	5	1	5	4	1	4	5	4	12333.036	-0.012
	0	0	5	1	5	4	1	4	4	3	12333.092	0.001
	0	0	5	1	5	4	1	4	6	5	12333.149	-0.004
	0	0	5	1	5	4	1	4	4	4	12335.029	-0.022
*											12704.949	
*	1	1	5	2	4	4	2	3	5	4	<b>12705.055</b>	0.012
*											12705.245	
	1	1	5	2	4	4	2	3	6	5	<b>12705.345</b>	-0.018
	1	1	5	2	4	4	2	3	4	3	12705.402	0.003
	0	0	5	0	5	4	0	4	5	4	12985.958	0.004
	0	0	5	0	5	4	0	4	6	5	12986.030	0.009
	1	1	5	0	5	4	0	4	5	4	12998.505	0.004
	1	1	5	0	5	4	0	4	6	5	12998.581	0.008
*											13017.623	
*	1	1	5	2	3	4	2	2	5	4	<b>13017.720</b>	0.010
*											13017.878	
*	1	1	5	2	3	4	2	2	6	5	<b>13017.971</b>	-0.017
*											13017.935	
	1	1	5	2	3	4	2	2	4	3	<b>13018.025</b>	0.005
	1	1	5	1	4	4	1	3	6	5	13145.448	0.002
*	0	0	5	2	3	4	2	2	5	4	<b>13617.230</b> 13617.283	0.018
*	0	0	5	2	3	4	2	2	6	5	<b>13617.452</b> 13617.510	-0.015
*	0	0	5	2	4	4	2	3	5	4	13912.383	0.028
*	0	0	5	2	4	4	2	3	6	5	<b>13912.620</b> 13912.877	-0.007
	0	0	5	1	4	4	1	3	5	4	13925.251	-0.002
	0	0	5	1	4	4	1	3	4	3	13925.305	-0.019
	0	0	5	1	4	4	1	3	6	5	13925.358	0.003
	1	1	6	1	6	5	1	5	6	5	14711.516	-0.004
	1	1	6	1	6	5	1	5	5	4	14711.566	-0.005

Table E.1 continued...

$v'$	$v''$	$J'$	$K_1'$	$K_1'$	$J''$	$K_1''$	$K_1''$	$F'$	$F''$	Observed Frequency (MHz)	Obs-Calc (MHz)
1	1	6	1	6	5	1	5	7	6	14711.627	0.016
0	0	6	1	6	5	1	5	6	5	14804.812	0.003
0	0	6	1	6	5	1	5	7	6	14804.880	-0.001
*										15275.130	
	1	6	2	5	5	2	4	6	5	<b>15275.228</b>	0.006
*										15275.324	
	1	6	2	5	5	2	4	7	6	<b>15275.414</b>	-0.002
	1	6	0	6	5	0	5	7	6	15401.079	-0.035
	0	6	0	6	5	0	5	7	6	15429.449	0.022
	1	6	2	4	5	2	3	6	5	15791.135	0.003
	1	6	2	4	5	2	3	7	6	15791.280	-0.003
	0	6	2	4	5	2	3	6	5	16327.323	0.011
	0	6	2	4	5	2	3	7	6	16327.429	-0.010
	0	6	1	5	5	1	4	7	6	16671.887	-0.001
●	1	7	1	7	6	1	6	8	7	17240.945	-0.071
●	0	7	1	7	6	1	6	7	6	17261.629	-0.012
●	0	7	1	7	6	1	6	8	7	17261.708	0.013
●	1	7	0	7	6	0	6	8	7	17746.464	-0.059
●	0	7	0	7	6	0	6	8	7	17807.489	0.013
●	1	7	2	6	6	2	5	8	7	17852.831	-0.044

\* The doubled counterparts resulting from the second set of smaller splittings. The transitions in bold are the more intense of the two signals. If neither signal is bolded, the transitions were of similar intensity.

● Transitions were only observed in the chirped-pulse spectrum. These transitions were not included in the final fit. The residuals listed use the predicted frequency from the constants reported in the paper.

**Table E.2 D<sub>2</sub>O - Pyridine Transitions**

	v'	v''	J'	K <sub>1</sub> '	K <sub>1</sub> '	J''	K <sub>1</sub> ''	K <sub>1</sub> ''	F'	F''	Observed Frequency (MHz)	Obs- Calc (MHz)
*	0	0	1	0	1	0	0	0	1	1	2510.193 2510.218	-0.016
*	0	0	1	0	1	0	0	0	2	1	2511.513 2511.563	-0.015
*	0	0	1	0	1	0	0	0	0	1	2513.510	0.003
*	1	1	1	0	1	0	0	0	1	1	2538.761 2538.784 2538.807	-0.016
*	1	1	1	0	1	0	0	0	2	1	2540.144 2540.158	0.017
	1	1	1	0	1	0	0	0	0	1	2542.149	-0.003
	0	1	6	1	6	5	0	5	6	5	2827.200	0.010
	0	1	6	1	6	5	0	5	7	6	2827.268	-0.009
	0	1	7	1	7	6	0	6	7	6	4569.238	0.004
	0	1	7	1	7	6	0	6	6	5	4569.284	0.005
	0	1	7	1	7	6	0	6	8	7	4569.307	-0.004
	0	0	2	1	2	1	1	1	2	1	4674.701	0.006
	0	0	2	1	2	1	1	1	3	2	4676.050	-0.025
	0	0	2	1	2	1	1	1	1	0	4677.212	0.018
	0	0	2	0	2	1	0	1	2	2	5009.706	0.003
	0	0	2	0	2	1	0	1	1	0	5009.944	-0.003
	0	0	2	0	2	1	0	1	3	2	5011.133	0.001
	0	0	2	0	2	1	0	1	1	2	5011.941	0.014
	0	0	2	0	2	1	0	1	1	1	5013.234	-0.012
	0	0	2	1	1	1	1	0	2	1	5276.829	0.009
	0	0	2	1	1	1	1	0	3	2	5278.141	-0.023
	0	1	8	1	8	7	0	7	8	7	6378.610	-0.005
	0	1	8	1	8	7	0	7	9	8	6378.674	-0.002
*	1	1	3	1	3	2	1	2	3	2	6621.114 6621.143	-0.029
*	1	1	3	1	3	2	1	2	4	3	6621.866 6621.891	0.010
*	1	1	3	1	3	2	1	2	2	1	6622.125 6622.149	0.040
*	0	0	3	1	3	2	1	2	3	2	7020.874 7020.894	-0.014

Table E.2 continued...

	$v'$	$v''$	$J'$	$K_1'$	$K_1'$	$J''$	$K_1''$	$K_1''$	$F'$	$F''$	Observed Frequency (MHz)	Obs- Calc (MHz)
*	0	0	3	1	3	2	1	2	2	1	7021.222 7021.238	0.012
	0	0	3	1	3	2	1	2	4	3	7021.280	-0.012
	0	0	3	2	2	2	2	1	3	2	7045.388 7045.420 7045.483	-0.056
*	0	0	3	2	2	2	2	1	4	3	7046.267 7046.300	-0.011
*	0	0	3	2	2	2	2	1	2	1	7046.741 7046.764	0.068
	0	0	3	0	3	2	0	2	3	3	7485.833	0.002
	0	0	3	0	3	2	0	2	2	1	7487.074	0.003
	0	0	3	0	3	2	0	2	3	2	7487.264	0.004
	0	0	3	0	3	2	0	2	4	3	7487.342	0.004
	0	0	3	0	3	2	0	2	2	2	7489.295	0.000
	1	1	3	0	3	2	0	2	2	1	7541.888	-0.003
	1	1	3	0	3	2	0	2	3	2	7542.082	0.002
	1	1	3	0	3	2	0	2	4	3	7542.161	-0.002
	0	0	3	1	2	2	1	1	3	3	7910.230 7910.274	0.016
*	0	0	3	1	2	2	1	1	3	2	7910.610	-0.002
	0	0	3	1	2	2	1	1	4	3	7910.993	-0.005
	1	1	3	1	2	2	1	1	3	2	8354.687 8354.700	0.057
*	1	1	3	1	2	2	1	1	4	3	8355.590 8355.636	-0.011
*	1	1	3	1	2	2	1	1	2	1	8355.954 8355.983	-0.084
	1	1	4	1	4	3	1	3	4	3	9104.363	-0.029
	1	1	4	1	4	3	1	3	5	4	9104.737	0.011
	0	0	4	1	4	3	1	3	4	3	9370.053	-0.005
	0	0	4	1	4	3	1	3	3	2	9370.164	0.005
	0	0	4	1	4	3	1	3	5	4	9370.239	-0.004
	0	0	4	2	3	3	2	2	4	3	9644.449	-0.038
	0	0	4	2	3	3	2	2	5	4	9644.886	0.005
	0	0	4	2	3	3	2	2	3	2	9644.989	0.037



Table E.2 continued...

$v'$	$v''$	$J'$	$K_1'$	$K_1'$	$J''$	$K_1''$	$K_1''$	$F'$	$F''$	Observed Frequency (MHz)	Obs-Calc (MHz)
0	0	4	0	4	3	0	3	4	4	9926.427	0.002
0	0	4	0	4	3	0	3	3	2	9927.883	0.005
0	0	4	0	4	3	0	3	4	3	9927.937	0.005
0	0	4	0	4	3	0	3	5	4	9928.007	0.007
0	0	4	0	4	3	0	3	3	3	9929.919	0.006
1	1	4	0	4	3	0	3	3	2	9973.139	-0.001
1	1	4	0	4	3	0	3	4	3	9973.197	0.004
1	1	4	0	4	3	0	3	5	4	9973.266	0.001
0	0	4	2	2	3	2	1	4	3	10396.006	0.036
0	0	4	2	2	3	2	1	5	4	10396.378	-0.019
0	0	4	2	2	3	2	1	3	2	10396.433	-0.030
0	0	4	1	3	3	1	2	4	3	10536.124	0.003
0	0	4	1	3	3	1	2	3	2	10536.261	-0.008
0	0	4	1	3	3	1	2	5	4	10536.301	0.004
1	1	4	1	3	3	1	2	4	3	10865.306	0.055
1	1	4	1	3	3	1	2	5	4	10865.630	-0.009
1	1	4	1	3	3	1	2	3	2	10865.657	-0.036
1	1	5	1	5	4	1	4	5	4	11564.150	-0.012
1	1	5	1	5	4	1	4	6	5	11564.359	0.009
0	0	5	1	5	4	1	4	5	4	11718.588	-0.004
0	0	5	1	5	4	1	4	4	3	11718.641	0.007
0	0	5	1	5	4	1	4	6	5	11718.700	0.002
1	1	5	2	4	4	2	3	5	4	11924.439	0.003
1	1	5	2	4	4	2	3	6	5	11924.747	-0.010
•	1	5	2	3	4	2	2	5	4	12169.128	0.007
•	1	5	2	3	4	2	2	6	5	12169.384	-0.020
0	0	5	2	4	4	2	3	5	4	12207.202	-0.027
0	0	5	2	4	4	2	3	6	5	12207.454	0.001
0	0	5	2	4	4	2	3	4	3	12207.499	0.039
0	0	5	0	5	4	0	4	5	5	12320.288	0.000
0	0	5	0	5	4	0	4	5	4	12321.864	0.001
0	0	5	0	5	4	0	4	6	5	12321.933	0.004
0	0	5	0	5	4	0	4	4	4	12323.842	0.004
1	1	5	0	5	4	0	4	5	4	12344.220	0.009
1	1	5	0	5	4	0	4	6	5	12344.280	0.002
•	0	5	2	3	4	2	2	5	4	12864.091	0.050
•	0	5	2	3	4	2	2	6	5	12864.218	-0.022

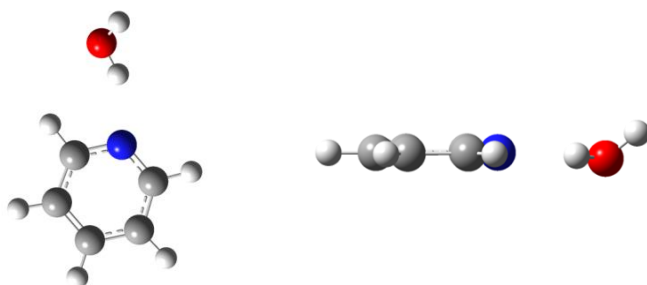
Table E.2 continued...

	$v'$	$v''$	$J'$	$K_{-1}'$	$K_1'$	$J''$	$K_{-1}''$	$K_1''$	$F'$	$F''$	Observed Frequency (MHz)	Obs-Calc (MHz)
	0	0	5	1	4	4	1	3	5	4	13150.574	0.003
	0	0	5	1	4	4	1	3	4	3	13150.623	-0.019
	0	0	5	1	4	4	1	3	6	5	13150.678	0.005
	1	1	5	1	4	4	1	3	5	4	13388.775	0.044
	1	1	5	1	4	4	1	3	4	3	13388.906	-0.017
	1	1	5	1	4	4	1	3	6	5	13388.947	0.017
	1	1	6	1	6	5	1	5	7	6	14010.401	0.026
•	0	0	6	1	6	5	1	5	7	6	14061.695	-0.035
•	1	1	6	2	5	5	2	4	6	5	14366.629	-0.002
•	1	1	6	2	5	5	2	4	7	6	14366.830	0.000
	1	1	6	0	6	5	0	5	7	6	14652.836	-0.040
	0	0	6	0	6	5	0	5	6	5	14661.214	0.002
	0	0	6	0	6	5	0	5	7	6	14661.277	-0.001
•	0	0	6	2	5	5	2	4	6	5	14749.814	-0.010
•	0	0	6	2	5	5	2	4	7	6	14749.968	-0.002
•	1	1	6	2	4	5	2	3	6	5	14771.297	0.003
•	1	1	6	2	4	5	2	3	7	6	14771.449	-0.004
•	0	0	6	2	4	5	2	3	6	5	15378.542	0.003
•	0	0	6	2	4	5	2	3	7	6	15378.630	-0.004
•	0	0	6	1	5	5	1	4	7	6	15750.012	-0.012
•	1	1	6	1	5	5	1	4	7	6	15901.788	-0.019
•	0	0	7	1	7	6	1	6	8	7	16394.923	0.013
•	1	1	7	1	7	6	1	6	8	7	16436.201	0.003
•	1	1	7	2	6	6	2	5	8	7	16820.975	0.012
	1	1	7	0	7	6	0	6	7	6	16905.585	0.012
	1	1	7	0	7	6	0	6	8	7	16905.614	-0.018
	0	0	7	0	7	6	0	6	7	6	16944.783	-0.007
	0	0	7	0	7	6	0	6	6	5	16944.824	0.003
	0	0	7	0	7	6	0	6	8	7	16944.876	0.022
•	0	0	7	2	6	6	2	5	8	7	17274.938	-0.003
•	1	1	7	2	5	6	2	4	8	7	17420.993	0.003
•	0	0	7	2	5	6	2	4	8	7	17944.986	-0.002

- \* Transitions were observed on the cavity but were not included in the fit. It was unclear if these transitions were deuterium hyperfine components or a result of the same secondary doubling observed in the H<sub>2</sub>O-pyridine spectrum. The most intense transition was used in the fit.
- Transitions were only observed in the chirped-pulse spectrum. These transitions were included in the final fit as they were necessary to improve the quality of the constants. This is in contrast to H<sub>2</sub>O, in which case, the transitions observed only on the chirped-pulse were not included because enough transitions were recorded with the cavity to satisfactorily fit the complex.

**Table E.3 H<sub>2</sub>O - Pyridine Minimum Energy Structure Coordinates**

M06-2X/6-311++G(3df,3pd)

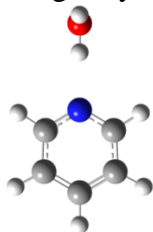


Atom	X	Y	Z
C	-0.252649	-0.858098	0.020209
C	1.045908	-1.346508	0.008049
C	2.093436	-0.439785	-0.006656
C	1.802675	0.915615	-0.009726
C	0.472122	1.306261	0.002509
N	-0.538898	0.442182	0.018269
H	3.118760	-0.782596	-0.016433
H	-1.105136	-1.526790	0.030042
H	1.223975	-2.411642	0.009411
H	2.586130	1.658818	-0.022354
H	0.206131	2.355807	-0.001296
O	-3.358447	-0.064761	-0.099019
H	-2.487992	0.360633	-0.042642
H	-3.870957	0.303672	0.621233

**Table E.4 In-Plane Rocking Motion Transition State Coordinates**

M06-2X/6-311++G(3df,3pd)

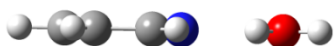
Imaginary Frequency:  $-36.64 \text{ cm}^{-1}$



Atom	X	Y	Z
C	-0.097465	1.140941	0.006258
C	-1.483478	1.192743	-0.000250
C	-2.189014	-0.000035	-0.003092
C	-1.483419	-1.192777	-0.000245
C	-0.097409	-1.140904	0.006263
N	0.586670	0.000036	0.010746
H	-3.270122	-0.000062	-0.008680
H	0.491234	2.049799	0.005765
H	-1.990490	2.146224	-0.004240
H	-1.990383	-2.146284	-0.004231
H	0.491336	-2.049732	0.005776
O	3.494946	-0.000015	-0.107630
H	2.524346	-0.000003	-0.068124
H	3.782531	0.000119	0.805950

**Table E.5 Free Proton Wag Transition State Coordinates**

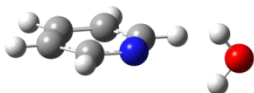
M06-2X/6-311++G(3df,3pd)

Imaginary Frequency:  $-138.96 \text{ cm}^{-1}$ 

Atom	X	Y	Z
C	0.276082	0.832104	-0.000018
C	-1.010724	1.350837	0.000218
C	-2.079592	0.469312	0.000389
C	-1.820992	-0.892507	0.000317
C	-0.499850	-1.314268	0.000076
N	0.531593	-0.474703	-0.000089
H	-3.096543	0.836379	0.000575
H	1.143075	1.481991	-0.000158
H	-1.163385	2.419901	0.000266
H	-2.621768	-1.617132	0.000444
H	-0.259329	-2.369996	0.000013
O	3.323600	0.105008	-0.000651
H	2.484754	-0.382650	-0.000475
H	4.013708	-0.558509	-0.000723

**Table E.6 Water Rotation Transition State Coordinates**

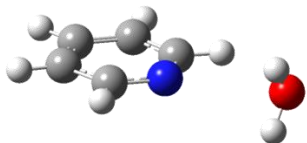
M06-2X/6-311++G(3df,3pd)

Imaginary Frequency:  $-242.17 \text{ cm}^{-1}$ 

Atom	X	Y	Z
C	0.296817	0.789509	-0.000001
C	-0.968617	1.360059	-0.000008
C	-2.071966	0.522284	-0.000008
C	-1.866259	-0.848492	-0.000002
C	-0.562024	-1.321232	0.000005
N	0.505187	-0.526003	0.000005
H	-3.073660	0.929196	-0.000014
H	1.186413	1.408688	-0.000001
H	-1.078468	2.434525	-0.000013
H	-2.694798	-1.541381	-0.000002
H	-0.365192	-2.386224	0.000010
O	3.454242	0.048207	0.000007
H	2.943879	-0.280610	-0.744455
H	2.943876	-0.280604	0.744470

### Table E.7 C<sub>2</sub> Rotation of Water Transition State Coordinates

Single point calculation of the presumed transition state during a C<sub>2</sub> rotation of the water at M06-2X/6-311++G(3df,3pd). From the transition state planar structure, the protons were rotated about the C<sub>2</sub> axis of water until they were perpendicular to the plane of the pyridine. The energy difference between this structure and the planar transition state was taken as the barrier for the rotation.



Atom	X	Y	Z
C	-0.278297	0.828790	-0.000106
C	1.006560	1.352354	0.000269
C	2.078793	0.474935	0.000302
C	1.825328	-0.887827	-0.000040
C	0.505772	-1.314527	-0.000402
N	-0.528998	-0.478973	-0.000436
H	3.094351	0.845858	0.000590
H	-1.147641	1.475500	-0.000146
H	1.155207	2.421985	0.000528
H	2.628817	-1.609453	-0.000030
H	0.269293	-2.371165	-0.000676
O	-3.325353	0.102152	-0.000792
H	-3.261343	-0.478424	0.773877
H	-3.261813	-0.471061	-0.764893

## Appendix F : Supplemental Material for Chapter 6

**Table F.1 Observed transitions for Kr-SO<sub>3</sub> and Kr-SO<sub>3</sub>-CO isotopologues.**

$J''$	$J'$	$ K $			Frequency [MHz]	(Obs.-calc.) [MHz]
$^{82}\text{Kr-}^{32}\text{SO}_3$						
1	2	0			3826.302	0.000
2	3	0			5739.343	0.000
$^{83}\text{Kr-}^{32}\text{SO}_3$						
$J''$	$J'$	$ K $	$F''$	$F'$		
1	2	0	9/2	7/2	3802.884	0.001
1	2	0	9/2	9/2	3804.688	-0.002
1	2	0	9/2	11/2	3804.688	-0.001
1	2	0	7/2	5/2	3804.905	0.000
1	2	0	11/2	13/2	3805.267	0.000
1	2	0	7/2	7/2	3807.433	0.000
1	2	0	11/2	9/2	3808.397	-0.001
1	2	0	11/2	11/2	3808.397	0.000
1	2	0	7/2	9/2	3809.241	0.001
2	3	0	9/2	7/2	5706.640	0.000
2	3	0	7/2	5/2	5706.874	0.000
2	3	0	11/2	13/2	5707.878	0.001
2	3	0	9/2	9/2	5707.988	0.000
2	3	0	11/2	9/2	5707.988	-0.002
2	3	0	13/2	15/2	5708.198	0.000
2	3	0	7/2	7/2	5708.448	0.001
2	3	0	9/2	11/2	5708.607	0.001
2	3	0	11/2	11/2	5708.607	-0.001
2	3	0	5/2	5/2	5709.401	-0.001
2	3	0	7/2	9/2	5709.795	-0.001
2	3	0	5/2	7/2	5710.980	0.005
2	3	0	13/2	13/2	5711.006	-0.001
2	3	0	13/2	11/2	5711.734	-0.004
$^{84}\text{Kr-}^{32}\text{SO}_3$						
1	2	0			3785.630	0.000
2	3	0			5678.335	0.000
$^{84}\text{Kr-}^{34}\text{SO}_3$						
1	2	0			3743.007	0.000
2	3	0			5614.404	0.000
$^{86}\text{Kr-}^{32}\text{SO}_3$						
1	2	0			3746.742	0.000
2	3	0			5620.006	0.000
$^{86}\text{Kr-}^{34}\text{SO}_3$						
1	2	0			3704.024	0.000

$J''$	$J'$	$ K $			Frequency [MHz]	(Obs.-calc.) [MHz]
2	3	0			5555.933	0.000
$^{82}\text{Kr}-^{32}\text{SO}_3-^{12}\text{CO}$						
3	4	3			3324.701	-0.001
3	4	0			3324.836	0.001
4	5	3			4155.848	0.001
4	5	0			4156.013	0.000
5	6	3			4986.972	0.000
5	6	0			4987.171	0.000
$^{82}\text{Kr}-^{32}\text{SO}_3-^{13}\text{CO}$						
3	4	3			3284.761	-0.001
3	4	0			3284.888	0.000
4	5	3			4105.925	0.002
4	5	0			4106.080	0.000
5	6	3			4927.063	-0.001
5	6	0			4927.252	0.000
$^{83}\text{Kr}-^{32}\text{SO}_3-^{12}\text{CO}$						
$J''$	$J'$	$ K $	$F''$	$F'$		
3	4	0	9/2	9/2	3307.598	0.000
3	4	0	13/2	15/2	3307.690	-0.001
3	4	0	15/2	17/2	3307.859	0.000
3	4	0	11/2	13/2	3307.903	0.003
3	4	0	9/2	11/2	3308.291	-0.001
$^{83}\text{Kr}-^{32}\text{SO}_3-^{13}\text{CO}$						
$J''$	$J'$	$ K $	$F''$	$F'$		
3	4	0	13/2	15/2	3267.878	0.000
3	4	0	15/2	17/2	3268.049	0.001
3	4	0	11/2	13/2	3268.088	-0.001
$^{84}\text{Kr}-^{32}\text{SO}_3-^{12}\text{CO}$						
3	4	3			3291.402	0.000
3	4	0			3291.532	0.001
4	5	3			4114.222	0.000
4	5	0			4114.383	0.000
5	6	3			4937.021	0.000
5	6	0			4937.215	0.000
6	7	3			5759.796	0.000
6	7	0			5760.022	0.000
$^{84}\text{Kr}-^{32}\text{SO}_3-^{13}\text{CO}$						
3	4	3			3251.723	0.000
3	4	0			3251.849	0.000
4	5	3			4064.625	0.001
4	5	0			4064.782	0.000
5	6	3			4877.502	-0.003



$J''$	$J'$	$ K $	Frequency [MHz]	(Obs.-calc.) [MHz]
5	6	0	4877.695	0.001
6	7	3	5690.363	0.000
6	7	0	5690.582	-0.001
$^{86}\text{Kr}-^{32}\text{SO}_3-^{12}\text{CO}$				
3	4	3	3259.407	-0.003
3	4	0	3259.540	0.002
4	5	3	4074.234	0.001
4	5	0	4074.392	0.000
5	6	3	4889.036	0.001
5	6	0	4889.226	-0.001
$^{86}\text{Kr}-^{32}\text{SO}_3-^{13}\text{CO}$				
3	4	3	3219.987	-0.001
3	4	0	3220.112	0.000
4	5	3	4024.956	0.003
4	5	0	4025.108	-0.001
5	6	3	4829.896	-0.002
5	6	0	4830.085	0.001